Experimental and Kinetic Modelling Study of Jet A-1/Ethanol Blend Combustion and Oxidation Stability

By:

Ahmad Syihan Auzani

Supervisors:

Prof M. Pourkashanian

Dr Kevin J. Hughes

A thesis submitted in partial fulfilment of the requirements
for the degree of Doctor of Philosophy

April 2020

Abstract

The increasing demand for air transportation leads to higher jet fuel consumption, and numerous researches have been dedicated to finding a sustainable alternative for fossil fuels, such as bioethanol. Fundamental studies on kerosene/ethanol blend have been reported in the literature; however, they lack a kinetic study and experimental validation. This work aims to provide an accurate kinetic model for simulating jet A-1/ethanol flames and the experimental validation.

The chemical structure of the jet A-1/ethanol flames and two jet fuel surrogates at three stoichiometries in a premixed flat flame-burner have been measured by employing a thermocouple, OH, NO PLIF thermometry, and gas analysis. The experimental data from this work and the literature validates the proposed reaction mechanism that comprises of 541 reactions among 85 species for modelling the jet A-1/ethanol flames. This models jet A-1 as 89% n-decane and 11% toluene while it has a better accuracy than the previous n-decane/toluene model.

The jet A-1 autoxidation characteristics have been evaluated by the PetroOXY fuel thermal stability tester, which showed a decrease with ethanol addition. Nine antioxidants have been tested to improve the oxidation stability of ethanol at 1 g/L. A reaction mechanism generator and a custom PetroOXY model have been employed for modelling jet fuel surrogates and ethanol, which were accurate for predicting the autoxidation of ethanol while optimisation to the mechanisms of jet fuel surrogate is required.

This work gives a novel contribution for the experimental database of jet A-1, ethanol, the blend, and jet fuel surrogates in a flat-flame burner as well as the application of a new approach of OH and NO PLIF quantification and thermometry. The simplified kinetic model of ethanol/jet A-1 facilitates further studies, such as CFD modelling. The ethanol addition to the oxidation stability of jet A-1 and the strategy to improve the ethanol stability are reported for the first time.

Acknowledgement

Contents

List of Figures

List of Tables

Nomenclature

Acronyms

AFRM   Aviation Fuel Reaction Mechanism

ASTM   American Society for Testing and Materials

ATJ   Alcohol to jet

BOC   British oxygen company

CCD   Charge-coupled device

CLA   Chemiluminescence analysis

CORSIA   The Carbon Offsetting and Reduction Scheme for International Aviation

DEF STAN   Ministry of Defence Standard

EN   European Standards

EU ETS   European Union Emission Trading System

FAME   Fatty acid methyl ester

FAR   Fuel-to-air ratio

FTIR   Fourier-transform infrared spectroscopy

GC   Gas chromatography

GCMS   Gas chromatography–mass spectrometry

GHG   Greenhouse gas

GRI   The Gas Research Institute

GTL   Gas-to-liquid

HEFA	Hydroprocessed esters and fatty acids
HPC	High-performance computer
HPLC	high performance liquid chromatography
IATA	The International Air Transport Association
ICAO	The International Civil Aviation Organization
JFTOT	Jet Fuel Thermal Oxidation Tester
JSR	Jet-stirred reactor
LLNL	Lawrence Livermore National Laboratory
MB	Methyl butanoate
MFC	Mass-flow controller
MPA	Magnetic Pressure Analysis
MTD	Methyl tridecanoate
Nd:YAG	Neodymium-doped yttrium aluminium garnet
NDIR	Non-dispersive infrared absorption method
PAH	Polycyclic Aromatic Hydrocarbon
PI-MBMS	Photonionization molecular-beam mass spectrometer
PID	Proportional integral derivative
PLIF	Planar laser-induced fluorescence
PRF	Primary Reference Fuel
PSR	Perfectly-stirred reactor
Pt	Platinum
QSS	Quasi-steady state
Rh	Rhodium
RME	Rapeseed methyl esters
RMG	Reaction Mechanism Genetrator

SEM   Scanning electron microscope

SPK   Synthetic paraffinic kerosene

U.N.   The United Nation

VOC   Volatile Organic Compounds

Species glossary

A   Antioxidant

C_2H_2 Acetylene

C_2H_3 Vinyl/ethylenyl

C_2H_4 Ethylene/ethene

C_2H_5O Ethoxy radical

C_2H_5 Ethyl

C_2H_6 Ethane

C_4H_2 Diacetylene

C_4H_4 Vinylacetylene

C_5H_5 Cyclopentadienyl

$C_6H_4O_2$ Benzoquinone

$C_6H_5CH_2$ Benzyl

$C_6H_5CH_3$ Toluene

C_6H_5CHO Benzaldehyde

C_6H_5CO Benzoyl radical

C_6H_5O Phenoxyl radical

C_6H_5 Phenyl

C_6H_6 Benzene

C_2H_5OH Ethanol

$CH_2(S)$ Singlet methylene/carbene

CH_2CHO	Vinoxy radical
CH_2CO	Ketene
CH_2OH	Hydroxymethyl
CH_2O	Formaldehyde
CH_2	Triplet methylene/carbene
CH_3CHOH	Hydroxyethyl
CH_3CHO	Acetaldehyde
CH_3CO	Acetyl
CH_3OH	Methanol
CH_3O	Methoxy
CH_3	Methyl
CH_4	Methane
CH	Methylidyne
CN	Cyanide
CO_2	Carbon dioxide
CO	Carbon monoxide
C	Carbon
H_2CN	Methylene amidogen
H_2O_2	Hydrogen peroxide
H_2O	Water
H_2	Hydrogen
$HCCO$	Ketenyl radical
HCN	Hydrogen cyanide
HCO	Formyl radical
HO_2	Hydroperoxyl

H	Hydrogen radical
I	Initiator
N_2O	Dinitrogenmonoxide
N_2	Nitrogen
NH	Amine
NO_3	Nitrate
NO_x	Nitrous oxide
NO	Nitric oxide
N	Nitrogen
O_2	Oxygen
OH	Hydroxide
O	Oxygen radical
$R^{\bullet}$	Alkyl radical group
RH	Alkane group
ROH	Alcohol group
ROOH	Hydroperoxide group
ROO	Peroxide group
RO	Alkoxy group
R	Alkane group
SO_2	Sulphur dioxide
SO_x	Sulphur oxide
DMH	Dimethylheptane
HOOQOO	hydroperoxyalkylperoxy radical
MH	Methylheptane
ROO	Hydroperoxyl group
TMP	trimethylpentane

Chapter 1

Introduction

1.1 Aviation Fuel Issues and Challenges

Since the first commercial flight in 1914, the aviation industry has grown rapidly and thousands of airports and other aviation facilities have been built all over the world to enable access to the air transportation. The International Air Transport Association (IATA) [1] reported that the number of passengers of air transportation increased by more than a hundred percent from 1,994 million in 2004 to 4,358 million of passengers in early 2018. The number of tonnes cargo that has been transported by air also increased from 40.9 million tonnes in 2004 to 63.6 million tonnes in early 2018. Clearly, to accommodate this demand on air transportation, the number of flights must be increased, and it was also reported by IATA that this increased from 23.8 million in 2004 to 39 million of flights in early 2018. The fact that the demand on air transportation is increasing lead to the expansion of the aviation business. IATA reported that the revenue of global commercial airlines has increased from 379 billion USD in 2014 to 834 billion USD in early 2018. Further details on the data are presented on Figure 1.1. Considering these trends and the growth of global population projection by the United Nation [20], the demand on air transportation is predicted to increase in the future.

The increasing demand on air transportation directly affected the consumption of aviation fuel, and its price contributed to approximately 30 percent of the total expenses for commercial airlines. Global jet fuel consumption spent more than 100 billion USD for more than 60 billion gallons of jet fuel which was consumed per year [1]. Figure 1.2 presents the global aviation fuel consumption from 2004 to 2018. The fuel is essential in the aviation industry since the operation of an aircraft requires energy which is carried by the fuel. If the utilisation of air transportation is projected to increase in the future, the consumption of aviation fuel will also increase following the trend of air transportation. The supply of jet fuel should be increased to fulfil the global demand of the aviation fuel.
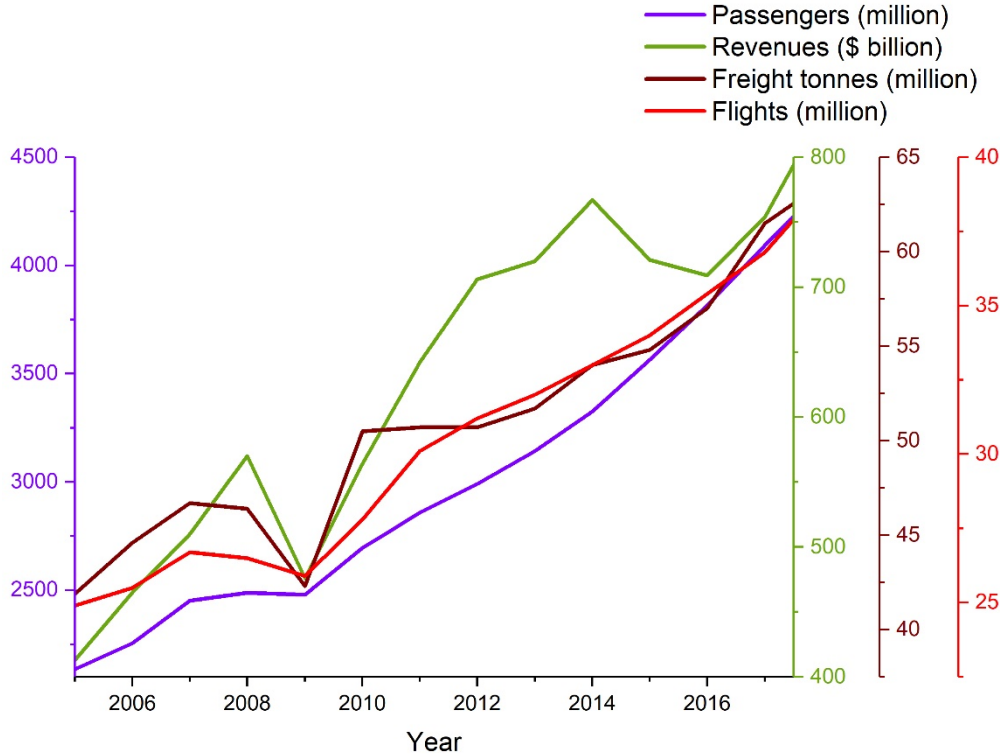
Figure 1.1: Aviation statistics of number of passengers, freight, flights, and revenues from 2004 to 2018 [1].

Since the 1950s when the commercial air transportation was growing, kerosene-based fuel, such as Jet A and Jet A-1, are utilised in most commercial aircraft in the world [21]. Jet A fuel is mostly utilised in the United States, while Jet A-1 is mostly used outside the United States. The main difference between these fuels is that Jet A-1 fuel has lower freezing point with -47°C while the Jet A freezing point is -40°C, therefore it is more suitable for international flights or low temperature flights. The lower freezing point of Jet A-1 fuel is desirable and the amount of it from a refinery is more than Jet A fuel. Consequently, these reasons made Jet A-1 fuel becomes more expensive than Jet A fuel. Considering the price and the availability of these fuels, Jet A has been chosen in the United States and from the performance of the fuel it is satisfactory. However, Jet B fuel is still utilised in Canada and Alaska to overcome the cold temperature. For military purposes, the US air force also uses petroleum-based fuel, such as JP-4 from wide-cut, kerosene-type JP-5 with a higher flash point, and JP-8. RP-3 fuel is used for commercial and military flights in China, while TS-1 and RT fuels are used for civil and military purposes, respectively, in Russia [22].

Emission from jet engines has been considered to contribute to environmental issues, such as air pollution, greenhouse gas emission, and global warming [23]. The major emissions from modern jet engines are carbon dioxide (CO_2), carbon monoxide (CO),
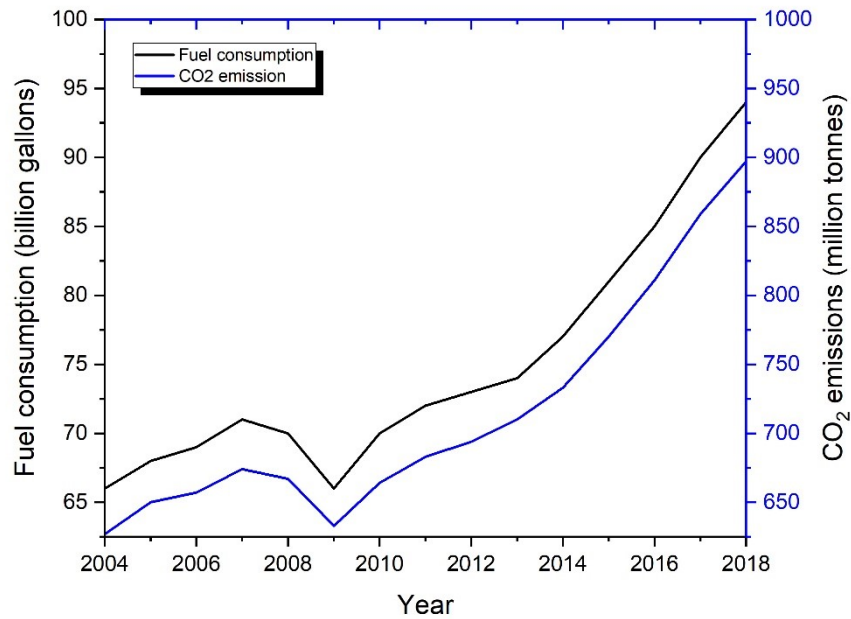
Figure 1.2: Global aviation fuel consumption and CO_2 emission from 2006 to 2016 [1].

nitrous oxide (NO_x), sulphur oxide (SO_x), particulates, volatile organic compounds (VOC), and water vapour (H_2O). As a consequence of utilising hydrocarbon fuel, CO_2 and H_2O are produced from an ideal combustion system, but CO_2 emission is responsible for initiating climate change because of the greenhouse effect. Figure 1.2 illustrates that the CO_2 emission is directly proportional to the jet fuel consumption, which increased from 600 million tonnes in 2004 to 900 million tonnes in 2018 and it contributes to more than 2 percent of the global CO_2 emission [1]. Water vapor is a major emission from hydrocarbon combustion. Releasing it at ground level is not considered as a serious problem, but when the aircraft is at higher altitude, then this may cause the formation of contrail and cirrus cloud [21]. Even though the effect of them is not yet confirmed, they may have an impact on climate change. CO is a toxic gas and it may occur when the combustion process is not complete as well as particulates and unburned hydrocarbon which appear as smoke or soot. These emissions can be reduced by the increasing combustion efficiency. However, increasing the efficiency of the combustion system escalates the pressure and temperature in the system which leads to the increasing of NO_x formation. NO_x causes a change of the ozone concentration which also leads to the enhancement of the greenhouse effect [21] [23]. Meanwhile, the SO_2 emission, which is correlated to particulate and aerosols formation, corresponds to the sulphur concentration in the jet fuel which is required to be lower than 3000 ppm by the Ministry of Defence Standard (DEF STAN) 91-91. Moreover, SO_2 and NO_x emission may cause acid rain because they may react

3

with oxygen, water, and other chemicals in the atmosphere to form sulfuric and nitric acid [24].

1.2 Ethanol as an Alternative Fuel

Considering the serious impact of the emissions from air transportation, the global society has been formulating efforts towards a greener aviation industry. In 2015, the United Nations Framework Convention on Climate Change formulated the Paris agreement which aims to control the global temperature increase to be less than 2°C in this century [25]. The European Commission has prepared strategies to mitigate the greenhouse gas (GHG) emission from the aviation sector through the EU Emission Trading System (EU ETS) which involves the promotion of biofuel and low carbon fuel [26]. Also, The International Civil Aviation Organization (ICAO) decided to implement the Carbon Offsetting and Reduction Scheme for International Aviation (CORSIA), in which one of its focus is employing sustainable alternative fuels for aviation [27].

The prospect of ethanol in the aviation industry becomes more promising after ASTM approved the utilisation of ethanol for producing alcohol-to-jet synthetic paraffinic kerosene (ATJ SPK) in 2016 [28, 29]. However, the use of direct ethanol for aircraft jet engine is not yet approved due to the different chemical and physical properties compared to the conventional jet fuel. The difference in properties may cause atomisation and combustion problem to the jet engine which was designed for conventional jet fuel [30]. The comparison of physical and chemical properties between Jet A-1 and ethanol is presented in Table 1.1. The density of ethanol is in the range of the ASTM standard while the freezing point of ethanol is much lower than the standard which is safer for low temperature flights. Further, ethanol is less viscous than jet A1 fuel which leads to better spray and atomisation characteristics [31]. The net heat of combustion or energy content determines the flight durability of an airplane, which ethanol has less energy content than commercial jet fuel. Also, the low flash point of ethanol would impact on the safety issue of the airplane.

Despite the technical issues that may appear because of the utilisation of ethanol as a jet fuel alternative, it offers benefits for environment and energy sustainability. While the conventional jet fuel has a sulphur content, ethanol has much less sulphur and aromatics which leads to minimum sulphur dioxide and particulate emission [36, 37]. Unlike fossil fuels, which are extracted from earth and releases carbon to the atmosphere through combustion process, ethanol and other bio-derived fuels are considered as a carbon neutral fuel since the carbon being released to the atmosphere comes from plants which absorbs carbon to grow [38]. Bioethanol is considered as a sustainable

Table 1.1: Comparison of physical and chemical properties of conventional jet fuel and ethanol.

Properties	Jet A or Jet A-1 [28]	Ethanol
Density/(kg/m^3) at 15 °C	775 to 840	790 [32]
Freezing point/°C	-40 to -47	-115 [33]
Viscosity/cSt at 20 °C	1.5 to 2.5 [34]	1.4 [31]
Net heat of combustion/(MJ/kg)	42.8	26.8 [31]
Flash point temperature/°C	38	13 [35]
Carbon/wt%	85.7 [34]	52.2 [35]
Hydrogen/wt%	14.3 [34]	13.1 [35]
Sulphur/wt%	0.3	-

fuel since it is derived from renewable resources such as sugar, starch, and cellulosic biomass which could yield more than 300 litres from a tonne of biomass [32].

Bioethanol production has increased in the last ten years and reached 25 billion gallons per year in 2015 as many countries have stated their commitment to decrease fossil fuels consumption [39]. It has been employed to replace gasoline for vehicles with 100 percent or less composition, which 1 litre of bioethanol is equivalent to 0.72 litre of gasoline [40]. Despite the fact that bioethanol has less energy content than conventional fuel, it offers several benefits, such as a higher-octane number which enables a higher compression ratio and faster combustion which minimises the knocking problem in the engine [39]. Blending bioethanol with gasoline would increase the fuel octane number with lower CO and CO_2 emission compared to a conventional octane enhancer. Bioethanol is low sulphur and oxygenated fuel that carries oxygen (C_2H_5OH), which enriches the combustion process with oxygen so the particulate, sulphur oxides, and nitric oxides emission decrease [39]. Study of performance and emission of bioethanol for a gasoline alternative for spark ignition engine has been performed by many researchers as well as for diesel alternative [41, 42]. Chansauria reported that ethanol addition to gasoline could smoothen the engine operation, increase the combustion performance, and has a higher efficiency due to a higher octane rating. The report also mentioned that by adding 15 percent ethanol to gasoline, the pollutant could be reduced to 71 percent while the power generation and engine efficiency increased. Moreover, by adding 5 percent of ethanol to gasoline, the unburned hydrocarbon concentration decreased by 6 percent while the carbon dioxide and NO_x concentration decreased with the increasing of ethanol concentration. In a diesel engine, ethanol addition without any additive to diesel fuel decreases the power and torque output of the engine due to lower energy

content and cetane number of ethanol compared to diesel fuel [42]. Ethanol addition to diesel fuel reduces the emission of soot and smoke, but different study reported different effect to the emission of NO_x, CO, CO_2 in different operating condition [42]. Tay et al. [43] highlighted the application of kerosene in diesel engines, thus the application of kerosene/bioethanol blend may be practical as the alternative fuel for diesel engines.

1.3   Importance of Kinetic Study

Combustion studies have been conducted for many years to generate energy efficiently from fuel and overcome the environmental issues related to air pollution involving many disciplines such as chemistry, physics, thermodynamics, fluid dynamics, heat transfer, mathematics, computation, etc [44]. Curran categorised combustion studies into several levels, which are quantum mechanics and reaction kinetic study, fuel chemistry, modelling study with reduced chemistry and practical application. Combustion kinetics has been an important tool for interpreting basic kinetics experimental studies, such as shock tubes and plug flow reactors which could support a CFD model to understand a complex phenomenon [45]. Many research groups or individual have been developing various chemical kinetic models for different fuels and different reactor models. One of the earliest kinetic model developments is from the Gas Research Institute who developed the GRI mechanism which is able to predict the emission from natural gas combustion [45]. The current GRI mechanism is version 3.0 which has been through many improvements from the previous version, such as NO_x mechanism addition, species and reaction reduction and the optimisation of kinetic parameters through various experimental data validation [46]. The Lawrence Livermore National Laboratory (LLNL) has been developing reaction mechanisms for iso-octane and heptane as a primary reference fuel (PRF) for modelling gasoline combustion [47]. Also, the CRECK modelling group provides a detailed reaction mechanism for most hydrocarbon fuels and the sub mechanisms such as biomass, alcohol, PRF, polycyclic aromatic hydrocarbon (PAH), and real fuel surrogates [48]. A joint research group has been developing a reaction mechanism, which is called the JetSurF mechanism, for modelling jet fuel surrogate containing n-alkane up to n-dodecane, cyclohexane, and mono-alkylated cyclohexane [49]. All these mechanisms are available online for everyone who needs kinetic tools for their modelling study of combustion that reduces the dependency on the experimental work which is limited to the resources, such as time, funding, and instrumentation. However, the reaction mechanisms are validated to a specific reactor condition and not suitable for various temperature, pressure, stoichiometric mixture, and many other reaction parameters [44].

1.4 Oxidation Stability

During distribution, storage or operational process, the fuel chemical and physical properties may change due to an exposure to higher temperature, pressure, or concentration of oxygen [50]. In this condition, oxidation reactions occur where oxygen reacts with fuel and produces peroxides and hydroperoxides [21]. Moreover, these products stay in the fuel and cause the formation of particulates and gums in fuel as well as damaging the elastomer in the fuel system. In terms of physical changes, the degraded fuel has a different colour, density, viscosity, energy content, etc, which may differ from the original fuel specification [50]. The particulates and gums may deposit in particular parts of the fuel system, such as filters, nozzles, heat exchangers and in addition to the change in physical characteristics, reduce the efficiency of the fuel flow, spray, and heat transfer [21].

Fuel stability is the property of the fuel to maintain its characteristics under different ambient conditions, such as temperature, oxygen concentration, and pressure [50]. Generally, the cause of fuel instability is identified from storage and real engine operation which are correlated to the property of storage and thermal stability of the fuel [21]. Basically, conventional jet fuel is designed to remain stable for a year and commonly consumed within months from the production date [21]. However, for some cases, jet fuel may be stored longer than usual, such as for a stock for emergency use in the military or in a small airport that consumes a small amount of fuel [21]. The longer storage time and higher storage temperature amplify the fuel degradation. The fuel degradation in the storage stage will enhance the instability issue during the real engine operation [50]. In modern turbine engines, jet fuel does not only work as an energy carrier, but also as a coolant for the engine system. The heat from the engine increases the the fuel temperature by up to 300 °C with the presence of autooxidation and 400 °C with pyrolysis [51]. At this stage, gums and particulates inhibit the fuel line and surface which reduce the efficiency of the engine system. Also, the maintenance cost and downtime to clean the engine will increase and this impacts on the aviation industry.

Considering the problems that may occur due to the fuel instability, many strategies to prevent the instability issues have been proposed as well as standard for aviation turbine fuel. Balster et al. [51] mentioned four strategies to minimise the fuel instability, and those are removing heteroatom impurities during refining process, improved fuel circulation system to improve component cooling, use of special alloys and coatings for the heated component surface, and the use of antioxidants, metal deactivators to minimise free radicals and dispersants which cause agglomeration [51]. Several standard test method for measuring fuel stability has been developed, such as JFTOT, which is based on ASTM D3241, a standard test method for thermal oxidation stability

of aviation turbine fuels. During the JFTOT test, the fuel sample is circulated at a certain flow rate through a heated line to replicate the real operating condition, and a stainless steel filter for collecting degraded fuel degradation products [28]. The standard specification for aviation turbine fuels, ASTM D1655, requires a maximum pressure drop 25 mmHg from the filter in a 2.5 hours test at 100 °C. Also, the addition of 24 mg/L of several antioxidants to the jet fuel is allowed by the standard jet fuel specification. Meanwhile, the PetroOXY method has been used to examine the jet fuel stability according to ASTM D7545, the standard test method for oxidation stability of middle distillate fuels. This method offers a rapid and small scale oxidation test where the fuel sample is pressurised and heated while the temperature and pressure in the testing chamber is measured. For biofuel, the Rancimat method has been used to evaluate the fuel stability according to EN 14112 and EN 14214. This test evaluates the fuel stability at elevated temperatures of approximately 110 °C and with air circulation. The lower temperature and oxygen concentration causes the Rancimat method to have a longer induction period compared to the PetroOXY method [52].

The trend of using biofuel as an alternative fuel has motivated researchers to study the biofuel stability. Karavalakis et al. [53] studied the stability of diesel/biodiesel blend using Rancimat method, which shown the increase of blended fuel instability with the increasing biodiesel concentration. Also, the stability characteristics of the biodiesel samples varies since it was derived from various animal fats and vegetable oils, which results in different compositions and chemical structures. To improve the stability of biodiesel, the antioxidants addition effect on the biodiesel stability has been studied. Zhou et al. [54] investigated the performance of four different antioxidants with different concentrations to enhance the biodiesel stability. The study indicated that each antioxidant has an unique impact to the biodiesel stability. With the further development of biodiesel resources, a study on biodiesel stability test and strategy to improve its stability has been proposed [55].

1.5 Knowledge Gap

1.5.1 Previous Studies on Ethanol as a Fuel

Considering the prospect of bioethanol for reducing the dependency to fossil fuels, many kinetics studies have been performed to understand ethanol oxidation through experimental and modelling works. A research group from Budapest compiled an available experimental data of ethanol from various reactor conditions and measurements on the ReSpecTh website [4]. These ethanol experimental studies provided more than 10,000 data points of the ignition delay time, laminar flame speed, and concentration of major species, which were used to develop an optimised ethanol reaction mechanism [56].

8

However, none of the major species measurements were taken from a premixed burner flame of an ethanol-air mixture, which might not be suitable for modelling a burner flame.

Recent work by Millan-Merino et al. [57] proposed a skeletal and reduced ethanol mechanism which consists of 66 and 14 reactions from 31 and 16 species, respectively, for various combustion experiments. The performance of the mechanisms was compared against notable ethanol mechanisms, such as San Diego [58], ARAMCO [59], LLNL [47], CRECK [48], and ELTE [56]. The skeletal and reduced mechanisms were able to simulate the laminar burning velocity of ethanol with the least error after the San Diego mechanism. The computational time of the skeletal and reduced mechanism was 71 and 93 percent faster compared to the San Diego mechanism. These mechanisms satisfied further comparison to the counter-flow flame, strain rate extinction, and auto-ignition experimental and simulated data from the San Diego Mechanism.

An experimental study of a premixed laminar flame of ethanol has been studied previously. Sarathy et al. [60] have summarised the existing literature of ethanol and other alcohol experimental and modelling work up to 2014. It is reported that many fundamental experimental works on ethanol have been performed with a counter-flow flame, constant volume reactor, shock tube, flow reactor, jet-stirred reactor, flat-flame burner, spherical/cylindrical vessel, and rapid compression machine with various pressure and other reaction parameters. Also, elementary reactions of ethanol, such as the H-Abstraction and decomposition, have been examined with various reactors at different temperatures and pressures with various detection methods, such as Laser-Induced Flourescence, Gas Chromatograph and Mass Spectrometry, Resonance Flouresence and Absorption. These experimental data have facilitated the development of an ethanol reaction mechanism towards more accurate models.

Sarathy et al. [60] summarised the previous ethanol kinetic modelling work as well as the experimental data that has been used as the validation. Egolfopoulos et al. [61] developed a model by targeting the experimental data from the laminar flame speed, species profiles of the flow reactor, and the ignition delay time. Marinov updated the rate parameters of ethanol decomposition and H-abstraction and validated the reaction mechanism against the ignition delay time, laminar flame speed of a combustion bomb and counter-flow flame, and species profiles from a jet-stirred and turbulent flow reactor [62]. Saxena et al. [63] developed an ethanol reaction mechanism which consists of 288 reactions among 57 species and has a NO_x mechanism. The mechanism, which is also well-known as the San Diego Mechanism, was validated against autoignition-delay data from a shock-tube, laminar flame speed, counterflow diffusion and premixed flame measurements. Also, Lee et al. [64] optimised an ethanol reaction mechanism development based on a rapid compression machine and shock tube experimental data.

The development of these mechanisms was focussed on the laminar flame speed, ignition delay, and counter-flow flame experimental data and was not validated against burner flame experimental studies, which may be inaccurate for modelling the burner flame.

Studies on a premixed burner flame of ethanol have been performed experimentally, as well as the reaction mechanism development. Leplat et al. [65] investigated ethanol/O_2/Ar combustion in a flat-flame burner with lean, stoichiometric, and rich mixtures at sub-atmospheric pressure, 50 mbar. The measurement of species concentration from this experiment, as well as from jet-stirred reactor, and published experimental data have been employed to develop an ethanol reaction mechanism, which is in good agreement with the experimental data. Ergut et al. [66] studied an ethanol/O_2/N_2 flame in a flat-flame burner at atmospheric pressure and rich mixture of 2.5. The modelling study of this work showed a good agreement with the species concentration from the flat-flame species measurement at 10 mm from the burner surface.

Also, ethanol flat flame studies have been conducted for lower and higher atmospheric pressure with different mixtures. Kasper et al. [67] conducted experimental investigation of ethanol/oxygen/argon combustion in a flat-flame burner, which measured the temperature and species concentration at different positions above the burner surface at 50 mbar, and stoichiometric mixture of 1 and 2.57. Leplat et al. [68] investigated an experimental study on stoichiometric ethanol/oxygen/argon combustion in a flat-flame burner at 50 mbar and compared the performance of the Dunphy, Dagaut, Norton, and Marinov Mechanisms with the measured species profile mole fraction at several positions up to 1.5 cm above the burner surface. It was concluded from the comparison that the mechanisms were in a good agreement with the major species concentration profiles and required improvement for modelling minor species concentration profiles. Tran et al. [69] studied a premixed laminar flame of ethanol in a flat-flame burner at 6.7 kPa, 333 K and stoichiometric ratio 0.7, 1.0, and 1.3. 20 species concentrations were measured at different positions above the burner surface using online gas chromatography. For the kinetics modelling study, Tran et al. [69] developed a reaction mechanism that employs several reactions from previous studies and this is suitable for modelling all the measured species concentrations.

The study of ethanol-air combustion in a flat-flame burner at atmospheric pressure and temperatures of 298 to 358 K have been performed by Konnov et al. [70] from 0.65 to 1.55 equivalence ratio range. Van Lipzig et al. also studied the laminar burning velocity of ethanol using the heat flux method at atmospheric pressure, 0.6-1.5 equivalence ratio, and 298 and 338 K [71]. Both studies were focused on the introduction of the heat flux method to measure the laminar burning velocity of ethanol in a flat-flame burner while the measurement of species concentration and temperature profiles were not included in this study. Knorsch et al. [12] used the heat flux method for measuring

the laminar burning velocity of ethanol at 373 and 423 K with a fuel-to-air ratio from 0.65 to 1.6. However, this work was focused on the comparison of the laminar flame speed measurement results against other publication, while the kinetics modelling and species concentration measurement study were not included. Gillespie [72] measured the laminar flame speed of ethanol/air flame with a flat-flame burner at 358 K, atmospheric pressure, and 0.60 to 1.55 equivalence ratio. The measurement results were compared against an ethanol reaction Mechanism by Mittal et al. [73] and Metcalfe et al. [74] including the sensitivity analysis for the elementary reactions, but the species concentration profile was not discussed.

Measurement and modelling of major and intermediate species concentration of ethanol/oxygen/argon combustion in a flat-flame burner at 4 kPa has been performed by Xu et al [75]. In this study, major species, $C_1, C_2,$ and C_3 intermediate species concentration were collected by a photoionization mass spectrometer, while the temperature profile was collected by a 0.1 mm Pt–6%/Rh/Pt–30%Rh thermocouple. Furthermore, the measured species concentrations were compared against the ethanol mechanisms from Marinov, Zhao, Saxena, and the GRI-based mechanism. It was found that revisions to the reaction rate of several elementary reactions and in addition to the missing C_1–C_3 intermediate species are required to model the experimental results. The revised version of the reaction mechanism has a better agreement with the measured species concentration profile compared to the previous reaction mechanisms.

Liang et al. [76] measured the laminar burning velocity of ethanol/air flame using a cylindrical combustion chamber at 383 K, 0.1 MPa, and stoichiometric mixture of 0.7 to 1.6. For the kinetic modelling, the ethanol mechanism from Li [77] was selected to model the premixed laminar flame using the PREMIX program and for the laminar flame speed simulation, the reaction mechanism from Marinov and Saxena were included. The modelling study was able to identify the elementary reactions that were sensitive to the laminar flame speed by changing the water concentration through a sensitivity analysis.

1.5.2 Previous Studies on Jet Fuel

Real jet fuels consist of numerous hydrocarbons [78] which makes it more difficult to model compared to a pure substance. A carbon number distribution ranging from 8 to 16 is commonly found in a kerosene-type jet fuel, while the carbon number distribution of 5 to 15 is commonly found in wide-cut jet fuel, and mostly member of paraffin, naphthene, and aromatic class [21]. Surrogate models have been proposed to simplify the jet fuel components, including single, binary, ternary, and multicomponent blends to represent the kinetic model of jet fuel combustion [79, 80]. The performance of the surrogate models were evaluated based on their accuracy to represent real jet fuel

characteristics of combustion and kinetics study. Numerous fundamental combustion experiments on real jet fuels and surrogates have been performed in different reactors and conditions as well as the proposed reaction mechanisms. Many of them have been reviewed by Dagaut et al., Honnet et al., and Alekseev et al. [18, 79, 80].

Flat-flame burner experiments have been employed to investigate the combustion of kerosene-based jet fuel and its surrogates. Delfau et al. [81] studied n-decane/oxygen/ argon combustion in a flat-flame burner at 6 kPa, and equivalence ratio of 1.9. A temperature profile was obtained from a measurement using a thermocouple for the input of the flame simulation, which the simulated species profiles were in a close agreement with the measured species profile using the beam-mass spectrometry technique. Vovelle et al. [82] compared the production of aromatics hydrocarbons in an oxygen/argon premixed decane and kerosene flame at 6 kPa, equivalence ratio of 2.2 in a flat-flame burner. This study resulted in temperature and species concentration profiles from a coated thermocouple and molecular beam mass spectrometry, respectively. Several elementary reactions were added to the previous kerosene mechanism which agreed with the measured species profile, including acetylene, benzene, phenyl acetylene and vinyl benzene. A similar study for comparing the formation of soot and aromatics hydrocarbon from jet A-1 and n-decane flame in a flat flame burner was also performed by Vovelle et al. [83]. A further experimental and modelling study of the comparison between the chemical structure of a kerosene and decane flame was conducted by Douté et al. [84, 85]. In the experimental part, n-decane/oxygen/nitrogen, as well as kerosene/oxygen/nitrogen, flame structures were compared in a flat-flame burner at atmospheric pressure and rich mixture at 1.7 equivalence ratio. The species concentration profiles were measured using a probing method and gas chromatography analysis while the temperature profile was measured using a thermocouple. These experimental results were used to validate the kinetic modelling work in the later publication by comparing the simulated species fraction profile with the measured temperature profile input to the measured species concentration profile.

Kinetic schemes for modelling kerosene combustion have been proposed previously and validated with measurements from flat-flame burner experiments. Vovelle et al. [82] modelled kerosene as n-decane and toluene with ratio of 90 and 10 percent, respectively, in 207 reversible reactions among 39 species. The model was able to predict the major and aromatics species concentration profile from the experimental work, but this scheme does not have an NO_x mechanism as well as experimetal validation to NO and OH concentration. Lindstedt et al. [86] proposed 1085 reversible reactions among 193 species for modelling a kerosene flame with a surrogate of n-decane and toluene by 89 to 11 mole percent, respectively. The model was validated against the experimental data of a premixed laminar flame from Doute et al. [84] and Delfau et al. [81], which

shows less than 15 percent error for major species and approximately 50 percent for a hydrogen concentration profile.

Riesmeier et al. [87] validated the kerosene mechanism from Bikas et al. [88, 89] against the premixed laminar flame results from Douté et al. [84] . The reaction rate parameters were updated in order to approach the experimental validation data. The reaction mechanism consists of 600 reactions among 67 species, which was able to assist a CFD code for modelling a flamelet model in a gas turbine combustion chamber. The experimental data from Douté et al. [84] was employed by Violi et al. [90] to develop a reaction mechanism of JP-8.

In the past two decades, the Energy Research Group at the University of Leeds, and now at the University of Sheffield, has developed several aviation fuels reaction mechanisms (AFRM). Patterson et al. [91] developed a reaction mechanism of kerosene using a surrogate model of 89 and 11 percent of a decane and toluene mixture with experimental validation from the jet-stirred reactor from Cathonnet et al. [92], pre-mixed laminar flame from Vovelle et al. [83] and Douté et al. [84] and counter-flow diffusion flame from their work. From this study, the first generation of the AFRM was produced consisting of 440 mostly reversible reactions and 84 species, which is able to model the targetted experimental validation of kerosene combustion. Further work on AFRM was performed by Kyne et al. [93] for the reduction of the AFRM to 165 reactions among 60 species based on reaction rate analysis, which was not reducing its accuracy for predicting the laminar burning velocity of kerosene. Other reaction mechanism reduction methods were performed by Elliott et al. [94,95] who utilised a genetic algorithm method which was able to optimise the reaction rate parameters towards the experimental data validation. The compared simulation results of a premixed laminar flame to the experimental data from Doute et al. [84] and a jet-stirred reactor to the experimental data from Dagaut et al. [96] showed that the reaction mechanism from this optimisation method outperformed the previous versions of AFRM in terms of predicting the experimental data.

The next generation of the AFRMs were developed by the Energy Research Group at the University of Leeds to accomodate novel jet fuel resources from fatty-acid methyl esters (FAME), methyl butanoate (MB), methyl tridecanoate (MTD), and synthetic "Gas-to-liquid" (GTL) fuel. Catalanotti et al. [97] developed a reaction mechanism to accomodate jet fuel mixtures of kerosene and FAME, which was represented as methyl butanoate. The kerosene sub mechanism was obtained from the original AFRM, while the MB mechanism was taken from the available literature. Similar reactions that exist in both sub mechanisms was removed from the MB sub mechanism, which results in 1556 reactions among 280 species. Perfectly-stirred reactor simulation results were compared against the available jet-stirred reactor experiment of kerosene and the

original kerosene mechanism. The comparison showed that the performance of the combined reaction mechanism behaved differently compared to the original kerosene mechanism. Further work by Catalanotti et al. [98] added methyl tridecanoate (MTD) to the reaction mechanism to represent the bio jet fuel component. However, these reaction mechanisms were not validated against kerosene/MB or kerosene/MTD due to the lack of experimental data. Later experimental studies for validating the reaction mechanism of biofuel, Fischer-Tropsch, biodiesel, and kerosene blends in a flat-flame burner were performed to develop and optimise the proposed reaction mechanism [99, 100].

1.5.3 Previous Studies on Ethanol-Kerosene Blend

Considering the sustainability of ethanol, many fundamental combustion studies have been conducted to understand the characteristics of a conventional fuel blended with ethanol. Xu et al. [101] investigated the effect of ethanol and methanol addition to reference fuels, heptane/toluene flame premixed with oxygen and argon at 4 kPa in a flat-flame burner. Species concentration detection, which used photonionization molecular-beam mass spectrometer (PI-MBMS) technique, was compared against a kinetic model, which was developed from several sub-mechanisms of individual fuels. The results show that the presence of ethanol does not affect fuel degradation products, while increases the concentration of intermediate products, such as formaldehyde and acetaldehyde. The kinetic model was able to predict the measured mole fraction and was used to discover the reactivity of the OH and HO_2 reactions with the presence of alcohol through a sensitivity analysis.

Despite the fact that direct use of ethanol is not approved for aviation turbine fuel, fundamental combustion researches have been performed to study ethanol blended jet fuel. Khan et al. [102] investigated kerosene/ethanol blends with various ethanol concentration below 20 percent in a wick stove because kerosene has been used as an energy resource for cooking. From this study, it was concluded that no modification was required to the wick stove for ethanol addition up to 20 percent and the maximum thermal efficiency was found at 5 percent of ethanol blend. This study is lacking in measurement instrumentation and no kinetic model was proposed.

An experimental study of a kerosene/ethanol blend in a cylindrical combustor was performed by Patra et al. [103] which focused on flame brightness, temperature of the combustor wall, CO, and CO_2 concentration at the exhaust. The study discovered that by increasing the ethanol concentration to 5 and 10 percent, the flame luminosity was reduced due to lower soot production while the flicker frequency remained the same. The temperature of the combustor wall was decreased with the increasing of the ethanol concentration while the CO and CO_2 concentrations at the exhaust were

decreased because of the lower carbon content of ethanol. This study did not involve flame measurements inside the combustion chamber or any modelling work.

An experimental study of the spray characteristics of ethanol blended jet fuel was conducted by Song et al. [104] with a high-pressure common rail injection system. This study was focused on the penetration of the spray tip, cone angle, area, and concentration distribution of the spray. The comparison between several ethanol concentrations up to 30 percent shows that 20 percent of ethanol blend demonstrated ideal spray characteristics of an aviation gas turbine. The combustion characteristics of Jet A-1/ethanol flame droplets have been investigated by Rao et al. [30] for several ethanol concentration up to 50 percent. The combustion of the droplets was observed by imaging tools and image analysis. It was discovered that unlike the individual fuel components that burned smoothly, the blend indicated a disruptive nature, such as puffing, micro and abrupt explosion. Also, the variation in the ethanol concentration in the blend did not affect the explosion diameter and the bubble growth rate. An experimental study of the atomisation of kerosene/ethanol fuel in an acoustic field was performed by Ju et al. [105] using high-speed imaging. This study resulted in the influence of the acoustic field being bigger to that for ethanol than kerosene and this was because of the smaller size of the ethanol droplet. However, these studies did not include the combustion of the fuel blends.

Among the available reaction mechanisms in the literature, the detailed CRECK mechanism [48] is suitable for modelling a kerosene/ethanol flame because of the inclusion of ethanol species as well as jet fuel surrogates. Moreover, many experimental studies have been performed to validate its sub mechanisms at various conditions and different reactors. However, according to the CRECK Modelling Group website, validation to experimental flat-flame data has not been performed for ethanol and kerosene.

1.5.4 Previous Studies on Oxidation Stability

Considering the importance of the oxidation stability properties of jet fuel, many researches have been performed to study the stability characteristics of the fuel using PetroOxy as well as other methods. Sicard et al. [106] studied the oxidation stability of n-dodecane as a jet fuel surrogate using PetroOXY method and gas chromatograph to analyse the gas and liquid products. The test was performed at 150 °C and 700 kPa and the analysis was focused on the pressure drop and detection of species concentration during the test. From the GC analysis, it is shown that the concentration of n-dodecane was decreasing with time and other products were formed, such as alcohols, ketones, and acid carboxylic from the reaction with oxygen in the liquid phase which is estimated approximately to be 70 ppm. After the oxygen in the liquid phase was consumed, the oxidation reaction was stopped and new reactions started to produce

esters and lactones through decarbonylations and condensation reactions.

The study of the oxidation of Synthetic Paraffinic Kerosene (SPK) and fuel surrogates has been performed by Webster et al. [107], who employed a custom thermal stability rig, PetroOXY, high performance liquid chromatography (HPLC), Fourier-transform infrared spectroscopy (FTIR), and GC method to measure the oxidation products. In this study, C_9 to C_{14} alkanes, toluene, methyl cyclohexane, and trimethyl pentane were tested at 140 °C and initial pressure of 700 kPa and the pressure was observed to have a 10 percent pressure drop. From the study, it was found that the surrogate fuel and SPK oxidation stability was similar to hydrotreated jet fuel for military use, which required approximately 5 hours for the induction period. The species detection methods were able to identify polar species, furanones, alkyldihydrofuranones in the fuel samples.

Experimental and modelling studies of real jet fuel and its surrogate components have been studied by Mielczarek [108] using PetroOXY method and reaction mechanism generator (RMG). It was found that RMG could accurately simulate the oxidation of normal paraffinic hydrocarbon, but struggles with iso paraffinic hydrocarbon. The PetroOXY test results were used to validate the RMG model, but no species measurement was used from this test to validate the model. The initial oxygen concentration for the modelling work was obtained from an approximation using Henry's Law which the initial oxygen concentration value in liquid phase was similar for all solvents. However, the initial oxygen concentration should vary with different fuel samples as it has different Henry constants and maximum pressure during the PetroOXY test, which affects the initial oxygen concentration.

The PetroOXY method was used by Rawson et al. [109] to study the oxidation stability of alternative jet fuels with a monoaromatic blending with a GCMS for analysing the oxidised sample. The study found that the monoaromatic and iso-paraffinic concentration in the fuel affected the induction time of the fuel blends. It was identified that the addition of p-cymene to synfuel increased the hydroperoxides concentration while the trialkyl aromatic addition increased the fuel stability by extending the induction period. Comparison between conventional Merox and hydroprocessed fuels showed that Merox had better oxidation stability based on the PetroOXY induction period. Further work by Rawson et al. [110] investigated the effect of antioxidants in addition to aged Merox and hydroprocessed jet fuels oxidation stability. The PetroOXY test at 700 kPa and 140 °C was used up to 10 percent pressure drop as well as the GCMS method to identify the antioxidants concentration in the samples. All fuels in the induction period of the PetroOXY test were improved with the addition of the antioxidants. The results showed that the antioxidant addition had only a minor effect on the formation of peroxides. The antioxidant addition to Merox fuel only improve the

fuel stability slightly since Merox fuel is sufficiently stable. The study on antioxidant addition showed that the peroxides were measurable after several weeks of storage, which indicates that the antioxidants were not effective for inhibiting the formation of peroxides.

Identification of secondary and tertiary oxidation products of alternative and conventional jet fuel using the GC method was performed by Webster et al. [111]. A custom rig and PetroOXY device were employed to apply thermal stress to the fuel sample. The results showed that this method was able to identify the secondary and tertiary oxidation products of the fuel samples.

The effect of cyclic molecules addition to alternative jet fuel was studied by Amara et al. [112]. The alternative fuel was SPK from Hydroprocessed Esters and Fatty Acids (HEFA-SPK) which was tested using JFTOT and PetroOXY method to assess its thermal and oxidation stability. The results shows that the HEFA-SPK was less stable compared to real jet fuel and this is due to the lack of a cyclic compound. Further, the addition of Alkylbenzenes improved the HEFA-SPK induction time of the PetroOXY test. The study showed that the stability of the HEFA-SPK could be improved by adding decalin, tetralin, and methylbenzenes, such as toluene and xylene at low concentration.

A detailed reaction mechanism of toluene autooxidation was proposed by Mielczarek et al. [113]. The RMG program was employed to generate the reaction mechanism which consist of 2309 reactions among 173 species. The thermodynamic data of 32 key species were updated using a quantum chemistry calculation which qualitatively improved the model compared to the original version from RMG. The PetroOXY method was used to validate this model which involved experimental data from three different temperatures. The model was not able to predict the induction period of the PetroOXY test and a sensitivity analysis discovered that the rate parameters had little impact on the temperature.

Oxidation stability of Jet A-1 fuel blended with rapeseed methyl esters (RME) was investigated by Baczewski et al. [114]. The oxidation stability of five different blending composition of both fuels was measured using PetroOXY method. It was found that the addition of Jet A-1 fuel improved the oxidation stability of RME by extending the induction period of the PetroOXY test. However, this study is limited to preliminary findings and a further study should be performed.

Further identification of oxidation products in conventional and alternative jet fuels was performed by Webster et al. [115] by implementing two-dimensional gas chromatography and accurate mass time-of-flight mass spectrometry. From this study, tens of thousands of species were identified in the termally oxidised fuel samples. However, this study was limited to the development of a species identification technique and re-

quires further study in order to explain the oxidation mechanism based on the species finding.

A recent study by Chatelain et al. [116] presented experimental and modelling study of the autoxidation of octane isomers such as n-octane (C8), 2-methylheptane (MH), 2,5-dimethylhexane (DMH), and the 2,2,4-trimethylpentane (TMP). The experimental work involved the PetroOXY test at 140 °C and 700 kPa up to 10 percent pressure drop and the oxidised samples were analysed in a GCMS to analyse their species components. The results showed that the reactivity of TMP decreases exponentially with the branchings number. The modelling work employed the RMG code for generating the reaction mechanism with thermochemical and transport libraries from the GRI 3.0 mechanism and a model of zero-dimensional reactor. The model performed well in reproducing the temperature dependence of the oxidation, but less accurately predict the branching effect for n-octane and DMH. Sensitivity and rate of production analysis identified that ROO and HOOQOO radicals were involved in the fuel consumption.

1.6 Research Objectives

Regardless of the current limitation in the air transportation technology and policy in employing ethanol as an alternative fuel, the kinetics aspect of ethanol, jet fuel and the blends are considered in this study. Reflecting on the works that have been presented in the literature review, this idea leads to questions on the kinetic aspects and leaves a knowledge gap in the literature. Therefore, the objectives of this study are as follows:

- Evaluate the existing reaction mechanisms of jet fuel and ethanol and develop a model for predicting an ethanol/jet fuel flame with experimental validation from the literature and the current work.

- Establish a rig for flat-flame burner experiment for investigating an ethanol/jet fuel flame with the available measurement techniques as well as the comparison to real jet fuel, surrogates, and ethanol.

- Investigate the effect of ethanol addition to jet fuel oxidation stability through experimental and kinetic modelling work as well as the evaluation of antioxidants for improving the fuel stability.

1.7 Structure of the Thesis

The organisation of this thesis are as follows:

- **Chapter 1: Introduction**

  This chapter introduces the reader to the background problems and the urgency of this research by providing facts and data, such as the energy supply, demand, environmental issues and the prospective of bioethanol. Furthermore, a review of the previous work is presented to identify the knowledge gap in this area of research. Then, the description of this research is presented including the scope, objectives, and contribution of this work to the development of combustion and kinetics studies.

- **Chapter 2: Literature Review**

  This chapter provides basic theories that are mentioned in the thesis discussion and a review of the previous study and relevant literature of this topic. This chapter supports the identification of the knowledge gap that is mentioned in the previous chapter to ensure the originality and novelty of this work.

- **Chapter 3: Burner Flame Experiment Setup**

  This chapter describes the experimental work and set up for preparing the premixed laminar flame study as well as the details of the instrumentations that were used for the measurement and diagnostics. Also, the problems that were found during the experimental preparation and attempts to solve the issue are presented to assist in the improvements in future works.

- **Chapter 4: Burner Flame Experiment Results**

  This chapter presents the experimental results and further analysis that are obtained by performing the measurement and diagnostics of a premixed laminar flame using different mixtures and this is followed by a discussion of the results. The fuels that have been investigated are real jet A-1 fuel, two surrogates, and a blend of ethanol and jet A-1 fuel in three different stoichiometric mixtures with air. The flame diagnostics comprises of both intrusive and non-intrusive temperature measurement, major emission species gas analysis, OH and NO radicals detection.

- **Chapter 5: Kinetic Modelling**

  This chapter explains the development of the reaction mechanism for modelling ethanol, jet fuel, and the mixture for various combustion reactors. This involves the validation of the proposed mechanism as well as performance evaluation of notable reaction mechanisms against the available experimental data from the literature. Reaction path analyser and sensitivity analysis tools are employed to explain the transformation of species in the reactor models.

- **Chapter 6: Oxidation Stability**

This chapter presents the experimental work for the assessment of the oxidation stability of the jet fuel, surrogates, ethanol, and blends using PetroOXY method. This includes the experimental setup, testing method, results, and discussion about the results. This chapter demonstrates the modelling work to simulate the oxidation stability test. The models are validated against the experimental data that is obtained from the PetroOXY test. Also, the discussion about the model performance for predicting the experimental data is presented as well as the sensitivity and reaction path analysis.

- **Chapter 8: Conclusion and Future Works**
  This chapter summarises all the findings that have been presented in the previous chapters. Also, suggestion for future works is provided for the continuation and improvement of this research.

Chapter 2

Literature Review

2.1 Chemical Kinetics

Chemical kinetics is a part of physical chemistry which studies the quantitative rate of chemical reactions and the aspects that affects the rate, such as temperature, pressure and species in the reaction system. This has been employed to explain the reaction path from the initial reactants to the final products, the determination of the duration of the process, and to identify the factors that control the system, such as slow elementary reactions. This study involves an experimental study to assess the rate of the reactions, development of a theoretical model of a reaction mechanism, and the prediction of the chemical process [117].

A chemical reaction is a transformation from one species to another through a chemical reaction while a combustion reaction is a reaction between the fuel and the oxidiser to form combustion products [118]. A combustion reaction can be expressed in a single stoichiometric reaction or overall reaction where the molar ratio of the reactant species is determined. However, this rarely occurs in a real chemical system because intermediates are produced from the initial reactants and this forms more reaction steps [119]. Each reaction step is called an elementary reaction, and the combination of the elementary reactions form a reaction mechanism.

2.1.1 Reaction Rate

A general combustion reaction of fuel (F) and oxidiser (O) to form combustion products (P) can be described as F + O $\longrightarrow$ P. The reaction rate of this reaction, r, can be determined experimentally by measuring the change of fuel concentration or oxidiser with respect to time as follows:

$$r = -\frac{d[\text{F}]}{dt} = -\frac{d[\text{O}]}{dt} \tag{2.1}$$

From the measurement of the change of the reactant concentration with time, a reaction rate equation can be expressed as follows:

$$r = k[\text{F}]^a[\text{O}]^b \tag{2.2}$$

where a and b are the reaction order of the fuel and oxidiser, respectively, which can be determined by experimental measurement. To obtain a, the fuel concentration is varied while the oxidiser concentration remains constant, and the reverse to acquire b. The negative symbol represents that the reaction consumes the fuel and oxidiser to form the combustion products. Meanwhile, k is the rate constant of the reaction, which changes with temperature and sometimes with pressure.

Arrhenius [120] proposed a theory which states that a molecule requires a minimum energy of E_a to react. The energy is obtained from collisions between the reactant molecules that are caused by the temperature. The Arrhenius equation expresses the temperature dependence of the rate constant, and it is given as follows:

$$k = A\,exp(-\frac{E_a}{RT}) \tag{2.3}$$

where A is the collision frequency factor while $exp(E_a/RT)$ is the Boltzmann factor, which indicates the fraction of the collisions that possess a higher energy level than the activation energy, E_a [117], R is the universal gas constant, and T is the temperature.

$$\ln k = \ln A - \frac{E_a}{RT} \tag{2.4}$$

The natural logarithmic of Equation (2.3) becomes Equation (2.4), and this is commonly used in the kinetic studies as it follows a linear correlation of the rate constant and the inverse of temperature. However, these equations often cannot be used to describe a wide temperature range. To overcome this issue, a modified Arrhenius equation was proposed, which is given by.

$$k = A\left(\frac{T}{T_{ref}}\right)^n exp(-\frac{E_a}{RT}) \tag{2.5}$$

where n is an arbitrary factor to account for the non-linearity in $\ln k$ as a function of $1/T$. While T_{ref} is the reference temperature, usually 1 K. On substituting the value of T_{ref} into Equation (2.5) yields:

$$k = AT^n exp(-\frac{E_a}{RT}) \tag{2.6}$$

and the natural logarithmic form is expressed as follows:

$$\ln k = \ln AT^n - \frac{E_a}{RT} \tag{2.7}$$

The values of A, n, and E_a are unique in each elementary reaction, and they are used to describe the rate of a reaction in a kinetic model.

The rate of reaction of some isomerisation and decomposition reactions can be pressure dependent at a given temperature [119]. At high pressure, the reaction rate is first-order and pressure independent, while at low pressure, it is second-order and linearly dependent on the pressure. Lindemann et al. [121] and Hinshelwood [119] observed this phenomenon in cyclopropane decomposition. They found that the cyclopropane became rovibrationally excited by the collisions with other molecules. Consequently, the cyclopropane molecule reacted through the isomerisation process, thus resulting in propene or returned to the non-excited state through other collisions with other molecules. In this reaction, only one species experiences chemical transformation, and this is called a unimolecular reaction. At an intermediate pressure, the reaction rate can be calculated using the Lindemann approach while at high and low pressure, the Lindemann and Arrhenius formula can be used to derive the pressure-dependent reaction as expressed in Equation (2.6).

The information of the elementary reactions is commonly written in a CHEMKIN format as illustrated in the following example:

```
!Reaction 1
2O+M<=>O2+M                              1.200E+17   -1.000         .00
H2/ 2.40/ H2O/15.40/ CH4/ 2.00/ CO/ 1.75/ CO2/ 3.60/ C2H6/ 3.00/ AR/  .83/
!Reaction 2
O+CO(+M)<=>CO2(+M)                       1.800E+10    .000     2385.00
   LOW/ 6.020E+14     .000    3000.00/
H2/2.00/ O2/6.00/ H2O/6.00/ CH4/2.00/ CO/1.50/ CO2/3.50/ C2H6/3.00/ AR/ .50/
```

It is taken from the GRI Mechanism 3.0 [46]. A reaction mechanism file must list the elements and species that are involved in the reaction. Then, all of the elementary reactions with the stoichiometric coefficient must be listed as well as the value of the rate parameters, such as A, n, and E_a. Special symbols can be used for indicating the participation of an arbitrary third body (+M), pressure-dependent rate reaction ((+M)), photon (hv), electron (E) and ignored comments (!). For the third body participation, the information of the third body efficiency must be listed below the reaction, while for the pressure-dependent reaction, fall-off formulation (TROE) and low pressure limit parameters (LOW) must be supplied after the reaction.

2.1.2 Thermodynamics

During the reaction, energy in the system can be released or consumed by the reaction, and this is known as an exothermic or endothermic process, respectively. The energy conservation in the reactor system is analysed using thermodynamics, which is

employed for calculating the heat of formation, equilibrium constant, and equilibrium concentration [122]. The calculation requires the value of thermodynamic parameters, such as the heat capacity at constant pressure (C_p), enthalpy (H), and entropy (S) of the reactants and products in the system.

For computational purposes, NASA polynomials have been used to define the value of the thermodynamic parameters of a species, and for calculating C_p, Equation (2.8) is used:

$$\frac{C_p}{R} = \sum_{n=1}^{N} a_n T^{n-1} = a_1 T^0 + a_2 T^1 + a_3 T^2 + ... + a_n T^{n-1} \tag{2.8}$$

The enthalpy can be obtained from the first integral of the C_p with temperature, and this yields the following Equation:

$$\frac{H}{R} = \int_{T_0}^{T} C_p dT = a_1 T^1 + \frac{a_2}{2} T^2 + \frac{a_3}{3} T^3 + ... + \frac{a_n}{n} T^{n-1} \tag{2.9}$$

Meanwhile, the entropy can be acquired from equation:

$$\frac{S}{R} = \int_{T_0}^{T} \frac{C_p}{T} dT = a_1 \ln T + a_2 T + \frac{a_3}{2} T^2 + \frac{a_4}{3} T^3 + ... + \frac{a_n}{n-1} T^{n-1} \tag{2.10}$$

where R is the universal gas constant.

From the heat capacity, enthalpy and entropy, more thermodynamic parameters can be obtained. The final combustion temperature can be calculated using the first law of thermodynamics and the Hess law, which states that the standard enthalpy of an overall reaction is equal to the sum of the enthalpy of the elementary reactions [122]. On using the following equation:

$$\Delta H_f = \sum_{products} (\nu H_f) - \sum_{reactants} (\nu H_f) \tag{2.11}$$

enthalpy of the overall reaction can be obtained, on dividing by with the heat capacity, the temperature of the reaction can be acquired. Here, ν is the stoichiometric coefficient, while H_f is the heat formation of the products and reactants. The equilibrium constant, K_{eq}, which is the ratio of the forward (k_f) and the reverse (k_r) reaction rate can also be derived from these thermodynamic parameters using the following equation:

$$K_{eq} = \frac{k_f}{k_r} = \exp\left(-\frac{\Delta G}{RT}\right) \tag{2.12}$$

G is the Gibbs free energy which can be calculated as follows:

$$G = H - TS \tag{2.13}$$

The polynomial coefficients are commonly written in a NASA polynomial and as an example:

24

```
O2                 TPIS89O  2              G   200.000  3500.000  1000.000     1
 3.28253784E+00 1.48308754E-03-7.57966669E-07 2.09470555E-10-2.16717794E-14     2
-1.08845772E+03 5.45323129E+00 3.78245636E+00-2.99673416E-03 9.84730201E-06     3
-9.68129509E-09 3.24372837E-12-1.06394356E+03 3.65767573E+00                     4
```

which is taken from the GRI mechanism 3.0 [46]. The first line informs the species name, followed by the date, atomic formula, phase of the species, low, high, intermediate temperature, and the line number. The second line contains the value of coefficients a_1 to a_5 that is used for the coefficient inputs for Equation (2.8), (2.9), and (2.10) for high temperature range. The third line denotes the value of the coefficients a_6 and a_7 for the higher temperature range followed by a_1, a_2 and a_3 for the lower temperature range. The fourth line contains the value of the coefficient a_4, a_5, a_6, and a_7 for the lower temperature range.

2.2 Chemical Kinetic Tools

2.2.1 CHEMKIN Package

One of the many well-known chemical kinetics modelling software is the CHEMKIN package software, which was developed by the Sandia National Laboratories, Reaction Design, and now ANSYS. The CHEMKIN package was initially introduced in 1980 by Kee et al. [2] for simulating a kinetic model and has been updated in several versions for improvement and features addition. The program consists of a gas-phase subroutine library and an interpreter, which processes the reaction mechanism and thermodynamics data input to a data file for the gas-phase subroutine library. The subroutine library consists of about one hundred subroutines that update the information of the thermodynamics, reaction rate properties, and the equation of state for the application code. A schematic of the structure of the CHEMKIN package is shown in Figure 2.1. Since the first version, the updates involve the capability to calculate the rate of pressure-dependent, reversible reactions, and simplified method to solve the governing stiff differential equation.
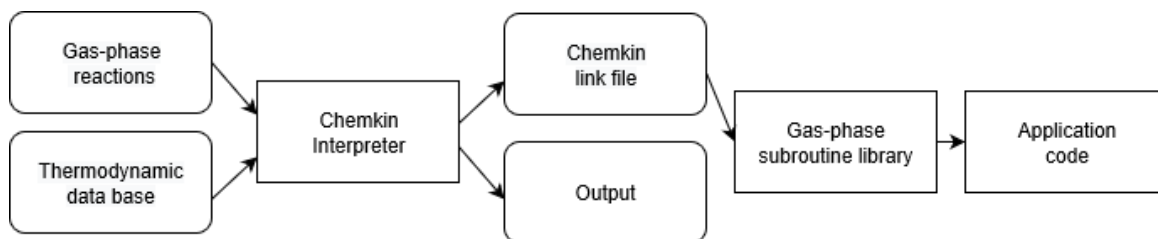
Figure 2.1: Schematic of the CHEMKIN package structure [2].

The application codes that were used in this work are PREMIX, PSR, and SENKIN.

Premix is utilised to model the one-dimensional freely propagating flames and burner-stabilised flames, while PSR and SENKIN are utilised to model other combustion processes, such as the species profile and the ignition delay time.

CHEMKIN has several packages, and one version may be different from another version or package. Nevertheless, the governing equations in the CHEMKIN software are common to all the versions and packages. Some minor differences of the equations from different versions and packages of CHEMKIN are neglected for the purposes of this research.

2.2.2 PSR

The Perfectly-Stirred Reactor (PSR) is a Fortran program that was introduced by Glarborg et al. [3] for modelling the species composition and the steady-state temperature in a perfectly-stirred reactor. Experimentally, the continuously-stirred reactor has been applied for the study of a chemical process as well as combustion, and this method has been found to be useful when studying the overall and elementary reaction rates of the reaction process through the measurement of the species concentration at the inlet and outlet of the reactor. Both the experiment and the model of this system are relatively simple. Thus the computing time and requirement can be minimised for a large reaction mechanism.

Figure 2.2 illustrates a schematic of a perfectly-stirred reactor and the boundary conditions. The reactor wall is non-reactive and insulated in order to minimise the heat loss and has an inlet and outlet ducts, where reactants and products enter and exit the reactor at a specified flow rate. The flow is designed to be turbulent, so the reactants are assumed to be uniformly mixed inside the reactor by high-velocity injection or mechanical mixer, with no species or temperature gradient, and the reactions are only controlled by the reaction rates. The flow rate, $\dot{m}$ and the volume of the reactor, V determine the residence time, τ, which measures the duration for which the reactants undergo chemical processes inside the reactor as expressed as follows:

$$\tau = \frac{\rho V}{\dot{m}} \tag{2.14}$$

The density, ρ, can be calculated as follows:

$$\rho = \frac{P\overline{W}}{RT} \tag{2.15}$$

where P, R, and T are the pressure, the universal gas constant, and temperature, respectively, while $\overline{W}$ is the average of the molecular weight of the mixture.

The PSR program solves the governing non-linear algebraic equations and uses a hybrid Newton/time-integration method. When the Newton method fails to converge, the time integration of the transient problem provided a trial solution to find
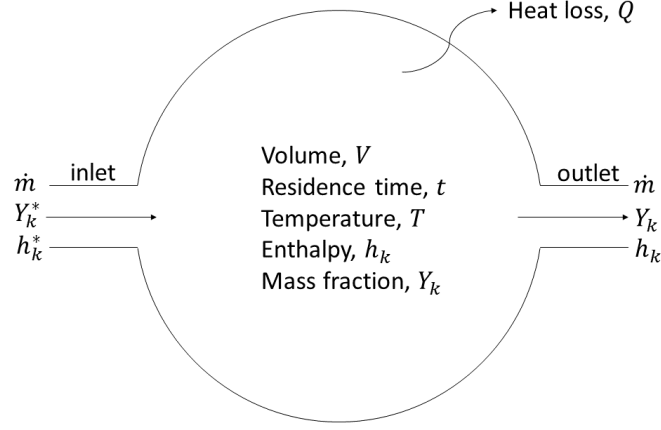
Figure 2.2: Schematic of a perfectly-stirred reactor [3].

the convergence of the Newton method. The program uses the finite-rate elementary reaction and requires the CHEMKIN package to interpret the reaction mechanism and the thermodynamic data. The conservation of mass and species is described as follows:

$$\dot{m}(Y_k - Y_k^*) - \dot{\omega}_k W_k V = 0 \tag{2.16}$$

where $\dot{m}$ is the mass flow rate; $\dot{\omega}_k$, W_k, Y_k^* and Y_k are the volumetric molar rate of production, molar mass, the mass fraction of the kth species at the inlet, and the outlet of the reactor, respectively. $\dot{\omega}_k$ can be obtained by solving the reaction mechanism according to the forward rate of the modified Arrhenius equation, which is described in Equation (2.6). Meanwhile, the conservation of energy is expressed as follows:

$$\dot{m} \sum_{k=1}^{K} (Y_k h_k - Y_k^* h_k^*) + Q = 0 \tag{2.17}$$

where Q is the heat loss and h_k is the specific enthalpy of the kth species. $k + 1$ algebraic equations can be derived from Equation (2.16) and (2.17) resulting in the solution for the steady-state temperature and mass fractions of the species. For the transient problem, mass conservation can be calculated analogously using:

$$\frac{dY_k}{dt} = -\frac{1}{\tau}(Y_k - Y_k^*) + \frac{\dot{\omega} W_k}{\rho} \tag{2.18}$$

while the energy balance at constant pressure can be solve using:

$$\frac{dh}{dt} = -\frac{1}{\tau} \sum_{k=1}^{K} (Y_k h_k - Y_k^* h_k^*) - \frac{Q}{\rho V} \tag{2.19}$$

By re-arranging the equation of mass-weightted enthalpy, h, to temperature and merging Equations (2.18) and (2.19), the transient energy can be solved by using:

$$c_p \frac{dT}{dt} = \frac{1}{\tau} \sum_{k=1}^{K} Y_k^*(h_k^* - h_k) - \sum_{k=1}^{K} \frac{h_k \dot{\omega}_k W_k}{\rho} - \frac{Q}{\rho V} \tag{2.20}$$

The rate-of-production and sensitivity analysis are also available for the further analysis of the simulation results.

2.2.3 PREMIX Code

Premix is a Fortran program that was introduced by Kee et al. for modelling species profiles and temperature in a laminar-premixed flame [123]. There are two configurations that are available in this program, namely a burner-stabilised and a freely-propagating flame. The burner-stabilised case requires a known mass flow rate while the temperature can be calculated by the energy equation or given as an input from an experimental measurement, which is more common and more accurate as the chemistry relies on the temperature profile. The accuracy of the energy equation can be improved by measuring or eliminating the heat loss from the flame to the environment. The freely-propagating flame model calculates the laminar burning velocity, species profile, and the temperature of a premixed flame using the energy equation. The governing equation for an isobaric one-dimensional flame are mass continuity, energy, and species conversion, and equation of state, which are expressed as follows:

$$\dot{M} = \rho u A \tag{2.21}$$

$$\dot{M}\frac{dT}{dx} - \frac{1}{c_p}\frac{d}{dx}\lambda A\frac{dT}{dx} + \frac{A}{c_p}\sum_{k=1}^{K}\rho Y_k V_k c_{pk}\frac{dT}{dx} + \frac{A}{c_p}\sum_{k=1}^{K}\dot{\omega}_k h_k W_k = 0 \tag{2.22}$$

$$\dot{M}\frac{dY_k}{dx} + \frac{d}{dx}(\rho A Y_k V_k) - A\dot{\omega}_k W_k = 0 \tag{2.23}$$

$$\rho = \frac{p\overline{W}}{RT} \tag{2.24}$$

Where $\dot{M}$ is the mass flow rate, λ is the thermal conductivity of the mixture, V_k is the diffusion velocity of the kth species, and $\dot{\omega}_k$ is the production rate of species k which is calculated by solving the chemistry input using the forward Arrhenius coefficient and Equation (2.6). The thermodynamic and reaction mechanism data are supplied by the CHEMKIN package.

PREMIX requires transport data which consists of species name, geometry, Lennard-Jones well depth (ε/k_b), Lennard-Jones collision diameter (σ), dipole moment (μ), polarisability (α), and rotational relaxation (Z_{rot}). The value for the species geometry can be 0, 1, or 2 for a single atom, linear, or non-linear, respectively. An example of transport data from the GRI Mechanism 3.0 [46] is as follows:

```
C              0    71.400    3.298    0.000    0.000    0.000 ! *
CH             1    80.000    2.750    0.000    0.000    0.000
CH4            2   141.400    3.746    0.000    2.600   13.000
O2             1   107.400    3.458    0.000    1.600    3.800
OH             1    80.000    2.750    0.000    0.000    0.000
```

The data is interpreted by the TRANSPORT software, which was introduced by Kee et al. [124], in a transport library.

The combustion gas mixture generally consists of more than one species and the transport properties of the mixture may be calculated using the mixture-averaged or a multicomponent diffusion model. The diffusion velocity, V_k, for the mixture-averaged model can be calculated using Equation (2.25) and for the multicomponent transport model using Equation (2.26):

$$V_k = \mathsf{V}_k + \mathsf{W}_k + V_c \tag{2.25}$$

$$V_k = \mathsf{V}_k + \mathsf{W}_k \tag{2.26}$$

Where V_c is the velocity correction, which is used to satisfy the sum of the mass fraction in Equation (2.27):

$$\sum_{k=1}^{K} Y_k V_k = 0 \tag{2.27}$$

W_k is the non-zero thermal diffusion velocity, which is included for species with low molecular weight, such as He, H, or H_2. The non-zero thermal diffusion velocity is determined using Equation (2.28):

$$W_k = \frac{D_{km}\Theta_k}{X_k}\frac{1}{T}\frac{dT}{dx} \tag{2.28}$$

with the function of thermal diffusion ratio, Θ_k, which represents the diffusion of lightweight species from low to high-temperature section. Where V_k is the ordinary diffusion velocity which is calculated using the Curtiss-Hirschfelder approximation, which is expressed in Equation (2.29):

$$\mathsf{V}_k = -D_{km}\frac{1}{X_k}\frac{dX_k}{dx} \tag{2.29}$$

for mixture averaged model. D_{km} is the mixture-averaged diffusion coefficient, which is calculated using Equation (2.30):

$$D_{km} = \frac{1 - Y_k}{\sum_{j \neq k}^{K}\frac{X_j}{D_{kj}}} \tag{2.30}$$

D_{kj} is the binary diffusion coefficient, and X_k is the mole fraction of species k.

In the multicomponent transport model, the ordinary diffusion velocity is defined as follows:

$$\mathsf{V}_k = \frac{1}{X_k\overline{W}}\sum_{j \neq k}^{K} W_j D_{k,j}\mathbf{d_j} \tag{2.31}$$

where $\overline{W}$ is the average of the species molar mass, W_j is the molar mass of species j, and $\mathbf{d_j}$ is defined by:

$$\mathbf{d_j} = \nabla X_k + (X_k - Y_k)\frac{1}{P}\nabla P \tag{2.32}$$

Meanwhile, the thermal diffusion velocity is calculated using:

$$W_k = \frac{(D_k)^T}{\rho Y_k} \frac{1}{T} \nabla T \tag{2.33}$$

where $(D_k)^T$ is the thermal diffusion coefficient of species k. The multicomponent transport model is preferable and more accurate than the mixture-averaged model for cases in which the thermal diffusion effect is important.

2.2.4 SENKIN

SENKIN is a program for simulating the time-dependent chemical kinetics of a uniform gas mixture in a closed system using the finite reaction rate for the reaction mechanism [125]. The output of the program provides the simulated species concentration and the temperature with respect to time as well as a tool for a sensitivity analysis. The program was designed for the modelling of a reactor with five different conditions, namely adiabatic and constant pressure; adiabatic and constant volume; adiabatic and specified volume function of time; constant pressure and temperature; and constant pressure and specified temperature function of time. For combustion studies, this is suitable for modelling a shock tube, rapid compression machine, and bomb reactor.

For all these cases, the initial temperature, pressure, and species concentration of the mixture are given, while the density is calculated using an equation of state. The chemical species production rate, $\dot{\omega}_k$, is calculated according to thermodynamics and forward reaction rate reactions in the modified Arrhenius form in Equation (2.6) from the CHEMKIN package. As SENKIN simulates a closed reactor, there is no mass entering or leaving the system i.e. $dm/dt = 0$. The mass of the kth species, m_k can be calculated from the molar production rate, $\dot{\omega}_k$ and volume of the system, V as follows:

$$\frac{dm_k}{dt} = V \dot{\omega}_k W_k \tag{2.34}$$

On re-arranging Equation (2.34) with the specific volume, $\nu = V/m$, mass fraction can be calculated as follows:

$$\frac{dY_k}{dt} = \nu \dot{\omega}_k W_k \tag{2.35}$$

For the cases with no specified temperature, the energy equation thermodynamics law is required to derive the energy equation. In an adiabatic closed system, the energy equation may be expressed as follows:

$$c_v \frac{dT}{dt} + p \frac{dv}{dt} + \nu \sum_{k=1}^{K} e_k \dot{\omega}_k W_k = 0 \tag{2.36}$$

where c_v is the heat capacity of the total species at constant volume or $c_v = \sum_{k=1}^{K} Y_k c_{v,k}$, e_k is the internal energy of species k, while p is the pressure.

2.2.5 Sensitivity Analysis

Sensitivity analysis is a tool to determine the effect of the change of a parameter to the results of the simulation. This method is useful in identifying the most important parameters in the model as well as the uncertainty of the model based on the uncertainty of the parameter using an uncertainty analysis method. Turanyi [119] suggested that model validation is incomplete without a sensitivity analysis since the inaccurate parameters may be found to be in an agreement with the model and experimental data. According to the scale of the sensitivity analysis, there are local and global sensitivity analyses, which can be performed using many different methods.

2.2.6 Cantera

Cantera [126] is an alternative software package to the CHEMKIN packages for modelling problems which involve chemical kinetics, thermodynamics, and transport phenomena. Unlike CHEMKIN, which has been commercialised by ANSYS, it is an open-source software and can be freely downloaded. It has been widely used for modelling combustion studies, such as premixed laminar flame, closed, stirred reactor, etc. It can be installed as an imported library in several platforms, such as Matlab, Python or C++, and it is easier for the users to develop the program. Also, it is easier to be executed by the University's high-performance computing server for faster execution time. Similar to CHEMKIN, it requires the reaction mechanism, thermodynamics, and transport data, but it must be converted to `.cti` or `.xml` format, which can be achieved by using the code `ck2cti.py`.

2.2.7 RMG

Reaction Mechanism Generator (RMG) was introduced by Gao et al. [127] for creating a detailed reaction mechanism from a database of recognised reaction mechanism and estimation methods. The program predicts reactions that are possible between the species, then determines the kinetic and thermodynamic parameters. The species and reactions are categorised into functional groups and templates to determine the reactions for similar species. The thermodynamic data of the species is calculated using the Benson group method or quantum chemistry. The generated mechanism is provided in the CHEMKIN format and can be imported to another program, such as CHEMKIN or Cantera.

RMG has the feature of being able to generate a reaction mechanism for a liquid phase reaction. The ratio of species concentration at equilibrium in the gas ($C_{k,g}$) and liquid phase ($C_{k,l}$) is defined by a partition coefficient, C_K, which may be expressed as

follows:

$$C_K = \left(\frac{C_{k,l}}{C_{k,g}}\right)_{eq} \tag{2.37}$$

The chemical potential of a species k is calculated as follows:

$$\mu_k = \mu_k^* + RT \ln C_K \tag{2.38}$$

and the change in the Gibbs free energy of the species k may be calculated as follows:

$$\Delta G_{k,l} = -RT \ln C_K = -RT \ln \left(\frac{C_{k,l}}{C_{k,g}}\right)_{eq} \tag{2.39}$$

The interaction between the solute and the solvent is calculated using Abraham's Linear Solvation Energy Realationship which is expressed as follows:

$$\log_{10} C_K = c + aA + bB + sS + eE + lL \tag{2.40}$$

A, B, S, E, and L represent the properties of the solute, which is obtained from experimental data, while c, a, b, s, e, and l represent the properties of the solvent, which are obtained from several linear regression on partition coefficient data from a library database. The terms aA and bB are related to the free energy change from the hydrogen bonds formation between the solute and the solvent. The terms sS and eE are related to the the intermolecular interactions, while the term lL is related to the free energy change of the cavity formation, and c is a correction factor.

The change in the first order temperature dependant Gibbs energy of the solvent, ΔG_{solv}, is calculated as follows:

$$\Delta G_{solv}(T) = \Delta H_{solv}^o - T\Delta S_{solv}^o \tag{2.41}$$

the change of enthalpy of the solvent, ΔH_{solv}^o, is determined as follows:

$$\Delta H_{solv}^o = c' + a'A + b'B + e'E + s'S + l'L \tag{2.42}$$

where the value of c', a', b', e', s', and l' are obtained from a regression of the experimental data. The effective rate constant, k_{eff} for reactions with diffusion limited transport is given by:

$$k_{eff} = \frac{4\pi r D k_r}{4\pi r D + k_r} \tag{2.43}$$

where r is the total of the radii of the reactants, k_r is the intrinsic reaction rate, and D is the total of the diffusivities of the species.

2.3 Equivalence Ratio

The equivalence ratio or stoichiometric mixture is a parameter, which is used to express the ratio of the fuel and oxidiser mixture in a combustion reaction. By changing the

equivalence ratio of the fuel and oxidiser mixture, the characteristics of the combustion reaction may change [128]. Therefore, it is essential to know the value of the equivalence ratio in a combustion reaction, especially in the kinetic studies.

The equivalence ratio is represented by the Greek symbol ϕ, and it is equivalent to the ratio of the fuel-to-oxidiser in the reaction compared to the fuel-to-oxidiser ratio in the stoichiometric condition. In the stoichiometric reaction, which is used for the comparison, all the fuel and the oxidiser molecules were assumed to react entirely without any remaining molecules which are not reacted, i.e. it is the amount of oxidiser which is sufficient to oxidise the amount of fuel. The amount of fuel and oxidiser in the calculation may be expressed in mole, mass, or volume fraction as long as a consistent unit is used for calculating the ratio of the fuel and the oxidiser. If the amount of the fuel and oxidiser in the reaction is precisely similar to the stoichiometric condition, the value of the equivalence ratio is 1 and this is said to be stoichiometric. If it is more than the stoichiometric condition, then the value of the equivalence ratio is more than 1 and this is said to be a fuel-rich condition. If it is less than the stoichiometric condition, then the value of the equivalence ratio is less than 1, i.e. a fuel-lean condition.

The equations:

$$\phi = \frac{FAR_{reaction}}{FAR_{stoichiometric}} \tag{2.44}$$

$$\phi = \frac{\left(\frac{n_{fuel}}{n_{air}}\right)_{reaction}}{\left(\frac{n_{fuel}}{n_{air}}\right)_{stoichiometric}} \tag{2.45}$$

express the mathematical definition of the equivalence ratio, where $FAR_{reaction}$ and $FAR_{stoichiometric}$ are the ratio between the fuel and the oxidiser ratio in the reaction and the stoichiometric condition, respectively. While n_{fuel} and $n_{oxidiser}$ are the amounts of the fuel and oxidiser, respectively, in the mole basis, and these variables could be substituted by mass, volume, or molar fraction.

2.4 Development of the Reaction Mechanisms

Reaction mechanisms can be categorised into several levels according to the complexity and accuracy of the reactions and the species that are involved in the model [129]. The first level is the perfect fidelity model, which consists of true reactions parameters, species, and thermodynamics that are involved in a reaction process based on nature. Many researches have been dedicated to achieving this level of detail through researches. However, these efforts have not unveiled all the phenomena and thus resulting in the second level of mechanism accuracy, which is a detailed chemistry model. The detailed chemistry is relatively large in terms of the number of species and reactions and therefore it demands more computing capacity for the execution of the model. The effort employed to simplify the detailed mechanism without sacrificing the

accuracy of the main species reactions results in the third level of mechanism accuracy, which is the reduced mechanism of the detailed chemistry scheme. The fourth level of mechanism accuracy is the empirical model, which is constructed for specific experimental data validation.

There are many methods that can be used to reduce a reaction mechanism, such as a sensitivity-based analysis, quasi-steady-state analysis, and species lumping [119]. The sensitivity analysis-based reduction method identifies the redundant unimportant species and reactions and then removes them from the reaction mechanism. The species lumping method identifies similar species reactions and merges them into the fewer number of reactions and species. The quasi-steady state (QSS) method identifies the QSS species, which are usually intermediates, low-concentration, and highly reactive. Then, the QSS species production rate is set to zero in order to reduce the reaction step. These reduction methods have been used to simplify a reaction mechanism to be more focused on the important species with an optimum number of reactions and species.

A reaction mechanism undergoes updates in its development with the increase in the direct and indirect experimental validation. Turanyi [4] summarised the step-by-step tutorial for optimising a reaction mechanism, and this is illustrated in Figure 2.3. There are many databases that provides the experimental data, such as ReSpecTh [4], NIST [130], PrIME [131], Cloudflame [131], ChemKED [132], and ChemConnect [133]. The selection of the data must be applied to filter the inaccurate results from the accurate experimental data. The accuracy of the model can be determined from the deviation to the experimental data.
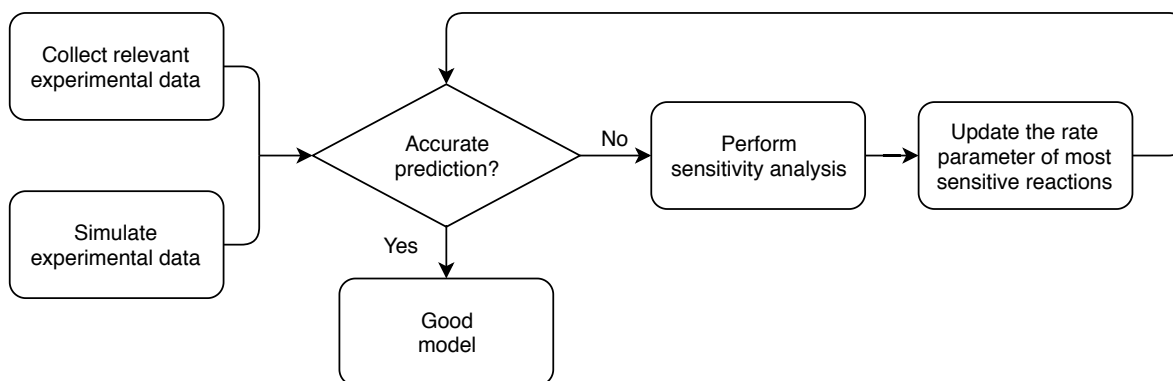
Figure 2.3: Schematic of the steps in the optimising of a reaction mechanism [4].

2.5 Gas-Phase Oxidation Mechanisms

The complexity of a reaction mechanism depends on the structure of the fuel. A larger hydrocarbon oxidation model has more elementary reactions than a smaller fuel. Also, the larger hydrocarbon mechanism involves several smaller sub-mechanisms since its breaks into a smaller species during the combustion processes.

2.5.1 H_2 / O_2

The hydrogen oxidation mechanism is important since hydrogen is one of the major components of a hydrocarbon and possible initiations of hydrogen oxidation are as follows:

$$H_2 + M \longrightarrow 2\,H + M \tag{R.2.1}$$

$$H_2 + O_2 \longrightarrow H + HO_2 \tag{R.2.2}$$

The Reaction R.2.1 is the initiation reaction at high temperature, while Reaction R.2.2 is that at low temperature [117].

The formation of a hydrogen atom from the initiation step causes chain reactions that involve oxygen and radicals as follows [117]:

$$H + O_2 \rightleftharpoons OH + O \tag{R.2.3}$$

$$O + H_2 \rightleftharpoons H + OH \tag{R.2.4}$$

$$H_2 + OH \rightleftharpoons H + H_2O \tag{R.2.5}$$

$$O + H_2O \rightleftharpoons 2\,OH \tag{R.2.6}$$

Chain terminating steps involve the production of $O_2, H_2,$ and H_2O via third body recombination reactions. There are 11 more reactions that must be involved when the H_2O_2 and HO_2 species are considered in the reaction mechanism. Numerous reaction mechanisms have been proposed for the modelling of hydrogen combustion and with validation against many experimental data [134, 135]. With the increasing experimental data validation, the reaction mechanism has been optimised to accurately model a wider range of pressures, temperatures, and mixtures. Consequently, earlier hydrogen combustion mechanisms have been invalidated and replaced with more recent mechanisms.

The early development of the hydrogen mechanism was focused on modelling a single experimental data set, which leads to uncertainties in the elementary reaction parameters. Ó Conaire et al. [136] attempted to construct a hydrogen mechanism with more than one targetted experimental dataset. The structure of the mechanism was based on revisions to the rate parameters in the initial reactions, which were taken from Kim et al. [137] and Mueller et al. [138]. The validation data was obtained from a variety of shock tubes, flame speeds, burner-flames, and flow reactor measurements. A

comparison the performance with the previous mechanisms showed that the mechanism was better in terms of the consistency and the availability of diluent species.

Recent work by Varga et al. [135] have optimised the hydrogen combustion mechanism developed by Keromes et al. [134] against numerous direct and indirect experimental data. The indirect measurement consists of more than a hundred data sets from shock tubes, rapid compression machines, and flame speed measurements. A local sensitivity analysis was performed to identify 11 reactions that have the most influence on the simulation of the experimental data. After optimising the reaction rate and the third body collision efficiency parameters, a more accurate hydrogen mechanism for 800 to 2300 K, 0.1 to 65 bar, and 0.2 to 5.0 equivalence ratio was obtained. The mechanism was compared to 13 previous hydrogen mechanisms and it had the least error among the compared mechanisms.

2.5.2 CO

The carbon Monoxide (CO) mechanism is the most important mechanism after the hydrogen mechanism since all hydrocarbons combustion forms carbon dioxide in addition to water. In hydrocarbon combustion, the fuel produces carbon monoxide and oxidises to carbon dioxide [139]. The oxidation of CO is relatively slow, but it can be faster with the presence of water or hydrogen because CO oxidation with a hydroxyl radical is faster compared to with O_2 and O. This caused difficulties in the early development of the hydrogen mechanism because of the impurities in the hydrogen [140]. The carbon monoxide oxidation is relatively simple, and is given by the following reactions:

$$CO + O + M \rightleftharpoons CO_2 + M \tag{R.2.7}$$

$$CO + O_2 \rightleftharpoons CO_2 + O \tag{R.2.8}$$

With the presence of a hydrogen atom, the oxidation mechanism becomes related to the hydrogen/oxygen reactions through the following reactions:

$$CO + OH \rightleftharpoons CO_2 + H \tag{R.2.9}$$

$$CO + HO_2 \rightleftharpoons CO_2 + OH \tag{R.2.10}$$

These reactions are important at very high pressure and the early steps in the hydrocarbon oxidation, where the H_2O species is at high concentration. Reaction (R.2.9) is the main route of CO_2 production, but it depends on the concentration of the OH radical. The reaction between OH and other species is faster than the Reaction (R.2.9), and therefore the presence of hydrocarbon species reduces the oxidation of CO to CO_2. When all the intermediates fragments and original hydrocarbon are consumed, the OH concentration increases and oxidises CO to CO_2through the Reaction (R.2.9).

The CO and H_2 combustion mechanisms have been updated with the increased publication of direct and indirect experimental studies. An experimental study of

H_2/CO combustion in a variable pressure flow reactor for the pressure and temperature ranges of 0.3 to 15.7 atm and 850 to 1040 K, respectively, were conducted by Mueller et al. [138]. From this study, measurement of the H_2, O_2, and H_2O species concentration and temperature were obtained. The data was combined with the recent publication of rate parameters and other indirect measurements to construct a H_2/CO combustion reaction mechanisms. The proposed kinetic model was able to accurately simulate the targetted experimental data and produced a new explosion limit of H_2/O_2/N_2 mixture from 0.4 to 6.5 atm.

Further development of the H_2/CO model was performed by Davis et al. [141] who updated the reaction mechanism with the latest thermodynamic, kinetic, and transport data of the related species. The model was able to predict most of the H_2/CO experimental data. Further improvement of the model was performed by optimising the rate parameters to the targetted indirect measurement data from various reactors, and this removed the discrepancies between the model and the validation.

Saxena and Williams [142] suggested several revisions to the CO and H_2 initiation as well as the three-body recombination and chaperon efficiencies. The revisions resulted in good agreement between the model and the targetted indirect measurement form of the laminar flame speed, extinction of the diffusion flame, and ignition delay times. Furthermore, Sun et al. [143] measured the laminar flame speed of various mixing ratios of CO/H_2/air and CO, H_2, O_2 mixtures in an isobaric spherical vessel at pressures up to 40 atm. A reaction mechanism based on the recent publication of reaction rate parameters was able to predict the experimental data as well as other published indirect measurements from a counterflow flame, flow reactor, and shock tube. Li et al. [144] published species concentration data for formaldehyde combustion in a variable pressure flow reactor at 850 to 950 K and 1.5 to 6.0 atm. The data, together with other published data from the literature, were utilised to update the mechanism of CO/H_2O/H_2/O_2. The proposed mechanism was able to simulate a wide range of experimental results from the laminar burning velocity, shock tube ignition delay time, and flow reactor species concentration.

2.5.3 C_1-C_2 Hydrocarbons

Methane is an aliphatic hydrocarbon with a single carbon atom. Apart from the fact that methane is the major constituent of natural gas, its mechanism is important in hydrocarbon combustion where larger hydrocarbons break down to smaller fragments, such as CH_4 [128]. Therefore, before considering a larger hydrocarbon, methane combustion should be studied earlier based on the hierarchy of the reaction mechanism.

The methane mechanism starts with H atom abstraction to form a methyl radical through the following possible reactions [117]:

$$CH_4 + M \rightleftharpoons CH_3 + H + M \qquad (R.2.11)$$

$$CH_4 + O_2 \rightleftharpoons CH_3 + HO_2 \qquad (R.2.12)$$

$$CH_4 + H \rightleftharpoons CH_3 + H_2 \qquad (R.2.13)$$

$$CH_4 + OH \rightleftharpoons CH_3 + H_2O \qquad (R.2.14)$$

$$CH_4 + O \rightleftharpoons CH_3 + OH \qquad (R.2.15)$$

$$CH_4 + HO_2 \rightleftharpoons CH_3 + H_2O_2 \qquad (R.2.16)$$
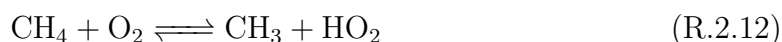
Subsequently, the methyl radical reacts with O_2 through the following possible reactions as the major routes of the methyl radical oxidation [117]:

$$CH_3 + O_2 \rightleftharpoons CH_3O + O \qquad (R.2.17)$$

$$CH_3 + O_2 \rightleftharpoons HCO + H_2O \qquad (R.2.18)$$

$$CH_3 + O_2 \rightleftharpoons CH_2O + OH \qquad (R.2.19)$$

The methyl radicals can form larger hydrocarbon species, through the following reactions:

$$CH_3 + CH_3 \rightleftharpoons C_2H_6 \qquad (R.2.20)$$

$$CH_3 + CH_3 \rightleftharpoons C_2H_5 + H \qquad (R.2.21)$$

$$CH_3 + CH_3 \rightleftharpoons C_2H_4 + H_2 \qquad (R.2.22)$$
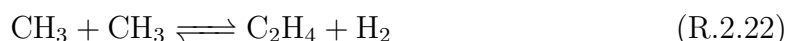
Recombination between methyl and methylene can occur, especially in a rich mixtures where methyl radical is at high concentration.

The other radicals that can also react with the methyl radical are through the following reactions [117]:

$$CH_3 + OH \rightleftharpoons CH_3O + H \qquad (R.2.23)$$

$$CH_3 + CH_2O \rightleftharpoons CH_4 + HCO \qquad (R.2.24)$$

$$CH_3 + HCO \rightleftharpoons CH_4 + CO \qquad (R.2.25)$$

$$CH_3 + HO_2 \rightleftharpoons CH_3O + OH \qquad (R.2.26)$$

At a very high temperature, the methyl radical can undergo a hydrogen atom elimination through the reaction [117]:

$$CH_3 + M \rightleftharpoons CH_2 + H + M \qquad (R.2.27)$$

Also, a singlet methylene radical ($CH_2(S)$) can be produced from the reaction [128]:

$$CH_3 + OH \rightleftharpoons CH_2(S) + H_2O \qquad (R.2.28)$$
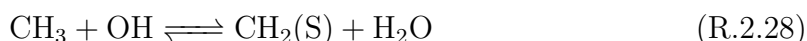
which is a very reactive species. It is mainly converted to a more stable triplet CH_2 radical through collisions with other molecules. Both CH_2 and $CH_2(S)$ radicals can react with O_2 to produce OH radical which accelerate the overall reaction as follows:

$$CH_2(S) + O_2 \rightleftharpoons CO + H + OH \qquad (R.2.29)$$

$$CH_2 + O_2 \rightleftharpoons HCO + OH \qquad (R.2.30)$$

Some CH_2 yield the CH radical through the H atom abstraction which is rapidly attacked by H_2O or O_2. These mechanism may be expressed as follows [128]:

$$CH_2 + H \rightleftharpoons CH + H_2 \tag{R.2.31}$$

$$CH_2 + H_2O \rightleftharpoons CH_2O + H \tag{R.2.32}$$

$$CH_2 + O_2 \rightleftharpoons HCO + O \tag{R.2.33}$$

The methoxy radical from Reactions (R.2.23) and (R.2.26) can react with other radicals to form formaldehyde [117]. Furthermore, formaldehyde reacts with OH or O_2 to form formyl radical and it forms carbon monoxide as expressed in the following :

$$CH_2O + OH \rightleftharpoons HCO + H_2O \tag{R.2.34}$$

$$CH_2O + O_2 \rightleftharpoons HCO + HO_2 \tag{R.2.35}$$

$$HCO + M \rightleftharpoons H + CO + M \tag{R.2.36}$$

$$HCO + O_2 \rightleftharpoons CO + HO_2 \tag{R.2.37}$$
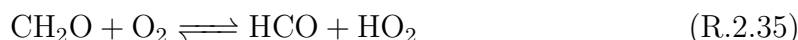
In a methane flame where the H, O, and OH radicals are at higher concentration, the methyl radical main consumption is through the Reaction (R.2.26) and the following reaction [128]:

$$CH_3 + O \rightleftharpoons CH_2O + H \tag{R.2.38}$$

Formaldehyde forms formyl radical through reaction (R.2.34) and the following reaction:

$$CH_2O + H \rightleftharpoons HCO + H_2 \tag{R.2.39}$$
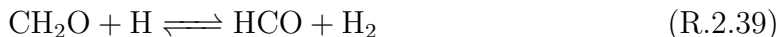
Furthermore, formyl radical yields CO from its reaction with hydrogen atom or oxygen.

The main species in the discussion of the C_2 mechanism are ethane (C_2H_6), ethylene (C_2H_4), and acetylene (C_2H_2), which not only can be found as fuels, but also intermediate species in a hydrocarbon combustion [128]. The initial step in the ethane oxidation is the H atom abstraction to form ethyl radical, through reactions with H, O, and OH as expressed as follows:

$$C_2H_6 + H \rightleftharpoons C_2H_5 + H_2 \tag{R.2.40}$$

$$C_2H_6 + O \rightleftharpoons C_2H_5 + OH \tag{R.2.41}$$

$$C_2H_6 + OH \rightleftharpoons C_2H_5 + H_2O \tag{R.2.42}$$
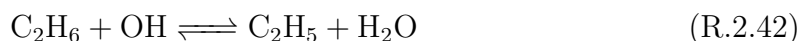
Ethyl radical rapidly undergoes another H atom abstraction, thus resulting in ethylene through reactions with the H atom and O_2 or a third body reaction. Alternatively, it reacts with O_2 and produces acetaldehyde (CH_3CHO) or reacts with the O atom to form CH_3 and CH_2O in a fuel-lean mixture as follows [128]:

$$C_2H_5 + H \rightleftharpoons C_2H_4 + H_2 \tag{R.2.43}$$

$$C_2H_5 + O_2 \rightleftharpoons C_2H_4 + HO_2 \tag{R.2.44}$$

$$C_2H_5 + M \rightleftharpoons C_2H_4 + H + M \qquad (R.2.45)$$

$$C_2H_5 + O_2 \rightleftharpoons CH_3CHO + OH \qquad (R.2.46)$$

$$C_2H_5 + O \rightleftharpoons CH_3 + CH_2O \qquad (R.2.47)$$

Acetaldehyde reacts with the OH, O and H atoms to form the CH_3CO radical, then it decomposes to CH_3 and CO as follows [128]:

$$CH_3CHO + H \rightleftharpoons CH_3CO + H_2 \qquad (R.2.48)$$

$$CH_3CHO + O \rightleftharpoons CH_3CO + OH \qquad (R.2.49)$$

$$CH_3CHO + OH \rightleftharpoons CH_3CO + H_2O \qquad (R.2.50)$$

$$CH_3CHO + M \rightleftharpoons CH_3 + CO + M \qquad (R.2.51)$$
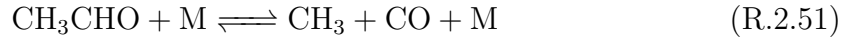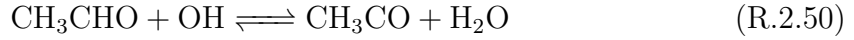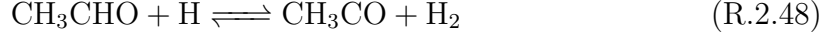
Unlike alkane, ethylene does not need H atom abstraction prior to the oxidation because its double bond is attractive to the OH and O atom. The following reaction accelerates the oxidation process because the CH_3 and HCO radicals create secondary branching steps:

$$C_2H_4 + O \rightleftharpoons CH_3 + HCO \qquad (R.2.52)$$

In a fuel-rich mixture, ethylene consumption by the H atom abstraction through the reaction with H and OH becomes important and this results in the vinyl radical (C_2H_3). Vinyl is relatively a reactive species and mostly reacts with O_2, resulting in formaldehyde, HCO, acetaldehyde, and oxygen atom. Acetaldehyde then reacts to form C_1 radical species while other vinyl reactions with the O_2 and H atom to form acetylene, which is the major species for fuel-rich methane combustion. Furthermore, acetylene rapidly reacts with the O atom resulting in the carbon monoxide, methylene, H atom, and ketenyl radical, which is reactive and reacts with the H atom resulting in the methylene radical and carbon monoxide [128]:

$$C_2H_3 + O_2 \longrightarrow CH_2O + HCO \qquad (R.2.53)$$

$$C_2H_3 + O_2 \longrightarrow CH_2CHO + O \qquad (R.2.54)$$

$$C_2H_2 + O \longrightarrow CH_2 + CO \qquad (R.2.55)$$

$$C_2H_2 + O \longrightarrow HCCO + H \qquad (R.2.56)$$

$$HCCO + H \longrightarrow CH^\bullet + CO \qquad (R.2.57)$$

Many researches have been devoted much effort in updating the oxidation mechanism involving the C_1 to C_2 hydrocarbons with more recent direct and indirect experimental data. Hughes et al. [145] developed a reaction mechanism for methane consisting of the oxidation mechanisms of hydrogen, carbon monoxide, ethane, and ethene. The reaction mechanism was obtained from the optimisation rate parameters of previously published reaction mechanisms. The rate parameters were updated with the experimental data from the European kinetics group and tuned the reaction rate parameters to approach the targetted experimental data from the laminar flame velocity, species profiles, and

ignition delay times [146]. Agreement between the targetted experimental data and the predictions was achieved, except for the prediction of the laminar burning velocity of rich methane flames. The authors suggested that the mechanism is lacking important reactions or have inaccurate rate parameters. One of the most successful methane mechanism is the GRI Mech 3.0 [46] which has been validated with a wide range of experimental data.

2.5.4 C_1-C_2 Alcohol

Alcohol is an organic compound which has a hydroxyl function group (C_1-C_2) attached to a carbon atom. The simplest alcohols are methanol and ethanol which have one and two carbon atoms, respectively. Methanol oxidation starts with the reaction that breaks the C-H bonds, which is preferable than the O-H bond. However, when the radical species is not present, the the initial reaction of methanol oxidation may be expressed as follows [117]:

$$CH_3OH + M \longrightarrow CH_3 + OH + M \qquad (R.2.58)$$

$$CH_3OH + O_2 \longrightarrow CH_2OH + HO_2 \qquad (R.2.59)$$
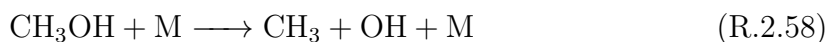
When the radical species is present, it reacts with the OH, O, and H atom resulting in CH_2OH. Subsequently, CH_2OH reacts with oxygen, or third body reaction, producing CH_2O. Also, CH_3OH could react with the H, O, and OH radicals to form CH_3O. Then, these species yields carbon monoxide and carbon dioxide.

The C-C bond of ethanol is the weakest bond in the compound and breaks at a high temperature through the reaction with the oxygen or third body reactions [128].

$$C_2H_5OH + M \longrightarrow CH_3 + CH_2OH + M \qquad (R.2.60)$$

$$C_2H_5OH + O_2 \longrightarrow CH_3CHOH + HO_2 \qquad (R.2.61)$$

When the radical species appears, it reacts with ethanol and produces the hydroxyethyl radical through the following reactions [117]:

$$C_2H_5OH + OH \longrightarrow CH_3CHOH + H_2O \qquad (R.2.62)$$

$$C_2H_5OH + H \longrightarrow CH_3CHOH + H_2 \qquad (R.2.63)$$

$$C_2H_5OH + O \longrightarrow CH_3CHOH + OH \qquad (R.2.64)$$

$$C_2H_5OH + HO_2 \longrightarrow CH_3CHOH + H_2O_2 \qquad (R.2.65)$$

$$C_2H_5OH + CH_3 \longrightarrow CH_3CHOH + CH_4 \qquad (R.2.66)$$
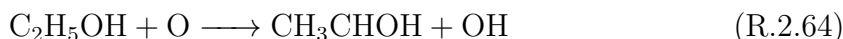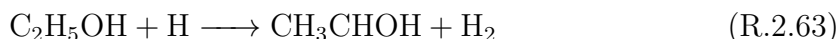
Then, the hydroxyethyl radical reacts with radical species, such as H, OH, O, CH_3, and HO_2 to form CH_3CO and it breaks to CH_3 and CO. Subsequently, the methyl radical forms methane or ethane through the recombination Reaction (R.2.20) and undergoes the reaction mechanism of C_1-C_2, which was explained in the previous section.

2.5.5 Higher Alkanes

Alkanes or paraffins are a saturated, single-bonded hydrocarbon, which has the general molecular formula of C_nH_{2n+2}. For paraffin, which has more than two carbon atom, it ultimately breaks to the C_1 and C_2 species and follows their oxidation mechanism [128]. The initiation of the higher alkane oxidation starts with H atom abstraction, and then the breakdown of $R^\bullet$, before the radical species appears, starts with the breaking of the C-C bonds because they are weaker than the C-H bonds:

$$R^\bullet + M \longrightarrow R_1{}^\bullet + R_2{}^\bullet + M \tag{R.2.67}$$

The hydrocarbon radicals, $R_1{}^\bullet$ and $R_2{}^\bullet$, undergo H atom elimination, thus resulting into alkene or olefins and hydrogen atoms. Furthermore, the H atoms react with oxygen and result in the more radical species, O and OH. With the presence of the radical species, more initiation reactions become possible, namely:

$$RH + OH \longrightarrow R^\bullet + H_2O \tag{R.2.68}$$
$$RH + H \longrightarrow R^\bullet + H_2 \tag{R.2.69}$$
$$RH + O \longrightarrow R^\bullet + OH \tag{R.2.70}$$

Afterwards, the $R^\bullet$ breaks into the alkene and H atom through the H atom abstraction reaction or breaks into a smaller fraction by following the β-scission rule. Then, alkenes react with O atoms, thus producing formyl radicals (HCO) and formaldehyde (H_2CO), which leads to the oxidation mechanism of CO:

$$R^\bullet + M \longrightarrow R_7C{=}CR_8 + H + M \tag{R.2.71}$$
$$R^\bullet + M \longrightarrow R_9C{=}CR_{10} + R_{11} + M \tag{R.2.72}$$
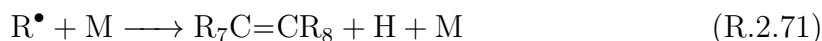
2.5.6 Aromatics

Aromatic hydrocarbons are compounds which satisfy the aromaticity rules, such as the Hückel rule, cyclic-planar shaped, etc. Benzene and toluene are examples of aromatic hydrocarbons which have been considered as components of jet fuel as well as gasoline and the precursor of soot formation. The oxidation of benzene begins with the H abtom abstraction reaction producing phenyl, which tends to be recombined with the hydrogen atom to form benzene. Meanwhile, the rest of the phenyl radical reacts with oxygen to produce the phenoxyl radical (C_6H_5O) and the O atom or benzoquinone ($C_6H_4O_2$) and OH radical. Also, benzene can react with O atom to form cyclopentadienyl (C_5H_5) and formyl radical (HCO) directly, namely [128]

$$C_6H_6 + H \longrightarrow C_6H_5 + H_2 \tag{R.2.73}$$
$$C_6H_6 + OH \longrightarrow C_6H_5 + H_2O \tag{R.2.74}$$
$$C_6H_5 + H + M \longrightarrow C_6H_6 + M \tag{R.2.75}$$

$$C_6H_6 + O + M \longrightarrow C_6H_5O + H \tag{R.2.76}$$

$$C_6H_6 + O \longrightarrow C_5H_5 + HCO \tag{R.2.77}$$
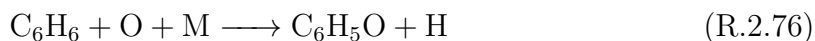
Benzene is also able to react with the O atom, which creates the C-O bond in the phenoxyl radical, which can recombine with the H atom and thus yield phenol. Also, the phenoxyl radical can form the cyclopentadienyl radical (C_5H_5) and CO through thermal decomposition. Then, the cyclopentadienyl radical reacts with the H atom and yields cyclopentadiene (C_5H_6):

$$C_6H_5O + H + M \longrightarrow C_6H_5OH + M \tag{R.2.78}$$

$$C_6H_5O + M \longrightarrow C_5H_5 + CO + M \tag{R.2.79}$$
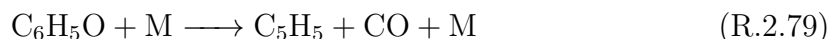
There is uncertainty in the reaction after C_5H_5 and C_5H_6 in determining the transition from cyclic to non-cyclic compound [128]. Further, the C_5H_5 species reacts with the O, OH, HO_2 radicals, and third body reactions thus resulting in cyclopentadianone (C_5H_4O). Subsequent reaction of cyclopentadianone with third body reactions yields vinylacetylene (C_4H_4), diacetylene (C_4H_2), and acetylene C_2H_2. For toluene, the oxidation mechanism is analogous with benzene, which starts with H-abstraction reactions then the dissociation of alkyl functional group and this leads to benzyl radical formation. The benzyl radical undergoes reactions with the O, OH, HO_2, and CO radicals resulting in vinylacetylene (C_4H_4), diacetylene (C_4H_2), and acetylene (C_2H_2) [128]:

$$C_6H_5CH_3 + (H, OH) \longrightarrow C_6H_5CH_2 + (H_2, H_2O) \tag{R.2.80}$$

$$C_6H_5CH_2 + (O, HO_2) \longrightarrow C_6H_5CHO + (H, H + OH \tag{R.2.81}$$

$$C_6H_5CHO + (H, OH, O_2) \longrightarrow C_6H_5CO + (H_2, H_2O, HO_2) \tag{R.2.82}$$

$$C_6H_5CO + M \longrightarrow C_6H_5 + CO + M \tag{R.2.83}$$

2.5.7 NO$_x$

Nitric oxides (NO$_x$) consists primarily of NO and NO_2, which can be produced in a combustion process that involves nitrogen. Studies of NO$_x$ mechanism has been performed previously [147] and three routes are known as being responsible for the formation of NO$_x$. The routes are thermal NO$_x$, prompt NO$_x$, and fuel NO$_x$, which are discussed in the following section. Thermal NO$_x$ is produced from the reactions of the NO$_x$ mechanism, which is temperature-dependent and important at high temperature. The thermal NO$_x$ mechanism is also known as the Zeldovich mechanism and may be expressed as follows:

$$O + N_2 \rightleftharpoons NO + N \tag{R.2.84}$$

$$N + O_2 \rightleftharpoons NO + O \tag{R.2.85}$$

$$N + OH \rightleftharpoons NO + H \tag{R.2.86}$$

Since the thermal NO_x reactions involves O and OH radicals, it depends on the mechanism of the fuel oxidation.

At low temperature and lean mixture, N_2O is formed and involved in the reaction mechanisms, namely

$$O + N_2 + M \rightleftharpoons N_2O + M \tag{R.2.87}$$

$$H + N_2O \rightleftharpoons NO + NH \tag{R.2.88}$$

$$O + N_2O \rightleftharpoons NO + NO \tag{R.2.89}$$
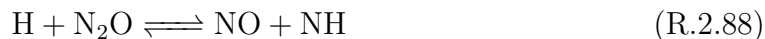
The second route was named by Fenimore as the prompt NO_x because this mechanism is much faster than the thermal NO_x. This is caused by the reaction between the hydrocarbon radicals, such as CH, CH_2, C_2, C_2H, and C with the nitrogen molecule, producing amines or hydrocyanic acid. The important reactions are expressed in the following reactions, which are ultimately converts to NO_x [117]:

$$CH + N_2 \rightleftharpoons HCN + N \tag{R.2.90}$$

$$CH_2 + N_2 \rightleftharpoons HCN + NH \tag{R.2.91}$$

$$CH_2 + N_2 \rightleftharpoons H_2CN + N \tag{R.2.92}$$

$$C + N_2 \rightleftharpoons CN + N \tag{R.2.93}$$

The third route is the fuel NO_x, which is the fuel-bound nitrogen, and this is also converted rapidly to smaller H/C/N compounds, such as amines or hydrocyanic acid, and ultimately NO_x [117].

2.5.8 Surrogates of Jet Fuel

The construction of the jet fuel surrogate is frequently performed by combining the oxidation mechanism of the fuel constituents, such as alkanes, aromatics, and pollutants mechanisms. For example, the first generation of AFRM [91], which used n-decane and toluene as the surrogate, was built by combining the oxidation mechanisms of each fuel as well as the NO_x mechanism. Nowadays, the mechanism can be considered to be outdated and require updates as the sub-mechanism has been updated. The C_1-C_3 reactions in the mechanism were taken from the GRI Mechanism version 2.11 while the GRI Mechanism is now at version 3.0. Similar reaction mechanisms combination method was also employed for further extension of the AFRM mechanism to alternative fuels by Catalanotti et al. [98].

The Aachen surrogate model [80] was built to represent kerosene with n-decane and trimethyl benzene. Similar to the AFRM, this mechanism was built by merging the n-decane mechanism [88] and trimethylbenzene. Before the n-decane sub-mechanism was merged with trimethyl benzene, it was validated with the available experimental data

from the literature. It was found that an improvement to the mechanism was required for modelling ignition delay times in low-temperature shock-tube data. Adjustment to several reaction rate parameters was able to optimise the n-decane mechanism to the targeted experimental data. Furthermore, the optimised n-decane mechanism was assembled with 1,2,4-trimethylbenzene mechanism, resulting in a jet fuel surrogate mechanism which consists of 900 reactions and 122 species. A real kerosene and surrogate mixture was used in the experiments associated with this work to test the accuracy of the surrogate model. The experiment comprised of strain rate extinction, autoignition, and soot volume fraction from a counter-flow diffusion flame and the model accurately predicted the data except for the soot formation. At the peak of the soot profile, a significant discrepancy was found between the model and the experimental data. This mechanism is lacking from validation of other major species profiles from similar and different reactors.

Another attempt to construct an accurate surrogate model of jet fuel was performed by Humer et al. [148]. Several surrogate mixtures, as well as real jet fuels, were studied in a counterflow diffusion flame and this resulted data of the temperature at ignition. The surrogate mixtures consist of n-alkane, cycloalkanes, and aromatics with a volumetric percentage of 60, 20, and 20 percent, respectively. The n-alkane component is represented by n-decane or n-dodecane, while the cycloalkane component is represented by methylcyclohexane, and the aromatic component is represented by toluene or o-xylene. The results of the experiment shows that the surrogate mixtures agree with the real Jet-A and JP-8. The reduced CRECK mechanism [48], which consists of 4890 reactions and 173 species, was able to predict the experimental data. However, this experiment is also lacking in the species concentration measurement and requires wider validation.

2.6 Liquid-Phase Oxidation of Hydrocarbon

The first step of hydrocarbon oxidation in the liquid phase is the diffusion of oxygen gas into the liquid hydrocarbon which occurs rapidly compared to the oxidation reactions [19]. Therefore, this process does not affect the kinetic aspects of the oxidation process, such as the rate parameters of the reactions. Henry's law is used to calculate the concentration of oxygen that dissolves to the liquid phase and this method has been used in the previous studies [108, 113]. The mathematical description of Henry's law is expresed as follows:

$$[O_2] = \gamma \times p_{O_2} \tag{2.46}$$

where $[O_2]$ is the concentration of oxygen in the liquid phase, p_{O_2} is the partial pressure of oxygen, and γ is the Henry's coefficient. The value of the coefficient is unique for

different solvents and the value for selected fuels in this study is presented in Table 2.1. Also, this process can be integrated into an elementary reaction and reacts with the alkyl radical to form the alkoxyl radical as expressed as follows:

$$O_{2\text{gas}} \rightleftharpoons O_{2\text{liquid}} \tag{R.2.94}$$

$$R^\bullet + O_2 \longrightarrow RO_2{}^\bullet \tag{R.2.95}$$
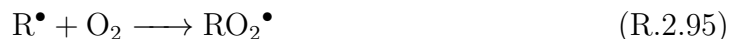
The initiation step of the hydrocarbon oxidation reaction is the H atom abstraction from the hydrocarbon through the thermal decomposition or the reaction with metal ion, ultraviolet, or oxygen [19, 149] as expressed in the following reactions:

$$RH + I \longrightarrow R^\bullet \tag{R.2.96}$$

$$RH + O_2 \longrightarrow R^\bullet + HO_2 \tag{R.2.97}$$

If the hydroperoxides species are present, initiation through Reaction (R.2.98) and (R.2.99) becomes possible:

$$ROOH \longrightarrow RO^\bullet + HO^\bullet \tag{R.2.98}$$

$$2\,ROOH \longrightarrow RO_2{}^\bullet + RO^\bullet + H_2O \tag{R.2.99}$$

Alkyl radicals that are formed from the initiation steps yield hydroperoxides, which are the main product of the oxidation of aliphatic and alkylaromatic hydrocarbon [19]. Hydroperoxides concentration in the oxidised solvent is proportional to the depletion of oxygen in the oxidation process and the structure depends on the oxidised solvent. Subsequently, hydroperoxides may decompose to form alcohols, ketones, aldehydes, acids, epoxy, alkanes, olefins, or radicals as follows:

$$R^\bullet + O_2 \longrightarrow RO_2{}^\bullet \tag{R.2.100}$$

$$RO_2{}^\bullet + RH \longrightarrow ROOH + R^\bullet \tag{R.2.101}$$

$$RO_2{}^\bullet + R^\bullet \longrightarrow ROOR \tag{R.2.102}$$

The radicals that are formed from the previous steps recombine to yield stable products through the termination steps:

$$RO_2{}^\bullet + RO_2{}^\bullet \longrightarrow ROH + O_2 + R_1C(O)R_2 \tag{R.2.103}$$

$$H^\bullet + O_2 \longrightarrow HO_2{}^\bullet \tag{R.2.104}$$

$$HO_2{}^\bullet + HO_2{}^\bullet \longrightarrow H_2O_2 + O_2 \tag{R.2.105}$$

$$R^\bullet + R^\bullet \longrightarrow RR \tag{R.2.106}$$

The role of antioxidants (A) in the oxidation mechanism of hydrocarbon is the terminating the chain reaction by accepting the peroxyl radicals [19]. In the case of phenolic antioxidants, it reacts with peroxyl radical and yield quinone or quinolide peroxide:

$$RO_2{}^\bullet + AH \longrightarrow ROOH + A^\bullet \tag{R.2.107}$$

$$RO_2{}^\bullet + A^\bullet \longrightarrow \text{Products} \tag{R.2.108}$$

Table 2.1: Henry's Coefficients for Some Selected Solvents [19].

Solvent	Temperature/K	$\gamma \times 10^3/(mol.L^{-1}atm^{-1})$
o-xylene	298	9.22
Methylcyclohexane	298	12.5
Decane	298	11.2
Dodecane	298	8.14
Ethanol	298	9.92
Kerosene, $\rho = 810 \ kg/m^3$	291	3.44

2.7   Concluding Section

This chapter has extended the literature review that has been started in the previous chapter. In the first chapter, the issues and challenges in aviation industry, especially in the search of alternative fuels has been introduced in Section 1.1. Despite the fact that the direct use of ethanol is not yet approved, evidence on the interest of researches in testing ethanol as drop-in jet fuel has been highlighted in Section 1.5.3. Furthermore, the motivation on using ethanol as alternative jet fuel has increased since policies have been approved in many countries, especially those with high potential of ethanol resources, for reducing the dependency on fossil fuel and increasing the use of renewables, such as ethanol, as reviewed in Section 1.2.

Numerous studies on the benefit of using ethanol for a blend of diesel and gasoline are available in the literature. This includes fundamental studies, such as flame experiments, and real application studies, such as engine observations. However, only a few publications can be found on the fundamental study of the use of ethanol as a drop-in jet fuel as reviewed in Section 1.5.3. This includes a wick stove [102], cylindrical combustor [103], spray [104], as well as droplet combustion characteristics [30], acoustics [105] and kinetics [48]. The kinetic aspect was performed by the kinetic modelling group in Politecnico di Milano, which focused on the development of a detailed reaction mechanism for modelling a wide range of fuels. This reaction mechanism may able to predict the kinetic behaviour of the jet fuel and ethanol blend flame, but its accuracy is questionable since it has not validated to an experimental data of the fuel blend flame.

This work addresses these gaps and proposes an experimental and modelling study of the combustion kinetics of the ethanol/jet fuel flame. Firstly, a literature review on the previous studies of the model and experimental data of jet fuel flames has been performed in Section 1.5.2. This results in the identification of the problem in the definition of the jet fuel composition because the real jet fuel consist a wide range of

hydrocarbons and this becomes difficulties in the modelling work. Surrogate models have been proposed, such as Aachen [80] and San Diego [148] surrogates, and indicated similar characteristics in several reactors compared to the real jet fuel. This work aims to extend the validation of these surrogate models to the premixed flat-flame burner experiment.

Ethanol flames have been extensively studied as reviewed in Section 1.5.1. This study aims to fill the missing experimental data of a premixed flat-flame burner study of ethanol at atmospheric pressure to the targetted lean, rich, and stoichiometric mixtures with different measurement methods such as PLIF and gas analysis. Also, this study aims to use ethanol flames as a more accurate reference for quantifying the measurement of OH and NO radicals in the flames. This should improve the results from Catalanotti [5], which used a methane flame for the calibration reference which was generated from a different burner and might cause an inaccurate calibration due to a different laser setup.

The importance of the thermal stability properties of fuels and the study of biodiesel stability has been introduced in Section 1.4. Many researches of the oxidation stability of real and surrogate jet fuels have been reviewed in Section 1.5.4. The use of ethanol as drop-in jet fuel has not been found in the literature and this may lead to the lower oxidation stability performance of the fuel blend due to the difference in the properties of the fuels. This study aims to investigate the effect of ethanol addition to the real and surrogate jet fuels oxidation stability as well as the assessment of antioxidants for improving the stability of the fuel blends.

In Section 2.1, the established kinetic theories has been introduced as well as the tools for modelling fuel oxidation in many different reactors which were presented in Section 2.2. Moreover, the reaction mechanism of hydrocarbon fuels has been reviewed from well-known combustion textbooks and journal publications in Section 2.5 as well as the liquid phase oxidation mechanism in Section 2.6. These reviews are useful for the author to select accurate models for developing the reaction mechanism and modelling the experimental works of this study.

Chapter 3

Burner Flame Experiment Setup

This chapter describes the experimental setup for the premixed-laminar burner flame study. The experiment rig was built in the Laser Laboratory of Ella Armitage Building, University of Sheffield. All of the experimental procedures have been assessed and approved by the Health and Safety inspector of the Mechanical Engineering Department before the experimental work started. The Health and Safety assessment requires detailed paperwork including an updated rig identifications, risk assessments, CoSHH forms, standard operational, emergency and normal shut down procedures, training, and maintenance records for each experiment apparatus.

3.1 Flat-Flame Burner

A flat-flame burner has been used as a standard method for combustion studies for many years to study the premixed flame structure [60], such as temperature and species profile or to calibrate a measurement instrument [150]. A commercial flat-flame burner, such as the Mckenna burner is available to be purchased online or alternatively a customised flat-flame burner is also possible to be manufactured as demonstrated by Catalanotti [5]. The burner was able to generate a stable premixed flame with a wide stoichiometry from lean to rich mixture. In this study, a customised flat-flame burner from the work of Catalanotti [5] was used to study a premixed laminar flame of liquid fuels while the standard McKenna burner was utilised to test the measurement instruments with methane gas.

A schematic of the customised flat-flame burner is illustrated in Figure 3.1 [5]. The fuel was placed in a fuel tank which was pressurised with oxygen-free nitrogen up to 4.5 bar. The pressure difference allowed the fuel to flow from the tank and reach the burner. Its flow rate was controlled by a mass-flow controller (MFC), which could accurately regulate the flow rate. In the atomiser, the fuel was introduced with the primary air supply which assisted the atomising process. Afterwards, the fuel and air spray that

was produced by the atomiser was mixed with the secondary air, which supplied the remaining amount of the air requirement to fulfil the targetted equivalence ratio. The atomiser position was locked by a nut and adjustable to tune the gap between the atomiser nozzle and the housing which affect the stability of the flame. Subsequently, the fuel and air mixture flowed through a pipe containing metal shavings to enhance the mixing of the fuel and air gas. Further, a honeycomb air straightener, which consists of many small holes, was placed after the metal shaving in order to form a laminar flow. Finally the fuel/air gas mixture escaped through a holed plate where the flame was stabilised. The pipe wall, where the fuel and air mixture flowed, was heated up to 190 °C to enhance the vaporisation. The heating was achieved by an electric heater and controlled by a proportional integral derivative (PID), which activates the heater when the temperature dropped to 180 °C and deactivates it when the temperature reaches 190 °C.

Refurbishment and maintenance of the customised burner were required after the burner was used by Catalanotti for the study of bio-jet fuels [5]. The atomiser was cleaned by flowing acetone through the nozzle to remove any existing gum from the previous use. The electric heater and the PID controller was replaced with a new component as well as the insulation to protect the heat escaping from the ceramic tube, which coated the pipe. The insulation was made from a foil-faced single-sided wool, which was wrapped around the ceramic tube and then covered with the burner's case from metal plates.

Several mesh wires were tested to find the best geometry of the flat-flame as well as the flame stability. The meshes which were made from metal wire were not the ideal choice as they glowed red due to the heat from the flame. Consequently, the premixed fuel/air gas was ignited before the gas escaped the burner surface. This caused the flame to become stable below the burner surface and was not ideal for temperature or gas analysis probing since the fuel/air mixture had reacted below the mesh surface and generated final combustion products which inhabit the surface of the burner and upwards. After several trials, an optimised mesh was found from a metal plate, which was drilled to make several holes to represent the mesh wire. This was found to eliminate the surface glowing problem and produced a stable flat-flame above the burner surface. A sketch of this mesh is presented in Figure 3.2 and the wider surface was placed facing the burner pipe and sealed with metal tape to ensure that the gas did not leak through the joint. Moreover, a metal tape was used to fasten the connection between the mesh and the pipe as well as to seal the joint from any leakage.
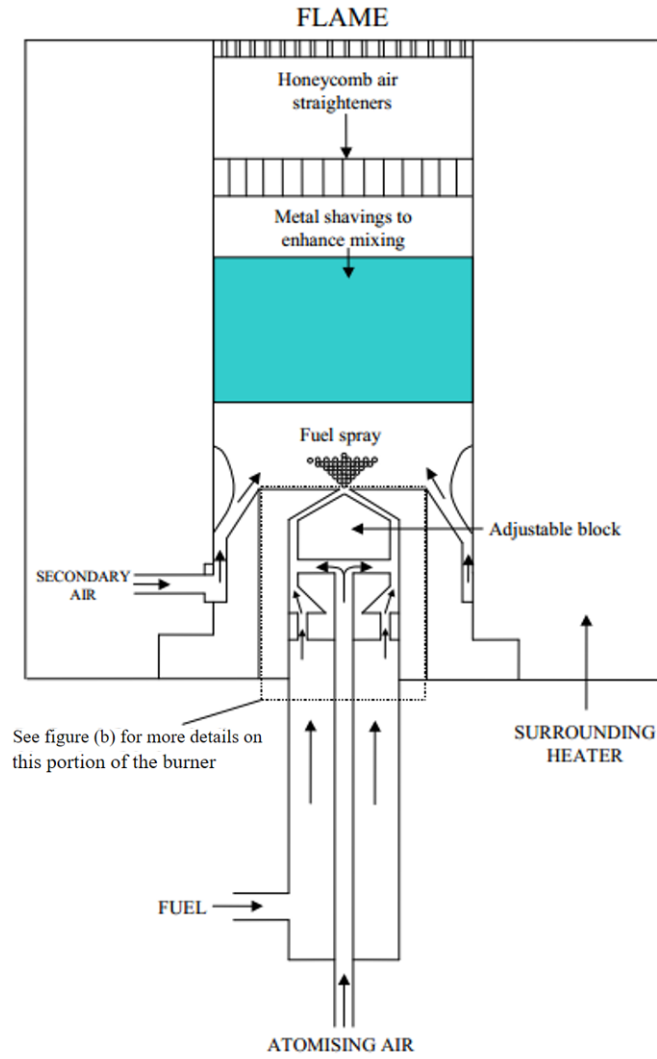
(a)
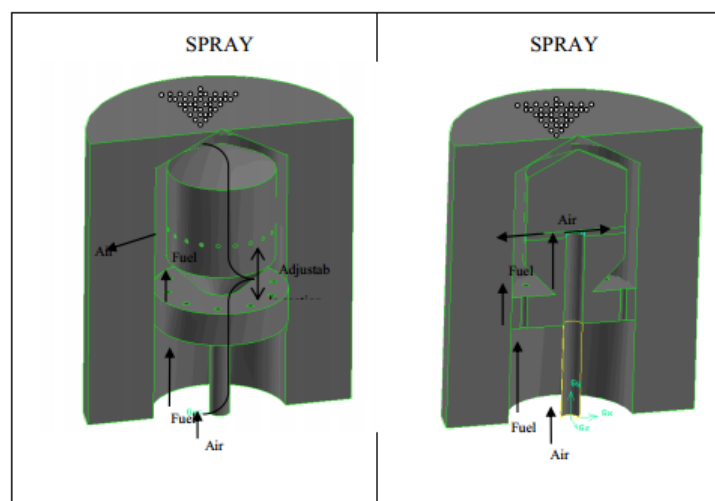
(b)

Figure 3.1: Schematic of (a) the customised flat-flame burner and (b) the detailed section of the atomiser. Source: Catalanotti [5].

51
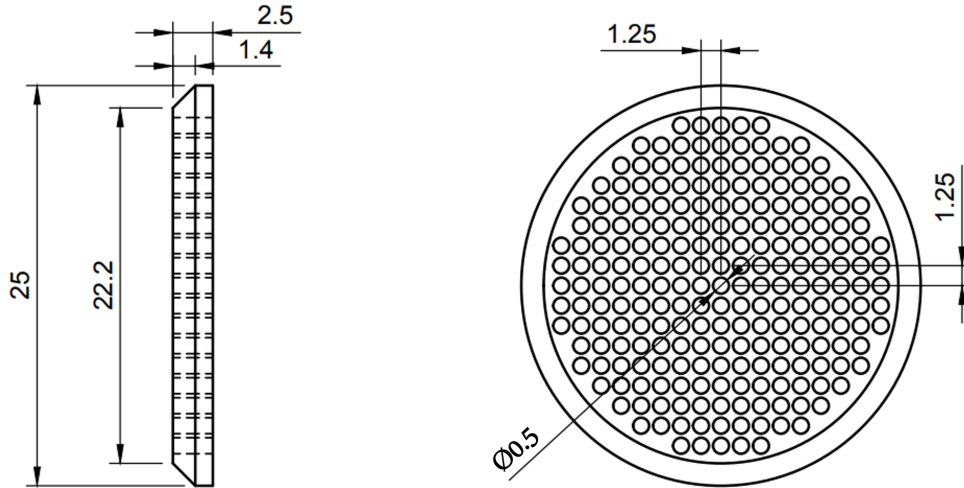
Figure 3.2: A sketch of the brass mesh, dimensions are expressed in mm.

There are several factors that affect the stability of the flame apart from the mesh, such as nozzle position, primary and secondary air ratio, fuel flow rate, and the cavity in the fuel flow. If these parameters were not set at the optimised value, the flame would be unstable. The nozzle was inserted onto the burner and was not necessarily placed at the end of the tube. It was found that the most stable flame was achieved when the nozzle was positioned 2 cm away from the top end of the tube. This allowed the liquid fuel to accumulate inside the atomiser and produce a stable spray. The primary airflow rate was set to 0.2 litres per minute for a less viscous fuel such as ethanol and 0.25 litre per minute for a more viscous fuel such as real kerosene. When the primary airflow rate was too high, the fuel flushes rapidly from the atomiser and this causes instability. There was also a small amount of gas trapped inside the fuel pipeline and this also caused flame instability due to the unstable fuel supply. By optimising these parameters, a stable flame was achieved and this resulted in minimum fluctuations in the flame measurements.

3.1.1 Fuels

In this study, five different fuels were investigated involving the lean, rich, and stoichiometric mixture. The lean, near stoichiometric, and rich mixtures were aimed at 0.86, 1.07 and 1.28 equivalence ratio, respectively, which were the upper and lower stability limits of the burner. Tables 3.1 and 3.2 show the detailed information on the fuel and the flow rates that were used in this study. The air was supplied from a compressor while the oxygen-free nitrogen gas (99.998%) for pressurising the fuel tank was supplied from a gas cylinder, which was supplied by BOC. The airflow was controlled by an MFC to obtain an accurate flow rate. The Surrogate A was proposed by Honnet et al. [80] and its components were n-decane and 1,2,4 trimethylbenzene

with weight ratios 80 and 20 per cent, respectively. Meanwhile, the Surrogate B was n-dodecane, methylcyclohexane, and o-xylene with volumetric ratios 60, 20, and 20 per cent, respectively, which was proposed by Humer et al. [148].

When replacing a fuel sample by another sample, a cleaning procedure was performed to maintain the purity of the fuel. The fuel tank was drained by opening the fuel valve and pressurising the tank with nitrogen. When the tank was emptied, it was flushed with acetone several times then rested for several minutes to allow the solvents to evaporate. The burner was cleaned by flowing air for several minutes and heated to 190°C, so that the remaining fuel will be evaporated and removed from the atomiser. When the fuel system had been cleaned, the tank was filled with the other fuel samples. Before sealing the fuel tank, nitrogen gas was supplied to the tank so the oxygen concentration inside the fuel tank can be minimised. After several seconds, the tank was sealed by fastening the bolts and the tank was pressurised by the nitrogen gas up to 4.5 bar.

Table 3.1: Supplier and quality of the fuels.

Solvent	Supplier	Quality
Jet A-1	Shell	Real fuel
Decane	Sigma-Aldrich	Anhydrous, $\geq 99\%$
Dodecane	Sigma-Aldrich	Anhydrous, $\geq 99\%$
Ethanol	Fisher	HPLC, 99.8%
Methylcyclohexane	Alfa Aesar	99%
O-xylene	Alfa Aesar	99%
1,2,4 trimethylbenzene	Sigma-Aldrich	98%

Table 3.2: Flow rates of the fuels and air of the measured flames.

Fuel	Fuel flow rate /(g/s)			Total air flow rate /(L/s)
	ϕ=0.86	ϕ=1.07	ϕ=1.28	
Jet A-1	6.155×10^{-3}	7.693×10^{-3}	9.232×10^{-3}	8.737×10^{-2}
Ethanol	5.061×10^{-3}	6.327×10^{-3}	7.592×10^{-3}	4.411×10^{-2}
E50	5.024×10^{-3}	6.280×10^{-3}	7.536×10^{-3}	5.773×10^{-2}
Surrogate A	5.812×10^{-3}	7.265×10^{-3}	8.718×10^{-3}	8.32×10^{-2}
Surrogate B	5.845×10^{-3}	7.307×10^{-3}	8.768×10^{-3}	8.204×10^{-2}

3.1.2 Mass Flow Controller Calibration

The air flow to the burner was supplied by two MFCs from Brooks Instrument 4800 series which were controlled by a Brooks Instrument 0254 controller. Meanwhile, the liquid fuels were supplied to the burner by a Brooks Instrument Flomega MFC which was controlled by a Brooks Instrument 0152 controller. To ensure the accuracy of the MFCs, a calibration procedure was performed by using a glass tube and bubble. This procedure was able to measure the actual flow rate that was generated by the MFC. The glass tube was filled with a small amount of soap solution so a bubble could be generated. The bubble moved with the increasing of the air volume inside the tube. The time that was required for the bubble to travel between two points in the glass tube was measured and this yielded the volumetric flow rate from the known distance and tube diameter. For a low flow rate, a 10 cm distance was used while for a larger flow rate, a 50 cm distance was used because of the lifetime of the bubble. For the air MFCs, at least three different flow rates of air were measured to obtain the linear correlation between the MFC set point and the actual flow rate.

For the liquid MFC calibration, the actual fuel flow rate was measured using an accurate scale, TB-125D from Denver Instrument Germany, which has an accuracy of 0.1 mg. The outflow from the MFC filled a beaker which was mounted on the scale so the mass of the fuel inside the beaker could be measured. The mass of the fuel inside the beaker was recorded for at least 10 minutes so the actual mass flow rate could be determined. The liquid MFC was calibrated at more than three different points so that the linear correlation between the MFC set point and the actual flow rate can be accurately determined. Also, the evaporation rate of the liquid fuels at the room condition was measured to obtain an accurate measurement. The calibration results of the gas and liquid MFCs are presented in Figure 3.3.

3.2 Thermocouple

The temperature profile of the flames that were produced from the flat-flame burner was measured to understand the characteristics of the chemical kinetics, calibration of the PLIF measurement, and supply the required information for the input of the burner-stabilised flame simulation using the CHEMKIN PRO software. A type-R thermocouple, which was made of platinum and 13/87 per cent rhodium/platinum wires, was employed to measure the temperature at different positions above the burner surface. It was supplied by Omega and specified that it has a wire diameter of 50 µm by the manufacturer. The size of the thermocouple was aimed to be as thin as possible to minimise the disruption to the flame flow during the exposure of the thermocouple wire. However, the 50 µm thermocouple was not durable to measure the Jet A-1 flame
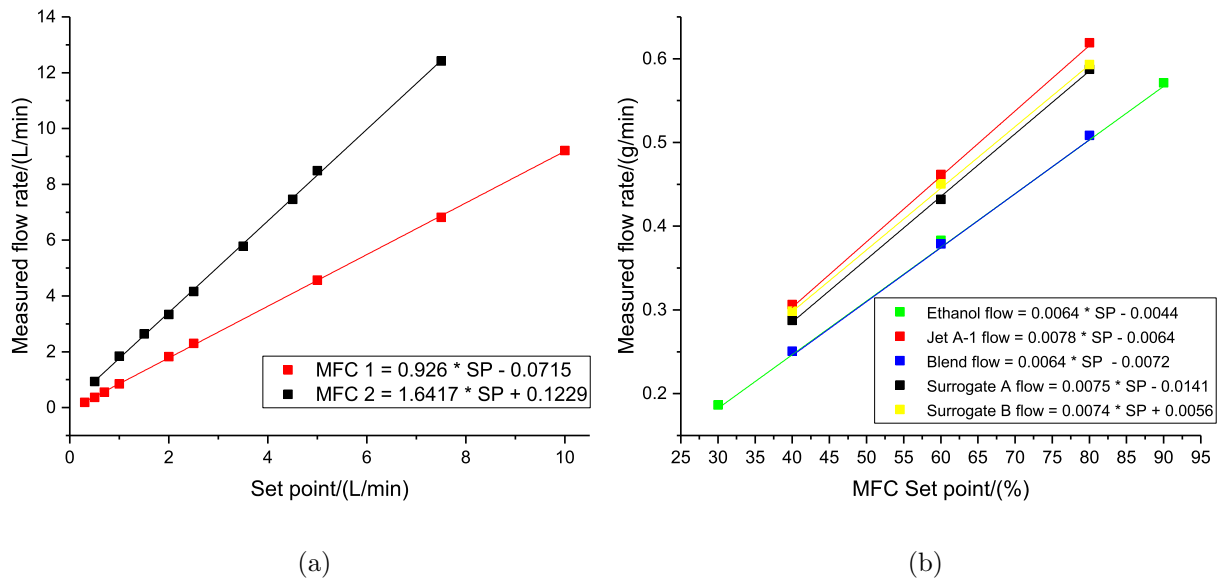
Figure 3.3: Calibration results of (a) air and (b) liquid MFC.

and its surrogates due to the higher temperature and flow rate, which results in the breaking of the thermocouple wire. Alternatively, a larger thermocouple wire, 75 µm wire diameter, was employed to measure the Jet fuel and surrogates flames. According to the manufacturer, the bead diameter of the thermocouple is approximately 2.5 to 3 times larger than the wire diameter.

The thermocouple was coated with a thin layer of silica to minimise any reactions that may occur on the surface of the thermocouple bead that would distort the temperature measurements [151, 152]. The method that was used to put a thin layer of silica on the thermocouple wire surface was by exposing the thermocouple wire to a diffusion flame from a gas-blowing torch. The gas-blowing torch was fuelled by natural gas, which was poisoned with hexamethyldisiloxane vapour. The natural gas was a commercial product, which was supplied to the laser laboratory while the hexamethyldisiloxane was provided by Sigma-Aldrich with a purity of ≥98 per cent. In addition, the exposure of the thermocouple wire to the flame from the gas-blowing torch could remove the bend near the bead that may occur during the manufacture process of the thermocouple, so the thermocouple was maintained to be as straight as possible. The exposure of the thermocouple to the flame from the gas-blowing torch must be limited because the thermocouple wire could break due to excess heat from the flame and thickness of the silica layer. A quick exposure of the flame was sufficient to make the thermocouple wires glow red and leave a thin silica layer on the thermocouple. Once the thermocouple was coated, the colour will turn from a silvery metal to white.

The coated thermocouple wire was observed under a scanning electron microscope

(SEM) to find the actual diameter of the thermocouple wire before and after the coating. The microscope was Carl Zeiss EVO MA15: variable pressure W SEM with 80 mm X-Max SDD detector- secondary. However, it was difficult to find the thermocouple bead once it was taken to the microscope. Moreover, the silica layer was damaged because of the contact inside the package during the transport to the microscope facility. Therefore, the given dimension from the manufacturer was used for further analysis. The visual result from the microscope observation is presented in Figure 3.4, which has a magnification factor of 500.
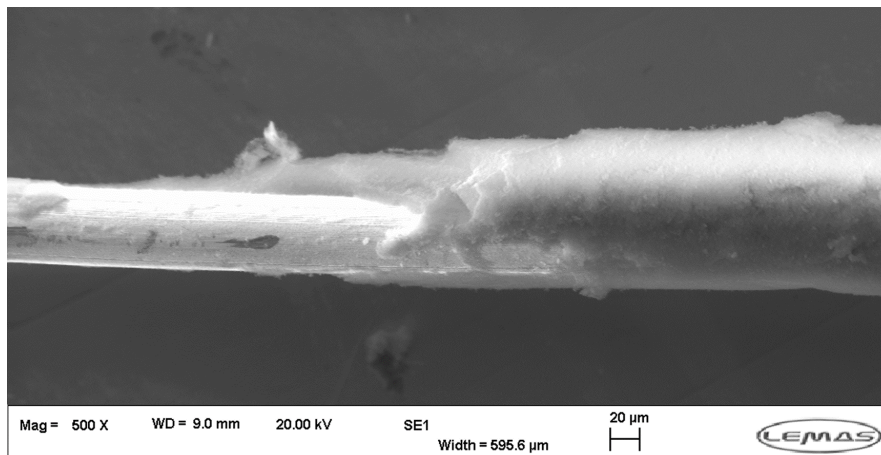
Figure 3.4: Photograph of a coated thermocouple wire observed under a scanning electron microscope.

During the exposure to the flame, the thermocouple wire received heat and expanded. The expansion of the thermocouple wire during the flame measurement was not desired because it could make the measurement inaccurate. The position of the thermocouple bead could shift because the thermocouple wire was losing tension and slackening. To solve this issue, the thermocouple wire was stretched horizontally with a slight tension and a spring was placed in the platinum-rhodium wire of the thermocouple. The spring was made by closely coiling the platinum-rhodium wire to a 2-mm tube. The platinum-rhodium side was chosen ahead of the platinum side because it has a better elasticity, which is required to produce a decent spring. Before the spring-wired thermocouple was exposed to the flame, it requires approximately 2.5 mm stretch to maintain its tension and compensate the expansion during the exposure to the flame. An excess tension and heat exposure to the wire would break the thermocouple. Adversely, the lack of tension could make the thermocouple flutter and vibrate severely, which leads to inaccurate measurements and thermocouple damage. Therefore, the tension of the thermocouple should be properly adjusted. Figure 3.5 illustrates the configuration of the thermocouple that was used in this experiment.

There were 14 points of measurement that were located along the vertical axis above

the centre part of the burner surface. The first measurement point was 0 mm above the burner surface that was obtained by touching the thermocouple bead to the burner surface. The next measurements were at 0.2 mm increments up to 1.4 mm, then 1.7, 2, 2.5, 3, 5, and 10 mm above the burner. The gap between the thermocouple and the burner surface was changed by moving the burner in the downward direction by adjusting the XYZ traverse system where the burner was mounted. The movement of the traverse system was calibrated to verify its movement accuracy by calibrating the value of the unit per motor revolution value to the actually measured displacement of the traverse system table. All the movement of the traverse system was controlled by its software, which required manual input from the user.
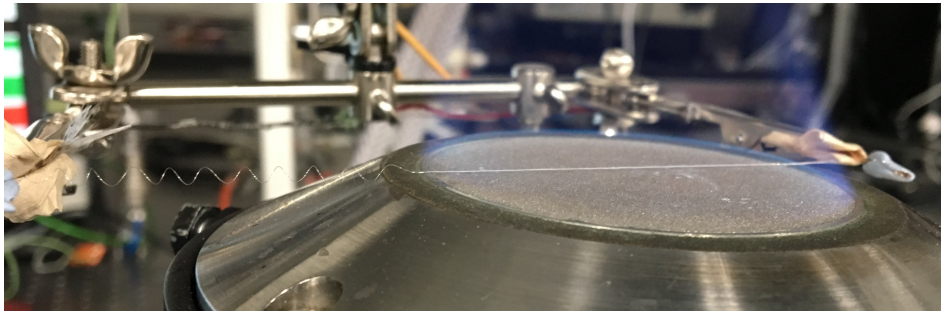
Figure 3.5: Illustration of the thermocouple configuration.

The thermocouple wire was connected to a type-R extension wire, which was supplied by Omega, to deliver the electric signal to the data logger. The extension wire was insulated to minimise the noise and to prevent the signal loss due to contact with the metal holder. The data logger was an Omega Multiscan 1200, which recorded and wrote the signal from the thermocouple to a data file. For each position, the measurement was repeated at least 100 times for a period of 15 seconds. The data file from the data logger software, Chartview, was processed to obtain the average and standard deviation value of the data.

The thermocouple reading required a correction due to the heat loss from the wire and bead to the environment through radiation. A coated thermocouple tends to have a lower temperature reading compared to the uncoated thermocouple due to the larger diameter and possibly catalytic reactions on the uncoated wire in flame. To calculate the heat loss by radiation, a correction method by Kaskan [152] was used in this study. The temperature difference due to radiation, ΔT_{rad}, was calculated using the following equation:

$$T = T_{raw} + \Delta T_{rad} = T_{raw} + \frac{1.25\,\epsilon\,\sigma\,T_{raw}^4\,d^{0.75}}{\lambda}\left(\frac{\eta}{\rho\,\nu}\right) \tag{3.1}$$

and added to the raw measurement, T_{raw}, to obtain the corrected value, T. ϵ is the emissivity of the surface of the thermocouple bead, which is 0.22 for silica-coated wire,

while σ is the Boltzmann constant which is 5.67×10^{-8} Js^{-1}m^{-2}K^{-4}. The diameter of the thermocouple bead, d, is $125\,\mu$m for the $50\,\mu$m wire and $187.5\,\mu$m for the $75\,\mu$m wire, which were obtained from 2.5 times of the wire diameter. The thermal conductivity of the gases, λ, was assumed for air at 1000 K which is 0.18 Js^{-1}m^{-1}K^{-1} while the viscosity of the gases, η, was assumed as air with composition 21/79 per cent of O_2/N_2 and calculated with the Cantera Python code and GRI 3.0 Mechanism at the measured temperature. The multiplication of density, ρ, and velocity, ν, yields the area mass flow rate (kg m^{-2}s^{-1}) which was the sum of the air and the fuel mass flow rates over the area of the burner surface, 4.91 cm^2, which was obtained from known diameter of the burner surface, 2.5 cm.

3.3 Gas Analysis

The gas analysis was performed to each flame that was studied to measure the concentration of the major species (O_2, CO, CO_2, and NO_x), which were used to validate the kinetic models. The gas analysers that were used for this study were Horiba VA-3002 and VA-3113, which received the gas sample from a sampling unit, VS-3004. The sampling unit was responsible for pumping the gas sample from the sampling probe to the unit and distributing it to the analysers. The gas sample was treated in the sampling unit to remove the water content, filter any solid contaminant, and adjust the temperature of the gas sample. Also, the sampling unit distributed the operational gas, nitrogen, to the analysers.

The VA-3113 analyser was responsible for detecting SO_x and CO_2 using the Dual-Beam Non-Dispersive Infrared Absorption Method (NDIR) as well as O_2 using the Magnetic Pressure Analysis (MPA) method. However, in this study, the fuels were assumed as being sulphur-free and the SO_x concentration was not measured. The VA-3002 was responsible for detecting the NO_x concentration using the chemiluminescence analysis (CLA) method and CO concentration using the NDIR method. The NDIR and MPA method in the analysers have the uncertainty of 0.5 per cent while the CLA method has uncertainty of 0.5 and 1 per cent for the full and 100 ppm range, respectively, according to the manufacturer datasheets.

The NDIR method works by emitting an infrared signal to the sample cell and the reference cell. The sample cell was filled with the gas sample while the reference cell was filled with nitrogen gas. The reference cell does not absorb the infrared beam while the molecules in the sample cell absorb a specific wavelength of the beam. The detector identifies the energy difference between these two cells and produces a signal. Furthermore, the signal was amplified and processed into the final reading.

The detection of NO_x species in the CLA method uses ozone (O_3) to generate

chemiluminescence light. When NO reacts with O_3, it oxidises into NO_2 and some of them are exited into the $NO_2{}^{\bullet}$ radical. When it returns to the ground state, light (hv) is emitted and creates chemiluminescence. These processes occur rapidly and are not interrupted by the presence of other gases. The chemiluminescence light intensity is proportional to the concentration of NO. The light is captured by a photodiode and its intensity is processed to the final reading. The reaction mechanism of these processes are expressed in Reactions (R.3.1) and (R.3.2).

$$NO + O_3 \longrightarrow NO_2{}^{\bullet} + O_2 \qquad\qquad\qquad (R.3.1)$$
$$NO_2{}^{\bullet} \longrightarrow NO_2 + hv \qquad\qquad\qquad (R.3.2)$$

The MPA method uses the paramagnetic properties of oxygen to detect its concentration. In the analyser, a non-uniform magnetic field is created and the gas sample flows through this field. When the oxygen molecule is present in the gas, it is attracted towards the stronger magnetic field and increases the pressure in that field. The oxygen accumulation is removed by the non-magnetic gas flow, which is nitrogen. Furthermore, the pressure difference is measured by a pressure sensor and translated into the oxygen concentration reading.

The reading of the gas analyser may shift after a period of time. According to the manufacturer datasheet, it could reach up to 2 per cent after 2 weeks. To maintain its accuracy, the analyser was calibrated daily using a reference gas. The reference gas was supplied by BOC and certified for the accuracy of the gas concentration. The calibration procedure was by flowing the reference gas to the analyser and adjust the reading of the analyser to the certified concentration of the gas cylinder and zero for the zero gas. There are two reference gases that were required for this procedure, which were zero and span gas. The zero gas is the reference where there is no concentration of the major gas species while the span gas is the gas with a known concentration of the major gas species. The zero gas was obtained from the nitrogen which was used for the operational gas of the analyser. Meanwhile, the span gas for the major species was mixed in a gas cylinder which was balanced with nitrogen, except oxygen which was calibrated using the atmospheric air. The composition of the span gas and the range of the measurement are presented in Table 3.3. The span and the operational gas were supplied at 0.2 and 1 bar, respectively.

Table 3.3: Concentration of the span gases for the calibration of the gas analyser and the measurement range.

Gas	Span concentration	Measurement range
SO_2	48.8 ppm	1000 ppm
O_2	21 percent (air)	50 percent
CO_2	7.6 percent	50 percent
NO	102 ppm	500 ppm
CO	0.5 percent and 5172 ppm	20 percent and 5000 ppm
Zero and operational (N_2)	100 percent	N/A

The gas sample was collected by introducing a quartz probe to the flame and it was pulled towards the gas analyser by the analyser pump. The gas sample line was heated to 160°C using a heated line system to prevent condensation of the water vapour from the gas sample. The measurement points were similar to the temperature measurement, which were 0.2 mm increment up to 1.4 mm, then 1.7, 2, 2.5, 3, 5, and 10 mm above the burner and positioned using the XYZ traverse system. The 0 mm was obtained by touching the quartz probe tip to the surface of the burner. After the probe was positioned to the measurement point, the analyser was given more than 2 minutes to let the sample reach the analyser and stabilise the reading. When the reading was stabilised, 200 measurements were recorded in a period of 30 seconds. The data acquisition employed the Omega Multiscan 1200 which captured each species reading to a channel and generate an output in a data file. Furthermore, the data file was processed to obtain the average and the standard deviation from the 200 measurements.

The probe was specially designed in order to minimise the disruption to the flame and quench the gas sample so the combustion reaction could be stopped. The probe was made from quartz which is suitable for a high-temperature sampling and it has a tapered-shape end to avoid any accumulation of the gas sample at the tip of the pinhole. Also, this allowed the gas sample to be quenched by the expansion of the probe diameter, which is known as aerodynamic quenching [153]. Without quenching, the gas sample continuously reacts in the flame and produce the final combustion product composition. It was manufactured in the University of Sheffield's glass workshop by Daniel Jackson.

The pinhole diameter controlled the sample flow rate to the analyser, where the smaller diameter results in a larger pressure drop and leads to smaller flow rate. The pinhole diameter for the optimised probe was approximately 0.1 to 0.4 mm according to the manufacturer, which generated 0.1 L/min of gas sample flow rate. The gap between

the inner and outer wall was approximately 1.5 to 2 mm. The inner and outer walls were connected by a partition, which was also used to ensure the water flows to the conical part of the probe and absorb the heat from the probe wall before leaving the quartz probe. Without this partition, the water flows directly from the inlet to the outlet tube without circulation to the bottom part of the flame. In this study, aerodynamic quenching was not enough to suspend the reaction of the gas sample. The reading of the quartz probe showed no difference at various positions of the flame. To solve this problem, an additional quenching method was added. The water-cooled probe was found to be effective for quenching the gas sample, which showed the expected gas concentration profile in the different positions of the flame. The water flowed in the gap between the outer and inner wall, so it coated the inner wall and carried the heat away with the flow. The flow rate was measured with a measuring beaker and a timer, which indicated 1.26 L/min from the average of seven repetition and standard deviation of 0.006255 L/min. The water temperature was measured using a type-K thermocouple and showed a steady reading at 21 °C. Sketches and the photograph of the water-cooled quartz probe are presented in Figure 3.6 and 3.7, respectively.
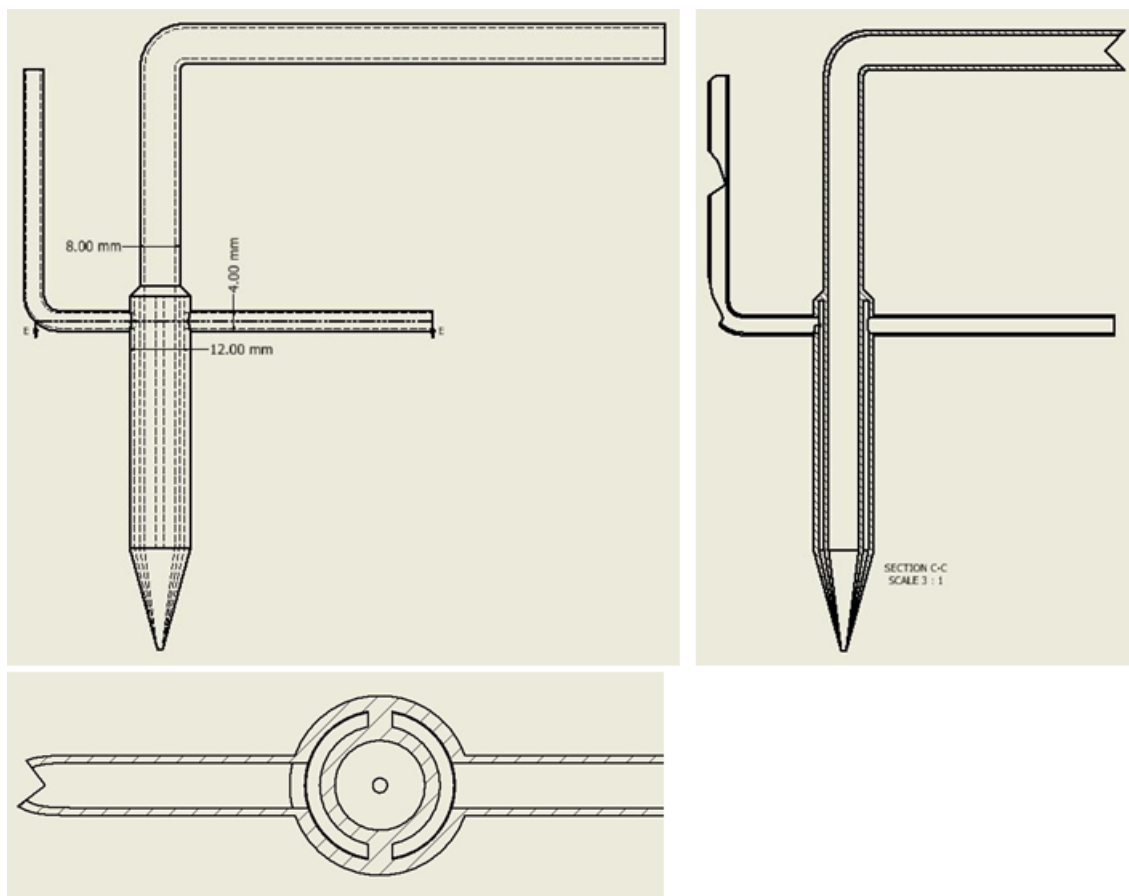
Figure 3.6: Sketches of the water-cooled quartz probe.

Previously, several prototypes of quartz probes were tested to collect the combus-

tion gas from the measured flames, but none of them was able to produce the expected species profile. The main problem that was found in these probes was the inability of the probes to generate the desired quenching of the gas sample. Consequently, the reading of the gas analyser showed a low concentration of oxygen and high concentration of carbon dioxide because the combustion reaction continuously proceeds after the gas sample entered the probe. The development of the design of the quartz probe prototypes is shown in Figure 3.8. The design ideas were based on the literature review of the previous work of flame gas sampling documentation with a trial and error approach. The probe designs in the literature sometimes are difficult to manufacture because of its complicated geometry and small dimension. Therefore, in developing the probe prototypes, the referred designs were modified to accommodate the tolerance and capability of the manufacturing facility.
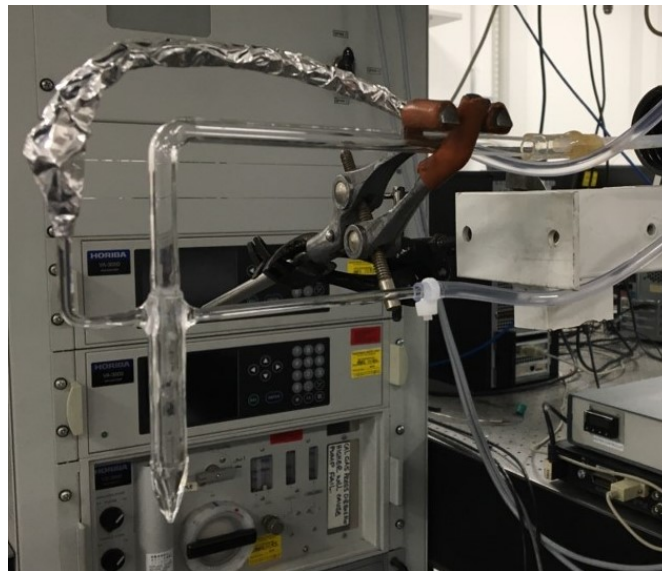
Figure 3.7: Photograph of the water-cooled quartz probe.

Figure 3.8(a) is a photograph of the first prototype version of the quartz probe which was designed to duplicate the quartz probe that was used by Catalanotti [5] in her thesis. It was reported in the thesis that the quartz probe performed well and was able to measure the species concentration profile of jet fuel flames. However, it was difficult to find a manufacturer who was able to replicate the probe design, especially with a pinhole diameter of 0.075 mm. Alternatively, a similar quartz probe with a pinhole diameter of 0.1 to 0.2 mm was able to be manufactured at the end of a 3 mm tube. The 3 mm tube was 6 cm long and joined with an 8 mm tube through a 5 mm long conical reduction tube. Unfortunately, the reading of the analyser in a rich flame of a jet fuel surrogate found a high concentration of CO_2 and a low concentration of O_2, approximately 2 and 10 per cent, respectively, at the base of the flame which indicated that the probe failed to quench the gas sample. Therefore, it appears that

the combustion process continued when the gas sample entered the probe which causes the reduction of oxygen and production of carbon dioxide.

Figure 3.8(b) shows the second prototype of the probe, which was obtained by creating a sharp end from prototype A. Meanwhile, Figure 3.8(c) is a photograph of the third prototype which was acquired by cutting the 3 mm tube from the prototype A. These probes were tested for measuring a lean jet fuel surrogate to ensure the presence of oxygen at the gas sample at the base and top part of the flame. Using prototypes B and C, the analyser detected oxygen concentration at the base the flame approximately 5 and 6 per cent, while the carbon dioxide concentration was 11 and 5 per cent, respectively. It was assumed from this findings that the expansion zone of probe B was too small to allow the quenching while the prototype C has a too large pinhole diameter, which allowed more gas sample to enter the probe and it becomes more difficult to quench. Figure 3.8(d) shows the prototype D which has 1 mm pinhole diameter, and 4 mm tube diameter. This probe was able to produce the expected result, which shows almost 20 per cent of oxygen and 3 per cent of carbon dioxide at the base of the flame and represent the expected profiles of NO, O_2, and CO_2 for all the rest of the measurement points. However, the CO profile that was obtained using this tube was not stable and the repeatability of the data was not confirmed due to the inconsistent performance of the probe. After several minutes of flame exposure, the quenching ability of this probe was decreased due to the accumulation of soot and particles inside the probe and the characteristic of unknown materials which glowed red.

After the previous findings, the further development of the probe prototypes was focused on obtaining an optimal tip geometry which allows the quenching of the gas sample. This involved the modification of the size of the expansion zone length and pinhole diameter. Prototypes E, F, and G are presented in Figure 3.8(e), 3.8(f), and 3.8(g) which have an expansion zone of 2 cm for probe G and 3 cm for the other probes, while the pinhole diameter was tested at 1 mm for Probe G and sub-millimetre for the other probes. Meanwhile, Figure 3.8(h), 3.8(i), 3.8(j), and 3.8(k) show the next prototype of the probe with a shorter expansion zone, which are 5, 12, 17, and 20 mm for probes H, I, J, and K, respectively. The pinhole diameter of probe J was 1 mm while the diameter of the other probes is varied and smaller than 1 mm. Unfortunately, the results of the measurement test using these probe were not more promising than the previous prototypes, which resulted in less than a 10 percent of oxygen concentration reading at the base of the flame. The diameter of the pinhole affects the flow rate of the gas sample to the analyser. Consequently, a smaller diameter required a longer response time of up to 15 minutes with the smallest probe pinhole diameter for the analyser to generate a stable reading while a larger diameter leads to

a faster response time. Meanwhile, the modification to the expansion zone was able to generate a quenching for a short period of time. After several minutes, the probe wall became hotter due to the exposure to the flame and initiates a flame ignition inside the probe. The flaming phenomena was clearly observed in Figure 3.8(j) and also found in a smaller flame size in the other probes. This caused the consumption of the oxygen inside the probe and resulting in a lower concentration of oxygen and higher concentration of carbon dioxide in the gas samples.
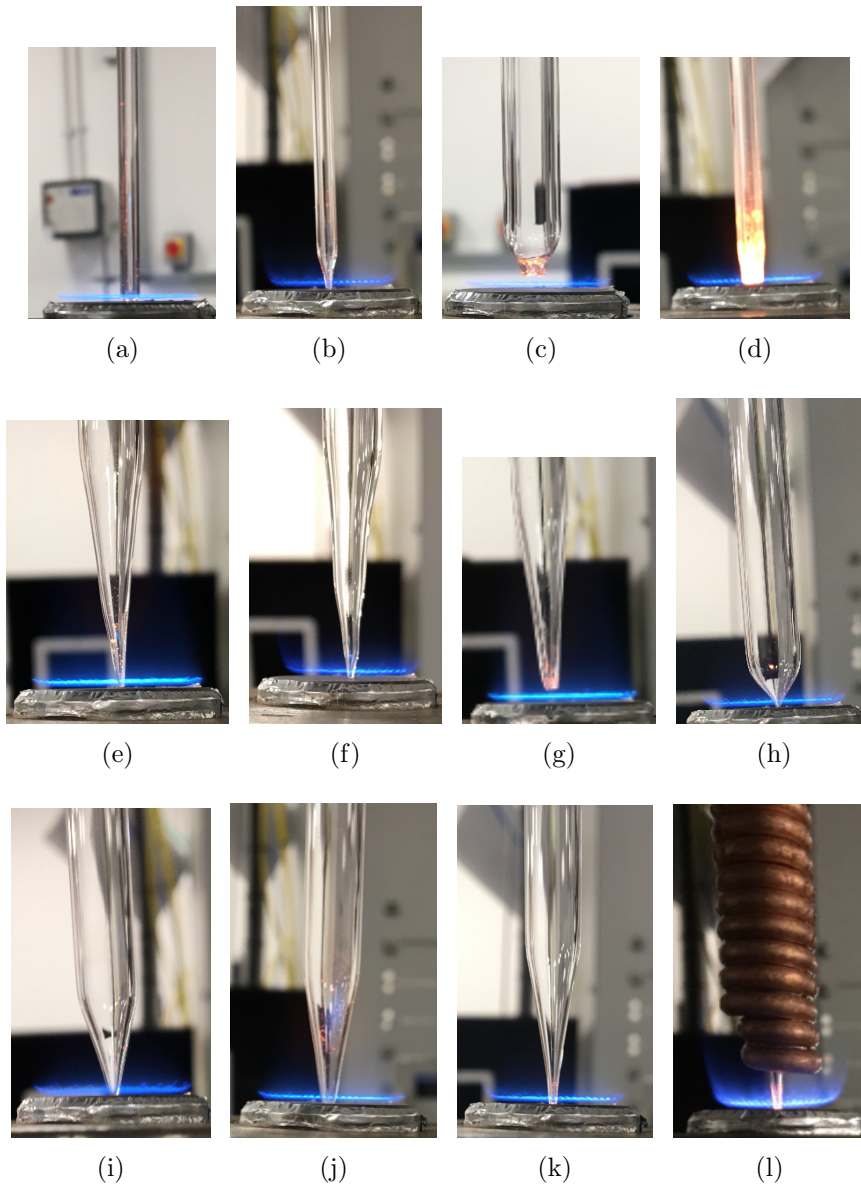
Figure 3.8: Previous prototypes of the sampling probes.

After the previous development and test of the probe prototype, it was concluded that aerodynamic quenching from the probe geometry was not enough and additional quenching method was required. The water-cooled probe has been used by many

researchers, but the University of Sheffield Glass Workshop was not able to manufacture the probe at that time. Alternatively, a copper tube was coiled in the Probe K and connected to a water supply to add extra quenching. Using this probe configuration, the oxygen concentration reading at the base of the flame could reach more than 10 per cent. From this test, it was concluded that the water cooling method is necessary and a design for a water-cooled probe was proposed to the University's glass workshop.

3.4 LIF

The laser-Induced Fluorescence (LIF) method has been used by many researchers to measure the concentration of small molecule species in a flame such as OH and NO. This technique offers advantages compared to the measurement with a physical probe, such as non-intrusive and simultaneous measurement. The exposure of a physical probe in a flame may disturb the flow of the flame, while the LIF method does not require a physical part to be exposed into the flame. The probe technique measures a single point each time, which depends on the position of the probe. Meanwhile, using the LIF method, the profile of the measured species can be obtained simultaneously in a 2D picture. The disadvantage of the LIF method compared to the measurement with a physical probe is that it results in a qualitative measurement of the species concentration. More effort is required to yield the quantification from the qualitative results through a calibration procedure.

3.4.1 Working Principle of LIF

The LIF method utilises the principle of fluorescence for detecting the density of the measured species in a flame, which is excited to a higher energy level by laser radiation and spontaneously emits light radiation when it returns to the original energy level. This is caused by the energy of the laser radiation photons matching the difference between the ground state and excited state energy level within the molecule, which becomes stimulated to the excited state.

The observed molecule, such as OH and NO, absorbs the photon from the laser pulse at a certain wavelength and undergoes a transition to a higher energy level. Generally, for the diatomic molecules, its total energy, E_{tot}, is the sum of the electronic energy level, E_e, vibrational energy level, E_v, and rotational energy level, E_J. The ground state of the electronic energy level is denoted as X, while the next higher level is denoted as A, B, etc. For each electronic energy level, there are several vibrational energy levels ($v = 0, 1, ...$), and for each vibrational levels there are several rotational energy levels ($J = 0, 1, ...$). Figure 3.9 illustrates the configuration of these energy levels [6].
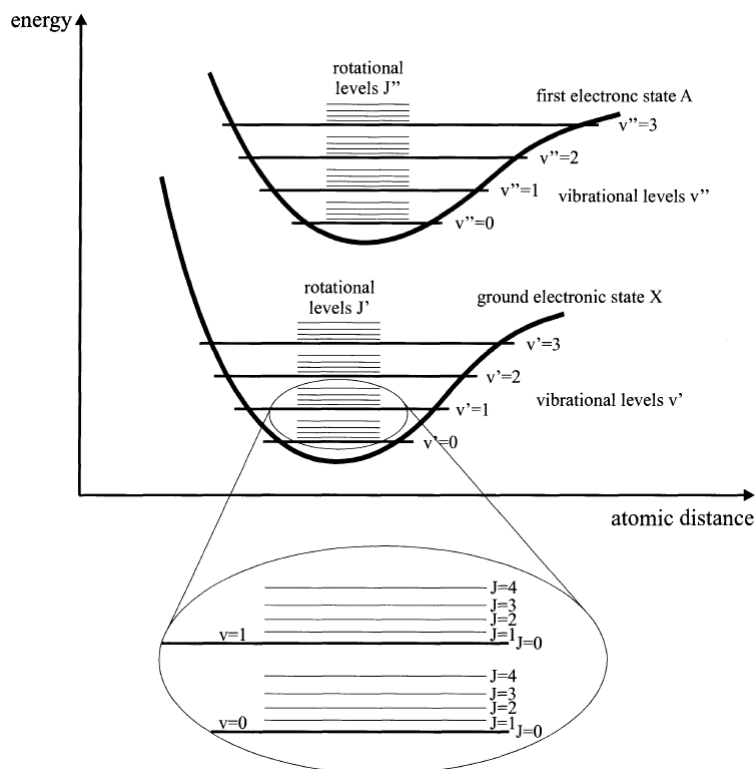
Figure 3.9: Illustration of the molecule energy level. Source: Mayinger [6].

During the exposure of the laser pulse, molecules of the measured species have several possible behaviours. It could absorb the incident photon and become excited to a higher electronic energy level, then returns to its original ground state with emitting photon at the same wavelength as the laser photon known as "resonance fluorescence". Collisions with the molecules in the flame may cause vibrational energy transfer (VET) and rotational energy transfer (RET) at the excited state and followed by photon emission through fluorescence at different wavelength to the laser. Finally, at the excited state, the molecule could collide with another molecule and relax to a lower electronic state, without emitting any photon, which is termed as collisional quenching. These possible processes are illustrated in Figure 3.10.

Based on quantum mechanics, there are rules for the allowed transitions known as selection rules. These state that the allowed change of the orbital angular momentum, ΔL, and the total angular momentum, ΔJ is 0 or ± 1. Following these rules, transitions can be categorised into several branches, such as P, Q, and R, which represents the transition with ΔJ equal to -1, 0 and +1, respectively. In practice, the selection rules can be broken, and weak satellite branches which correspond to $\Delta J = -2$ and $+2$ can be observed for the O and S band, respectively. The electron configuration of OH and NO are a doublet state with one unpaired electron in a $2p\pi$ orbital [154]. This electron has two possibilities of the spin quantum number, which is either positive

66

or negative. Consequently, the transition bands are divided into two sub-categories, which are denoted by subscript 1 and 2. The distribution of molecules over the ground electronic state is described by a vibrational and rotational energy levels Boltzmann distribution depending on the molecule characteristics and temperature. The LIF spectra and transition of diatomic molecules, such as OH, NO, CH, CN, CF, SiH, and N_2^+, can be simulated using LIFBASE [155]. In LIFBASE practice, the transition bands that the notation ends with "1" share the same ground state population in $J = N + 1/2$ (F1) while the notation that ends with "2" in $J = N - 1/2$ (F2).
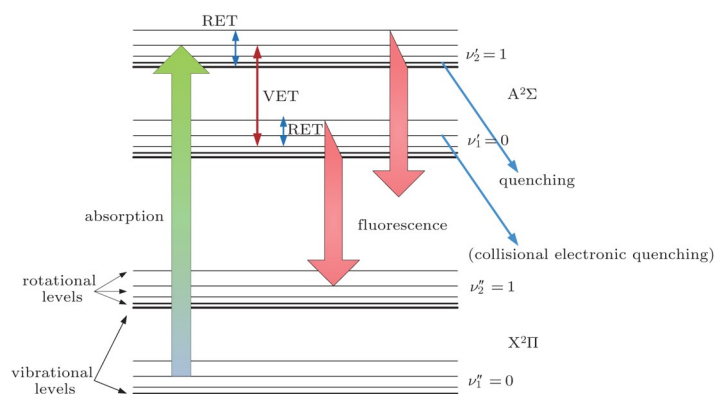
Figure 3.10: Possible transitions between energy levels of a diatomic molecule. Source: Shuang et al. [7].

3.4.2 Laser Setup

A new laser facility was purchased for the detection of the OH and NO species in this study. The configuration of the laser for OH measurement is illustrated in Figure 3.11 while a few changes of the harmonic generator is required for the NO measurement. The change is required because the laser beam wavelength for OH and NO measurement are different and which are approximately 283 and 226 nm, respectively. A pulsed Nd:YAG laser, Q-Smart 850 is used to pump a dye laser. The Nd:YAG laser generated a laser beam output at 1064 nm wavelength, and passed through a harmonic generator to double its frequency (2ω) for the OH measurement or triple frequency (3ω) for the NO measurement, then passed through a beam dump and a dichroic. It generated 532 and 355 nm for the OH and NO configuration, respectively, and supplied the laser beam for the dye laser. The dye laser model was a Sirah Cobra Stretch, and was able to tune the laser beam to the desired wavelength. The dye laser has a resonator and an amplifier cell which must be circulated with a dye solution. For the NO measurement, the composition of the dye solvent for the resonator was 0.2 g/L coumarin 2 in methanol and for the amplifier was 0.068 g/L. The methanol and coumarin 2 were supplied by Acros Organics with purity of 99.9 per cent and 99 per cent laser grade, respectively.

For the OH measurement the dye solvents were approximately 0.09 g/L of rhodamine 6G in ethanol for the resonator and 0.03 g/L for the amplifier.

The dye laser consists of multiple optical components which are very sensitive to the laser performance. The laser alignment procedure of the dye laser components was performed prior to the measurement to ensure that the dye laser was in the optimum alignment. When the dye laser was not well aligned, the quality of the laser beam became weaker and decreased the fluorescence intensity of the observed flame. The alignment involved the positioning of the mirrors, prisms, dye cells, and crystals, which were adjustable and checked for the direction and quality of the laser light. The quality of the dye solvent may degrade after a while of operation, which decreases the intensity of the laser beam. Replacement to the dye laser was performed when the beam quality was found to be significantly decreased, especially for NO measurement which used higher laser power and frequency.
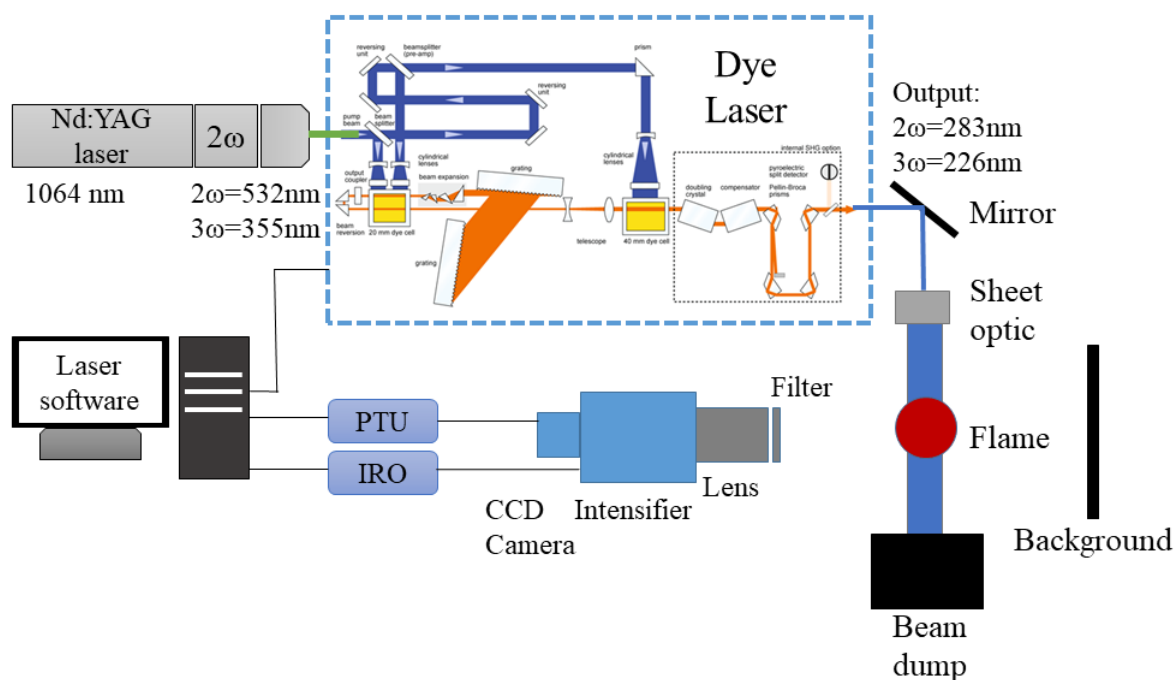
Figure 3.11: Schematic of the LIF measurement setup. Source: expanded from the Sirah dye laser manual.

The shape of the generated laser beam from the dye laser was typically a small dot and this required conversion to a vertical thin light sheet in order to generate a planar laser-induced fluorescence (PLIF) image. Thus, the output of the dye laser was directed to a laser sheet optic by using a mirror and the desired shape of the laser beam for the PLIF purpose was achieved. The laser sheet was directed to the middle part of the flame while its focus was maintained at approximately 2 mm thick at the middle part of the burner. Reflections of the laser beam from the exposure to the burner

surfaces to the camera may cause disturbance to the captured images. Therefore, an object with black body was positioned to block this reflection as well as a beam dump which was positioned at the end of the laser path.

The fluorescence from the flame was captured by a set of imaging devices which consisted of a charge-coupled device (CCD) camera, intensifier, lens, and a filter. The CCD camera model was M-lite which was purchased from LaVision as well as the intensifier. A special filter with a narrow wavelength of OH and NO fluorescence was used to minimise the light noise from other light sources other than the fluorescence signal. The lens was utilised to make the image focus on the flame region and allows maximum light intensity to enter the intensifier by fully opening the aperture setting. The intensifier captured the fluorescence signal from the input window and converted it into electrons by using a photo cathode, then the signal was strengthened and generated as light in the output window. Subsequently, the amplified signal was captured by the CCD camera and converted to a digital image which was collected by the imaging software, DaVis, in the paired computer. To obtain a high-quality image, several parameters of the imaging device, such as delay time, gate, and gain must be set at the optimum values. When these parameters were not set properly, the imaging device would miss the fluorescence signal.
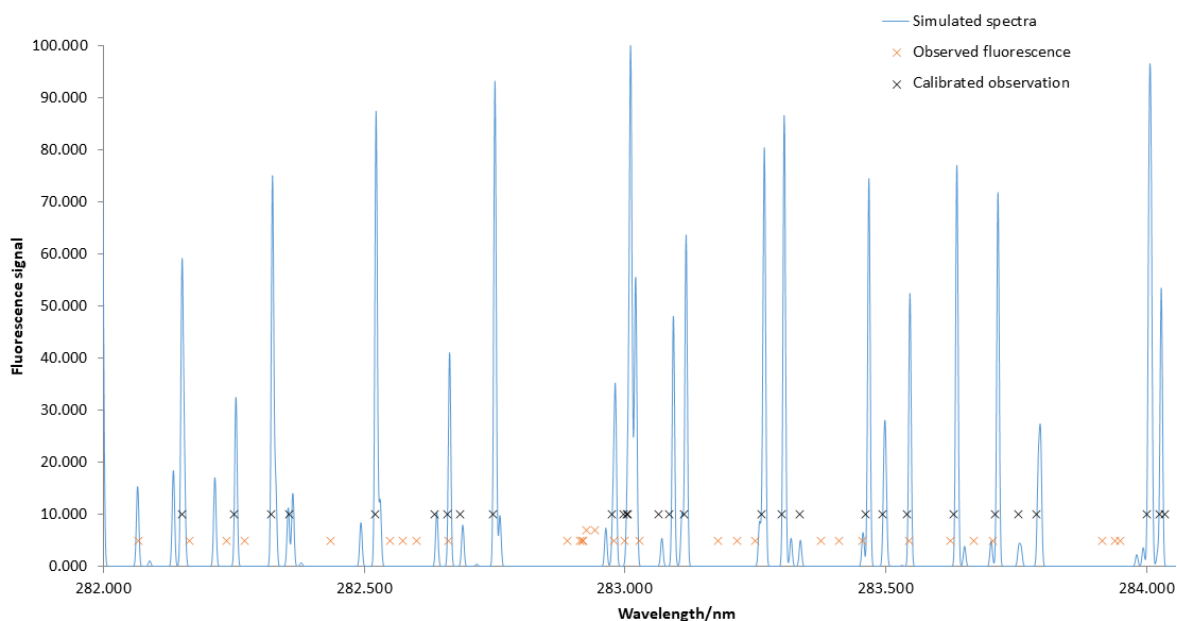
Figure 3.12: Calibration of the laser wavelength to the OH spectra from a LIFBASE simulation.

When the laser has been adjusted and the imaging system has captured a strong signal, the laser must be calibrated to know its actual wavelength. The inputted wavelength in the laser software may shift to the actual wavelength of the laser beam output. The calibration procedure involved a laser scanning to a wide laser wavelength,

approximately 2 nm with a resolution of 0.001 nm per second, which would produce fluorescence peaks when the laser wavelength was at the OH or NO transitions. The wavelengths which produced a fluorescence signal were recorded using recording software and matched to the simulated spectra from LIFBASE simulation. The offset value of the laser wavelength to the theoretical spectra can be determined from this procedure and used to calibrate the laser software wavelength input to match the targetted laser wavelength output. Figure 3.12 illustrates the calibration of the laser wavelength for the OH measurement, where the blue lines are the simulated spectra from a LIFBASE simulation, the orange symbols are the wavelengths which fluorescence peaks appeared, and the black symbols are the fitted data where the wavelengths were offset to 0.085 nm.

3.4.3 Measurement Procedure and Signal Processing

The laser system parameters that were used in this study are summarised in Table 3.4. The selected transitions involved the strongest transition, the most temperature sensitive transition pair and an off-resonance wavelength for the background noise correction. The transitions are from the $A^2\Sigma^+\leftarrow X^2\Pi$ (1,0) and (0,0) excitation state for OH and NO, respectively. The off-resonance frequency was selected to the near to the OH and NO measurement wavelength in order to minimise the movement of the dye laser grating. If the laser wavelength moved too much, it may cause the shifting of the laser alignment which impacts to the laser sheet quality.

The difference in the parameters of the laser imaging systems for OH and NO measurement was caused by the NO fluorescence signal which is relatively weaker than that of the OH. The strategy to improve the signal strength of the NO fluorescence were increasing the laser power, limiting the light entering the intensifier window by limiting its gate. The use of the narrower timing parameters required a more precise adjustment and this was performed with the assistance of an oscilloscope to monitor the timing of each parameter. The laser should be armed during the period of the intensifier gate was opened and the fluorescence signal should be captured before the gate was closed.

In order to maintain the quality of the laser dye, a higher intensifier gain and camera binning were used while the minimising the laser power. The use of higher intensifier gain would amplify the signal of the fluorescence. However, the signal of the noise was also amplified, but this could be solved by performing a background noise signal correction using the images from the off-resonance wavelength. The use of camera binning could increase the fluorescence signal by merging the signal intensity from several pixels into one. Consequently, the image would lose its resolution when binning was applied. This could be improved by placing the measured flame close to

the camera, so the size and resolution of the measured object would increase. The parameters of the Q-switch of the Nd:YAG laser were not changed from the original setting from the manufacturer.

Table 3.4: Laser settings for the OH and NO measurements in this study.

Parameter	OH	NO
Transition branch (wavelength)/nm	Q1(6) (282.926), Off A (282.963), R1(12) (281.9811), R2(2) (282.1263), Off B (282.101).	Q1(12) (226.0332), P2(22) (226.3461), Q2(15) (226.3268), Off C (226.3557).
Laser power/%	40	70
Intensifier gain/%	70	70
Intensifier gate/ns	10000	1000
Intensifier delay/ns	3400	3000
Phosphor decay time/ms	3	2
Camera binning	2x2	2x2
Camera exposure/ms	20	20
Laser reference time (dt)/µs	10	10
Q-switch delay max/µs	170	170
Q-switch delay min/µs	500	500
Laser pulse width/ns	5	5

At the beginning of the measurement procedure, the laser sheet quality for each wavelength was checked using a quartz cuvette which was filled with deionised water. The purpose of this procedure is to obtain the uniformity of the laser sheet and for calibrating the laser results. Generally, the intensity of the laser sheet was not uniform and vertically varied. From the image of the scattered laser light from the cuvette, the variation of the laser intensity in the vertical axis can be determined. The calibration of the laser results to the laser sheet intensity was by dividing its signal to the signal from the cuvette measurement. Figure 3.13(a) is the typical OH fluorescence signal from a flame at the R2(2) transition, while the Figure 3.13(b) is the image of the same flame when the laser wavelength is adjusted to the off-resonance zone. It is clearly visible from Figure 3.13(b) that the main background noise was the reflection of the laser light from the burner surface and this was not significant compared to the fluorescence signal. Figure 3.13(c) shows the quality of the laser beam at the OH R2(2) transition while Figure 3.13(d) presents the profile of the light intensity at the middle section of the laser sheet. Figures 3.13(c) and 3.13(d) inform that the laser sheet was moderately

uniform and severe fluctuations in the intensity were not found.

The image collection for a single wavelength measurement involved 500 repetitions in 50 seconds to ensure the repeatability of the collected data and to accumulate the dynamics of the flame and the laser. The images were recorded using the DaVis software and then processed using the same software to obtain an image which represents the average of the signal intensity from 500 images. Furthermore, The averaged image was exported to a Tecplot file for further analysis. Using the Tecplot software, the desired intensity data can be extracted by drawing a line on the observed image and the data was extracted and stored in a spreadsheet. The resolution of the data was 200 points per line and its length was approximately 15 mm which is positioned on the area of interest. The Tecplot software allows the extraction of the intensity data using the same measurement line for multiple frames, so the observed position was not shifted and had the same coordinate for multiple frames. This data can be used for further mathematical operation, such as subtraction and division to obtain the normalised data, quantification, and temperature measurement which will be discussed in the next chapter. This method is more efficient compared to the previous data processing method using a Matlab code that was developed by the author.
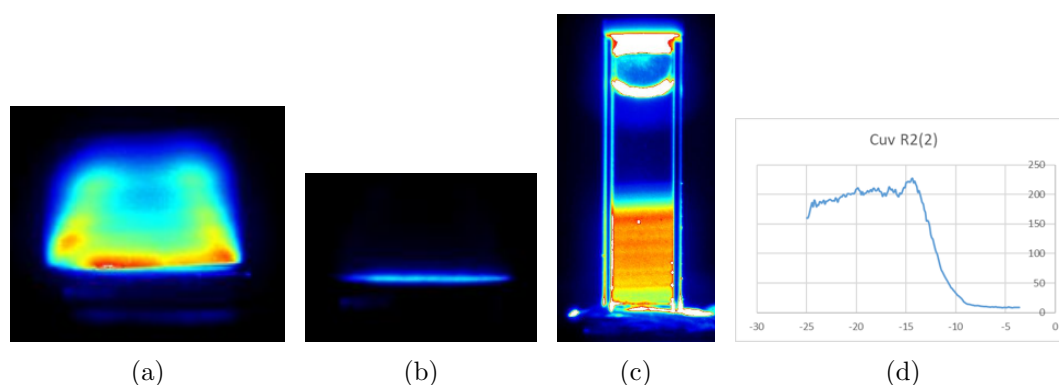
Figure 3.13: Examples of the signal from (a) the OH R2(2) transition, (b) off resonance 282.33 nm, (c) laser sheet calibration with a cuvette, and (d) the signal from the middle section of the cuvette for R2(2) wavelength.

3.5 Concluding Section

This chapter has explained the experimental setup of the burner flame experiment as well as the details of the materials, procedures, and instruments that were used in this study. All the exhaustive works for this experimental setup have been performed by the author with support from the laboratory technician, academics, students and engineers from the manufacturer of the instruments. This effort has successfully led

to the generation of various measurement data from the flame investigation which are presented in the next chapter. Improvement of several aspects of the experiment method may be possible, but due to the time limit of this study, the current setup was employed for the burner flame study.

Chapter 4

Burner Flame Experiment Results

This chapter presents the results of the burner flame experiment that was described in the previous chapter. The results comprise of the thermocouple temperature measurement, gas sampling, OH and NO PLIF data as well as the data processing, analysis and discussions are presented. The measured systems were the real jet A-1, ethanol, 50:50 jet A-1:ethanol by volume (E50), surrogate A and surrogate B flames, which were observed at near stoichiometric (1.07), lean (0.86) and rich (1.28) mixtures. The composition of the surrogate A was 80:20 n-decane:1,2,4 trimethylbenzene by weight, while the composition of the surrogate B was 60:20:20 n-dodecane:methylcyclohexane:o-xylene by volume.

4.1   Temperature Measurement

Temperature measurement in a premixed flat-flame burner study is important because it determines the kinetic behaviour of the combustion reactions. Most of the combustion reactions are temperature dependent and have different reaction rates at different temperatures. This leads to the effect of the temperature on the flame structure, such as the species concentration at various positions in the flame. Therefore, it is essential to supply the temperature profile of the flame for modelling with PREMIX code as explained in Section 2.2.3.

The adiabatic temperature of a flame can be calculated by knowing the total heat of formation, ΔH_f, and the heat capacity of all species, C_p as expressed in Equation (2.11). However, the flame was not adiabatic as it was reacting in an open system. The heat was released to the surroundings, such as the air and burner components, and also gained from the burner heater. Therefore, performing a temperature measurement using a thermocouple is more advisable in this study. The results of the temperature measurement are presented in Tables 4.1, 4.2, 4.3, 4.4, and 4.5 for the jet A-1, ethanol, E50, surrogate A, and surrogate B, respectively.

Table 4.1: Temperature measurement data of the Jet A-1 flames.

X	$\phi = 0.86$			$\phi = 1.07$			$\phi = 1.28$		
/mm	T_m/K	T_c/K	σ/K	T_m/K	T_c/K	σ/K	T_m/K	T_c/K	σ/K
0.0	956.2	969.6	20.4	1296.7	1344.4	24.8	1248.8	1289.5	14.5
0.2	988.8	1004.3	23.1	1546.9	1646.4	19.3	1228.2	1266.2	18.6
0.4	1059.1	1079.7	15.3	1683.6	1825.1	12.8	1247.6	1288.1	15.2
0.6	1234.7	1273.8	45.8	1741.9	1905.0	15.7	1252.3	1293.5	19.4
0.8	1514.5	1605.8	22.9	1754.9	1923.1	15.7	1547.7	1647.1	18.0
1.0	1650.3	1780.9	33.0	1772.8	1948.1	5.2	1705.6	1854.4	18.4
1.2	1715.1	1868.5	15.3	1783.7	1963.6	6.4	1750.0	1915.6	37.5
1.4	1731.4	1890.9	19.6	1821.0	2017.1	11.3	1779.9	1957.6	62.7
1.7	1763.7	1935.9	17.0	1835.3	2037.9	14.8	1800.3	1986.6	46.3
2.0	1770.5	1945.6	15.6	1828.4	2027.8	25.1	1818.3	2012.6	24.9
2.5	1780.3	1959.4	19.9	1838.3	2042.3	23.2	1825.7	2023.2	24.9
3.0	1818.8	2014.6	10.5	1854.3	2065.8	16.8	1833.3	2034.3	29.6
5.0	1814.9	2008.9	21.1	1847.6	2055.9	31.1	1829.9	2029.3	40.4
10.0	1795.1	1980.5	17.1	1837.1	2040.5	26.0	1813.9	2006.1	39.0

Table 4.2: Temperature measurement data of the ethanol flames.

X	$\phi = 0.86$			$\phi = 1.07$			$\phi = 1.28$		
/mm	T_m/K	T_c/K	σ/K	T_m/K	T_c/K	σ/K	T_m/K	T_c/K	σ/K
0.0	1091.3	1111.6	52.5	1187.1	1215.8	8.7	1133.8	1157.4	10.1
0.2	1107.6	1129.2	49.3	1217.4	1249.2	5.2	1158.0	1183.8	7.4
0.4	1089.2	1109.3	42.1	1229.1	1262.3	5.7	1167.9	1194.6	8.5
0.6	1071.8	1090.7	40.6	1239.3	1273.6	11.6	1183.8	1212.0	31.3
0.8	1163.5	1190.0	50.7	1495.8	1570.9	4.7	1284.5	1324.1	12.6
1.0	1284.5	1324.5	37.1	1630.1	1737.5	3.8	1443.7	1508.1	20.4
1.2	1614.3	1717.9	33.9	1677.0	1797.9	3.5	1611.0	1712.7	2.4
1.4	1619.0	1723.9	39.1	1692.0	1817.4	1.4	1645.0	1755.9	2.4
1.7	1659.7	1776.1	52.1	1695.1	1821.4	3.8	1676.3	1796.3	6.9
2.0	1632.5	1741.2	61.5	1697.8	1824.9	9.1	1677.0	1797.1	10.2
2.5	1622.1	1727.9	42.4	1697.2	1824.2	16.6	1671.9	1790.5	4.3
3.0	1648.8	1761.9	28.8	1686.6	1810.3	11.3	1665.4	1782.2	3.6
5.0	1612.8	1716.0	28.1	1684.8	1807.9	35.6	1663.5	1779.7	3.3
10.0	1615.1	1718.9	25.7	1679.4	1801.0	13.1	1654.5	1768.1	3.6

Table 4.3: Temperature measurement data of the E50 flames.

X	$\phi = 0.86$			$\phi = 1.07$			$\phi = 1.28$		
/mm	T_m/K	T_c/K	σ/K	T_m/K	T_c/K	σ/K	T_m/K	T_c/K	σ/K
0.0	1145.0	1168.6	40.8	1324.5	1367.5	6.5	1241.5	1274.3	48.6
0.2	1183.6	1210.5	51.7	1368.4	1417.7	35.1	1322.4	1365.0	22.7
0.4	1240.2	1273.0	66.8	1531.4	1610.1	16.1	1382.9	1434.2	10.3
0.6	1378.7	1429.6	40.4	1647.6	1754.3	16.3	1738.7	1871.8	12.8
0.8	1493.0	1564.0	53.0	1689.4	1807.8	18.6	1815.1	1974.4	15.9
1.0	1692.4	1811.9	47.9	1815.8	1975.6	15.6	1835.3	2002.0	4.6
1.2	1718.6	1846.0	34.6	1826.3	1990.0	18.6	1829.9	1994.6	2.9
1.4	1783.4	1932.0	46.5	1830.3	1995.5	20.6	1823.2	1985.4	1.8
1.7	1799.8	1954.2	71.1	1839.3	2007.9	10.5	1815.3	1974.7	2.0
2.0	1802.2	1957.4	52.3	1836.6	2004.2	15.5	1808.2	1964.9	1.7
2.5	1773.3	1918.4	63.2	1836.2	2003.7	12.5	1803.1	1958.1	2.5
3.0	1805.5	1962.0	32.3	1829.8	1994.8	15.3	1805.0	1960.6	13.3
5.0	1776.9	1923.4	50.2	1820.4	1981.9	14.4	1797.8	1950.9	3.4
10.0	1730.7	1861.9	47.0	1797.7	1951.0	11.0	1766.2	1908.4	4.3

Table 4.4: Temperature measurement data of the Surrogate A flames.

X	$\phi = 0.86$			$\phi = 1.07$			$\phi = 1.28$		
/mm	T_m/K	T_c/K	σ/K	T_m/K	T_c/K	σ/K	T_m/K	T_c/K	σ/K
0.0	924.3	936.2	26.0	1087.8	1111.0	10.5	1042.4	1061.8	16.8
0.2	1010.8	1027.9	69.3	1584.8	1696.0	110.0	1475.2	1557.5	182.0
0.4	1288.8	1336.0	164.8	1710.0	1862.6	139.6	1642.9	1771.7	126.9
0.6	1457.6	1536.3	159.6	1765.8	1940.2	11.4	1663.5	1799.1	41.2
0.8	1561.9	1666.9	109.9	1750.9	1919.3	5.6	1733.8	1894.9	21.8
1.0	1722.0	1879.6	24.9	1739.6	1903.5	16.6	1735.5	1897.3	24.5
1.2	1672.6	1812.2	39.4	1736.2	1898.8	20.4	1718.4	1873.7	37.7
1.4	1721.9	1879.4	8.5	1765.0	1939.1	20.8	1714.8	1868.6	10.2
1.7	1720.0	1876.8	25.2	1762.8	1935.9	36.0	1726.7	1885.0	22.1
2.0	1718.8	1875.2	11.5	1758.0	1929.2	5.1	1695.2	1841.9	8.1
2.5	1728.7	1888.9	14.5	1753.6	1923.0	11.8	1734.8	1896.2	18.0
3.0	1705.8	1857.3	10.6	1751.8	1920.5	24.7	1708.7	1860.3	8.4
5.0	1706.5	1858.3	14.7	1750.9	1919.2	20.8	1703.5	1853.2	11.5
10.0	1672.4	1812.0	24.0	1749.6	1917.5	20.5	1685.4	1828.6	7.0

Table 4.5: Temperature measurement data of the Surrogate B flames.

X	$\phi = 0.86$			$\phi = 1.07$			$\phi = 1.28$		
/mm	T_m/K	T_c/K	σ/K	T_m/K	T_c/K	σ/K	T_m/K	T_c/K	σ/K
0.0	1084.4	1107.5	179.1	1216.9	1254.0	6.4	1134.4	1162.0	3.0
0.2	1292.2	1340.0	176.1	1387.2	1451.2	10.5	1236.0	1275.4	50.4
0.4	1292.6	1340.4	177.6	1555.9	1659.1	11.2	1364.8	1424.4	120.2
0.6	1350.3	1407.7	209.9	1658.8	1793.5	3.8	1446.4	1522.3	88.7
0.8	1636.7	1764.5	70.5	1721.8	1879.2	6.5	1754.3	1923.7	5.4
1.0	1666.1	1803.8	97.4	1743.9	1909.8	3.7	1753.9	1923.2	2.7
1.2	1685.0	1829.2	52.2	1755.0	1925.4	3.2	1741.4	1905.7	2.2
1.4	1720.1	1877.3	26.2	1758.9	1930.7	3.8	1737.9	1900.9	2.3
1.7	1714.5	1869.5	27.1	1768.9	1944.8	6.2	1743.9	1909.3	2.0
2.0	1725.9	1885.3	23.8	1773.5	1951.4	6.9	1749.1	1916.4	1.7
2.5	1734.5	1897.3	23.6	1782.1	1963.6	14.0	1751.6	1919.9	2.5
3.0	1736.4	1899.9	25.2	1776.0	1954.9	18.4	1757.4	1928.1	2.4
5.0	1761.3	1934.7	17.2	1793.7	1980.2	15.4	1762.5	1935.2	2.1
10.0	1745.6	1912.7	33.9	1802.7	1993.1	22.2	1761.0	1933.1	3.2

X is the distance above the burner surface, while T_m is the average of the temperature data from the repeated measurement, T_i, and this was calculated using the following equation:

$$T_m = \frac{1}{n} \sum_{i=1}^{n=100} T_i \tag{4.1}$$

The variation among the data was assessed using a standard deviation formula as follows:

$$\sigma = \sqrt{\frac{\sum_{i=1}^{n=100}(T_i - T_m)^2}{n - 1}} \tag{4.2}$$

The corrected flame temperature, T_c, was calculated from the average temperature data, T_m, to compensate the heat loss due to radiation from the surface of the thermocouple bead, which was calculated using Equation (3.1). The ethanol and E50 flames were measured using a 50 μm thermocouple wire while the real and surrogate jet fuels were measured using a 75 μm thermocouple wire. More details on the temperature measurement method can be found in Section 3.2. Figures 4.1 presents the plots of the temperature data of all flames for a visual illustration of the temperature profiles and the standard deviations. For all flames, a similar trend of the temperature profiles were found where it started with the lowest temperature at the surface of the burner then reached the temperature peak at approximately 1.0 mm.

(a)

(b)

(c)

(d)

(e)
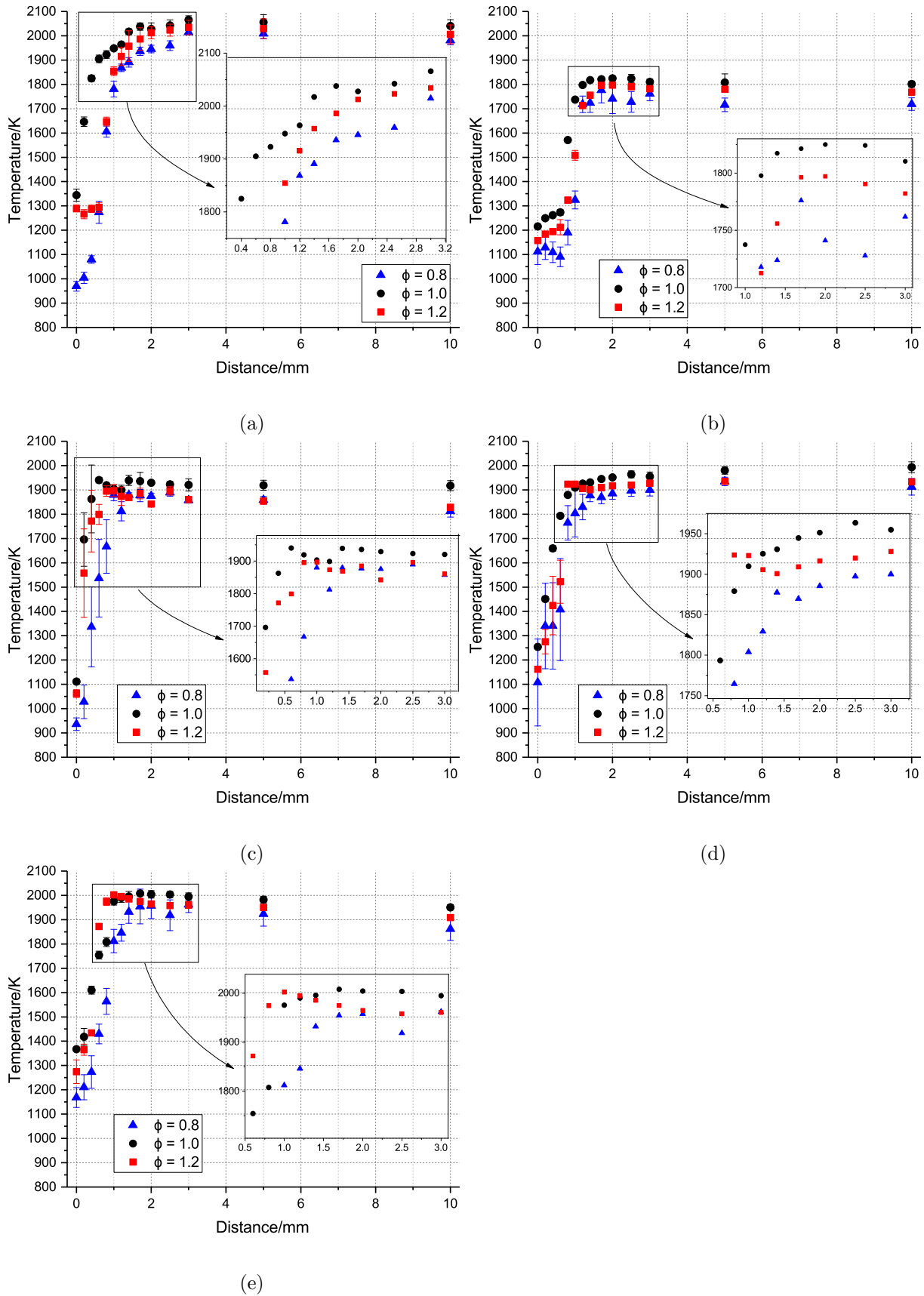
Figure 4.1: Plots of the corrected temperature data of (a) Jet A-1, (b) ethanol, (c) surrogate A, (d) surrogate B, and (e) E50, flames.

The temperatures at the surface of the burner were not similar for all flames despite the fact that the air and fuel gas mixture were preheated to the same temperature, 180 to 190°C or 453 to 463 K measured at the pipe outer surface. Apart from the heat from the unburned gas, the burner surface received more heat from the flame and this resulted in a higher temperature. While each flame had different temperature profiles thus the temperatures at the burner surface for different flames were also different.

In the first submillimetre of the flame region, there was an uncertainty in determining the position 0.0 mm above the burner surface. This was caused by the difficulty in positioning the thermocouple bead, so it was precisely touching the burner surface without excess tension in the thermocouple wire. Frequently, the thermocouple bead was overstretched to the burner due to the limitation of the visual judgement of the user in determining the gap between the thermocouple and the burner. Consequently, when the traverse system moved to the higher measurement point, the thermocouple wire and its holder moved upwards, but the thermocouple bead was still at the 0.0 mm position. This might lead to a slower temperature rise in the region from 0.0 to 1.0 mm as discovered in all ethanol flames and the rich jet A-1 flame.

For all flames, a gap between the burner surface and the flame was found and this is known as the flame lift-off distance. This distance separated the highest temperature region of the flame to the burner surface. This might also cause the slow temperature rise because the increase of the lift-off distance reduced the heat transfer to the burner surface. Compared to all mixtures, the lean flames had the most visible lifted distance. This was caused by the laminar burning velocity of the lean flames which were relatively slower compared to the rich and stoichiometric flames. Also, the lean flame was at the edge of the stability limit of the burner and close to blow off.

In all flames, the temperature correction value magnified with the increase of the distance of the burner. This was caused by the higher flame temperature at the upper measurement points compared to the burner surface. The higher temperature enhanced the heat transfer through radiation and increased the temperature correction value which depends on the measured flame temperature by the power of four as expressed in Equation (3.1). Moreover, the bead diameter also affected the temperature correction by power of 0.75. A larger bead diameter resulted in a larger bead surface which allows more heat flux escaping from the thermocouple through radiation process. Consequently, for the same temperature reading, real and surrogate jet fuel flames were corrected to a higher value compared to the ethanol and E50 flames, this is because they were measured using a larger thermocouple wire, 75 μm, while the later were measured using a 50 μm thermocouple. The bead diameter of the wire was specified as 2.5 times larger than the wire diameter which is 188 and 125 μm for the larger and smaller wires, respectively, and resulted in the larger correction value. After

the correction was performed, the range of temperature profiles of all flames became expanded because the lower temperature was corrected to a smaller value while the higher temperature was corrected to a significantly larger value.

The standard deviation of the flame temperature measurement, σ, represents the stability of the flame, where the more stable flame resulted in the less standard deviation and conversely, the less stable flame leads to a larger standard deviation. In a stable flame, the thermocouple recorded the least fluctuations in the temperature reading while the unstable flame the values of the temperature recording fluctuated more and resulted in the larger standard deviation.

The fluctuation of the temperature reading was caused by several factors from the flame and the thermocouple. In all flames, the largest fluctuation was found in the lean flame. This was because the lean flame was in the near blow-off condition, so it was considered as a less stable flame. The stoichiometric and the rich flames were relatively more stable and had less fluctuation. The surrogate A and B flames relatively had more fluctuation compared to the other flames. This might be caused by the instability of the fuel supply where a continuous flow was not generated because some air might be trapped inside the fuel lines and lead to the flame instability. Moreover, the use of a spring in the thermocouple configuration allowed the wire to vibrate due to the exposure to the flame flow. When the thermocouple wire vibrated, the bead moved with the vibration and recorded a larger fluctuation of temperature because of its movement. Also, the thermocouple system might have noise, but it contributed least to the fluctuation of the temperature measurement compared to the other factors, such as the flame instability and the thermocouple vibration.

The temperature profile of all flames increased rapidly from close to the burner surface and achieved the maximum temperature approximately at 1.0 to 2.0 mm. This indicated that the heat release rate from the combustion reactions increased rapidly and achieved the maximum value approximately at the maximum flame temperature position. Afterwards, the heat release rate value dropped significantly to approximately zero. This was indicated by the flame temperature profiles which were relatively steady after achieving the maximum temperature. For the rich flames, the unburned fuel might react with oxygen from the surrounding air and generate more heat through combustion reactions. This became possible since the burner did not have a shroud to prevent the interaction between the combustion gases and the surrounding air. The reaction between the unburned fuel with the surrounding air can be recognised from the appearance of a conical flame in the upper part of the flame. For the lean flames, this phenomenon was not found because it had sufficient oxygen from the unburned gas mixture and this resulted in a flat-shaped flame.

According to Glassman and Yetter [140], the flame temperature of hydrocarbon

fuels combustion in air at a constant pressure is mainly affected by the C/H ratio of the fuel and the equivalence ratio. Figure 4.2 summarises the flame temperatures at the final measurement point, 10.0 mm, for all fuel mixtures. For the same equivalence ratio, the real Jet A-1 flames had the highest while ethanol flames had the lowest flame temperature. The C/H ratio of the real jet fuel was higher than that of ethanol which was approximately 0.5 and 0.3, respectively. A higher C/H ratio results in a higher flame temperature because it has more C=C and C≡C bonds which have more potential energy than C−C and C−H bonds [128]. The real and surrogate jet fuel have more double-bonded carbon, especially from the aromatics content than ethanol which only has a single-bonded carbon. Also, a higher C/H ratio consumed less oxygen for oxidising the H atom to form H_2O. This means the amount of nitrogen, which exists with oxygen in air, in the combustion reaction was decreased and the higher flame temperature was achieved due to the smaller heat capacity. Meanwhile, replacing 50 per cent of the Jet A-1 volume with ethanol decreased the flame temperature by approximately 100 K as discovered in the E50 flame results. The E50 flames were approximately 150 K higher than the ethanol flames. Both surrogates had a lower maximum flame temperature compared to the real jet fuel and Surrogate A was lower than the Surrogate B flame. This indicated that both surrogates could not represent the real composition of the real jet fuel in terms of the temperature profile.

For all fuels, the highest flame temperature was achieved by the stoichiometric flame, then followed by the rich and the lean flames. This result is similar to the order of the gap of the equivalence ratio to the theoretical maximum temperature. The maximum temperature of hydrocarbon fuels combustion in air is predicted to be slightly richer than the stoichiometric ($1.0 < \phi < 1.1$) [140]. This is related to the average of the heat capacity of the combustion species which is smaller at the rich side. The lean and rich flames temperatures were lower than that of stoichiometric because the heat that was generated from the combustion process was consumed to heat the excess air and fuel in lean and rich mixtures, respectively. Therefore, the stoichiometric flames, which was the closest to the maximum temperature region, attained the highest temperature while the lean flame had the lowest temperature because it was furthest to the equivalence ratio of the maximum flame temperature.

Temperature measurements of real Jet A-1 flames were also performed by Catalanotti [5] using a similar experimental setup. The comparison of the standard deviation of the Jet A-1 flames temperature in the Catalanotti thesis and this study showed relatively similar value, which was approxymately less than 3 per cent. Similar to this study, Catalanotti found the highest temperature of the Jet A-1 flame at the stoichiometric flame, then followed by the rich and lean flames. There was a difference in the equivalence ratio for the rich flame, where this study aimed at 1.2 while Catalanotti

used 1.14. The temperature of the surface of the burner was higher in Catalanotti's work than in this study. This might be caused by the difference in the temperature and the performance of the burner heater, where in this study the burner temperature range was between 453 to 463 K and in Catalanotti's work was documented at 463 K. The higher is the unburned gas temperature, then the flame temperature will be higher and conversely. Moreover, in Catalanotti's documentation, the thermocouple wire was held using a ceramic tube instead of stretching it horizontally. This configuration leads to less accurate measurements because the thermocouple wire bent vertically and might be more affected by the flame temperature at the upper part of the flame. The final temperature of the Jet A-1 flames in this study was higher compared to that in Catalanotti's work. This might be caused by the use of a larger thermocouple wire in this work which resulted in a higher temperature correction value. Catalanotti used a 50 µm type-R thermocouple wire while this work used a 75 µm of the similar thermocouple.
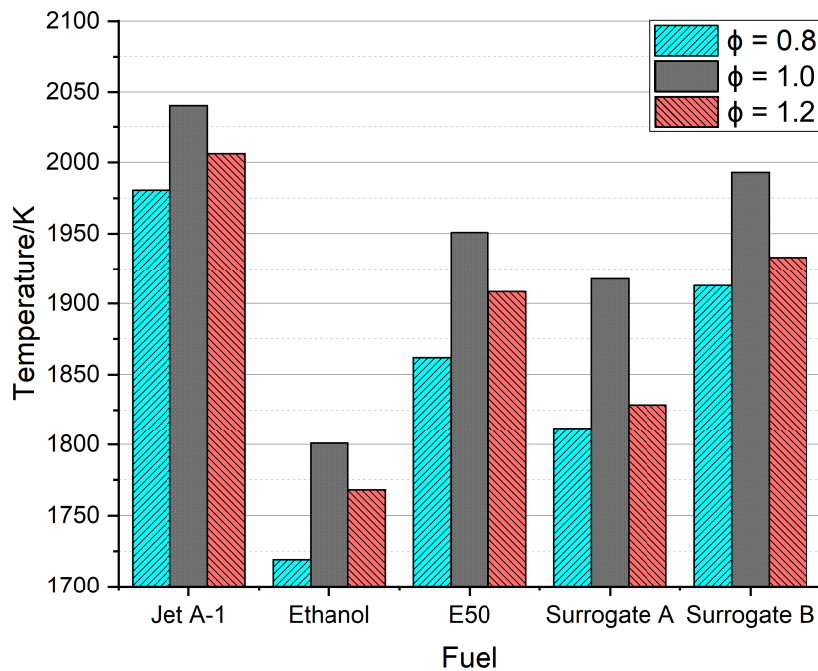
Figure 4.2: Comparison of the temperatures of the flames at 10 mm.

4.2 Gas Analysis

The concentration of the major combustion products, such as O_2, CO_2, CO, and NO_x, have been measured using the method that was described in Section 3.3. The results of the gas analysis of 15 different flames are presented in Tables 4.7 to 4.21. In the

tables, the average and standard deviation values of 200 repetition for each data point are presented which were obtained from Equation (4.1) and (4.2) with n equal to 200. The measurement points, X, were similar to that of the temperature measurement, so the effect of the temperature to the species concentration can be determined. Also, the consumption and formation of the combustion products are related to the reaction kinetics, which its rate parameters depend on the flame temperature.

Technical issues on the gas analyser were found during this measurement procedure where the analyser did not respond to the gas sample supply. The O_2 sensor stopped working during the measurement of the final points of lean ethanol and jet A-1 flames. Consequently, several points of O_2 concentration are missing from the results of these flames. A maintenance procedure has been performed to solve this issue, but this attempt could not recover the performance of the O_2 sensor. Therefore, the analyser was required to be repaired by the manufacturer and repetition of the measurement for these flames was not possible. A less severe problem was found on the NO_x sensor when the measurement of the surrogate B flames were completed. During the calibration procedure, the reading of the NO_x span gas was severely shifted to approximately 25 per cent for the ethanol flame measurement, where in the normal case, it should read 102 ppm. The severe shift in the NO_x sensor triggered the gas analyser alarm when the user tried to calibrate the span value and this disabled the calibration program of the analyser. Alternatively, the reading of the span gas was recorded daily for the NO_x and this data was used to calibrate the results of the NO_x reading. Assuming that the analyser NO_x reading is linearly related to the generated voltage output to the data logger as stated in the equipment manual, the uncalibrated NO_x reading can be calibrated by dividing it by the span reading and multiplied by the true NO_x concentration in the span gas as expressed below:

$$\text{Calibrated NO}_x \text{ reading} = \text{Measured NO}_x \times \frac{\text{Actual span concentration}}{\text{span reading}} \qquad (4.3)$$

and the recorded span readings are presented in Table 4.6. However, a major problem in the NO_x sensor was found during the measurement of the last two points of the stoichiometric and rich ethanol flames which resulted to the missing points in their NO_x concentration results. The NO_x analyser was required to be sent to the manufacturer for repair and repetition to these points was not possible.

Table 4.6: NO_x span gas reading in ppm.

Fuel	Flame		
	$\phi = 0.86$	$\phi = 1.07$	$\phi = 1.28$
Jet A-1	102	61.2	61.2
E50	42.5	44.4	44.4
Ethanol	23.6	23.6	23.6
Surrogate A	102	102	102
Surrogate B	120	120	120

(a)

(b)

(c)

(d)
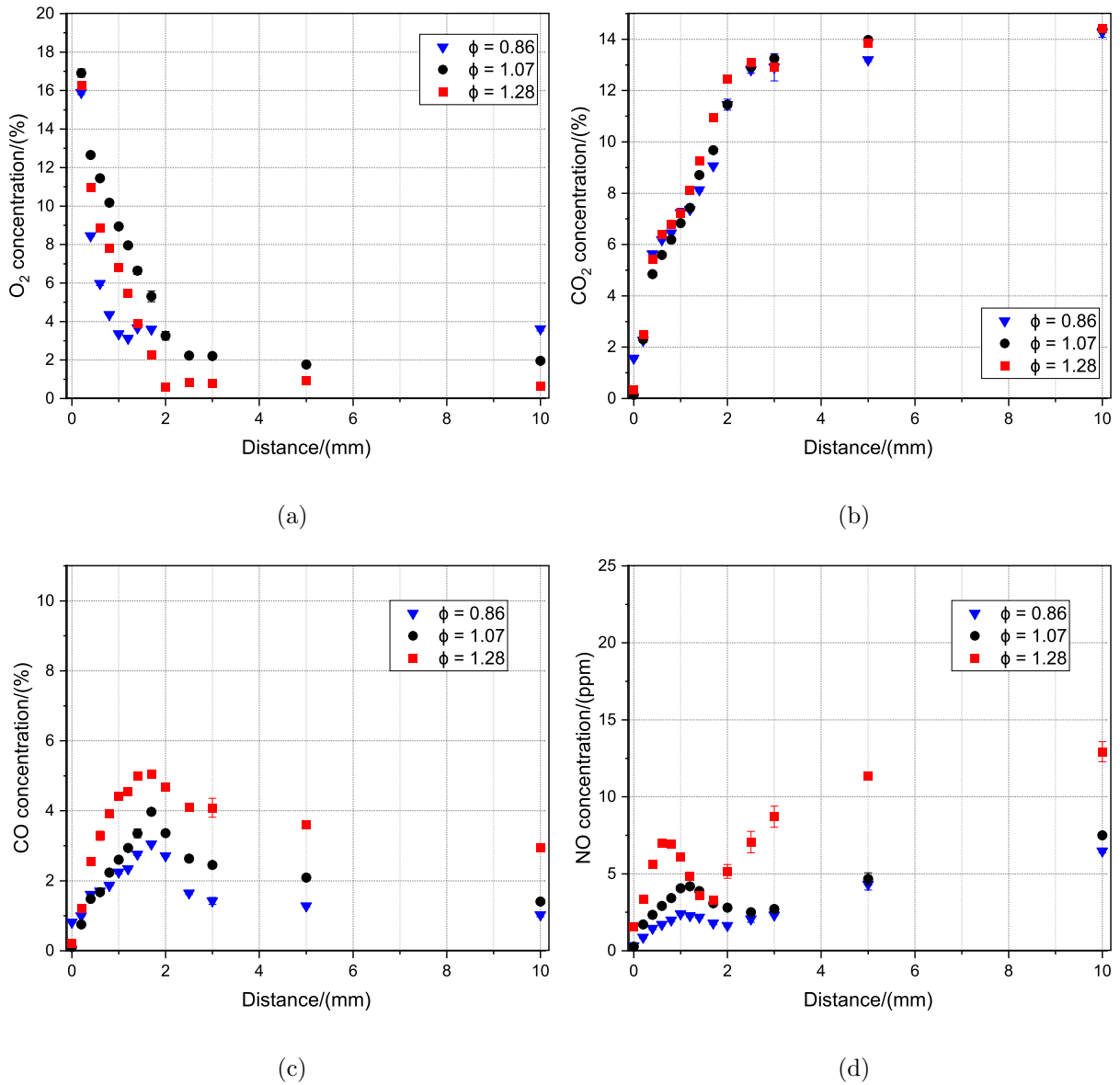
Figure 4.3: Concentration of (a) O_2, (b) CO_2, (c) CO, and (d) NO_x in lean, stoichiometric, and rich of a real Jet A-1 flames.

(a)

(b)

(c)

(d)
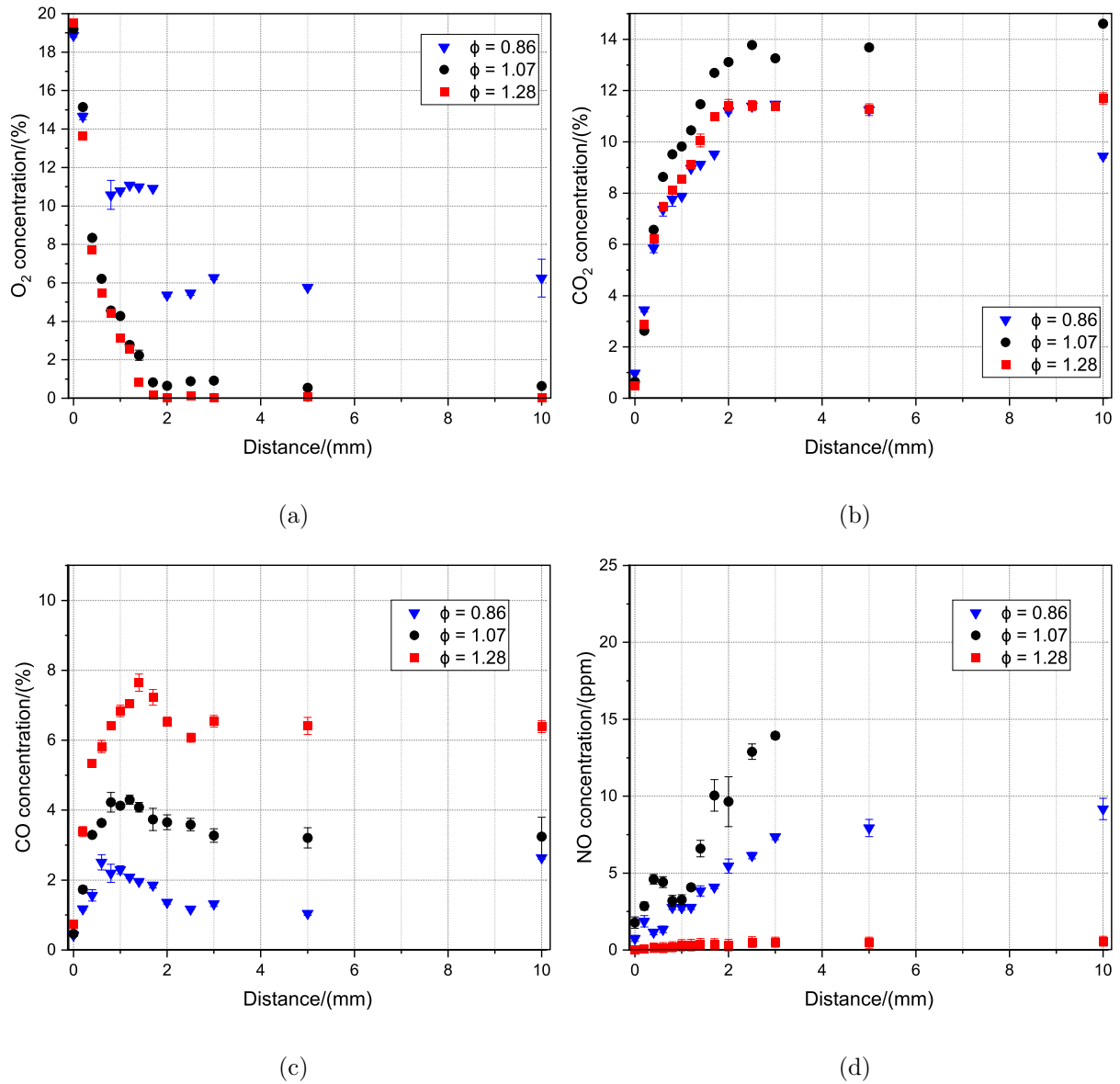
Figure 4.4: Concentration of (a) O_2, (b) CO_2, (c) CO, and (d) NO_x in lean, stoichiometric, and rich ethanol flames.

(a)

(b)

(c)

(d)
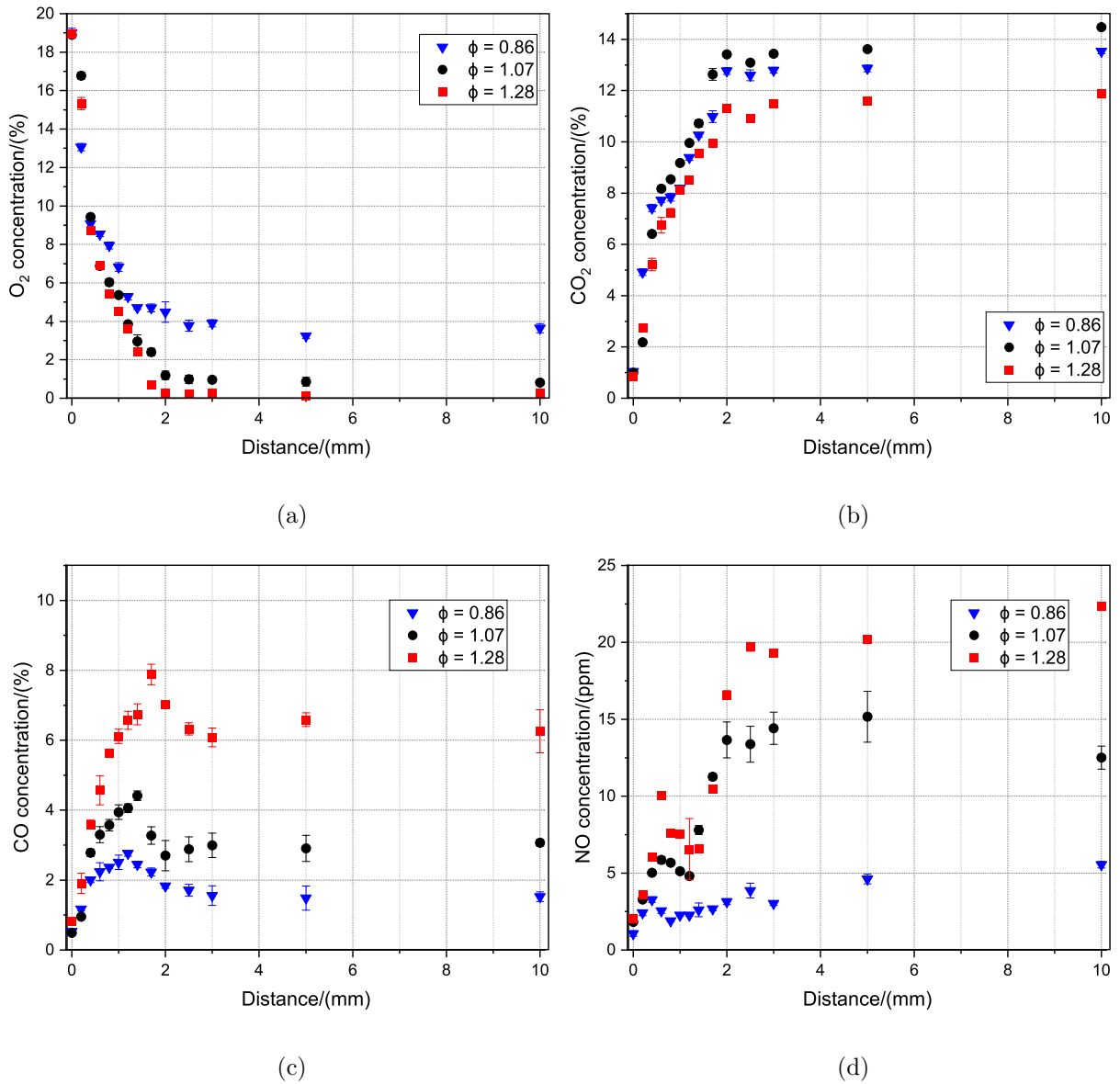
Figure 4.5: Concentration of (a) O_2, (b) CO_2, (c) CO, and (d) NO_x in lean, stoichiometric, and rich Jet A-1/ethanol flames.
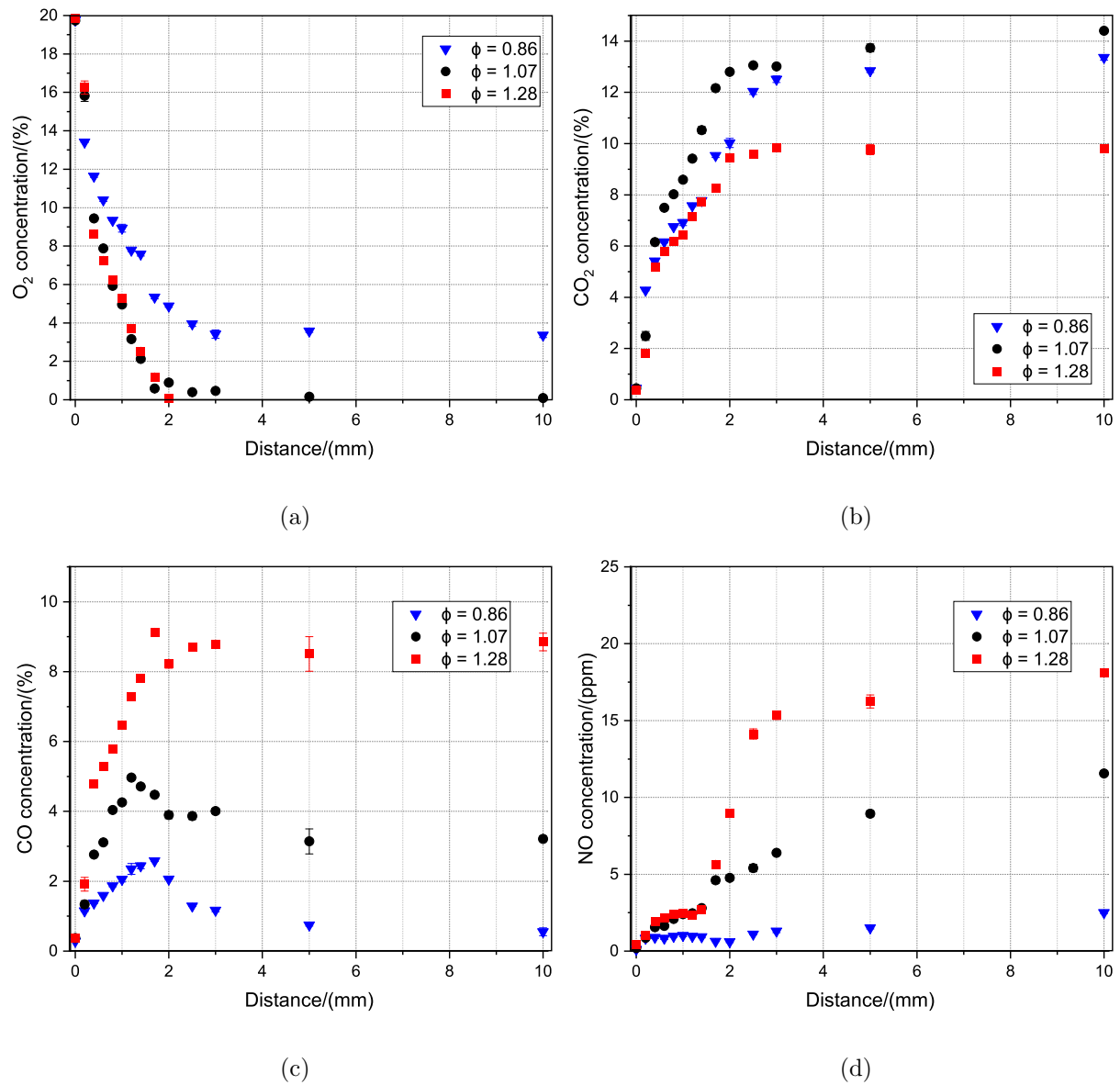
Figure 4.6: Concentration of (a) O_2, (b) CO_2, (c) CO, and (d) NO_x in lean, stoichiometric, and rich decane/trimethylbenzene flames.
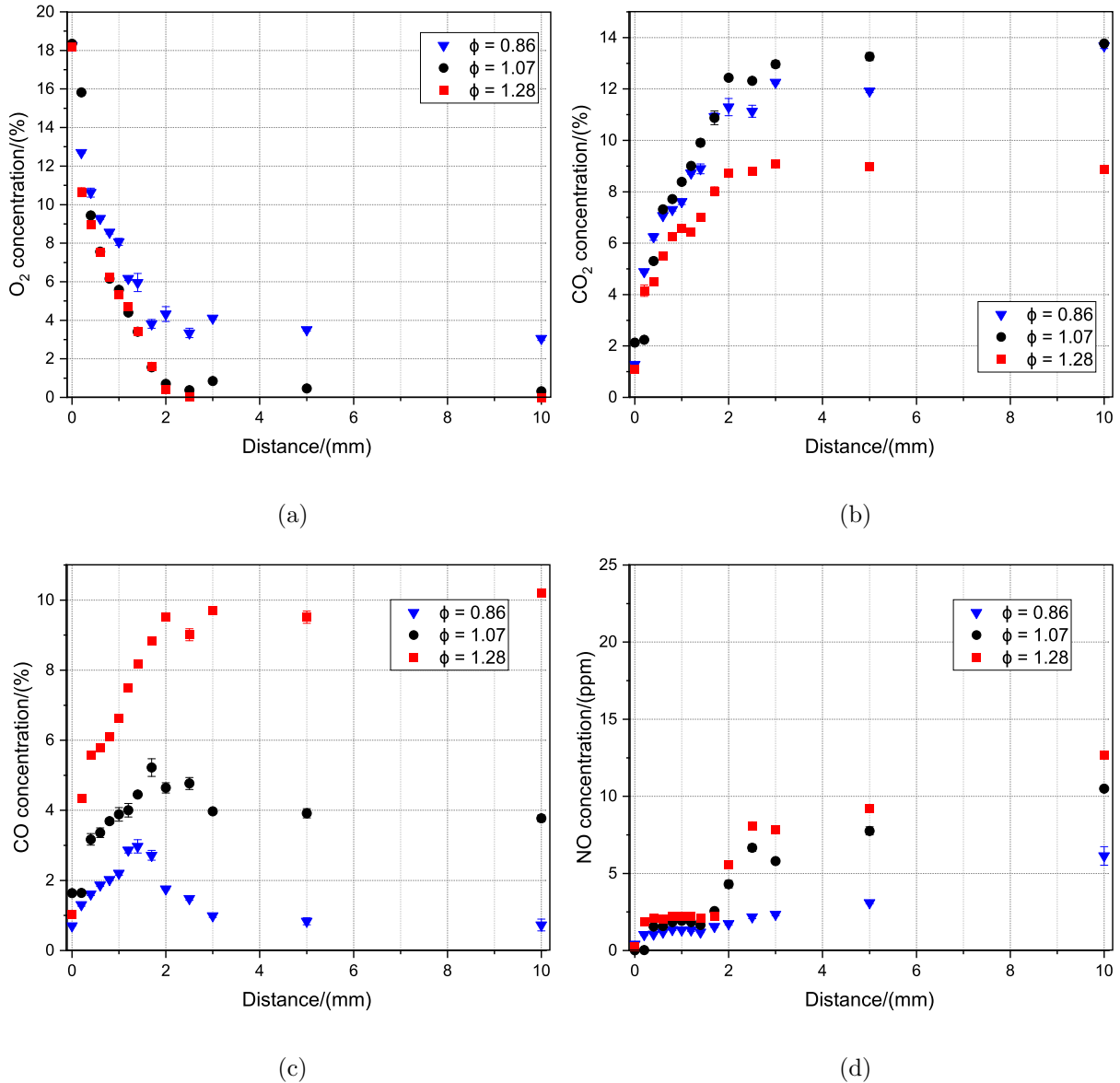
Figure 4.7: Concentration of (a) O_2, (b) CO_2, (c) CO, and (d) NO_x in lean, stoichiometric, and rich dodecane/o-xylene/methylcyclohexane flames.

The plots of the results of the gas analysis are presented in Figures 4.3 to 4.7 for the jet A-1, ethanol, E50, surrogate A and B, respectively. From these plots, the trends of the species concentration in flame were found to be similar in all flames. However, the magnitude of the species concentration was different in each flame because of the difference in the fuel characteristics and the mixture of the air-to-fuel ratio. Similar to the temperature results, the standard deviation, σ, represents the stability of the composition in the gas samples. A large deviation is caused by a severe instability of the species concentration in flames, which may be caused by the fluctuation of the flame. Unlike the temperature measurement which immediately responds to any flame

fluctuation by receiving an electrical signal from the thermocouple, the gas analyser requires more than 30 seconds to respond the change in the flame gas composition. Therefore, the temperature deviation is preferred to represent the flame fluctuation.

The values of the standard deviation were relatively low for most measurement points but with a few points which have a large fluctuation. For the O_2 measurement, most of the value of σ were less than 0.1 per cent, with several points being larger than 0.1 per cent. This error was considered as low compared to the peak of O_2 concentration which is approximately 20 per cent. A similar condition was found for the CO_2 measurement in all the flames, while the CO detection has the less error because a lower measurement range was used. In all the species measurements, the standard deviation value of the lean flames was relatively larger than that of the stoichiometric and rich flames because the lean flame was found to be the least stable and experience more fluctuation. This affects the stability of the gas sample composition as well as the temperature, which was presented in the previous section.

The standard deviation of the NO_x measurement in all flames are mostly lower than 1 ppm while the values of that in several data points were larger than 1 ppm. The NO_x measurement was the most difficult compared to the other species because the concentration was the lowest compared to the other species, which was ranged up to 500 ppm. Moreover, the performance of the NO_x analyser was not stable and this leads to a larger deviation in several points, such as in the rich E50 flame.

The oxygen profile shows approximately similar results for all fuels with the same equivalence ratio. For all flames, the oxygen concentration was approximately 18 to 20 per cent at the burner surface and then it dropped with increasing measurement point. The oxygen concentration became steady before reaching 3.0 mm and the concentration of oxygen from this point to 10 mm can represent the excess oxygen in the mixture. For the rich flames, the oxygen concentration at 3.0 to 10.0 was nearly zero because there were more fuels in the mixture than the stoichiometric condition, so all oxygen molecules were consumed to oxidise the fuel. Because the excess fuel was lacking of oxygen, more unburned hydrocarbon was found in the rich flames which reacted with oxygen from the surrounding air.

For the stoichiometric flames, the oxygen concentration at the downstream region of the flames was approximately similar to that of the rich flames. This was caused by the amount of oxygen in the mixture was calculated to be similar to that of the required amount to oxidise all the fuel in the mixture. Therefore, there should be no excess oxygen in the upper region of the flame. However, in the stoichiometric jet A-1 flame, the remaining oxygen concentration was approximately 2 per cent, which was supposed to be zero. This might be caused by the error from the determination of the molecular formula of the jet A-1. It was assumed that the molecular formula of

the jet A-1 was $C_{12}H_{22.93}$. Meanwhile, the actual jet A-1 fuel consists of hundreds of hydrocarbon and simplifying its molecular formula might not be accurate and cause over prediction of the oxygen requirement. Moreover, the diffusion of oxygen from the surrounding air to the flame region was also possible and this could increase the oxygen concentration in these flames.

For the lean flames, the remaining oxygen concentration at the higher region of the flame was approximately 4 per cent, except for the lean ethanol flame which is approximately 6 per cent. This was caused by the excess air in the unburned gas mixture compared to the required oxygen for oxidising the fuel. The excess air remained because there was not enough fuel to react with the excess air, which is the reverse of the rich flame. The missing data points in the lean jet A-1 flame between 2.0 to 5.0 mm can be considered as similar to the concentration in the lower and upper data points because the oxygen concentration in this flames stabilised at 4 per cent from 1.00 mm and then appeared as constant up to 10.0 mm. For the lean ethanol flame, the oxygen sensor was not performing well from 0.6 mm to 10.0 mm. Nevertheless, the oxygen sensor detected a high oxygen concentration which was approximately 6 per cent at 2.0 to 10.0 mm.

The concentration of oxygen at the base of the flame was expected to be approximately 20 per cent in all flames. However, the results showed that the oxygen concentration at close to the burner surface in all flame is less than 20 per cent. This might be caused by the characteristics of the burner and the probe. When preparing the probe for sampling the combustion gas, the probe nozzle was directed at the central hole of the mesh. Therefore, the unburned gas could enter the nozzle directly without experiencing ignition which might reduce the oxygen concentration. However, the suction pressure of the probe might withdraw the gas from the higher region, since the probe tip and the burner surface could not be a gas-tight connection. Unlike the thermocouple, excess pressure to the quartz probe might cause damage to the probe, such as a crack, which leads to gas and water leaks. Some other flat-flame burners were equipped with a water cooling feature which could remove the heat from the flame. Meanwhile, the flat-flame burner that was used in this study did not have any cooling method, so the heat from the flame might initiate the reaction between fuel and oxygen which could decrease the oxygen concentration. Moreover, this burner was equipped with a heater for evaporating the liquid spray from the fuel nozzle up to 463 K. The heat might also initiate the reaction between the fuels and the oxidiser below the burner surface.

The trend of the carbon dioxide profiles is similar in all flames while the magnitude of the peak was approximately similar for the flames with the same equivalence ratio. The CO_2 profiles behave reversely as the O_2 profile because the ultimate path of the oxygen molecules was CO_2 as well as H_2O. It can be expected that the water concen-

tration profile is similar to that of CO_2. Unfortunately, the gas analyser did not have a water concentration detector and the gas sample was separated from the water so it became a dry sample. At close to the burner surface, the CO_2 concentration is nearly zero because the concentration of O_2 is maximum at this point. Moreover, the source of the carbon atoms for the CO_2 production came from the fuel, which is at the highest concentration at this point. The CO_2 concentration increases with the consumption of O_2 and fuel and then peaked and stabilised at approximately 2.0 mm, where the concentration of O_2 also reaches the stable concentration value.

For all fuels, the highest CO_2 concentration was achieved by the stoichiometric flames which are approximately 14 percent and mostly followed by the lean and rich flames. The stoichiometric flames have the most complete fuel and O_2 conversion to CO_2 with the least remaining fuel and O_2, therefore it has the highest CO_2 concentration. The fuel in the lean flames has sufficient O_2 to convert the fuel to CO_2. However, because the lean flames have an excess oxygen concentration, the CO_2 concentration was decreased by the presence of excess O_2. The rich flames have the least maximum CO_2 concentration because the oxidation in these flames was not complete because of the lack of oxygen for the excess fuel.

The trend of the CO concentration is more interesting than the other profiles where it rises from adjacent to the burner surface then it peaked at approximately between 1.0 to 2.0 mm and finally it decreased and stabilised between 2.0 to 10.0 mm. This was caused by the reaction path of the carbon in the fuels, where the complex hydrocarbon decomposed to CO before it oxidised to CO_2. Therefore, the peak of CO dropped and converted to CO_2. The magnitude of the maximum CO concentration at the peak and at the upper region of the flame was affected mainly by the equivalence ratio for the same fuel. The rich flames have the highest CO concentration in this region because it the amount of oxygen molecule was not enough to oxidise the carbon atoms to CO_2. Consequently, the oxidation process became incomplete and the partial oxidation product, CO, became higher.

The stoichiometric and the lean flames were supposed to have sufficient oxygen to complete the oxidation of carbon to CO_2. Moreover, the gas analysis results showed that there was a slight O_2 concentration in the upper region of the stoichiometric flame and much more for the lean flames. In this case, the CO formation might be caused by the imperfect mixing of the fuel and oxidiser. Consequently, at some local area, the mixture might be richer and caused the incomplete combustion which resulted in the CO production. For the rich flames, the drop of the CO peak was not as significant as the stoichiometric and lean flames, especially in the rich surrogate flames where it dropped, then rises again. It might be caused by the reaction between the unburned fuel and the surrounding air at the boundary region of the flame. This reaction also

generated CO from te reaction and might be accumulated to the gas sample, which could increase the CO concentration reading.

The CO_2 and CO results can be correlated to check the accuracy of the oxygen concentration and vice versa. Similar to the oxygen concentration results, the CO_2 and CO concentration at close to the burner surface could not reach zero percent. This was caused for the similar reason of the reduction of the oxygen concentration at the similar measurement point. The CO_2 and CO concentrations increased due to the fact that the oxygen concentration decreased because CO_2 and CO are the final products of the carbon oxidation in these flames.

The NO_x concentration was smaller compared to O_2, CO, CO_2 where it was measured in ppm range while the others were in per cent. In all the flames, the concentration of NO was relatively increased with the higher measurement point. An anomaly was found in the lower region than 1.5 mm where the NO concentration peaked, then slightly dropped before it continuously increased with distance. Considering that the anomaly was found in the very low part of the flame, this might indicate that the flame was not perfectly flat. The flame appeared flat with slight peaks above the holes of the mesh. This might cause the anomaly in the NO profile where the early peak was caused by the lower flame surface and it increases after the probe measures the higher position than the higher flame surface and all the NO molecules were accumulated and this leads to the higher NO concentration.

The increasing of the NO_x concentration with the higher measurement points can be correlated with the temperature, where the higher temperature accelerates the formation of NO_x through the thermal NO_x mechanism. Referring to the results of the temperature measurement, the stoichiometric flames temperature were higher than the rich and lean flames. However, the maximum NO_x concentration in rich flames was higher than in the stoichiometric flames. This might be caused by the prompt NO_x mechanism where it involves reactions between the hydrocarbon radicals and the nitrogen molecules where the rich flames have more hydrocarbon concentration from the fuel compared to the other flame. Meanwhile, the temperature difference between the rich and stoichiometric flames was not very much different. It was also possible that the higher NO_x concentration in the rich flames was caused by the combustion product from the flame from the reaction between the unburned fuel and the surrounding air. In the lean flames, the NO_x concentration was the least compared to the others. This might be caused by the lowest temperature and hydrocarbon concentration in this flame which could decrease the reactivity of the thermal and prompt NO_x mechanism, respectively.

Comparison of the gas analysis results was also compared to the results from Catalanotti's work [5]. The excess oxygen concentration in the lean jet A-1 flame in her

work was similar to this work, which is approximately 4 per cent. The maximum CO_2 concentration was achieved by the stoichiometric flame and this is roughly similar to this work which is approximately 14 per cent. Also, the CO concentration for the rich and stoichiometric flames was about similar between this work and Catalanotti's work which were approximately 4 and 2 per cent, respectively. The NO_x measurement results between these works were different where it could reach 140 ppm in Catalanotti's work, while in this work can only reach 7 ppm for the 10.0 mm data point of the stoichiometric flame. The NO_x measurement in this work was not as accurate as the other species measurements due to the smaller concentration of NO_x and the instability of the NO_x sensor as described in the earlier part of this section. Moreover, the performance of the NO_x sensor was not well especially for the rich ethanol flame, but it could be seen that the trend of the NO_x profile in this flame was similar to the other flames except with a smaller magnitude. Therefore, the results of the NO_x detection using the gas analysis method will be compared with the PLIF method which will be discussed in the next section.

Table 4.7: Gas analysis results of the lean Jet A-1 flames.

X/mm	CO_2/%	σ/%	O_2%	σ/%	NO/ppm	σ/ppm	CO/%	σ/%
0.0	1.57	0.02	20.40	0.02	0.33	0.02	0.82	0.01
0.2	2.27	0.07	15.91	0.12	0.87	0.08	1.00	0.01
0.4	5.64	0.07	8.45	0.03	1.45	0.08	1.61	0.01
0.6	6.19	0.04	5.98	0.10	1.71	0.03	1.71	0.03
0.8	6.46	0.04	4.36	0.02	1.99	0.09	1.86	0.01
1.0	7.24	0.18	3.36	0.04	2.41	0.09	2.25	0.05
1.2	7.36	0.02	3.13	0.01	2.27	0.08	2.34	0.01
1.4	8.13	0.05	3.67	0.01	2.17	0.05	2.76	0.03
1.7	9.07	0.02	3.60	0.01	1.79	0.08	3.05	0.01
2.0	11.45	0.21	-	-	1.64	0.08	2.72	0.03
2.5	12.81	0.14	-	-	2.06	0.21	1.65	0.04
3.0	12.91	0.53	-	-	2.32	0.04	1.43	0.10
5.0	13.20	0.07	-	-	4.32	0.37	1.28	0.03
10.0	14.27	0.19	3.62	0.11	6.48	0.13	1.03	0.05

Table 4.8: Gas analysis results of the stoichiometric Jet A-1 flames.

X/mm	CO_2/%	σ/%	O_2%	σ/%	NO/ppm	σ/ppm	CO/%	σ/%
0.0	0.14	0.00	20.73	0.01	0.27	0.09	0.10	0.00
0.2	2.31	0.13	16.91	0.21	1.72	0.14	0.75	0.04
0.4	4.85	0.04	12.65	0.06	2.33	0.18	1.48	0.02
0.6	5.60	0.03	11.44	0.05	2.91	0.12	1.67	0.03
0.8	6.19	0.02	10.18	0.07	3.42	0.12	2.24	0.03
1.0	6.83	0.01	8.94	0.04	4.06	0.12	2.60	0.02
1.2	7.43	0.03	7.96	0.12	4.19	0.13	2.94	0.02
1.4	8.71	0.05	6.64	0.19	3.87	0.07	3.36	0.13
1.7	9.68	0.04	5.31	0.28	3.08	0.10	3.97	0.07
2.0	11.45	0.10	3.26	0.23	2.80	0.11	3.36	0.02
2.5	12.92	0.04	2.23	0.06	2.51	0.13	2.64	0.08
3.0	13.25	0.02	2.20	0.04	2.71	0.15	2.45	0.06
5.0	13.97	0.04	1.77	0.06	4.66	0.40	2.09	0.03
10.0	14.40	0.07	1.96	0.12	7.51	0.14	1.41	0.05

Table 4.9: Gas analysis results of the rich Jet A-1 flames.

X/mm	CO_2/%	σ/%	O_2%	σ/%	NO/ppm	σ/ppm	CO/%	σ/%
0.0	0.33	0.01	20.38	0.01	1.58	0.05	0.21	0.00
0.2	2.48	0.06	16.26	0.12	3.38	0.13	1.20	0.05
0.4	5.41	0.01	10.96	0.01	5.64	0.05	2.57	0.00
0.6	6.40	0.01	8.87	0.14	7.00	0.16	3.29	0.13
0.8	6.81	0.04	7.80	0.05	6.94	0.09	3.91	0.05
1.0	7.23	0.02	6.81	0.03	6.12	0.10	4.41	0.02
1.2	8.13	0.03	5.47	0.13	4.85	0.11	4.56	0.11
1.4	9.25	0.01	3.88	0.04	3.61	0.04	4.99	0.05
1.7	10.96	0.03	2.25	0.07	3.29	0.16	5.06	0.10
2.0	12.46	0.06	0.58	0.02	5.15	0.44	4.68	0.09
2.5	13.10	0.02	0.84	0.07	7.06	0.69	4.10	0.10
3.0	12.92	0.09	0.81	0.05	8.71	0.69	4.09	0.27
5.0	13.84	0.02	0.93	0.06	11.34	0.24	3.59	0.07
10.0	14.43	0.03	0.62	0.02	12.94	0.65	2.95	0.04

Table 4.10: Gas analysis results of the lean E50 flame.

X/mm	CO_2/%	σ/%	O_2%	σ/%	NO/ppm	σ/ppm	CO/%	σ/%
0.0	1.05	0.10	19.01	0.23	1.07	0.18	0.53	0.04
0.2	4.92	0.13	13.07	0.19	2.42	0.19	1.17	0.05
0.4	7.42	0.14	9.08	0.30	3.28	0.17	2.00	0.08
0.6	7.72	0.08	8.53	0.12	2.54	0.16	2.24	0.26
0.8	7.85	0.15	7.95	0.18	1.89	0.06	2.36	0.03
1.0	8.19	0.04	6.82	0.23	2.27	0.06	2.51	0.21
1.2	9.38	0.11	5.28	0.17	2.27	0.05	2.76	0.08
1.4	10.27	0.08	4.71	0.10	2.61	0.45	2.45	0.09
1.7	10.98	0.23	4.69	0.20	2.67	0.12	2.23	0.11
2.0	12.76	0.13	4.48	0.53	3.15	0.19	1.83	0.07
2.5	12.60	0.21	3.78	0.29	3.86	0.49	1.71	0.17
3.0	12.79	0.11	3.90	0.18	3.03	0.13	1.55	0.28
5.0	12.87	0.13	3.24	0.12	4.61	0.31	1.48	0.35
10.0	13.53	0.09	3.65	0.23	5.55	0.21	1.52	0.14

Table 4.11: Gas analysis results of the stoic E50 flame.

X/mm	CO_2/%	σ/%	O_2%	σ/%	NO/ppm	σ/ppm	CO/%	σ/%
0.0	0.99	0.00	18.90	0.02	1.82	0.06	0.49	0.02
0.2	2.18	0.09	16.78	0.17	3.28	0.13	0.95	0.06
0.4	6.41	0.04	9.43	0.15	5.02	0.13	2.78	0.10
0.6	8.17	0.11	6.88	0.19	5.86	0.22	3.30	0.23
0.8	8.54	0.02	6.03	0.18	5.68	0.06	3.57	0.16
1.0	9.18	0.04	5.37	0.11	5.13	0.19	3.94	0.21
1.2	9.96	0.05	3.85	0.04	4.81	0.18	4.06	0.12
1.4	10.72	0.13	2.95	0.34	7.80	0.28	4.41	0.14
1.7	12.63	0.23	2.40	0.19	11.26	0.21	3.27	0.25
2.0	13.41	0.08	1.19	0.22	13.65	1.17	2.70	0.43
2.5	13.09	0.07	0.98	0.22	13.38	1.16	2.88	0.35
3.0	13.44	0.08	0.96	0.09	14.42	1.04	3.00	0.35
5.0	13.62	0.07	0.86	0.23	15.17	1.66	2.91	0.37
10.0	14.47	0.07	0.81	0.06	12.51	0.75	3.07	0.09

Table 4.12: Gas analysis results of the rich E50 flame.

X/mm	CO_2/%	σ/%	O_2%	σ/%	NO/ppm	σ/ppm	CO/%	σ/%
0.0	0.84	0.02	18.95	0.01	2.03	0.18	0.81	0.01
0.2	2.76	0.09	15.32	0.31	3.62	0.14	1.91	0.29
0.4	5.22	0.24	8.73	0.09	6.03	0.07	3.59	0.13
0.6	6.75	0.30	6.92	0.14	10.04	14.61	4.57	0.42
0.8	7.24	0.17	5.42	0.09	7.59	0.21	5.64	0.06
1.0	8.10	0.13	4.53	0.06	7.55	0.19	6.11	0.21
1.2	8.49	0.12	3.60	0.06	6.56	1.99	6.57	0.26
1.4	9.54	0.16	2.43	0.05	6.58	0.18	6.74	0.30
1.7	9.94	0.04	0.70	0.05	10.49	0.16	7.88	0.29
2.0	11.30	0.07	0.27	0.05	16.59	0.28	7.04	0.10
2.5	10.91	0.10	0.21	0.05	19.69	0.26	6.32	0.18
3.0	11.48	0.10	0.28	0.04	19.29	0.14	6.08	0.27
5.0	11.58	0.05	0.14	0.06	20.18	0.19	6.59	0.20
10.0	11.88	0.09	0.28	0.04	22.34	0.21	6.26	0.61

Table 4.13: Gas analysis results of the lean ethanol flame.

X/mm	CO_2/%	σ/%	O_2%	σ/%	NO/ppm	σ/ppm	CO/%	σ/%
0.0	0.98	0.04	18.86	0.10	0.75	0.19	0.42	0.03
0.2	3.45	0.09	14.66	0.17	1.87	0.37	1.17	0.04
0.4	5.86	0.18	-	-	1.16	0.16	1.56	0.16
0.6	7.36	0.25	-	-	1.35	0.21	2.51	0.22
0.8	7.77	0.28	10.57	0.75	2.77	0.13	2.20	0.26
1.0	7.88	0.01	10.79	0.03	2.76	0.17	2.30	0.12
1.2	8.96	0.01	11.08	0.03	2.78	0.14	2.08	0.04
1.4	9.13	0.01	10.99	0.04	3.84	0.34	1.96	0.02
1.7	9.53	0.03	10.91	0.02	4.09	0.11	1.86	0.08
2.0	11.21	0.08	5.36	0.08	5.46	0.46	1.37	0.05
2.5	11.40	0.10	5.47	0.12	6.14	0.21	1.17	0.02
3.0	11.47	0.02	6.27	0.10	7.35	0.18	1.32	0.07
5.0	11.25	0.07	5.77	0.06	7.93	0.56	1.04	0.05
10.0	9.44	0.07	6.25	0.98	9.17	0.69	2.64	0.04

Table 4.14: Gas analysis results of the stoichiometric ethanol flame.

X/mm	CO_2/%	σ/%	O_2%	σ/%	NO/ppm	σ/ppm	CO/%	σ/%
0.0	0.64	0.00	19.20	0.01	1.78	0.37	0.47	0.01
0.2	2.63	0.07	15.14	0.14	2.85	0.26	1.73	0.10
0.4	6.57	0.07	8.34	0.07	4.60	0.31	3.30	0.03
0.6	8.63	0.01	6.22	0.10	4.41	0.35	3.63	0.07
0.8	9.52	0.03	4.56	0.04	3.20	0.35	4.23	0.28
1.0	9.82	0.04	4.28	0.06	3.27	0.33	4.12	0.03
1.2	10.45	0.09	2.77	0.15	4.08	0.18	4.30	0.13
1.4	11.47	0.11	2.23	0.27	6.60	0.54	4.08	0.14
1.7	12.69	0.04	0.82	0.05	10.05	1.03	3.74	0.32
2.0	13.12	0.06	0.65	0.04	9.65	1.62	3.65	0.21
2.5	13.78	0.07	0.88	0.02	12.90	0.50	3.59	0.18
3.0	13.26	0.05	0.92	0.11	13.94	0.21	3.27	0.19
5.0	13.68	0.10	0.54	0.06	-0.60	0.24	3.21	0.29
10.0	14.61	0.05	0.63	0.07	-0.62	0.26	3.25	0.55

Table 4.15: Gas analysis results of the rich ethanol flame.

X/mm	CO_2/%	σ/%	O_2%	σ/%	NO/ppm	σ/ppm	CO/%	σ/%
0.0	0.50	0.00	19.50	0.01	0.00	0.13	0.74	0.02
0.2	2.89	0.04	13.65	0.15	0.07	0.24	3.39	0.14
0.4	6.23	0.14	7.72	0.06	0.15	0.30	5.34	0.07
0.6	7.49	0.16	5.48	0.03	0.16	0.33	5.82	0.17
0.8	8.13	0.13	4.40	0.04	0.21	0.32	6.43	0.04
1.0	8.56	0.07	3.15	0.03	0.31	0.36	6.84	0.17
1.2	9.12	0.13	2.57	0.06	0.32	0.37	7.05	0.12
1.4	10.05	0.25	0.86	0.02	0.38	0.37	7.65	0.25
1.7	10.98	0.14	0.17	0.01	0.37	0.37	7.23	0.22
2.0	11.43	0.23	0.04	0.05	0.32	0.38	6.54	0.13
2.5	11.41	0.20	0.11	0.01	0.52	0.34	6.07	0.13
3.0	11.36	0.09	0.05	0.01	0.51	0.33	6.55	0.17
5.0	11.26	0.23	0.09	0.02	0.47	0.36	6.41	0.25
10.0	11.70	0.22	0.03	0.02	0.57	0.32	6.38	0.17

Table 4.16: Gas analysis results of the lean surrogate A flame.

X/mm	CO_2/%	σ/%	O_2%	σ/%	NO/ppm	σ/ppm	CO/%	σ/%
0.0	0.45	0.02	19.76	0.05	0.12	0.08	0.28	0.02
0.2	4.28	0.02	13.41	0.02	0.84	0.07	1.15	0.01
0.4	5.42	0.03	11.63	0.05	0.89	0.08	1.37	0.01
0.6	6.16	0.04	10.40	0.08	0.84	0.07	1.59	0.01
0.8	6.76	0.02	9.34	0.02	0.97	0.06	1.87	0.02
1.0	6.91	0.11	8.93	0.20	1.02	0.08	2.06	0.08
1.2	7.57	0.03	7.79	0.07	0.96	0.04	2.35	0.15
1.4	7.78	0.06	7.58	0.10	0.93	0.06	2.44	0.08
1.7	9.53	0.07	5.34	0.08	0.64	0.02	2.58	0.02
2.0	10.02	0.18	4.88	0.07	0.61	0.06	2.06	0.01
2.5	12.03	0.11	3.95	0.13	1.10	0.02	1.29	0.02
3.0	12.51	0.13	3.42	0.21	1.30	0.10	1.17	0.05
5.0	12.84	0.06	3.58	0.07	1.52	0.07	0.74	0.03
10.0	13.36	0.10	3.36	0.12	2.51	0.06	0.55	0.11

Table 4.17: Gas analysis results of the stoichiometric surrogate A flame.

X/mm	CO_2/%	σ/%	O_2%	σ/%	NO/ppm	σ/ppm	CO/%	σ/%
0.0	0.45	0.01	19.74	0.01	0.19	0.04	0.37	0.00
0.2	2.49	0.18	15.82	0.30	0.87	0.08	1.34	0.10
0.4	6.16	0.03	9.44	0.02	1.56	0.02	2.76	0.05
0.6	7.50	0.03	7.88	0.09	1.64	0.08	3.12	0.06
0.8	8.03	0.05	5.93	0.03	2.10	0.08	4.04	0.04
1.0	8.59	0.06	4.95	0.04	2.40	0.08	4.26	0.04
1.2	9.41	0.04	3.16	0.06	2.46	0.05	4.97	0.05
1.4	10.53	0.13	2.12	0.02	2.79	0.05	4.71	0.06
1.7	12.17	0.11	0.59	0.01	4.62	0.20	4.48	0.07
2.0	12.80	0.03	0.90	0.08	4.76	0.16	3.90	0.10
2.5	13.06	0.08	0.39	0.06	5.40	0.24	3.86	0.10
3.0	13.01	0.04	0.46	0.04	6.40	0.12	4.01	0.08
5.0	13.74	0.15	0.16	0.03	8.94	0.20	3.14	0.36
10.0	14.41	0.02	0.09	0.02	11.56	0.16	3.21	0.08

Table 4.18: Gas analysis results of the rich surrogate A flame.

X/mm	CO_2/%	σ/%	O_2%	σ/%	NO/ppm	σ/ppm	CO/%	σ/%
0.0	0.37	0.00	19.84	0.01	0.43	0.08	0.37	0.00
0.2	1.82	0.14	16.25	0.34	1.04	0.08	1.92	0.20
0.4	5.20	0.03	8.65	0.02	1.92	0.09	4.80	0.05
0.6	5.80	0.10	7.26	0.05	2.16	0.03	5.28	0.05
0.8	6.20	0.09	6.23	0.03	2.39	0.10	5.77	0.11
1.0	6.45	0.01	5.28	0.01	2.46	0.05	6.48	0.05
1.2	7.16	0.11	3.70	0.11	2.36	0.07	7.28	0.01
1.4	7.73	0.09	2.54	0.08	2.73	0.08	7.80	0.07
1.7	8.26	0.07	1.20	0.12	5.65	0.21	9.13	0.05
2.0	9.45	0.10	0.08	0.03	8.98	0.23	8.22	0.12
2.5	9.59	0.06	-0.05	0.01	14.13	0.33	8.70	0.06
3.0	9.86	0.03	-0.05	0.00	15.35	0.28	8.80	0.08
5.0	9.76	0.20	-0.05	0.01	16.24	0.43	8.51	0.49
10.0	9.80	0.06	-0.03	0.01	18.10	0.18	8.85	0.25

Table 4.19: Gas analysis results of the lean surrogate B flame.

X/mm	CO_2/%	σ/%	O_2%	σ/%	NO/ppm	σ/ppm	CO/%	σ/%
0.0	1.29	0.03	18.25	0.05	0.41	0.04	0.70	0.00
0.2	4.89	0.04	12.70	0.03	1.04	0.06	1.31	0.05
0.4	6.25	0.13	10.63	0.23	1.07	0.02	1.61	0.05
0.6	7.07	0.02	9.28	0.04	1.20	0.02	1.87	0.03
0.8	7.31	0.06	8.57	0.10	1.36	0.07	2.02	0.02
1.0	7.61	0.10	8.07	0.18	1.32	0.02	2.21	0.06
1.2	8.72	0.04	6.16	0.10	1.33	0.09	2.86	0.08
1.4	8.89	0.19	5.95	0.47	1.19	0.03	2.97	0.19
1.7	10.93	0.14	3.82	0.23	1.56	0.06	2.72	0.14
2.0	11.30	0.34	4.33	0.39	1.73	0.08	1.76	0.02
2.5	11.13	0.23	3.34	0.24	2.18	0.11	1.48	0.05
3.0	12.26	0.05	4.11	0.05	2.35	0.08	0.99	0.05
5.0	11.92	0.06	3.51	0.06	3.09	0.07	0.83	0.10
10.0	13.68	0.10	3.05	0.10	6.14	0.60	0.73	0.17

Table 4.20: Gas analysis results of the stoichiometric surrogate B flame.

X/mm	CO_2/%	σ/%	O_2%	σ/%	NO/ppm	σ/ppm	CO/%	σ/%
0.0	2.13	0.01	18.34	0.09	0.02	0.02	1.64	0.01
0.2	2.24	0.01	15.82	0.01	0.03	0.04	1.64	0.01
0.4	5.31	0.12	9.44	0.04	1.55	0.06	3.17	0.16
0.6	7.32	0.06	7.56	0.04	1.58	0.02	3.36	0.14
0.8	7.71	0.03	6.16	0.02	1.84	0.02	3.69	0.08
1.0	8.38	0.10	5.58	0.04	1.93	0.07	3.89	0.19
1.2	9.01	0.03	4.40	0.03	1.84	0.02	4.00	0.19
1.4	9.91	0.13	3.41	0.03	1.65	0.07	4.45	0.06
1.7	10.88	0.26	1.56	0.04	2.56	0.07	5.22	0.25
2.0	12.44	0.05	0.71	0.04	4.30	0.24	4.64	0.15
2.5	12.32	0.07	0.37	0.02	6.66	0.22	4.77	0.17
3.0	12.96	0.14	0.85	0.04	5.80	0.07	3.97	0.07
5.0	13.26	0.16	0.46	0.05	7.76	0.26	3.91	0.13
10.0	13.77	0.05	0.32	0.02	10.49	0.12	3.77	0.09

Table 4.21: Gas analysis results of the rich surrogate B flame.

X/mm	CO_2/%	σ/%	O_2%	σ/%	NO/ppm	σ/ppm	CO/%	σ/%
0.0	1.09	0.01	18.18	0.01	0.28	0.02	1.03	0.01
0.2	4.15	0.22	10.65	0.23	1.84	0.02	4.34	0.05
0.4	4.51	0.07	8.97	0.08	2.11	0.02	5.57	0.02
0.6	5.51	0.02	7.51	0.05	2.07	0.06	5.80	0.02
0.8	6.27	0.01	6.24	0.04	2.21	0.05	6.10	0.02
1.0	6.59	0.04	5.34	0.03	2.23	0.02	6.63	0.05
1.2	6.42	0.04	4.70	0.06	2.23	0.04	7.50	0.01
1.4	7.00	0.03	3.43	0.02	2.08	0.05	8.17	0.02
1.7	8.02	0.17	1.63	0.13	2.23	0.14	8.84	0.07
2.0	8.72	0.05	0.42	0.02	5.55	0.20	9.52	0.07
2.5	8.80	0.13	0.01	0.01	8.10	0.11	9.01	0.17
3.0	9.09	0.02	-0.01	0.01	7.82	0.10	9.71	0.10
5.0	8.97	0.04	-0.01	0.01	9.23	0.10	9.51	0.17
10.0	8.89	0.02	0.00	0.01	12.65	0.07	10.21	0.09

4.3 PLIF

The results of the detection of OH and NO radicals using the method that was described in Section 3.4 is reported in this section including the discussion. The discussion starts with the selection of the OH and NO transitions that were used in the experiment and the characteristics of those transitions. The list of these transitions can be found in Table 3.4 as well as their wavelengths. From the LIF imaging, the unprocessed images were obtained, and these contain the information of the intensity counts in the frames that were captured by the camera. A higher intensity count in an image pixel leads to higher photon energy or a brighter light. However, the higher intensity is not necessarily interpreted as the higher OH or NO concentration in the flame images.

The intensity counts that were captured by the camera were an accumulation of the scattered laser light, flame chemiluminescence, ambient light from the surrounding illumination, and the true fluorescence. To obtain the accurate concentration of the OH and NO radicals, these contaminations should be eliminated, so only the true fluorescence is considered for the species concentrations. The light contamination of these sources were minimised by applying the OH and NO filter to the camera which only allowed the light which has the wavelength of the OH and NO fluorescence while blocking the other light with a different wavelength. Even though the filter has a narrow wavelength, a minor non-fluorescence light could enter the camera and contaminate the fluorescence signal. Therefore, off-resonance images were recorded for each flame to subtract the light noise from the flame images and leaving only the fluorescence signal.

The fluorescence signal intensity, I_{LIF}, depends on several parameters, such as the laser intensity, I_{laser}, Boltzmann population of the OH and NO radicals at the ground state, $f_B(T)$, and the spectral parameters, which are the Einstein coefficient for spontaneous emission, A_{21} quenching, Q_{21}, and pre-dissociation rates, P [156]. For OH detection, this correlation can be expressed as follows:

$$I_{LIF} \sim BI_{laser}\Gamma\tau_L[\text{OH}]f_B(T)\sigma_{eff}\frac{A_{21}}{A_{21} + Q_{21} + P}F_{fl}\left(\frac{\Omega}{4\pi}\right)\epsilon\eta V \qquad (4.4)$$

The additional parameters were proposed by Arndt et al. [157] to involve the experimental parameters such as the laser energy absorption and the detector efficiencies, thus the correlation can be quantified. The absorption efficiency of the laser energy involves the Einstein absorption coefficient per speed of light, B, line width integral, Γ, and laser pulse length, τ_L. Meanwhile, the detector efficiency includes the fraction of fluorescence that is captured by the camera bandwidth, F_{fl}, solid angle fluorescence, Ω, transmission efficiency of the detector, ϵ, photoelectron efficiency of the detector, η, and the volume of the interaction, V.

In order to accurately quantify the total concentration of OH, [OH] or NO, [NO], the fluorescence signal must be normalised with all parameters in Equation (4.4). However,

this method cannot be done without an exhaustive work to find all the values of these parameters. It is always easier to retrieve the relative concentration of the radical species from the LIF results than the absolute concentration. A strategy to eliminate the involvement of these parameters in quantifying the LIF measurement has been performed by Arndt et al. [157], Schießl et al. [156], Hughes et al. [150], and Catalanotti [5] by using a standard reference. The standard reference can be a flame with a known OH concentration, which is observed by using the similar LIF setup that is used for detecting OH and NO radicals in the observed flames. It is essential that all of the laser and detection parameters are the same in both experiments.

The information about the species concentration in the reference flame can be obtained from a simulation. Therefore, the reference flame should be well studied and have an accurate model for the modelling purpose. The correlation between the LIF signal from the reference flame, I_{ref}, simulated OH concentration for the reference flame, $[OH]_{ref}$, the LIF signal from the observed flames, I_{LIF}, and the actual OH concentration in the observed flames, $[OH]$ can be expressed as follows:

$$[OH] = \frac{I_{LIF} \; \sigma_{eff(ref)} \; f_{B(ref)}}{I_{ref} \; \sigma_{eff} \; f_B}[OH]_{ref} \tag{4.5}$$

Equation (4.5) is also applicable for NO. By substituting the Equation (4.4) into Equation (4.5), the non-temperature dependent experimental parameters can be eliminated because they are similar in both the observed and reference flames. This leaves I_{laser}, which might vary with different flame LIF experiments, and the variation of the laser power has been considered by involving laser power normalisation using a cuvette measurement. The value for the effective quenching cross-section, σ_{eff}, which affects the spectral parameters that involves collisions, was taken from Tamura et al. [158]. According to Tamura et al., the effective quenching cross-section is temperature-dependent for OH and independent for NO. Meanwhile, the value of the Boltzmann population, f_B, at the flame temperature was obtained from the LIFBASE simulation.

The Boltzmann population of the OH and NO radicals at the ground state $X^2\Pi$ varies with temperature and different electronic-vibrational-rotational states. The LIFBASE software was used to simulate the LIF excitation spectra and the Boltzmann population for the selected transition in Table 3.4. For the species concentration measurement, a strong transition with the least variation with temperature is preferable. A weak transition leads to lower signal-to-noise ratio which causes inaccurate measurement. By using a strong and less sensitive transition with temperature variation, error due to population distribution correction can be minimised and minimum laser power is required.

A methane flame in a flat-flame burner has been used as a reference flame in many

research [150] [5]. This was caused by the fact that methane is the simplest hydrocarbon fuel and has been widely studied. As a result, an accurate kinetic model for methane is available, such as the GRI 3.0 mechanism. However, the use of methane in this study requires a different burner that is suitable for gaseous fuel. Moreover, the change in the experimental configuration may cause some error due to the differences in the experimental parameters between the reference and observed flame. Therefore, in this work, an ethanol flame was used as a reference flame as a substitution for methane. From the literature review, it is known that the ethanol flame has been widely studied and there exists an accurate model that has been validated over a wide range of experimental data that is available from the work of Olm et al. [56]. The reaction mechanism from Olm et al. was employed for predicting the actual OH concentration in the ethanol flame using PREMIX program. Furthermore, the Equation (4.5) can be used for predicting the actual OH concentration in the flame.

The sensitivity of the transition with temperature can be beneficial for temperature measurements using the LIF method. Several methods for LIF thermometry have been implemented to flames and this has been reviewed by Daily [159]. In this study, a pair of OH and NO transitions which are temperature sensitive were selected for LIF thermometry. Subsequently, the ratio of the LIF excitation spectra was calculated for the range of the flame temperatures which are approximately from 500 to 3000 K. Furthermore, the I_{LIF} for both transition were also obtained from the experimental results and their ratio was also calculated. Finally, the value of the experimental ratio was used to determine the flame temperature by using the temperature-transition ratio from the spectra simulation.

Many transitions LIF excitations have been simulated using the LIFBASE software and their behaviour in the temperature variation was evaluated. Figure 4.8 shows the results of this simulation for relatively strong and temperature-sensitive OH and NO transitions in the flame temperature range. Ideally, the simulated LIF excitation profile should be continuous, and the discontinuity in the figure was caused by the low resolution of the simulated wavelength. It can be identified that some transition has a consistent LIF excitation while others behave differently with temperature variation. For the NO concentration measurement, the $Q_1(12)$ transition is stronger compared to the other transition because this transition has a consistent and strong LIF excitation at the flame temperature range. Meanwhile, for the OH measurement, the $Q_1(6)$ and $Q_1(3)$ are relatively strong compared to the other transitions in the comparison. The $Q_1(6)$ was preferable than the $Q_1(3)$ transition because it is stronger at high-temperature region and possible to compare with the previous work while the $Q_1(3)$ LIF excitation decreases with the increasing of temperature.
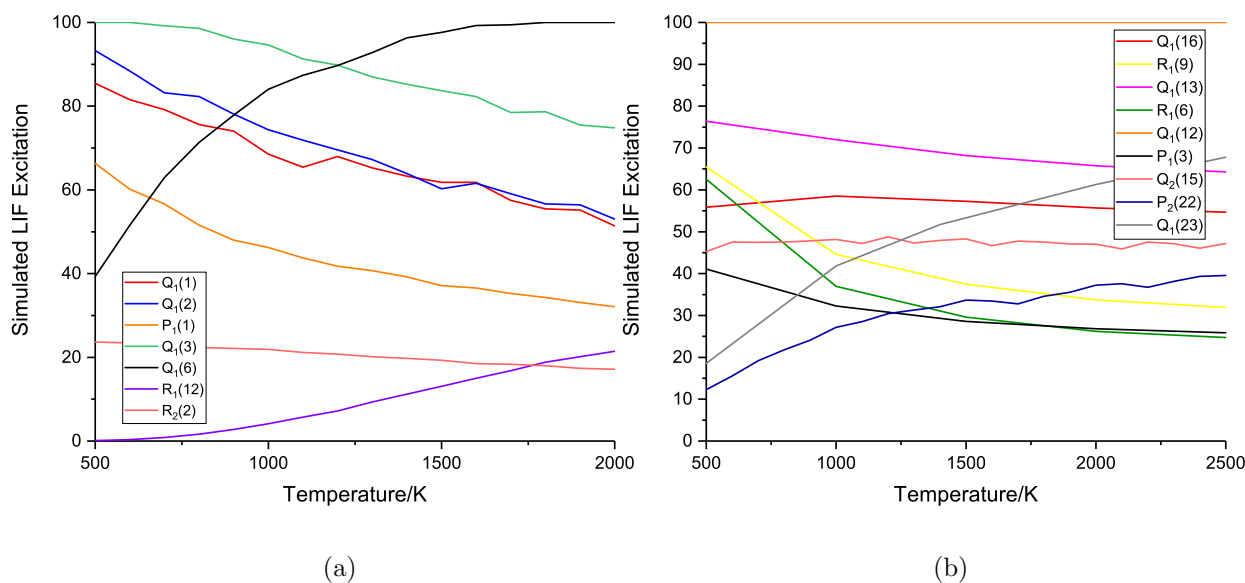
103

Figure 4.8: Simulated LIF excitation for several transitions at various temperature for (a) OH and (b) NO from the LIFBASE simulation.

For the temperature measurement purpose, the considered transitions in Figure 4.8 were paired by combining the selected transition and their ratio was calculated. The ratio of $R_2(2)$ and $R_1(12)$ was selected for the LIF thermometry from the OH detection while the ratio of $P_2(22)$ and $Q_2(15)$ was selected for that from the NO detection. The ratio of both pairs have a sensitive correlation to temperature and do not have multiple interpretations which leads to errors. Figure 4.9 shows the plot of the ratio in the flame temperature range for both OH and NO. A curve fitting was generated for both plots to assist in correlating the ratio of the flame LIF signal from both transitions to the associated temperature. Without normalisation, the LIF results show a higher signal at the lower flame temperature and a lower signal at the higher flame temperature. In Figure 4.8(b), several data points are slightly less smooth compared to those of the OH in Figure 4.8(a). This was caused by the resolution and discontinuity in the output of the LIFBASE simulation, where the corresponding wavelength for the $P_2(22)$ and $Q_2(15)$ transitions was skipped. Alternatively, the nearby wavelength was used to fit the skipped data points which leads to an inaccuracy of approximately 0.001 Å. Several attempts have been tried to solve this issue, such as narrowing the range of the simulation and increasing the simulation resolution. However, at several temperatures, the simulation results still skipped the desired wavelength and the simulated LIF excitation value from the nearby wavelength was used. For both ratio of OH and NO transitions, a fitted curve was generated to assist further calculation for the normalisation of the LIF signals.
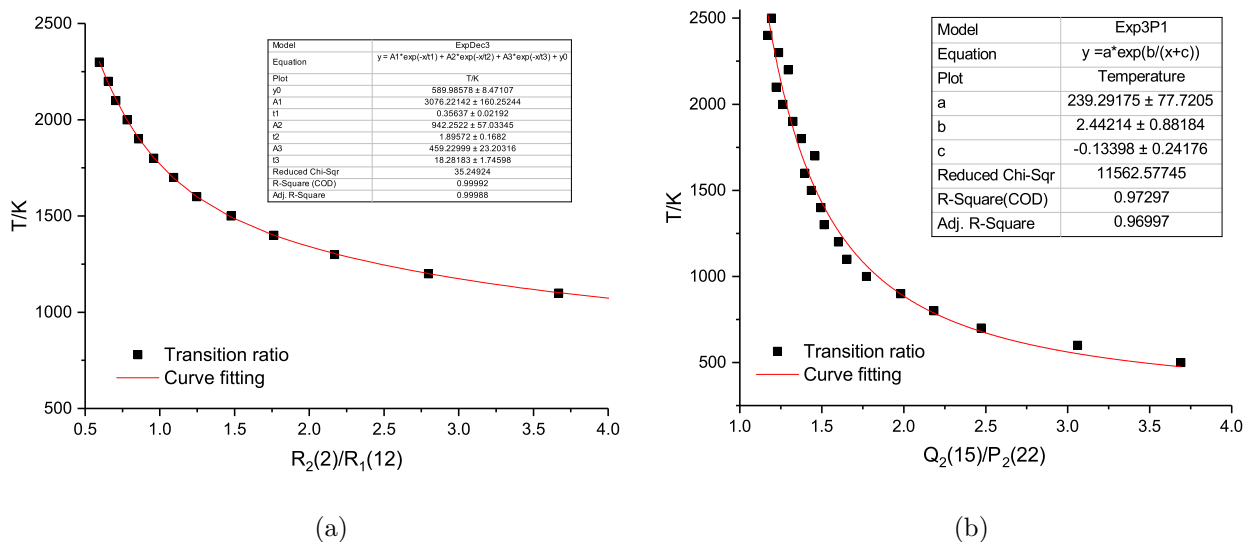
Model	ExpDec3
Equation	y = A1*exp(-x/t1) + A2*exp(-x/t2) + A3*exp(-x/t3) + y0
Plot	T/K
y0	589.98578 ± 8.47107
A1	3076.22142 ± 160.25244
t1	0.35637 ± 0.02192
A2	942.2522 ± 57.03345
t2	1.89572 ± 0.1682
A3	459.22999 ± 23.20316
t3	18.28183 ± 1.74598
Reduced Chi-Sqr	35.24924
R-Square (COD)	0.99992
Adj. R-Square	0.99988

Model	Exp3P1
Equation	y =a*exp(b/(x+c))
Plot	Temperature
a	239.29175 ± 77.7205
b	2.44214 ± 0.88184
c	-0.13398 ± 0.24176
Reduced Chi-Sqr	11562.57745
R-Square(COD)	0.97297
Adj. R-Square	0.96997

(a)   (b)

Figure 4.9: Ratio of the simulated LIF excitation at the selected transisitions at various temperature for (a) OH and (b) NO from the LIFBASE simulation.

(a)   (b)
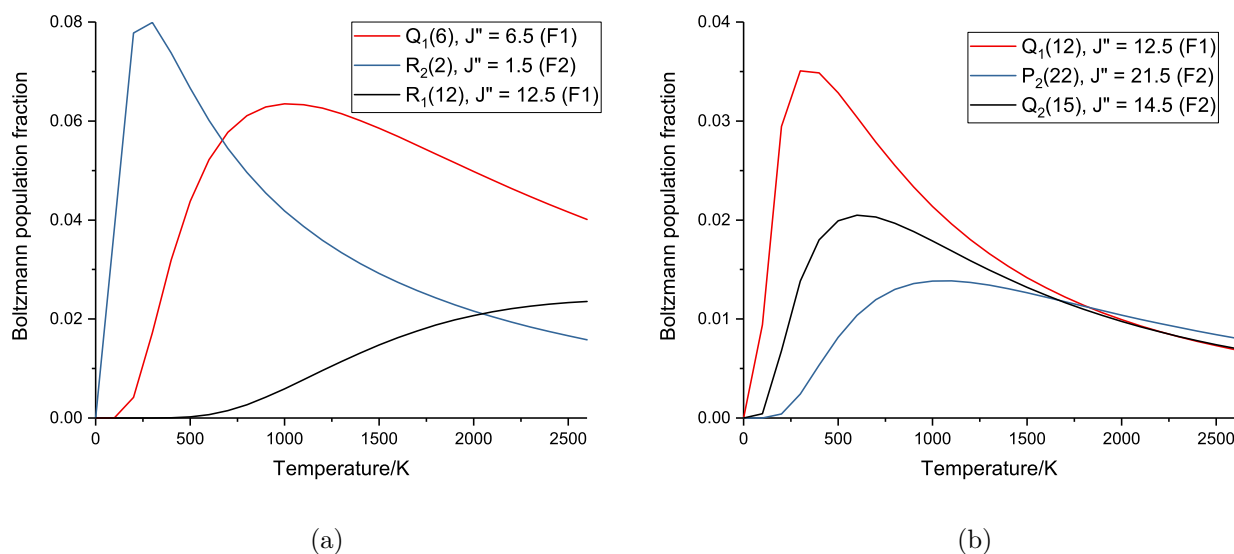
Figure 4.10: Simulated population fraction for several transitions at various temperature for (a) OH and (b) NO from the LIFBASE simulation.

Figure 4.10 shows the results of the Boltzmann population distribution for the OH and NO transitions that were used in this experiment. It indicates that the ground state population varies in all transitions with the temperature variation. The maximum population for each transition was peaked at lower than 1000 K, except for the $R_1(12)$ transition of NO, then drops with the increasing of the flame temperature. This implies that the normalisation of the LIF signal to the Boltzmann population is required for obtaining the accurate OH and NO concentration. Following the step-by-step procedure of the LIF data processing, the relative concentration of OH and NO

at the selected transitions is presented, followed by the quantification results, and the LIF thermometry.

4.3.1 Relative OH Concentration

Figure 4.12 shows the relative OH concentration in the observed flames at the $Q_1(6)$ transition. The signal has been normalised with the background signal, variation of the laser sheet intensity, Boltzmann population, and the quenching cross-section area. This result does not indicate the absolute OH concentration in the flame, but does indicate the variation of the OH concentration along the vertical axis from the burner surface. Also the level of the scale corresponds to the absolute OH concentration, where the higher OH concentration will result in the higher scale of the relative OH concentration.

The difficulty in performing the normalisation of the raw LIF signal was the higher resolution of the data points in the LIF images compared to the temperature measurement using a thermocouple that was presented in Section 4.1. The finest increment of the distance above the burner surface was 0.2 mm while in the LIF images, it was less than 0.1 mm. The flame temperature at each LIF data point was required for calculating the Boltzmann population and the quenching cress section area for the LIF signal normalisation. An interpolation method was used to supply the flame temperature data for each LIF data points. The upper and lower nearby data points from the temperature measurement were used for the interpolation calculation for the temperature data at the LIF data points. This interpolated temperature, T, were used to calculate the Boltzman population distribution from the curve fitting in Figure 4.11 and the quenching cross-section using the following expression [158]:

$$\sigma_{eff} = 20 \exp(\frac{384}{T}) \tag{4.6}$$

In all flames, the trend of the OH concentration is similar, where it was minimum at the surface of the burner. With the higher distance to the burner surface, the OH concentration rapidly increased to its peak before 2.0 mm. Afterwards, it dropped slowly until it reaches the equilibrium. In all flames, the highest peak of the OH profile was found in the lean flames, then followed by the stoichiometric and the rich flames. Compared to the study of a methane/air flames in a flat-flame burner by Cattolica [160], similar finding of the behaviour of the OH profile was found where the lean flames have the highest OH concentration peaks and then it decreases with the increasing of the fuel concentration.
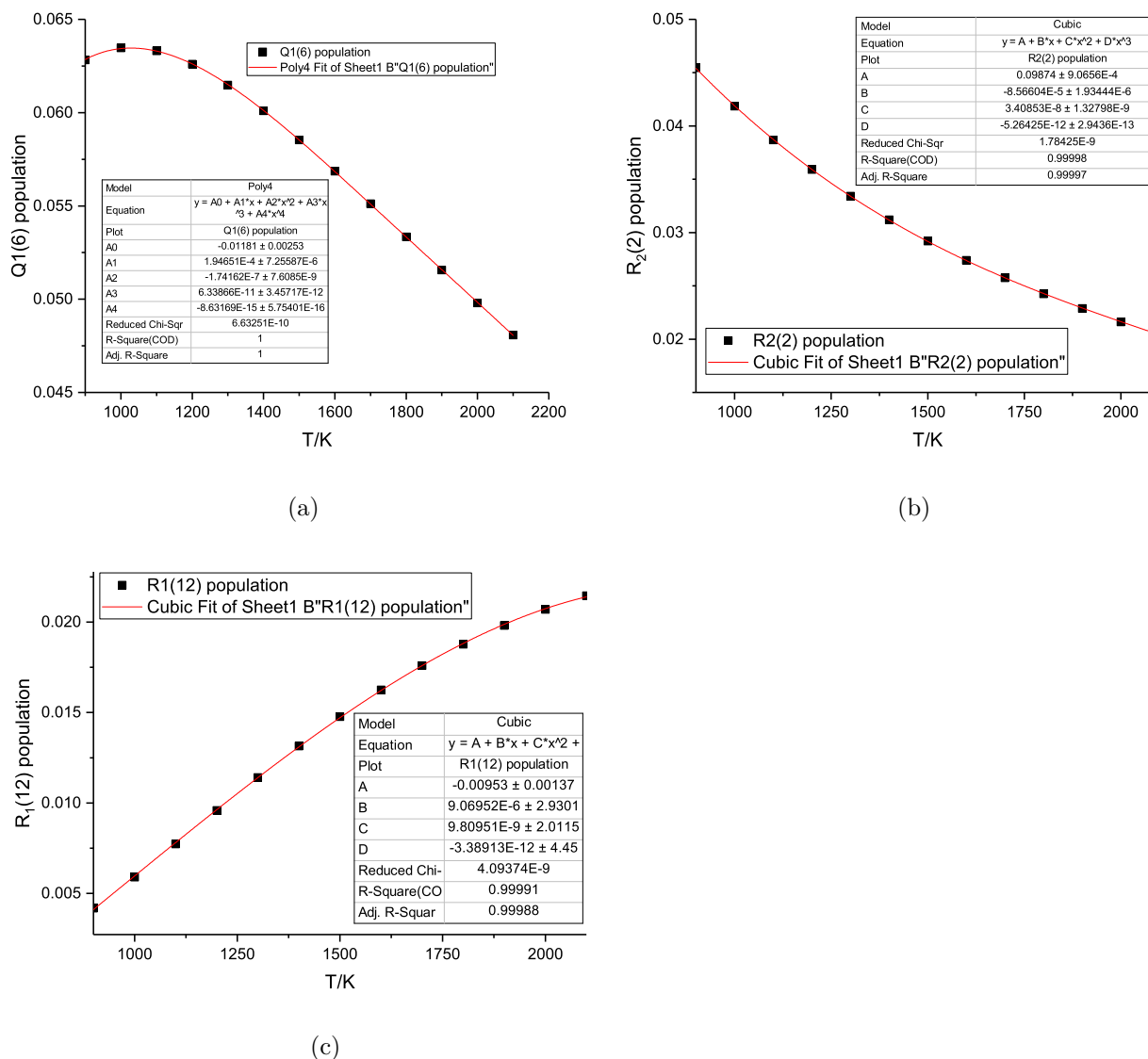
(a)

(b)

(c)

Figure 4.11: Curve fitting for the Boltzmann population for the $Q_1(6)$, $R_2(2)$, and $R_1(12)$ transitions at the flame temperature range.

The production of the OH radical was initiated by the hydrogen abstraction from the hydrocarbon fuel, which resulted in the production of the H radicals. Furthermore, the H radicals react with oxygen and produce OH radicals through reaction R.2.3. The production of the OH radicals was dominated by the H_2/O_2 reactions when the H-abstraction reactions have been terminated until the H_2/O_2 reactions nearly achieved equilibrium [160]. At this point, the OH concentration peak was formed and then it decayed with a different rate which the fastest decay rate was found in the lean, followed by the stoichiometric and the rich flames.

107

(a)

(b)

(c)
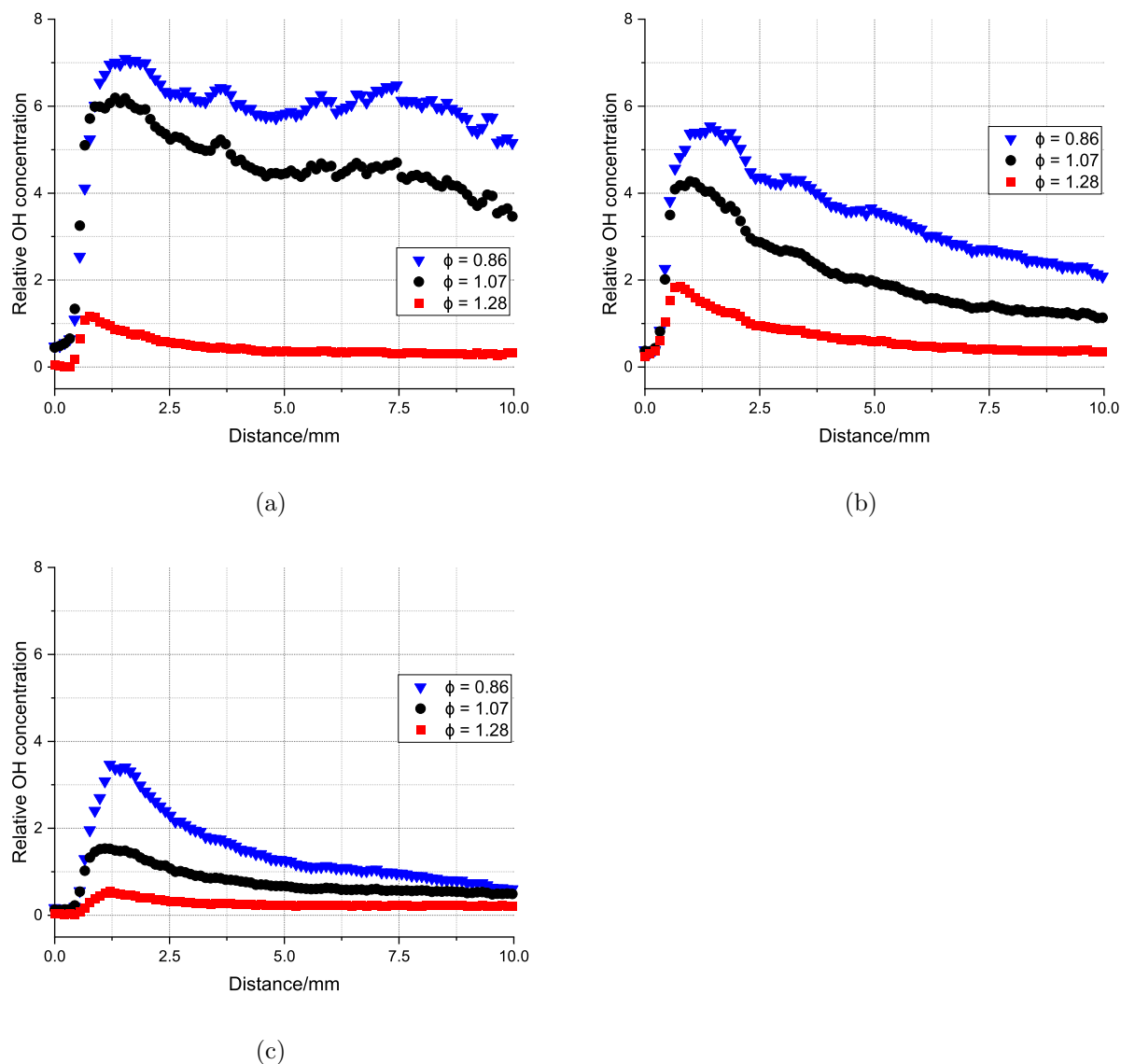
Figure 4.12: Relative OH concentration in (a) jet A-1, (b) E50, and (c) ethanol flames from the $Q_1(6)$ transition.

The equivalence ratio can be related to the amount of the oxygen molecule that was involved in the H_2/O_2 reactions, which the lean flames have more O_2 molecule and this leads to the higher OH concentration. Meanwhile, the less oxygen in the rich flames reduced the formation of the OH radicals. Considering the amount of ethanol, the pure jet A-1 flames have the highest OH concentration and this decreases with the increasing of the ethanol concentration in fuel. An exception was found in the rich E50 flame which has a higher OH peak concentration than the rich jet A-1 flame. For the same fuel flow rate and stoichiometry, the ethanol flames required less air which leads to the reduction of the OH formation.

Figure 4.13 shows the relative OH concentration from the $R_2(2)$ transition. A similar procedure to the relative concentration from the $Q_1(6)$ transition was performed to the raw LIF images from this transition. The difference from the $Q_1(6)$ transition is

that the $R_2(2)$ transition is a less strong LIF excitation as presented in Figure 4.8(a). Moreover, the OH population at the ground state is less compared to that in the $Q_1(6)$ transition as illustrated in Figure 4.10(a) at high temperature. Consequently, the raw signal intensity of the LIF images from this transition in less than that in the $Q_1(6)$ transition. It can be seen in Figure 4.13 that the scale is less than that in Figure 4.12. This might decrease the signal-to-noise ratio which causes a less accurate LIF measurement.

Similar to the previous results, the lean flames have the highest OH peak concentration, followed by the stoichiometric and rich flames. In this measurement, the OH profiles in the stoichiometric flames of the jet A-1, ethanol, and surrogate A are approximately similar to the lean flames. Moreover, with the increase of ethanol concentration, the OH peak concentration decreased, except in the rich E50 flame. Unlike in the $Q_1(6)$ transition in which the OH peak concentration of the rich E50 flame is higher than that in the rich jet A-1 and ethanol flames, in this transition, the OH peak concentration of the rich E50 flame is lower than that in the rich jet A-1 and ethanol flames.

The results for the surrogate A and B flames, which were not measured in the $Q_1(6)$ transition, are presented using this transition. All surrogate A and B flames have a nearly similar OH profile in terms of shape and scale with the discrepancy less than 0.5 of the scale. Compared to the OH profiles from the Jet A-1 flames, the lean and stoichiometric flames are nearly identical in the surrogates and real jet A-1 flames. For the rich flame, the OH concentration in the jet A-1 flame is much higher than that in the surrogate A and B flames. In the lean flames of the surrogate A and B, there was a significant noise at the lower region. This was caused by the scattering of the laser light from the surface of the burner that was not precisely removed by the background noise subtraction.
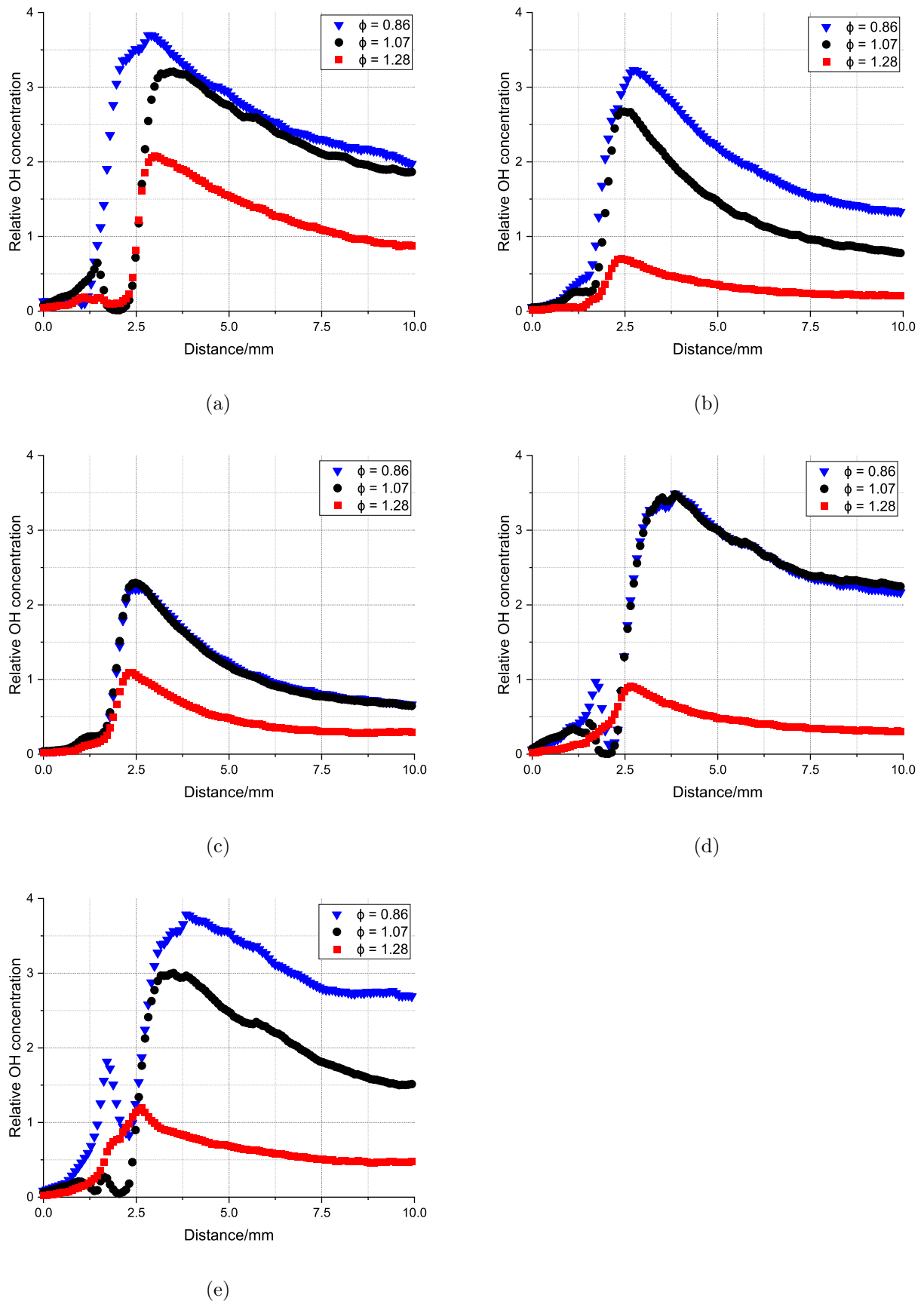
Figure 4.13: Relative OH concentration in (a) jet A-1, (b) E50, (c) ethanol, (d) Surrogate A, and (e) Surrogate B flames from the $R_2(2)$ transition.
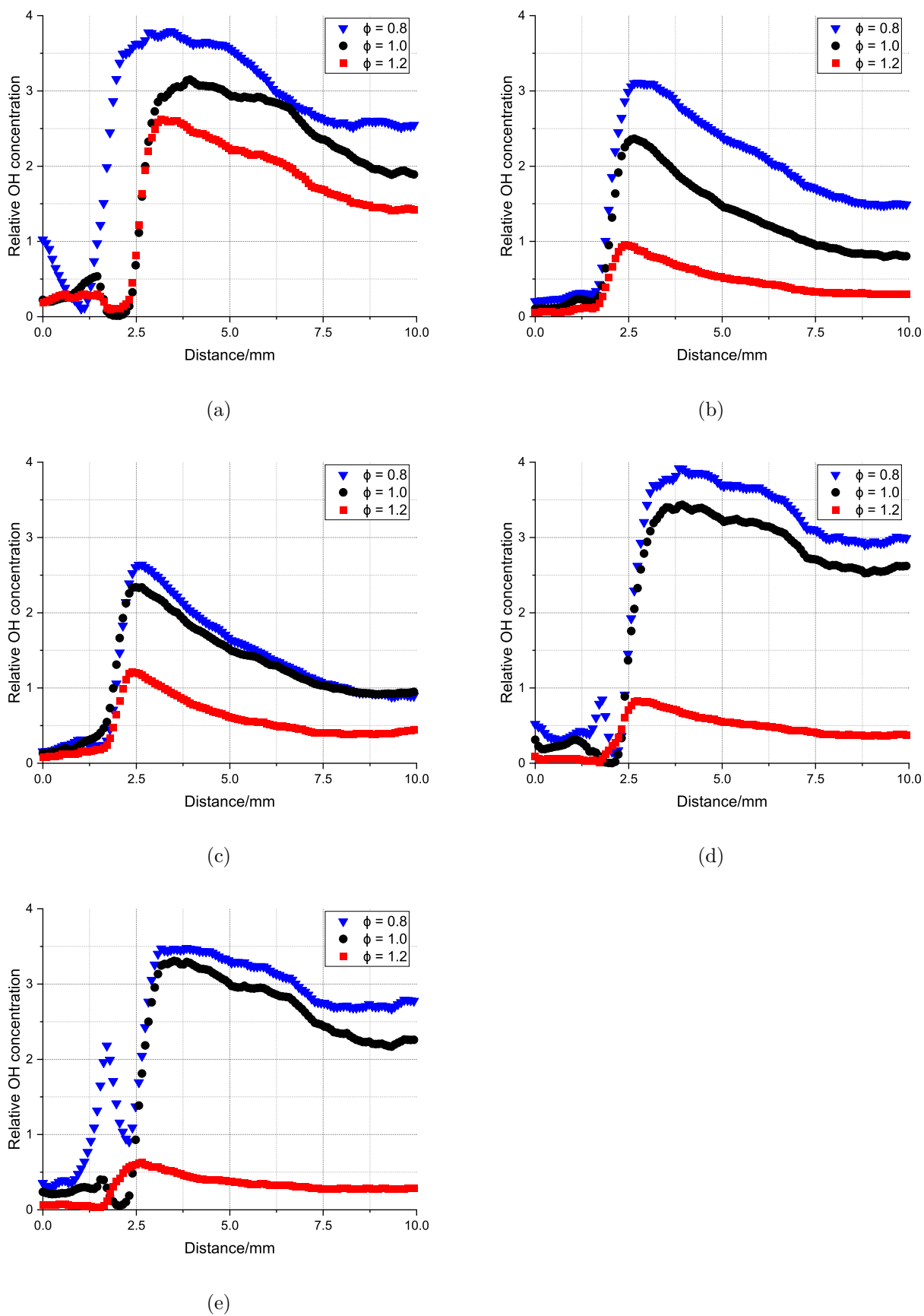
110

Figure 4.14: Relative OH concentration in (a) jet A-1, (b) E50, and (c) ethanol, (d) Surrogate A, and (e) Surrogate B flames from the $R_1(12)$ transition.

111

Figure 4.14 shows the relative OH concentration in all observed flames from the $R_1(12)$ transition. This transition is the least strong compared to the $Q_1(6)$ and $R_2(2)$ transitions below 1750 K. Identical to the previous transitions, the OH concentration in the lean flames were the highest followed by the stoichiometric and rich flames. The jet A-1 flames have the highest OH concentration, then with the increase of ethanol concentration in the fuel, it decreases. The OH profile in the surrogate A and B flames are nearly identical and represent the OH profile in the jet A-1 flames, except in the rich flame. The OH concentration in the rich jet A-1 flame is approximately three times higher than in the rich flames of the surrogates. Similar noise was also found in the lower region of the lean surrogates and real jet A-1 flames.

4.3.2 Relative NO Concentration

Figure 4.16 presents the relative NO concentration from the LIF measurement using the $Q_1(12)$ transition. This transition is the strongest compared to the other two NO transition as illustrated in Figure 4.8(b), which is consistent at the maximum value at various temperatures. Initially, the setting in Table 3.4 was used and it was found that the signal from the NO fluorescence was too weak. Compared to the OH measurement, the NO measurement was more difficult because of the amount of NO species in the flame is much less than that of OH, which is scaled in part per million. In order to improve the fluorescence signal from the NO species, the NO filter was removed from the camera lens. Consequently, the amount of light entering the camera was increased, to include the background noise.

A similar normalisation method to the relative OH profile was performed to the raw signal to obtain the relative NO concentration. The difference is that the quenching cross-section area for NO is assumed as not to be affected by the temperature. Meanwhile, the data for the Boltzmann population at the specified temperature is calculated from the curve fitting in Figure 4.15.

The NO profile for all the flames was similar and it rises from nearly zero to equilibrium at above 5.0 mm and then stabilises. The ethanol flames at all equivalence ratios indicate the least NO concentration compared to the other fuels. This may be caused by the temperature in the ethanol flames that are also the lowest among the other flames, which is approximately 200 K lower than the jet A-1 flames. The low temperature leads to the low reaction rate of the NO production through the thermal NO_x mechanism. The temperature difference in the ethanol flames was less than 100 K, with the stoichiometric flame as the hottest flame, followed by the rich and lean flames. In Figure 4.16(c), the profile of the rich flame are approximately similar to the stoichiometric flame. This might be caused by the NO production from the prompt NO_x mechanism, which is caused by the reaction between the nitrogen and hydrocar-

bon radicals. In the rich flame, the higher concentration of the fuel might increase the concentration of the hydrocarbon radicals and the NO production through this mechanism.
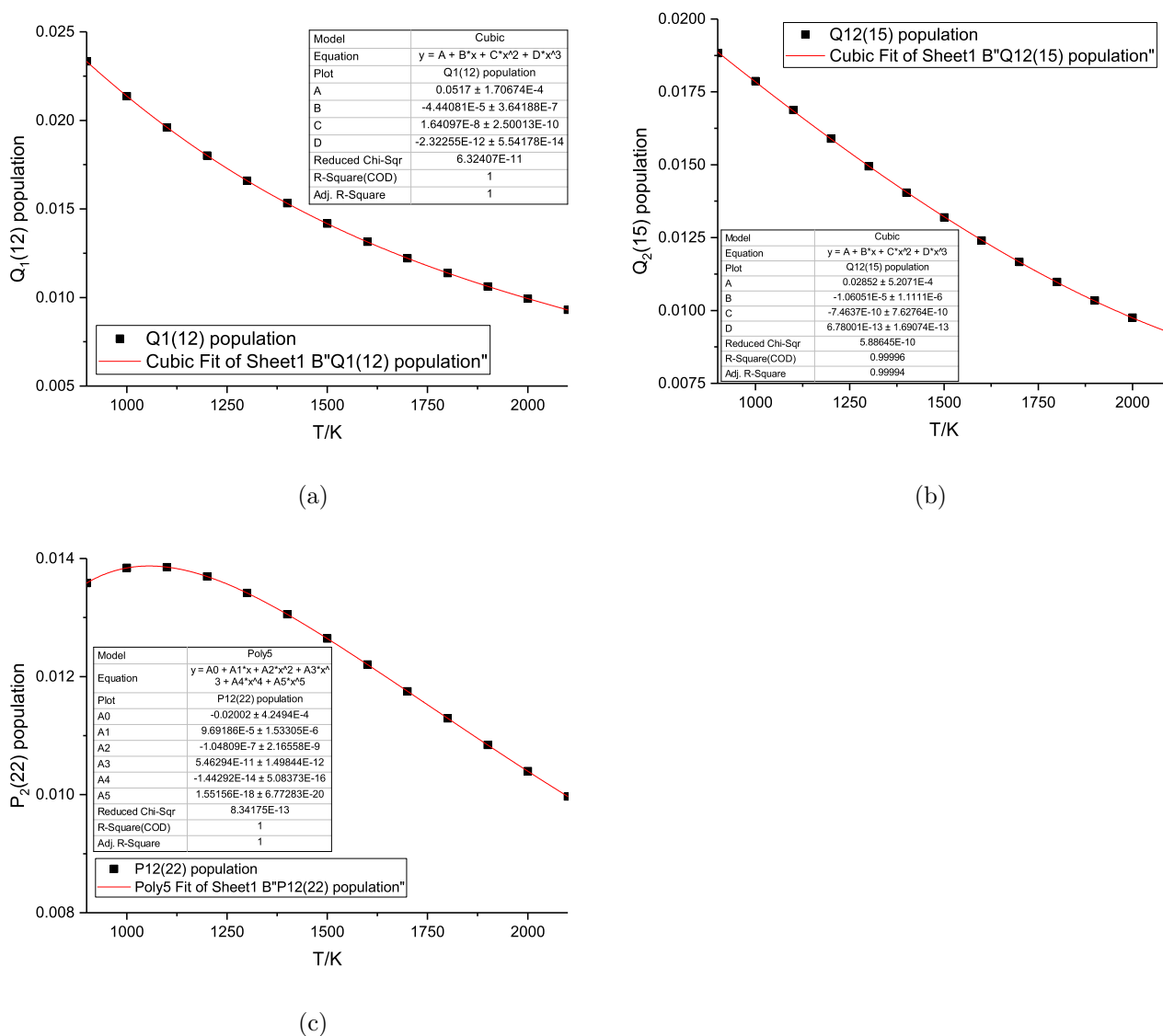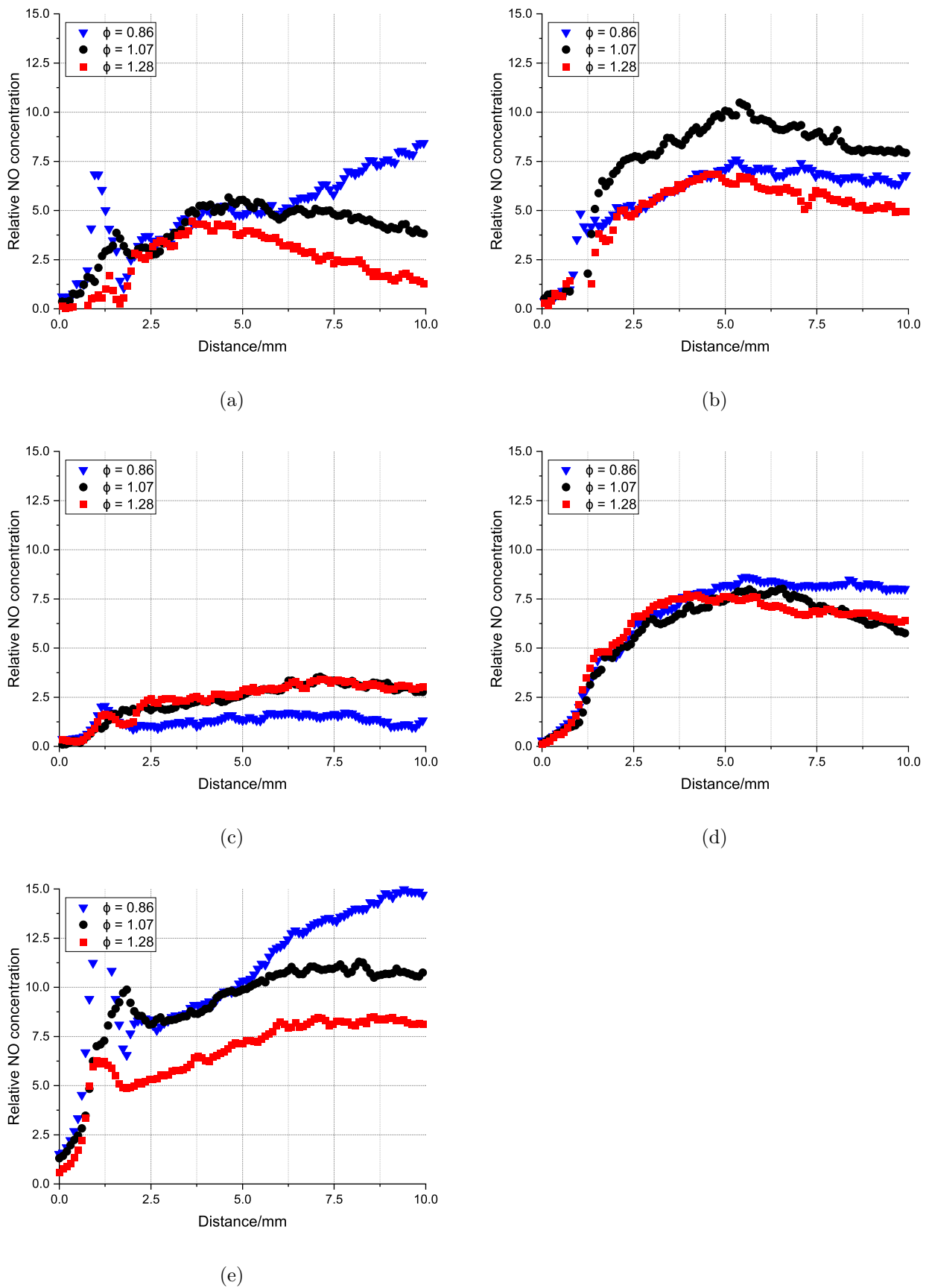

(a)

(b)

(c)

Figure 4.15: Curve fitting for the Boltzmann population in the $Q_1(12)$, $Q_2(15)$, and $P_2(22)$ transitions at the flame temperature range.

(a)

(b)

(c)

(d)

(e)

Figure 4.16: Relative NO concentration in (a) jet A-1, (b) E50, and (c) ethanol, (d) Surrogate A, and (e) Surrogate B flames from the $Q_1(12)$ transition.

The E50 flames have relatively a higher NO LIF signal compared to the jet A-1 flames, even though the flame temperature of the E50 flames are lower than the jet A-1 flames for each stoichiometry by approximately 100 K. This might be caused by a change in the experimental factor of the NO LIF experiment which was more difficult than the OH LIF. The temperature difference between the E50 flames is approximately 50 K with the stoichiometric has the highest and lean flames has the lowest flame temperature. The NO concentration in the stoichiometric flame was the highest compared to the lean and rich flames which are nearly similar in the region below 4.0 mm.

A higher NO signal than jet A-1 flames was found from the surrogate A and B flames despite the temperature of the jet A-1 flames being higher than the surrogates for all stoichiometry. The behaviour of the NO profile in the surrogate B flames is more similar to the jet A-1 flames where the rich flames have the lowest NO concentration while the profile of the lean and stoichiometric flames are about similar in the region below 5.0 mm. In the surrogate A flames, the NO profile was nearly similar between three stoichiometry and reaching approximately 7.5, which is nearly similar to the rich flame of surrogate B.

Figures 4.17 and 4.18 present the relative NO concentration of the observed flames from the $Q_2(15)$ and $P_2(22)$ transitions, respectively. These transitions were used for measuring the flame temperature from the NO fluorescence signal, and the LIF images from these transitions can also be used for measuring the NO concentration in the flames. The main difference from the previous $Q_1(12)$ transition is that these transitions are less strong, therefore it can be seen from Figures 4.17 and 4.18 that the scale of the relative NO concentration is about half that of the scale in the $Q_1(12)$ transition. Apart from that, ideally, the results of the relative concentration from the $Q_2(15)$ and $P_2(22)$ transitions should be similar to that from the $Q_1(12)$ transition after normalisation to the raw images has been performed. However, differences are found between these transitions, therefore the discrepancies between these transitions are highlighted.

In the jet A-1 flames, discrepancy of the NO profiles were found, which the stoichiometric flames have relatively higher NO in the results from the $Q_2(15)$ and $P_2(22)$ transitions, unlike the $Q_1(12)$ transition, which the NO profile becomes higher than rich and stoichiometric at higher region than 5.0 mm. The NO profile of the lean flame in the $Q_1(12)$ and $Q_2(15)$ transitions is very close to that of the stoichiometric flame, while at the $P_2(22)$ transition the lean flame becomes the lowest at the region below than 5.0 mm. Relating these findings to the temperature profile of these flames, the result from the $P_2(22)$ transition follows the trend of the flame temperature, in which the order are similar between the flame temperature and the NO profile in the lower region.

The NO profile of the Surrogate A and ethanol flames are consistent in all transitions and all stoichiometry. In the ethanol flames, the level of the NO concentration is relatively similar to the flame temperature profile, where the stoichiometric and rich have the higher NO concentration, then followed by the lean flame. In the surrogate A flames, the profile of the NO concentration is relatively close between each other in all transitions. At higher flame region, the NO profile of the rich and stoichiometric flames dropped while the profile of the lean flame remained at the equilibrium.

In the case of the E50 flames, all transitions indicate that the stoichiometric flame has the highest NO concentration compared to the other stoichiometry. This is supported by the fact that the stoichiometric flame has the highest flame temperature which enhances the NO production from the thermal mechanism. There are discrepancy in the rich and lean flames in all three transitions, and the $Q_1(12)$ and $Q_2(15)$ transitions indicate a higher NO concentration in the lean rather than the rich flame, while the $P_2(22)$ transition shows a higher NO concentration in the rich flame than in the lean flame. Referring to the prompt and thermal mechanism, the result from the $P_2(22)$ transition is more appropriate. This was caused by the fact that the rich flame has a higher flame temperature and hydrocarbon concentration than the lean flame, which promotes the thermal and prompt NO_x mechanism.

In the surrogate B flame, there is an inconsistent behaviour in the NO profile of the lean flame, and in the $Q_1(12)$ transition, it is higher than that of stoichiometric and rich flames. Meanwhile, at the $P_2(22)$ transition it was lowest in the lower region of the flame and becomes higher than the rich flame in the region higher than 5.0 mm. The overlapping behaviour of the lean and rich flames at the $P_2(22)$ and close at the $Q_2(15)$ transitions may be related to the close temperature profile for both flames which is approximately 20 K higher for the rich flame.
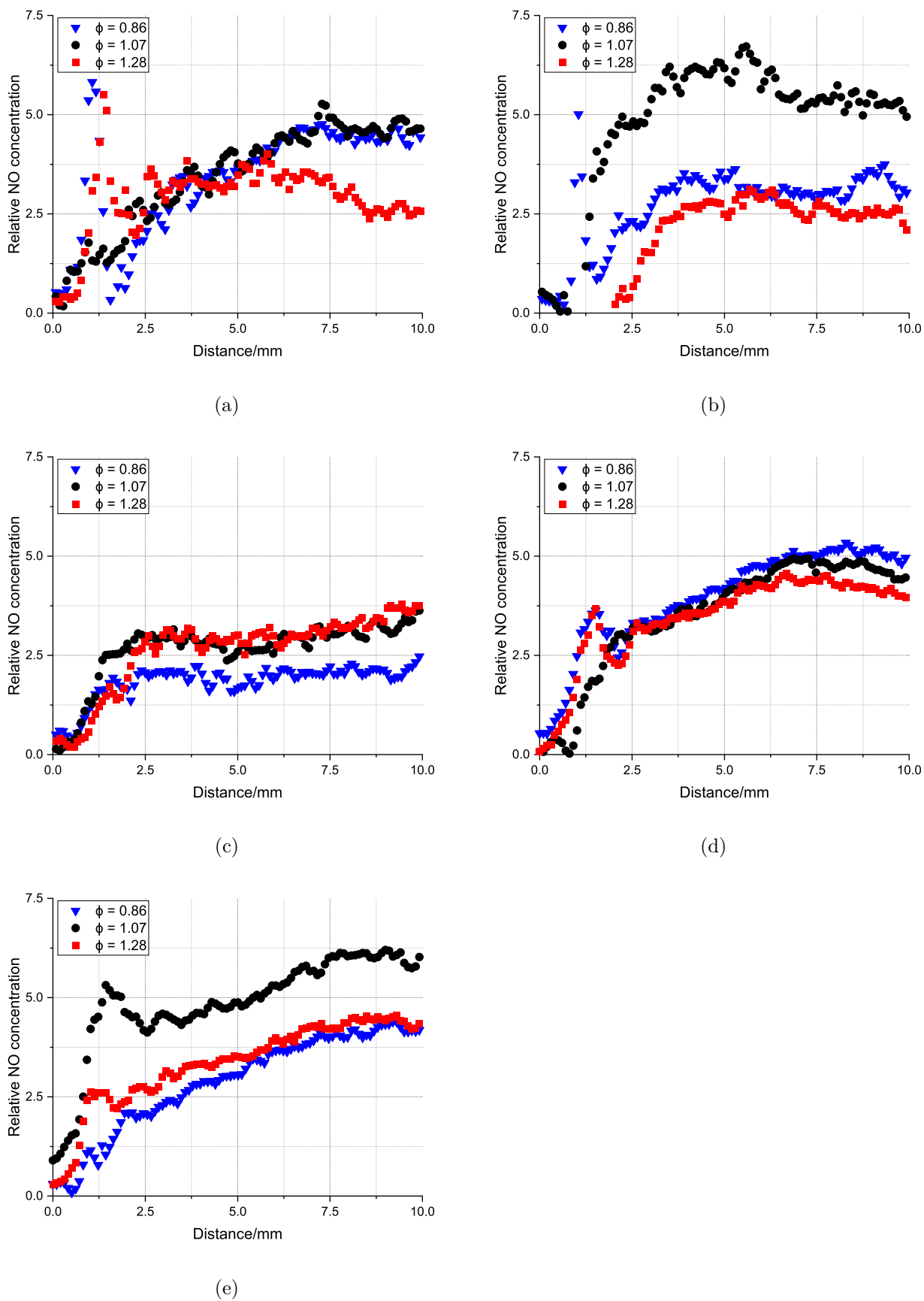
(a)

(b)

(c)

(d)

(e)

Figure 4.17: Relative NO concentration in (a) jet A-1, (b) E50, and (c) ethanol, (d) Surrogate A, and (e) Surrogate B flames from the $Q_2(15)$ transition.
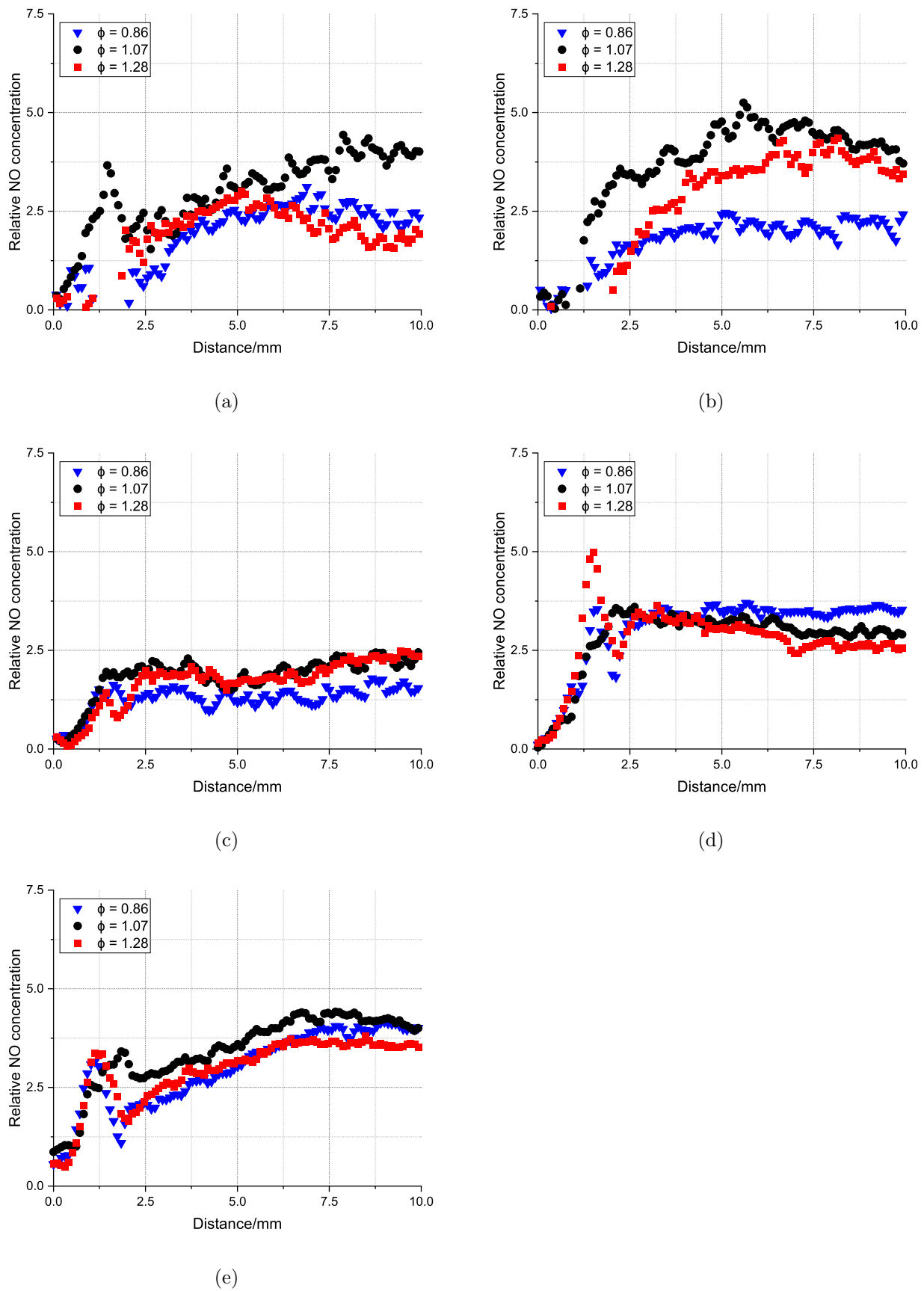
Figure 4.18: Relative NO concentration in (a) jet A-1, (b) E50, and (c) ethanol, (d) Surrogate A, and (e) Surrogate B flames from the $P_2(22)$ transition.

4.3.3 OH Quantification

After obtaining the relative concentration of the OH and NO radicals in the observed flames, the next data processing is to quantify the concentration of both species. This becomes possible by the availability of an accurate kinetic model of a flame that can be used as a reference that is comparable to the LIF signal of the identical flame. Then, a ratio can be obtained to convert the scale in the relative concentration to mole fraction unit. A burner flame simulation has been performed using the PREMIX program and the ethanol reaction mechanism by Olm et al. [56] (ELTE) for simulating the lean, stoichiometric, and rich ethanol flames. This mechanism does not have the NO_x mechanism, and alternatively, the recent skeletal NO_x mechanism from the Hy-Chem group [161] was imported to the ELTE ethanol mechanism. This was performed by using the features of the merging mechanism in the ANSYS Reaction Workbench program, with the reactions and species data from the NO_x mechanism, that already exists in the ELTE mechanism, were ignored. Similar boundary condition to the experimented ethanol flames was specified in the input of the PREMIX program. The results of the simulated OH and NO concentration in the flames are presented in Figure 4.19. The comparison of the simulation and experimental results of the ethanol flames are summarised in Tables 4.22 and 4.23 for OH and NO, respectively.

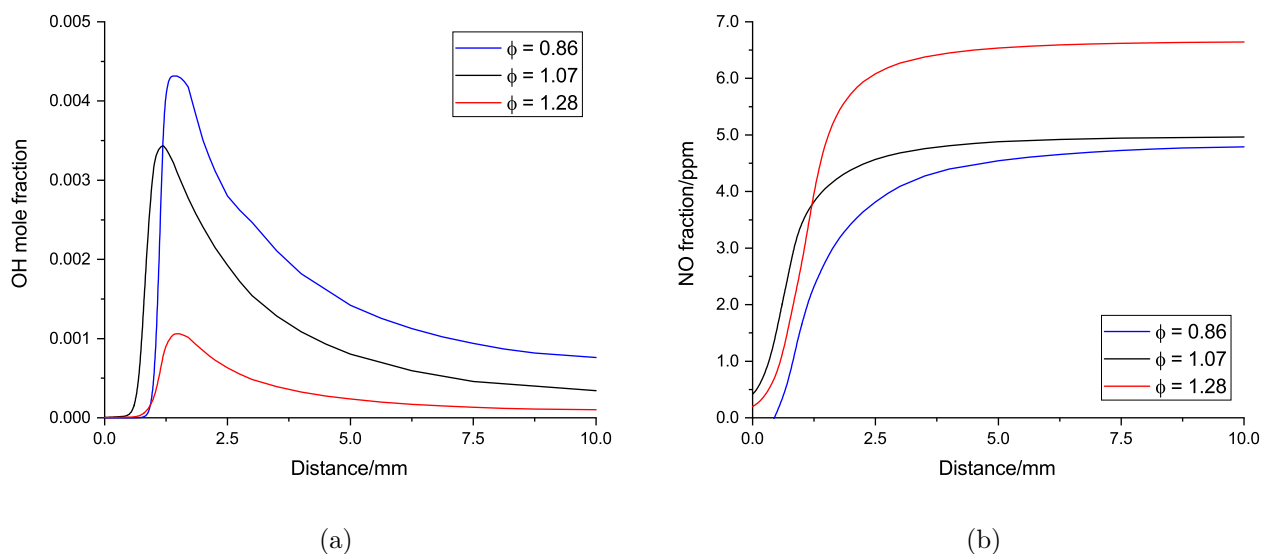(a)   (b)

Figure 4.19: Simulated (a) OH and (b) NO concentration for the ethanol reference flames from PREMIX simulation.

The trend of the simulated OH concentration is similar to the relative OH concentration for the ethanol flames, where it started from zero at the burner surface, then rapidly increased to the peak and decreased to the equilibrium concentration. There are discrepancies between the simulated and experimental data in terms of the determination of the equilibrium position. In the simulated data, the OH concentration

119

achieved the equilibrium at approximately 5.0 mm for the rich flame and 7.5 mm for the stoichiometric and lean flames. The peak of the OH concentration is predicted to occur at approximately 1.2 to 1.5 mm from the burner surface. In the experiment results, the peaks are also located differently for each flame, which is 1.2 mm for the $Q_1(6)$ while 2.5 mm for the $R_2(2)$, and $R_1(12)$ transitions. The equilibrium position in the experimental data is relatively higher than the prediction, except in the $Q_1(6)$ transition.

In order to obtain an accurate ratio between the simulated and the experimental data, the value of the OH concentration is selected from the peak of the simulation and experiment profiles, which is presented in Table 4.22. The ratio, $[OH]_{ref}/I_{ref}$, was calculated for every stoichiometry and transition. Then the average of the ratio can be obtained from the ratio in the lean, stoichiometric, and rich flames. It is observed that there is a discrepancy between the simulation and the experiment data in determining the OH concentration, where the lean flame has higher a OH concentration than the stoichiometric flame in the experimental result, while in the simulation it is lower than that in the stoichiometric. The simulation results have been checked with the original ELTE mechanism for a possible error due to the merging procedure. It was found that the original mechanism shows a similar trend, where the stoichiometric flame has a higher OH concentration peak than the other stoichiometry.

After finding the value of the average ratio, $[OH]_{ref}/I_{ref}$, it can be used to quantify the relative OH concentration by the multiplication operation in Equation (4.5). The results of the OH quantification are presented in Figure 4.20, 4.21, and 4.22 for the $Q_1(6)$, $R_2(2)$, and $R_1(12)$ transitions, respectively. The quantification procedure does not change the profile of the OH concentration, which is exactly similar to the relative OH concentration, and it only normalises the scale to the mole fraction unit from the multiplication operation.

Table 4.22: Comparison of the simulated and experimental data of the OH peaks for ethanols flames at the $Q_1(6)$, $R_2(2)$, and $R_1(12)$ transitions.

ϕ	Simulation		$Q_1(6)$			$R_2(2)$			$R_1(12)$		
	$[OH]_{ref}$	X/mm	$[OH]_{ref}$	X/mm	$[OH]_{ref}/I_{ref}$	$[OH]_{ref}$	X/mm	$[OH]_{ref}/I_{ref}$	$[OH]_{ref}$	X/mm	$[OH]_{ref}/I_{ref}$
0.86	4.32E-03	1.40	3.4631	1.2	1.25E-03	2.20997	2.5	1.95E-03	2.60235	2.5	1.66E-03
1.07	3.43E-03	1.20	1.53094	1.2	2.24E-03	2.29314	2.5	1.50E-03	2.33797	2.5	1.47E-03
1.28	1.06E-03	1.48	0.54227	1.2	1.96E-03	1.06157	2.5	1.00E-03	1.20707	2.5	8.80E-04
Average					1.82E-03			1.48E-03			1.34E-03

Table 4.23: Comparison of the simulated and experimental data of the NO peaks for the ethanol flames at the $Q_1(12)$, $Q_2(15)$, and $P_2(22)$ transitions.

ϕ	Simulation		$Q_1(12)$			$Q_2(15)$			$P_2(22)$		
	$[NO]_{ref}$	X/mm	$[NO]_{ref}$	X/mm	$[NO]_{ref}/I_{ref}$	$[NO]_{ref}$	X/mm	$[NO]_{ref}/I_{ref}$	$[NO]_{ref}$	X/mm	$[NO]_{ref}/I_{ref}$
0.86	4.79E-06	10.0	1.31706	10.0	3.64E-06	2.47191	10.0	1.94E-06	1.5398	10.0	3.11E-06
1.07	4.97E-06	10.0	2.76861	10.0	1.79E-06	3.62905	10.0	1.37E-06	2.44838	10.0	2.03E-06
1.28	6.64E-06	10.0	3.01895	10.0	2.20E-06	3.74405	10.0	1.77E-06	2.34181	10.0	2.84E-06
Average					2.54E-06			1.69E-06			2.66E-06

The measurement result of the OH concentration should be similar between the OH transitions. However, a discrepancy was found between the quantification results of the OH measurement from the $Q_1(6)$, $R_2(2)$, and $R_1(12)$ transitions. The quantification of the OH profile from the $Q_1(6)$ transitions indicates that the highest OH concentration is approximately 0.8 per cent, which is found at the lean jet A-1 flame. This is approximately three times higher than that in the other transitions, which for the same flame, it indicates approximately 0.25 per cent for the $R_2(2)$ and a slightly lower value for the $R_1(12)$ transition. This may be caused by the inconsistency in the experimental data of the OH profile of the flames reference. The stoichiometric flame, which has the highest OH concentration peak according to the simulation, has a low OH profile compared to the jet A-1 and E50 flames in the $Q_1(6)$ transitions. Meanwhile, the experimental data of the OH concentration peak of the stoichiometric ethanol flame in the other transitions are higher and similar to that in the stoichiometric jet A-1, E50, surrogate A and B flames. This causes a higher indication of the OH concentration in the $Q_1(6)$ transition and lower at the other transitions.

Compared to the OH concentration measurement results by Catalanotti [5], the OH concentration peak for the stoichiometric jet A-1 flame in this study is higher than that in Catalanotti's work, which is approximately 0.7 per cent in this work and 0.35 per cent in Catalanotti's. Despite that the similar transition was used for both experiment, different flame reference was used. Catalanotti used methane/air with the GRI 3.0 kinetic model as the reference while this work used ethanol as the flame reference, which may cause the discrepancy between both results.
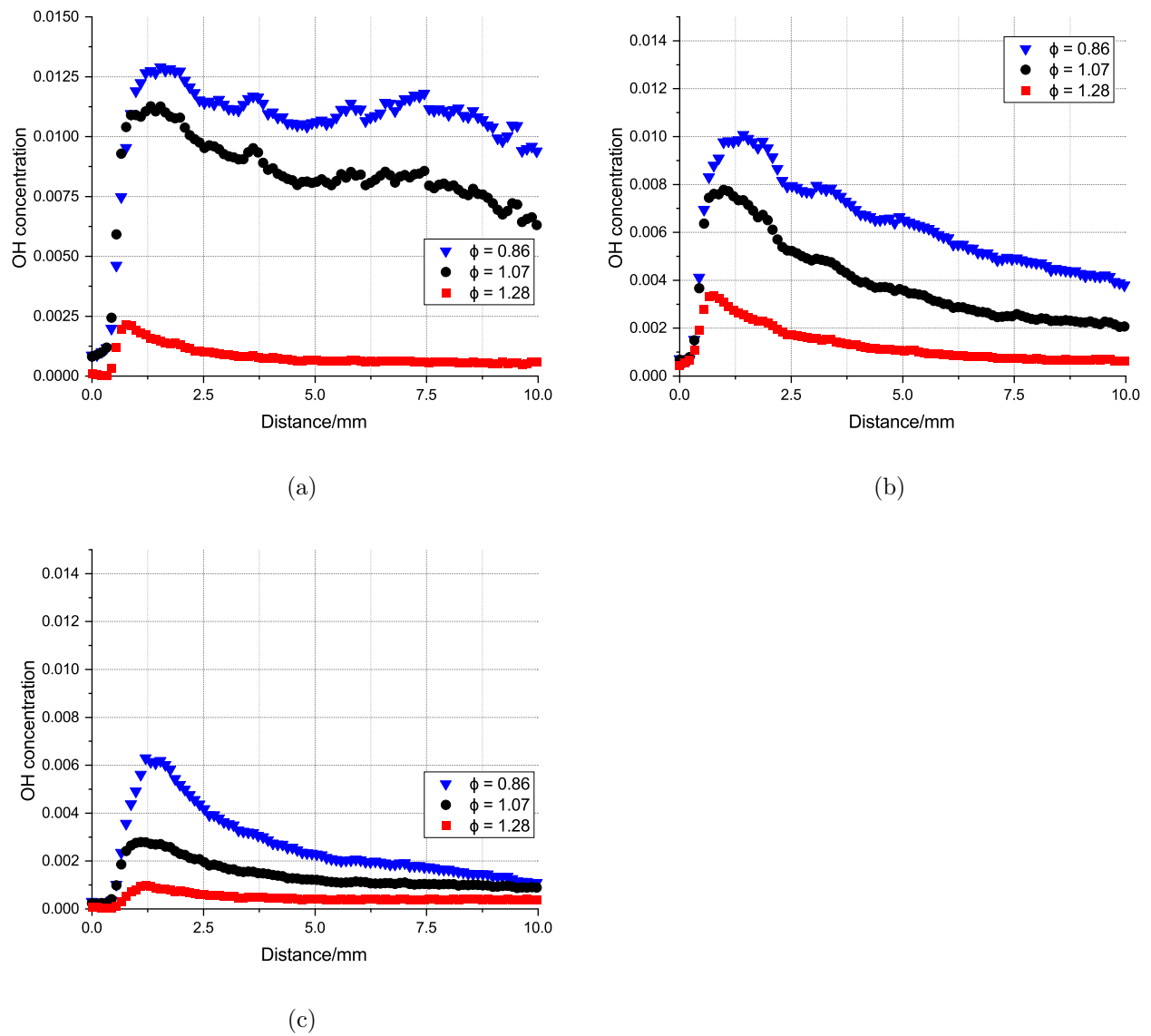
(a)

(b)

(c)

Figure 4.20: Quantified OH concentration in (a) jet A-1, (b) E50, and (c) ethanol flames from the $Q_1(6)$ transition.
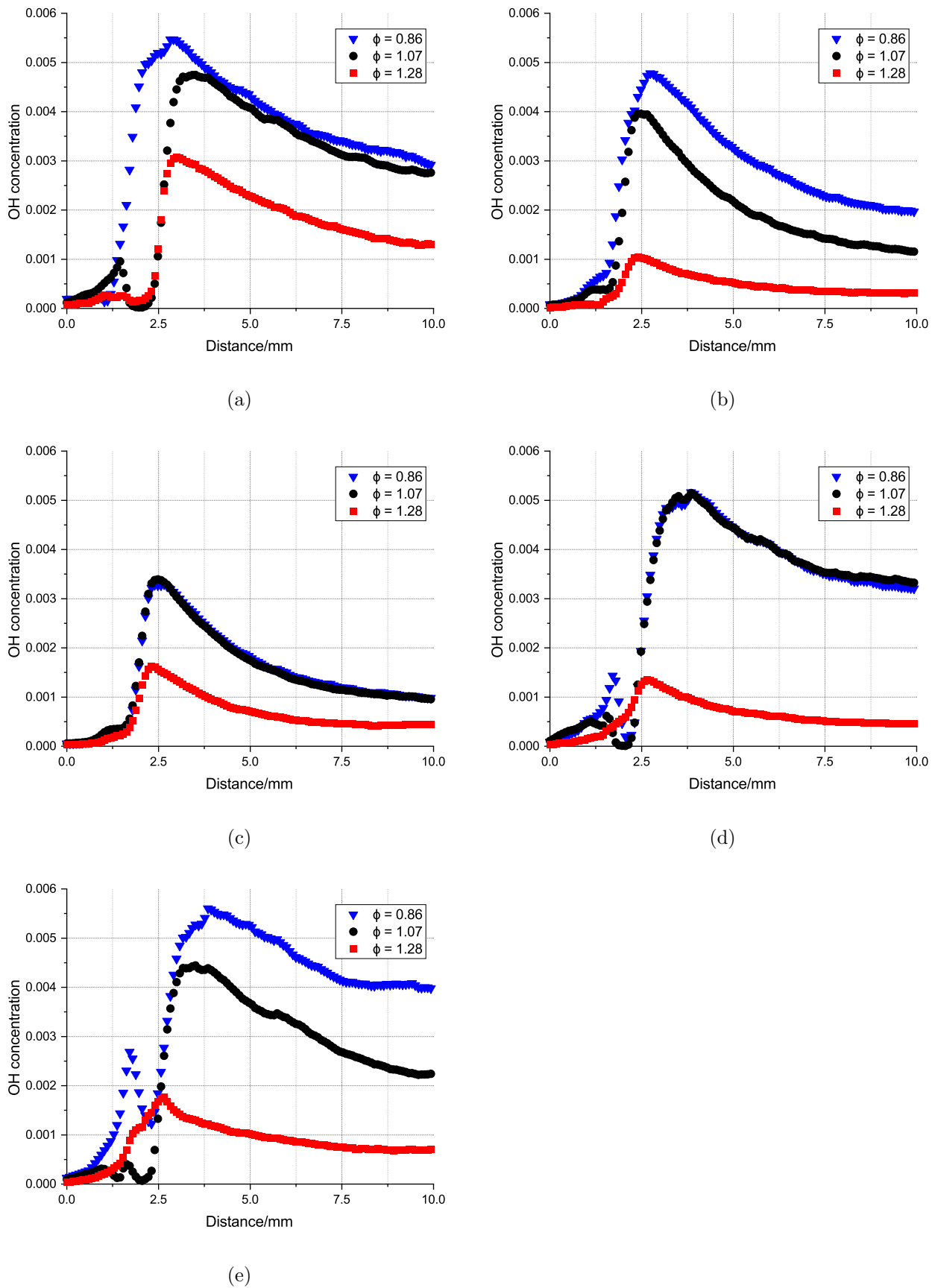
123

Figure 4.21: Quantified OH concentration in (a) jet A-1, (b) E50, (c) ethanol, (d) Surrogate A, and (e) Surrogate B flames from the $R_2(2)$ transition.
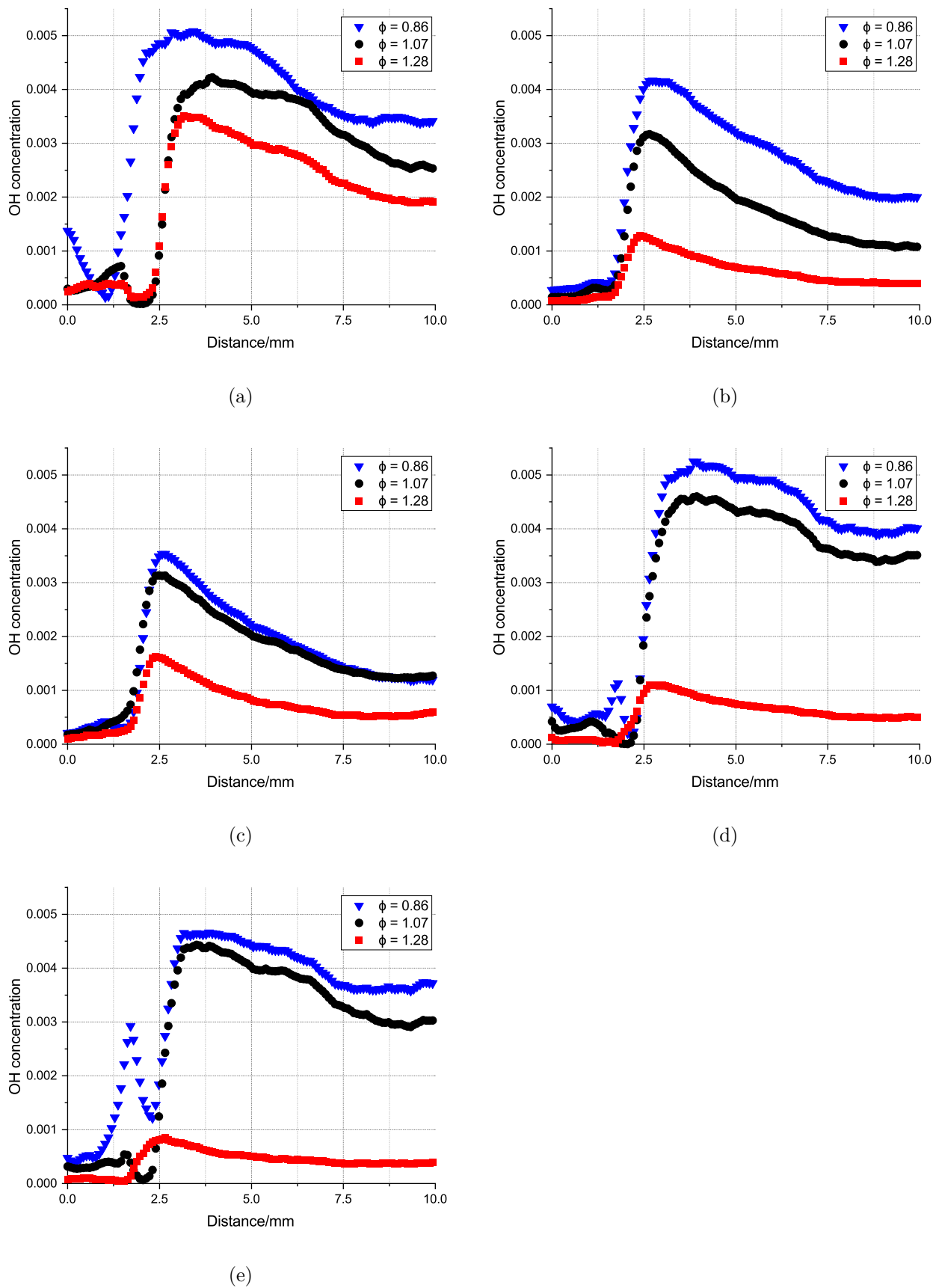
124

Figure 4.22: Quantified OH concentration in (a) jet A-1, (b) E50, and (c) ethanol, (d) Surrogate A, and (e) Surrogate B flames from the $R_1(12)$ transition.

4.3.4 NO Quantification

A similar procedure that was used for the quantification of the OH concentration was applied to the relative NO concentration. The kinetic model was able to predict the NO profile in the ethanol flames as presented in Figure 4.19(b), where it increases from zero and stabilises at the equilibrium concentration. Unlike the OH profile which has a concentration peak, the NO profile relatively stable after reaching the equilibrium. Therefore, the comparison with the kinetic model is focused at 10.0 mm above the burner surface, with the assumption that at this position, the concentration of NO has reached the equilibrium. Table 4.23 summarises the experimental and simulated NO concentrations at 10.0 mm as well as the values of the $[NO]_{ref}/I_{ref}$. The discrepancy between the simulation and the experiment result was found in the NO concentration of the stoichiometric and the rich flames, where in the simulation the rich flame has the highest NO concentration with 2 ppm higher than the stoichiometric flame. Meanwhile, the experimental data indicates a similar NO concentration between the stoichiometric and rich flames.

In the $Q_1(12)$ and $Q_2(15)$ transitions, the value of $[NO]_{ref}/I_{ref}$ in the lean, rich, and stoichiometric flames varies by less than 1 ppm and 1.2 ppm for the $P_2(22)$ transition. The average of the ratios was taken for each transition and multiplied by the relative NO concentration to obtain the quantified NO profile. Figures 4.23, 4.24, and 4.25 show the quantification results for the $Q_1(12)$, $Q_2(15)$, and $P_2(22)$ transitions, respectively. The quantification procedure only converts the relative scale of the corrected NO LIF signal to part per million (ppm) while the curve remains the same.

The NO measurement results from the PLIF method can complement the results from the gas analysis method in Section 4.2, which has several issues with the performance of the NO_x sensor. In the case of the ethanol flames, the gas analyser failed to measure the higher region of the stoichiometric flame and the rich flame. The gas analyser indicates that the NO concentration in the lean flame has approximately 8 ppm at 10.0 mm while the LIF method shows approximately 5 ppm from all transitions. Meanwhile, for the NO concentration in the rich flame, where the gas analyser showed nearly zero, the LIF method indicates 10 ppm in the $Q_1(12)$ and 7.5 ppm in the $Q_2(15)$, and $P_2(22)$ transitions which is similar to that of the stoichiometric flame.
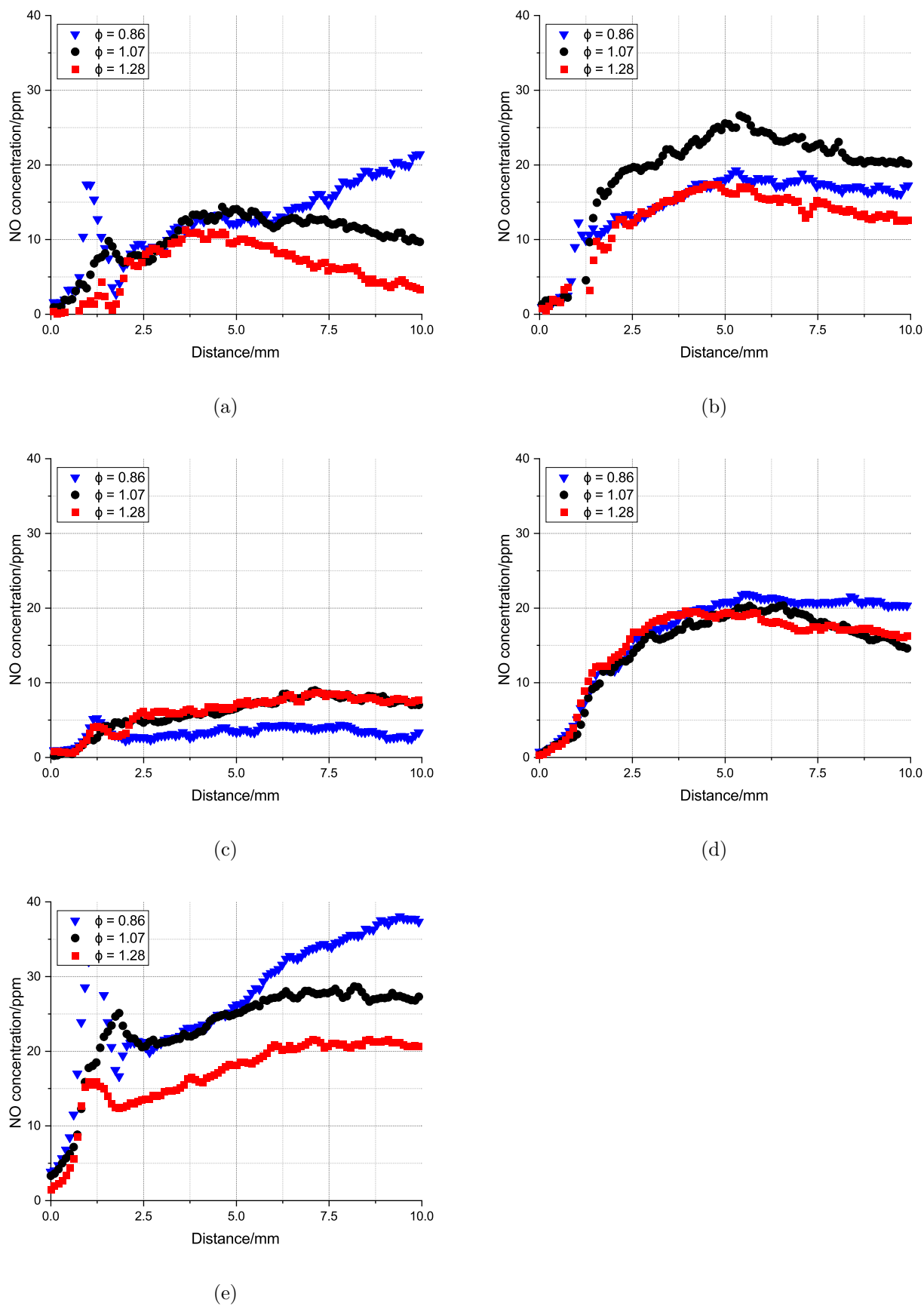
(a)

(b)

(c)

(d)

(e)

Figure 4.23: Quantified NO concentration in (a) jet A-1, (b) E50, and (c) ethanol, (d) Surrogate A, and (e) Surrogate B flames from the $Q_1(12)$ transition.
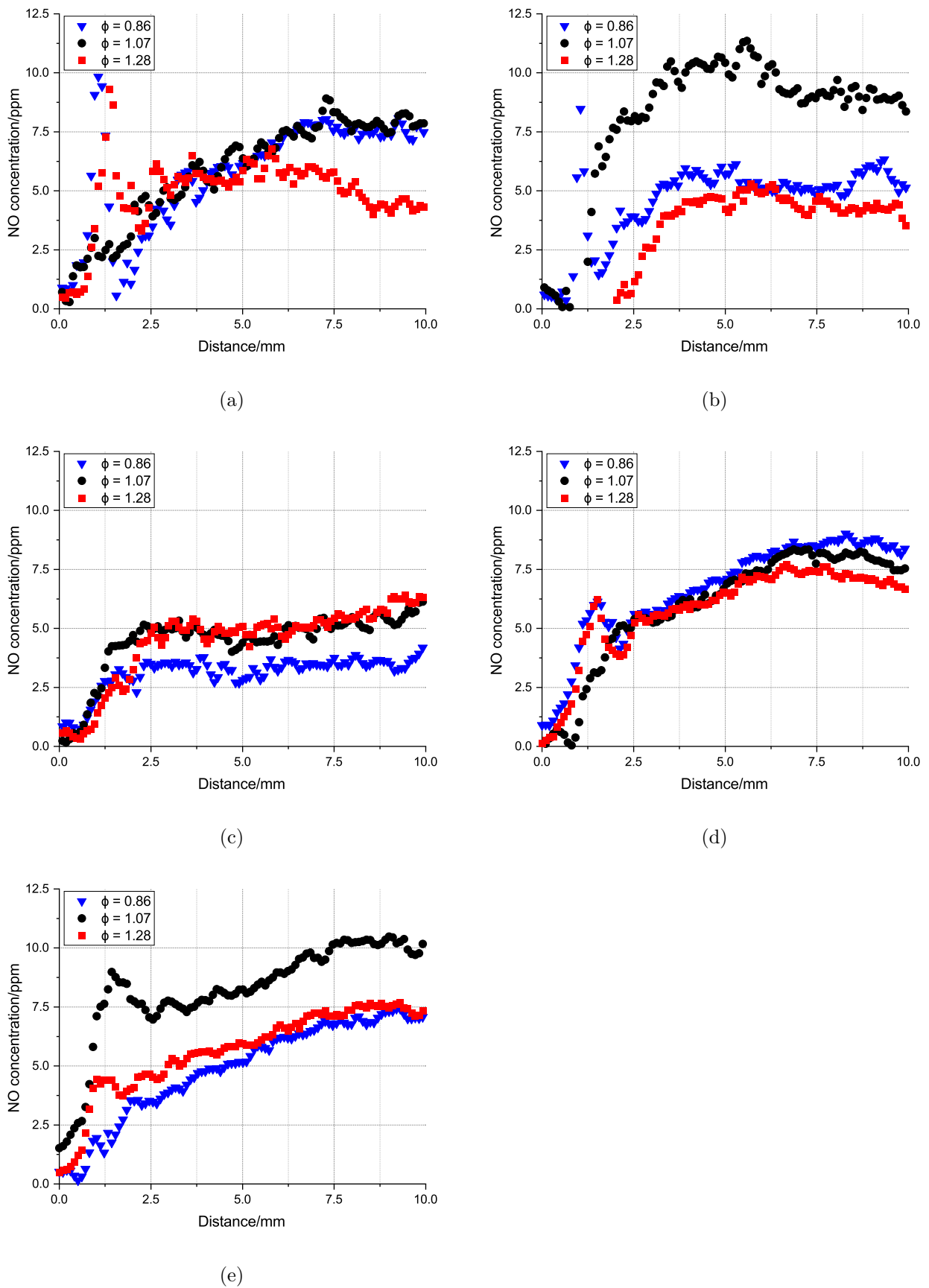
Figure 4.24: Quantified NO concentration in (a) jet A-1, (b) E50, and (c) ethanol, (d) Surrogate A, and (e) Surrogate B flames from the $Q_2(15)$ transition.

128

The addition of ethanol jet A-1 indicates a higher NO formation in the stoichiometric and rich flames by approximately 100 per cent based on the gas analysis. This information is supported by the LIF results, except the rich flame in the $Q_2(15)$ transition, which shows a similar NO level between both rich flames. However, this finding might be debatable considering the technical difficulties in the NOx sensor and NO LIF experiment as well as the lower flame temperature of E50 flames than jet A-1. In the gas analyser, the NO_x reading was the sum of the NO and NO_2, while in the PLIF method, only the NO radicals were detected. The amount of NO_2 in the flames is much smaller than the NO based on the ethanol flame simulation and this can be neglected when comparing both methods. Meanwhile, in the lean flame, ethanol addition results in the lower NO_x emission based on the PLIF method in all the transitions, while the gas analysis shows a similar concentration between both lean flames. However, a large discrepancy was found between the gas analysis and the $Q_1(12)$ transition in quantifying the NO concentration in the lean and stoichiometric flames. Based on the gas analysis, the NO concentration in the stoichiometric flames were approximately 7 and 14 ppm for the jet A-1 and E50, respectively, while the $Q_1(12)$ transition obtained 15 and 30 ppm. For this case, the results from the $Q_2(15)$ transition is more similar to the gas analysis result. For the lean flame, the $Q_2(15)$ and $P_2(22)$ transitions are closer to the gas analysis result than the $Q_1(12)$ which indicated a higher NO emission.

For the comparison of the jet A-1 flames to the surrogate A and B, the gas analysis method was found to be the highest NO emission in the rich and this is followed by the stoichiometric and lean flames with a similar values. However, this trend was not found in the LIF method, where the stoichiometric flames have a relatively higher NO concentration than the other stoichiometry, except in the $Q_1(12)$ transition where the lean flame was indicated to have the highest NO concentration. Apart from these findings, the surrogate flames have a relatively similar NO concentration with jet A-1 flames for the same transition.

Compared to the NO measurement by Catalanotti [5], the LIF results from this work indicated less NO concentration, where Catalanotti's showed higher than 50 ppm for the lean a stoichiometric flames. This was caused by the different source of the reference, where in Catalanotti's work, the reading from the gas analysis of a methane flame burner was used rather than from the ethanol and PREMIX simulation. The calibration to the gas analysis reading was not possible for this work because of the failure and performance instability of the gas analyser. Therefore, the calibration to ethanol and PREMIX simulation was considered as the better method.
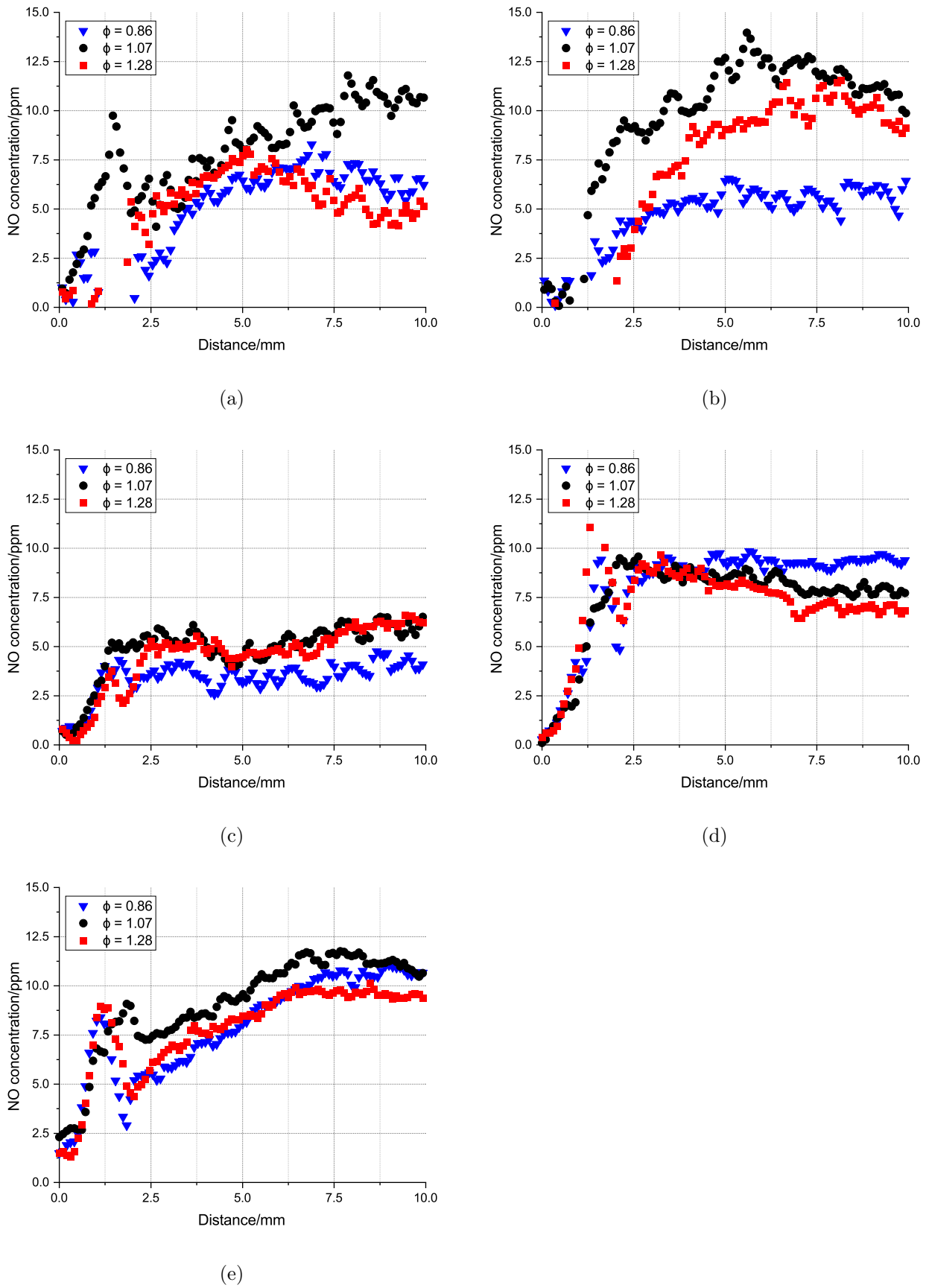
Figure 4.25: Quantified NO concentration in (a) jet A-1, (b) E50, and (c) ethanol, (d) Surrogate A, and (e) Surrogate B flames from the $P_2(22)$ transition.

4.3.5 LIF Thermometry

A further processing step of OH and NO signal is the obtaining of the flame temperature from the $R_2(2)$ and $R_1(12)$ transitions for the OH PLIF and the $Q_2(15)$ and $P_2(22)$ transitions for the NO PLIF signal. Figures 4.26 to 4.30 present the results of the OH thermometry while Figure 4.31 shows the results of the NO thermometry. The results of both OH and NO are compared to the temperature profile from the thermocouple probing in Section 4.1.
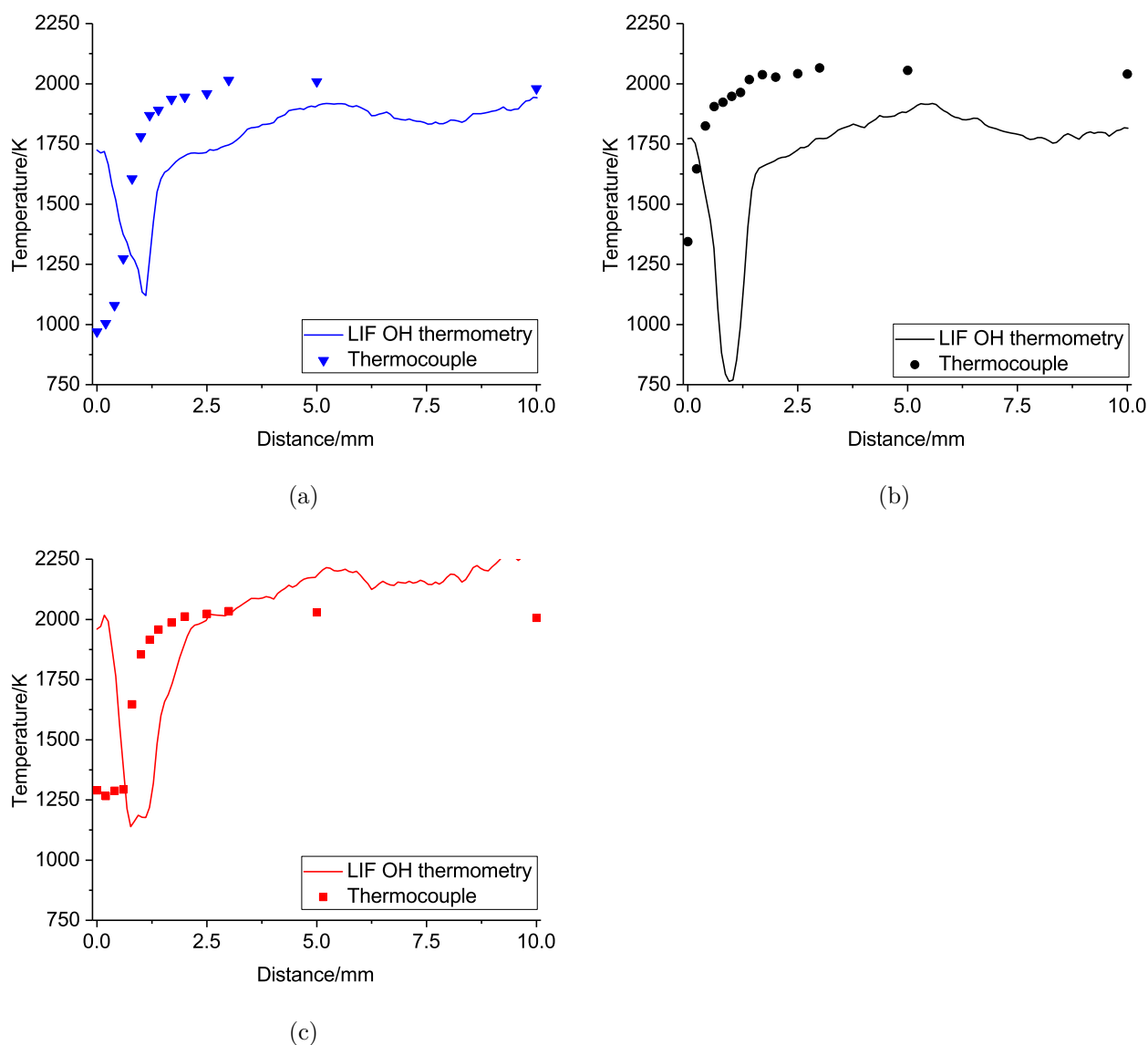

(a)

(b)

(c)

Figure 4.26: OH thermometry results in the jet A-1 flames for (a) $\phi = 0.86$, (b) $\phi = 1.07$, and (c) $\phi = 1.28$.
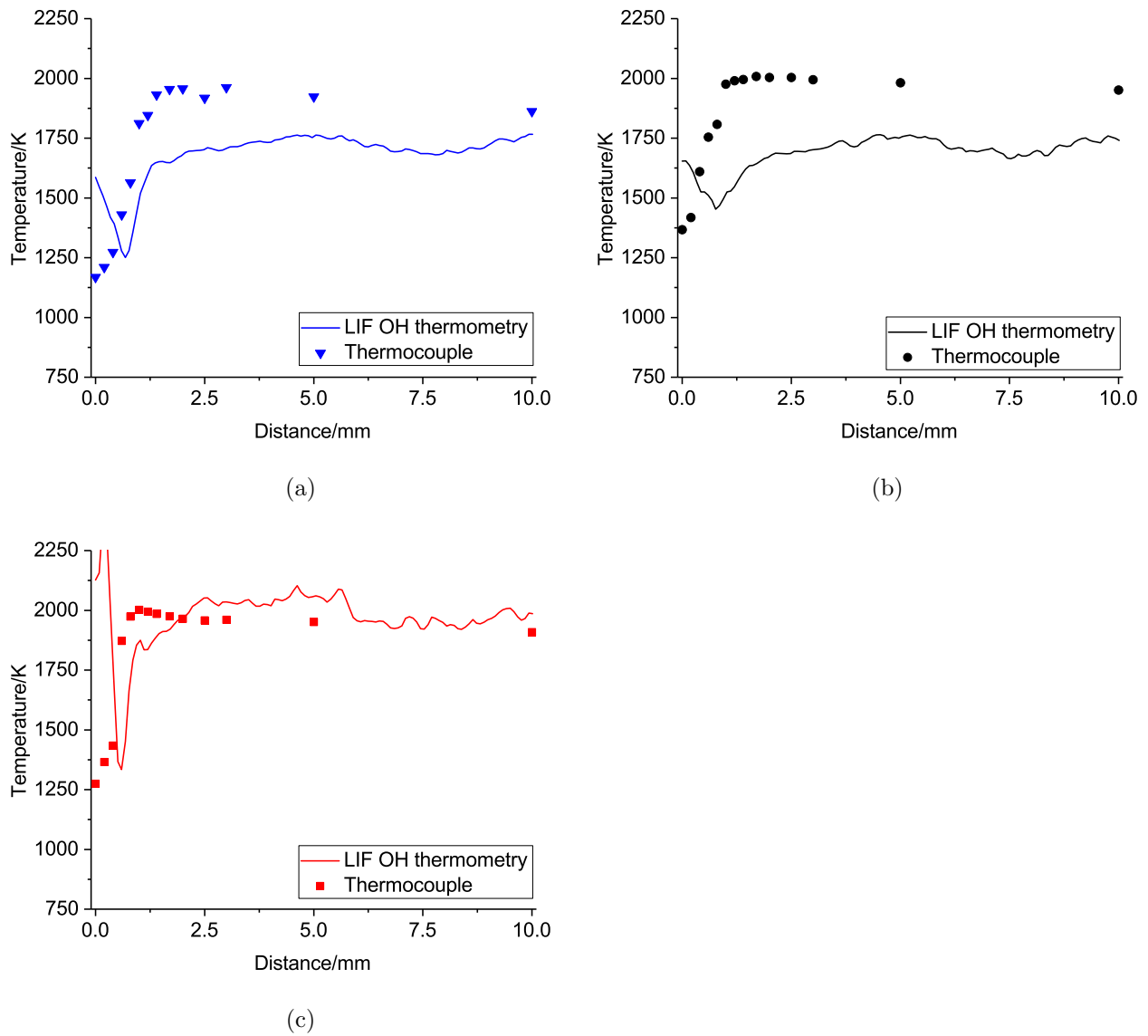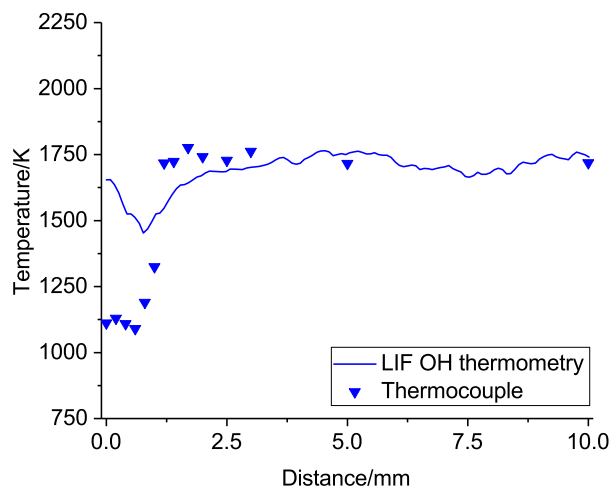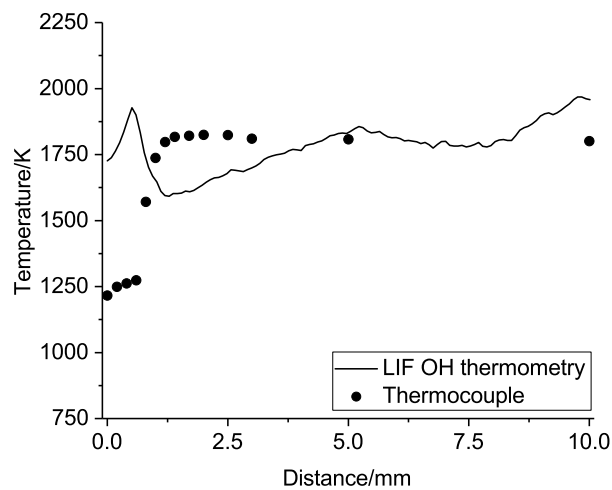
131

(a)

(b)

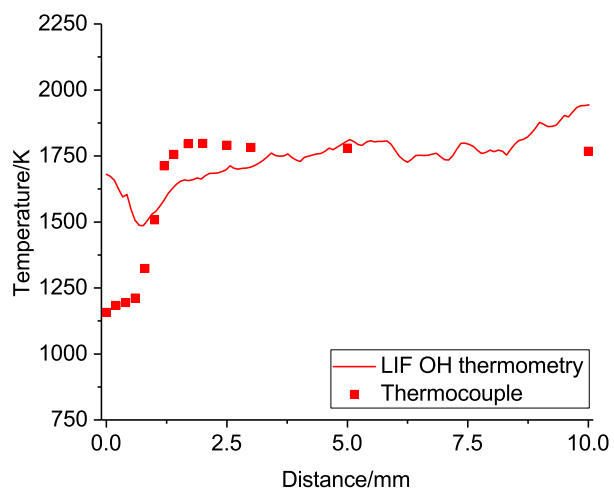(c)

Figure 4.27: OH thermometry results in E50 flames for (a) $\phi = 0.86$, (b) $\phi = 1.07$, and (c) $\phi = 1.28$.

(a)

(b)

(c)

Figure 4.28: OH thermometry results in ethanol flames for (a) $\phi = 0.86$, (b) $\phi = 1.07$, and (c) $\phi = 1.28$.
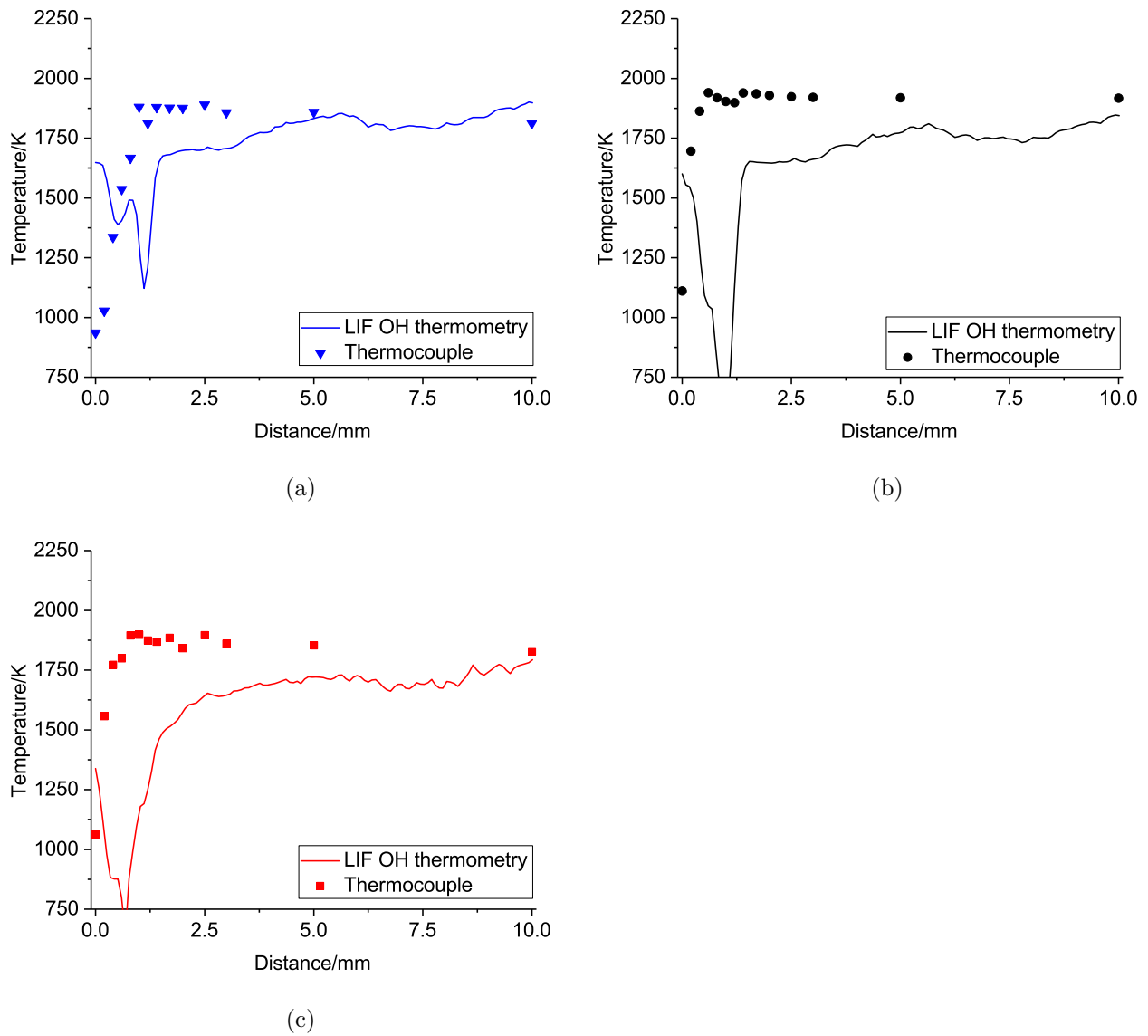
(a)

(b)

(c)

Figure 4.29: OH thermometry results in Surrogate A flames for (a) $\phi = 0.86$, (b) $\phi = 1.07$, and (c) $\phi = 1.28$.
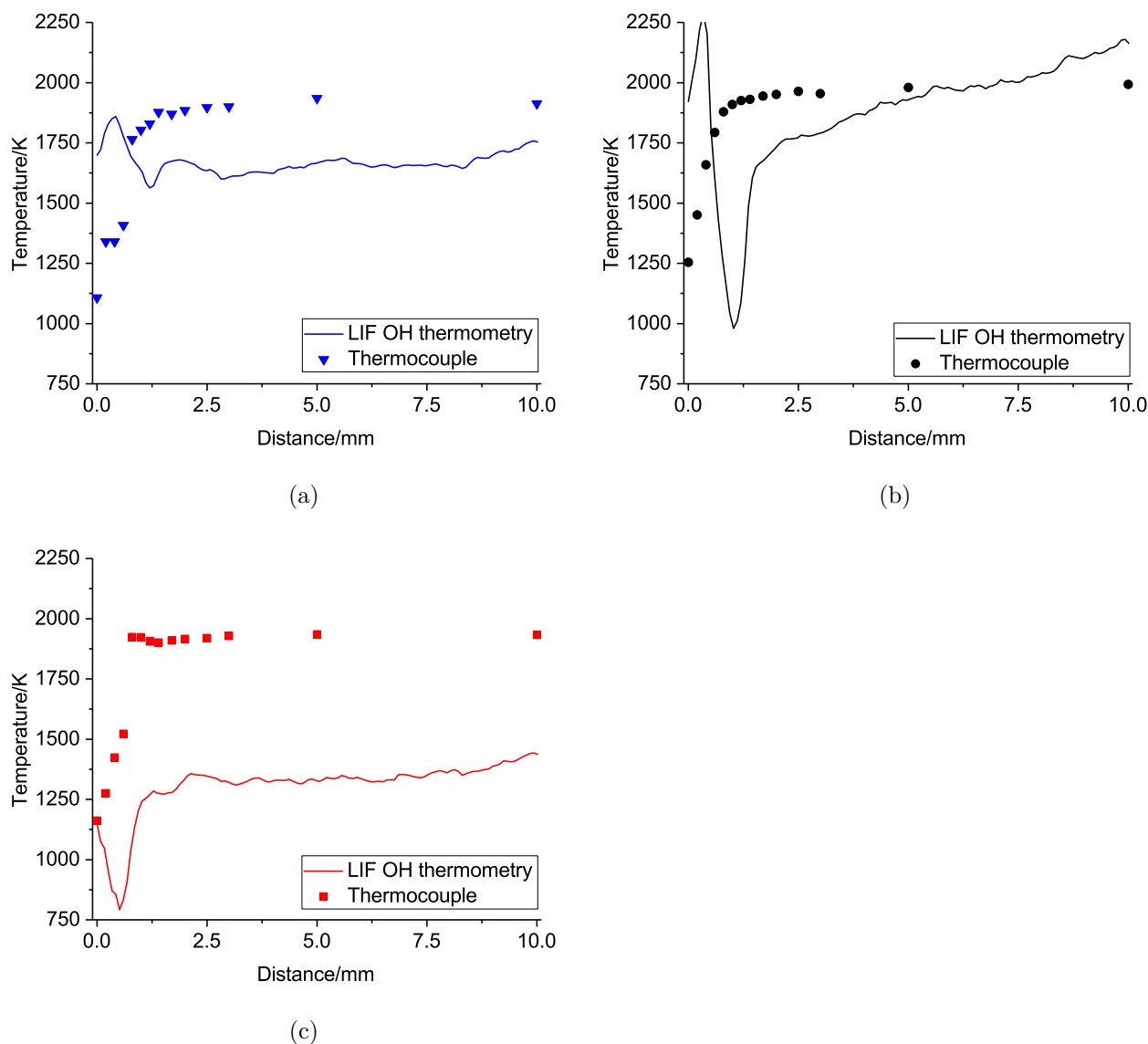
(a)

(b)

(c)

Figure 4.30: OH thermometry results in Surrogate B flames for (a) $\phi = 0.86$, (b) $\phi = 1.07$, and (c) $\phi = 1.28$.

The thermocouple probing technique is more widely used for the temperature measurement method in flames because it is simpler in terms of the experiment setup and data processing. The LIF thermometry offers advantages over the thermocouple method and also disadvantages. The main advantage of the LIF thermometry over the thermocouple method is that it is a non-intrusive method, whereas in the thermocouple method the exposure of the thermocouple to the flame may disturb the flame flow. Moreover, the chemical reaction between the thermocouple surface and the flame may change the characteristics of the thermocouple while the interaction with a high-temperature flame causes the expansion to the thermocouple wire which causes the thermocouple to lose its tension and displaced to an inaccurate position. Therefore, the thermocouple size for the flame temperature measurement is commonly aimed to be as small as possible, provided with a tension compensator, and surface coating.

Unfortunately, the tiny thermocouple has a higher risk to break when a higher flame flow velocity was applied, or alternatively, a larger thermocouple diameter is used to increase the strength of the thermocouple with the consequence of disturbing a larger part of the flame. Using the LIF thermometry, these problems can be avoided and advantages over the thermocouple method can be obtained. Unlike the thermocouple, which must be positioned at a certain position in order to obtain a single data point, the planar LIF thermometry can measure the whole part of the flame at once as long as the laser and the camera are exposed to all parts of the flame.
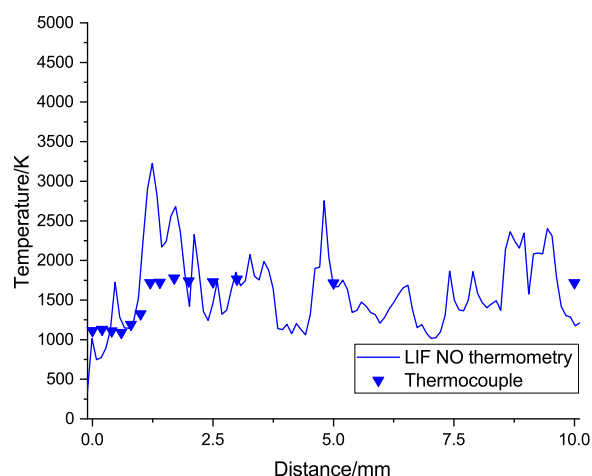

Figure 4.31: NO thermometry results in the ethanol flame for $\phi = 0.86$.

However, there are disadvantages of the PLIF thermometry over the thermocouple method, such as the more expensive and complicated experiment setup, requirement for optical access to the flame, dependency to the concentration of the observed particle, and more effort to process the LIF images to obtain the flame temperature. The optical access for the laser and camera to the flame is essential in the LIF thermometry, which makes this method unable to measure an optically closed vessel. The reflection of light from a solid surface might cause noise to the LIF signal and causes an inaccurate temperature reading. The LIF thermometry requires seeding species for emitting the fluorescence signal, and the species should be available in a relatively high concentration in order to allow a fine resolution of the temperature measurement. Ultimately, the raw LIF images requires further processing to obtain the flame temperature which involves the quantum behaviour of the electron at different temperature.

Comparing the OH LIF thermometry method to the thermocouple method, both methods agree on the profile of the flame temperature. The temperature profile started with the lowest temperature at the surface of the burner and it increased and stabilised after it reached the equilibrium. The OH LIF thermometry has difficulty in determining

the temperature in the lower flame region, which results in the discrepancy compared to the thermocouple method. This was caused by the low concentration of the OH radical in the lower flame region, where the OH concentration peak occurs at higher than 2.5 mm above the burner surface for the $R_2(2)$ and $R_1(12)$ transitions. The low OH concentration generated a low signal-to-noise ratio which causes inaccuracy in the ratio of the LIF signal along with the flame instability, and when this value is used to calculate the temperature using the temperature-ratio correlation in Figure 4.9(a), it results in an inaccurate temperature. Another reason is that in the lower flame region, the LIF images were contaminated by the reflection of the laser light by the burner surface. This background noise should have been eliminated once the normalisation procedure has been applied. However, it may be the case that the non-fluorescence signal from the off-resonance image was different from the non-fluorescence signal at the $R_2(2)$ and $R_1(12)$ transitions. Thus, when the background normalisation was performed, part of the non-resonance signal still remained at the corrected signal or if the non-resonance signal is higher at the off-resonance image, part of the fluorescence signal was corrupted. The scattered light at the burner surface does not only affect the very close distance from the burner but also the lower region of the flame because the position of the camera was slightly higher than the burner surface. This cause the burner surface to appear as not perfectly flat but slightly ellipsoidal and this overlapped with the fluorescence signal in the lower region. Most of the OH LIF thermometry results showed a relatively high temperature reading at close to the burner surface which decreases with the increasing of the distance to the burner surface before it increases to equilibrium analogue to the thermocouple results. The high temperature at close to the burner surface may not be trusted because of the error and the low concentration of the OH radicals at this location. The high temperature may be from the signal of the light reflection from the burner surface which was not perfectly corrected. Unlike the thermocouple which can measure the temperature of the burner surface, the LIF thermometry should not be able to predict the region where the OH radical was at a low concentration.

In the upper region, some of the LIF thermometry results are similar to the thermocouple result, while some of them are higher and lower than that. In the case that are in good agreement was achieved between both the methods, the flame was relatively stable and there was no major problem during the cuvette and noise normalisation procedure. Adversely, in the case which the under and overdeterminates the flame temperature occur, the flame fluctuation and the error due to the normalisation may cause the inaccurate temperature measurement. The fluctuation in the fuel flow caused by the flame becoming slightly rich or lean and this also shifts the signal of the OH fluorescence. If the behaviour of the flame is not similar in both transitions,

the thermometry results will be not accurate. In the case of the OH thermometry, a higher fluorescence signal in the $R_2(2)$ transition is higher than it should be, the LIF thermometry will result in the lower temperature, while the higher fluorescence signal in the $R_1(12)$ transitions will lead to the higher flame temperature.

In the case of the NO LIF thermometry, a more scattered data points were obtained compared to the results from the OH LIF thermometry, especially at the lower flame region. This is mainly caused by the concentration of the NO radicals in the flame which was much lower than the OH radicals, which ranges up to 50 ppm for the NO and 0.8 per cent for the OH radicals based on the quantification method in the previous section. Consequently, the fluorescence signal from the NO LIF was less intense than the OH LIF, and this leads to the inaccurate ratio of the LIF signal from both transitions which caused the inaccurate temperature measurement. A similar error was found in the determination of the flame temperature at the region closer to the burner surface and the reason of this is similar to that in the OH LIF thermometry case. In addition, the NO radicals concentration is low in the lower region of the flame, unlike the OH radicals which have a concentration peak before reaching equilibrium, and this causes an even lower NO LIF signal in the lower flame region. In the case of the NO thermometry, the higher signal in the $Q_2(15)$ leads to a lower flame temperature, while a higher signal from the $P_2(22)$ transitions lead to a higher flame temperature. On considering the concentration of the OH and NO radicals in flame and the thermometry results, the OH LIF thermometry is preferable than the NO.

4.3.6 Effect of the Surrounding Air and Error

The OH LIF results can be used to visualise the interaction of the flame gas with the surrounding air, which is the main difference between the PREMIX simulation results to the present experimental results. In the PREMIX simulation, the flame model is adiabatic and there is no mass transfer between the flame gas and the surrounding air. In order to validate the PREMIX simulation, the experimental burner is usually equipped with a shrouding gas which works as a protection layer to prevent the infiltration of the surrounding air to the flame. However, the flat-flame burner that is used in this study does not have such a facility and therefore a discrepancy with the PREMIX model may be possible.

Figures 4.32(a) and 4.32(c) illustrate the typical OH LIF image of the lean and rich flames, respectively, which in this case the surrogate B flame is taken as an example. This image is not normalised because it is difficult to obtain the laser sheet profile at the edge of the burner surface using the cuvette method. Seven vertical lines were drawn along the radial axis of the burner to obtain its OH fluorescence intensity count up across the lines up to 4000 counts, and this is presented in Figures 4.32(b) and

4.32(d)for the rich and lean flames, respectively. It can be seen that in the lean flame there was an accumulation of the OH radical near the burner surface, which is indicated by the OH fluorescence intensity peak while a similar accumulation was also found in the rich flame, but in a lower concentration. In the rich flame, the high OH radical concentration was also found at the edge of the flame region which directly interacts with the surrounding air. This was caused by the combustion of the excess fuel in the rich flame which does not have enough oxygen for the burner air supply. Analogous to the OH concentration profile along the vertical axis at the centre of the burner surface, the profile of OH at the edge was low in the region closest to the surrounding air, and this rise gives to peak and then decreases to the lower concentration. This can be interpreted from Figure 4.32 that the interaction with the surrounding air does not affect the central region of the flame and this isone of the main interests of this study. However, in the case of the gas analysis, the combustion products of the side flame might contaminate the gas sample which was collected by the probe in the middle flame region. This may be possible if the flow rate per area of the sampling probe is larger than the flow rate per area of the flame. The interference of the side flame combustion product should not enter the sampling probe if the probe is iso-kinetic, where the flow rate per area of the probe suction is similar to the flame gas velocity.
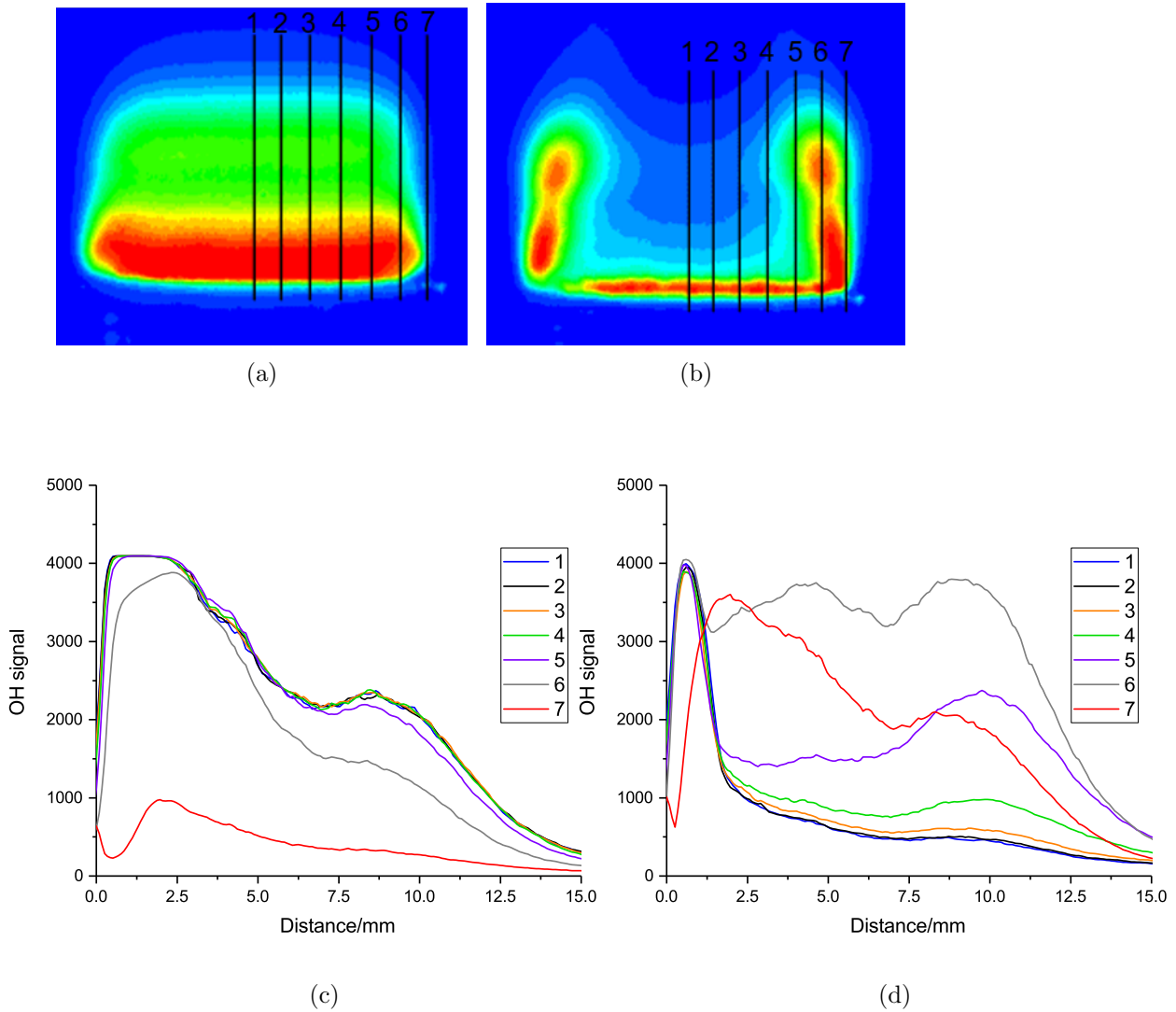
Figure 4.32: Uncorrected OH signals along radial axis for (a) lean, (b) rich Surrogate B flames and (c-d) their corresponding signals along the radial axis, respectively.

Unlike the measurement using the thermocouple and the gas analyser, obtaining the standard deviation of the averaged LIF image is more difficult for every data point. This was caused by the number of flame images, which is 500 frames, which requires an exhaustive effort to extract the data from each frame and then calculate the average and the standard deviation. Alternatively, the data processing tool in the laser imaging software was used to calculate the average of the LIF image intensity from the 500 images. Unfortunately, only the maximum and the minimum values of the LIF image dataset can be calculated using this feature. The datasets of the LIF images that were taken for the measurement were checked for its maximum standard deviation and the value varies up to 20 per cent of the image maximum count. There are two sources of the deviation in the flame images, which are the flame instability and the laser pulse. The cause of the flame instability is similar to the previous measurement

which was generated by the instability of the fuel flow, while the laser pulse produces the fluctuation of the fluorescence or scattered light intensity in flame and cuvettes.

There is an uncertainty in the determination of the distance above the burner surface in the LIF images, which is caused by the determination of the region close to the burner surface. In the LIF images, the burner surface did not appear to be flat but ellipsoidal due to the higher position of the camera. Practically, when drawing a line in Tecplot to extract the data points, the line was stretched from slightly below the burner surface up to approximately 20 mm above the burner surface to ensure that the main region of interest is extracted. Then the 0.0 mm distance was determined as to where the lowest part of the ellipse is located. The unit that was shown in the LIF images was not in millimetre, and to convert to that, the geometry of the cuvette was used as a reference. It is known from the measurements that the inner thickness of the cuvette wall is 10.0 mm and from this information, the reference scale was made. Then the conversion calculation can be expressed as follows:

$$X = X_o \frac{dX}{dX_o} - X_{surface} \tag{4.7}$$

where X is the distance in millimetre, X_o is the distance of the LIF image in an arbitrary unit, while $X_{surface}$ is the position of the burner surface after the conversion. The value of dX is 10.0 mm while the value of dX_o is the distance of the cuvette inner wall-to-wall distance in the arbitrary unit which is indicated by the laser imaging software.

4.4 Concluding Remarks

A burner flame experiment has been performed to study the temperature and chemical structure of real jet A-1, ethanol, jet A-1/ethanol blend, and two surrogates jet fuel flame. The temperature measurement was performed by employing a thermocouple wire and the LIF thermometry method, while the concentration of O_2, CO_2, CO, and NO_x were measured with an online gas analysis method, and the OH and NO radicals were measured by the PLIF technique. The temperature measurement indicates that the temperature of the ethanol flames are approximately 250 K lower than those of the jet A-1 flames, while when a 50 per cent ethanol addition was employed in the fuel mixture, the flame temperature is approximately 100 K lower than that of the jet A-1 flames. The temperature measurement to the jet fuel surrogates flames shows a lower temperature than the real jet A-1 flames. The LIF thermometry technique was performed to evaluate this method to measure the flame temperature using the ratio $R_2(2)$ / $R_1(12)$ and $Q_2(15)/P_2(22)$ in $A^2\Sigma^+ \leftarrow X^2\Pi$ (1,0) and (0,0) excitation state for OH and NO, respectively. It was found that the OH LIF thermometry is preferable than

NO, and difficulties were found in measuring the region closer to the burner surface. The OH detection, using the PLIF technique, shows a higher OH concentration in lean flames followed by the stoichiometric and rich flames. A relatively similar profile of the OH and NO concentration was found in the jet A-1 and surrogates flames, while ethanol flames have the lowest OH and NO profile and the addition of ethanol, decreases the OH concentration, but increases the NO concentration. The gas analysis results show similar O_2 and CO_2 for most flames with the same stoichiometry. Some of the NO_x results from the gas analysis were missing due to the technical problem with the gas analyser, but the NO LIF results can be used as an alternative. The CO profile is relatively similar in all lean flames, while in the stoichiometric and rich mixtures, the jet A-1 flames have a lower CO concentration while the surrogate flames have the highest CO concentration. These results will be compared with the modelling results in the next chapter and this approach is able to explain the details of the chemical reactions that affect the species concentrations in the flames.

Chapter 5

Kinetic Modelling

In this chapter, the study of the chemical structure of the jet A-1/ethanol flame was studied by using a kinetic model. This becomes possible by the availability of accurate reaction mechanisms of the oxidation of jet fuel surrogate components and ethanol in the literature. By using the kinetics simulation software, such as CHEMKIN, more detailed information of the flame behaviour, which cannot be detected through the experimental work in Chapter 4 can be obtained. However, the challenge is developing a reaction mechanism that can accurately model the jet A-1/ethanol flame, which consists of many sub-mechanisms. This chapter starts with the evaluation of the available reaction mechanisms of the fuel components from the literature, which needs to be selected as a starting point. Afterwards, all surrogate components in the jet A-1/ethanol flame are combined and the elements of the reaction mechanism are evaluated for possible simplification and improvement. Ultimately, the performance of the kinetic model is tested against available experimental data from the literature and the contribution of the elementary chemical reactions to the flame chemical structure is evaluated by using sensitivity and rate of production (ROP) analysis tools. Optimisation to uncertain reaction rates of elementary reaction may be performed to improve the accuracy of the kinetic model.

5.1   Development of the Reaction Mechanism

Study on the ethanol mechanism is relatively mature based on the availability of the published reaction mechanisms and experimental data as reviewed in Section 1.5.1. The ELTE ethanol mechanism [56] was selected as the starting point of the reaction mechanism development by considering the amount of the experimental data employed for validating this mechanism. This mechanism updated 45 reactions of the H_2/CO sub-mechanism in the ethanol mechanism from Saxena and Williams [63] based on their recent study of hydrogen and syngas combustion [162]. The H_2/CO sub-mechanism is

important in the hydrocarbon combustion since it is the final path of the oxidation of the hydrocarbon fuel.

The base mechanism has 48 species and 251 reactions and the subsequent development was the addition of the NO_x sub-mechanism. There is much available literature on the oxidation of nitrogen as well as the NO_x reaction mechanisms such as the Leeds NO_x [145, 163] and the GRI 3.0 mechanisms [46] which were published about two decades ago. Recently, Saggese et al. [161] proposed a skeletal NO_x mechanism which was developed to model a premixed-stagnation jet A flame at atmospheric pressure and various stoichiometric mixtures. This model was reduced from the detailed NO_x mechanism by Glarborg et al. [164], which performs approximately similar to the reduced mechanism in predicting the laminar flame speed, PSR, premixed flame, and ignition delay time of jet A flames. The 214 reactions among 49 species from the reduced NO_x mechanism by Saggese et al. [161] was added to the base mechanism and this resulted in 465 reactions and 68 species. This current stage of the reaction mechanism was used as a foundation for the further addition of the jet fuel surrogate.

The challenge of developing the reaction mechanism for the Jet A-1 fuel is in determining the surrogate jet fuel components to simplify the abundant chemical composition in the real jet fuel. Lindstedt and Maurice [86] proposed a binary surrogate of jet fuel which consists of aliphatic and aromatic hydrocarbon, which were represented by 89 per cent n-decane and 11 per cent toluene by molar fraction, respectively. The use of this surrogate composition by Lindstedt and Maurice to model the experimental data of premixed laminar flame of kerosene at $\phi = 1.7$ by Douté et al. [84] shows a good agreement in term of the species concentration profiles in the flame. The similar surrogate has been used by Kyne et al. [91] to model the chemical composition of a rich kerosene flame in a jet-stirred reactor (JSR) at elevated pressures, which shows a good agreement between the model results and the experimental data. The surrogate was also used by Catalanotti [98] to model the combustion of biokerosene, which is a mixture of kerosene and methyl tridecanoate, in a JSR and the model performed well in modelling the species concentration from the experimental data. Based on this finding, the author also considers n-decane/toluene as the surrogate component of the jet A-1 fuel.

A recent reduced model of n-decane oxidation was proposed by Chang et al. [165] which consists of 141 reactions and 40 species. This reduced model was constructed based on the detailed n-decane mechanism from Westbrook et al. [166], in which 12 steps of n-decane decomposition were taken from. These reactions describe the path of the n-decane reaction towards C_1–C_3 and C_5 species, which further merged with the detailed $H_2/CO/C_1$ mechanism from Li et al. [144] which was updated by Klippenstein et al. [167]. Considering that the $H_2/CO/C_1$ sub-mechanism in the ELTE mechanism is

more updated than that in the Li et al. [144] mechanism, the reaction rate parameters of similar reactions were preserved for the ethanol-NO_x base mechanism. The merging procedure resulted in 76 species and 506 reactions, in which 95 reactions are similar in both mechanisms, but they have different reaction rate parameters.

The final extension of the reaction mechanism is the addition of a toluene sub-mechanism to the current base mechanism. The sub-mechanism of toluene decomposition to benzene and smaller hydrocarbon was taken from the skeletal jet fuel (A1) mechanism of Stanford HyChem model [168, 169] which is described in 35 reactions. The final reaction mechanism consists of 541 reactions among 85 species that involves n-decane, toluene, ethanol, and NO_x sub-mechanism. Species that appears in more than one sub-mechanisms might have a duplicate thermodynamics and transport data, thus the data from the ELTE mechanism is preferred, followed by the NO_x, n-decane, and toluene mechanism. The performance of the merged mechanism may be different from the original mechanisms since there may be extra sources of species production and consumption from the other sub-mechanisms. To investigate the accuracy of the merged mechanism, validation with the published experimental data is presented in the following sections.

5.2 Burner-Stabilised Flame

The modelling of the burner stabilised flame is aimed to be identical to the experimental work in the previous chapter. The PREMIX program that was described in Section 2.2.3 was used by employing the fixed gas temperature mode and taking the temperature profiles in Section 4.1 as the temperature input. The total mass flow rate was calculated based on the information in Table 3.2 while the theoretical air model of $O_2/N_2/Ar$ was used with a molar ratio of 1/3.728/0.0446. Meanwhile, the use of a jet fuel surrogate caused a discrepancy in the oxidiser requirement between the real jet A-1 fuel and its surrogates. This was caused by the difference in the molecular formula of the real jet A-1 that was used in the experiment and the surrogates. Alternatively, the amount of the fuel fraction in the model was adjusted to match the equivalence ratio in the experiment while the theoretical air component matched the experiment flow rates. The mixture-averaged transport properties were used to reduce the computing time and prevent failure in the simulation.

For the simulated O_2, CO, and CO_2 concentrations, conversion to the dry basis is required to match the measured species concentrations from the gas analyser because of the application of the water vapour trap in the gas analyser sampling unit. The conversion was performed using the following equation [170]:

$$X_{dry} = \frac{X_{wet}}{1 - X_{H_2O}} \tag{5.1}$$

5.2.1 Ethanol Flames

Figure 5.1 shows the simulated concentration of ethanol, O_2, CO, CO_2, OH, and NO in the ethanol flames and a comparison with the measurement results from Chapter 4. Also the rate of production and sensitivity analysis of these species are presented in Figure 5.2 and 5.3, respectively. Only the prediction from the current mechanism is presented since it has similar prediction of the measured species to the ELTE mechanism as the widely validated mechanism for ethanol. This was caused by the use of the ELTE mechanism as the base of the current mechanism development which leads to similar results. Generally, the prediction from the model follows the trend of the experimental results while major and minor discrepancies were found in the quantified concentration.

The fuel fraction profile consists of only ethanol and this does not have an experimental data for the validation. The model indicates that for all flames, ethanol was consumed within 1.0 mm of the burner surface. At close to the burner surface the concentration of the ethanol was shifted from the initial concentration because some of the molecules were reacted to form other species, such as water. In the absence of radical species, ethanol molecules decomposed to water and ethylene (C_2H_4) or hydroxymethyl (CH_2OH) and methyl radical (CH_3). The presence of radicals leads to the production of more radicals and the ethoxy radical (C_2H_5O), which further decomposed to formaldehyde (CH_2O), formyl radical (CHO), carbon monoxide and carbon dioxide through the reaction with oxygen and the radical species. The ethanol reaction process was faster in the lean flame while the stoichiometric and rich flame were similar. In the rich case, the unburned hydrocarbon concentration was predicted at 2.3 % because of the lack of oxygen concentration.

The predicted oxygen concentration shows a good agreement with the experimental results for the stoichiometric and rich cases while a discrepancy was found in the lean case. Both the model and the experimental data for the lean flame shows excess oxygen in the upper flame region, but the model predicts a lower oxygen concentration. This disagreement might be caused by the technical issues with the oxygen sensor of the gas analyser that occurred during the experimental work with lean ethanol flame. At all stoichiometry, the oxygen concentration in ethanol flames was consumed rapidly up to 1.0 mm from the burner surface then reached the equilibrium at approximately at 3.0 mm from the burner surface. At below 1.0 mm from the burner surface, the oxygen molecule was mostly consumed by the ethoxy radical to form acetaldehyde (CH_3CHO) and hydroperoxyl (HO_2). Also, other hydrocarbon radicals consumed oxygen molecules and formed other radicals. In the upper region of the flames, the main reactions that controlled the consumption and production of oxygen are the hydroperoxyl, OH, H and O radicals.
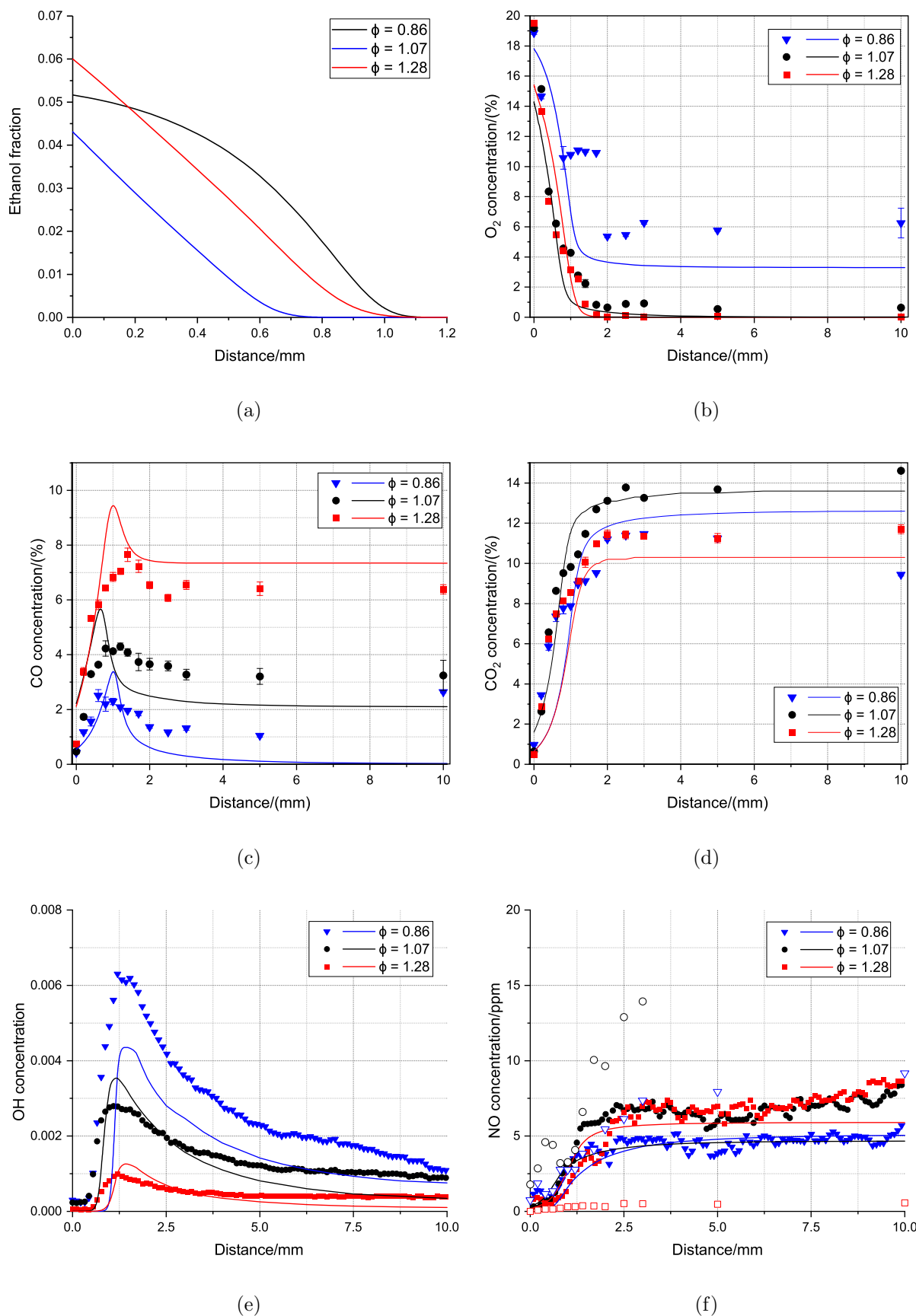
Figure 5.1: Simulated profiles of (a) ethanol, (b) O_2, (c) CO, (d) CO_2, (e) OH, and (f) NO of ethanol flames from PREMIX using the developed reaction mechanism.
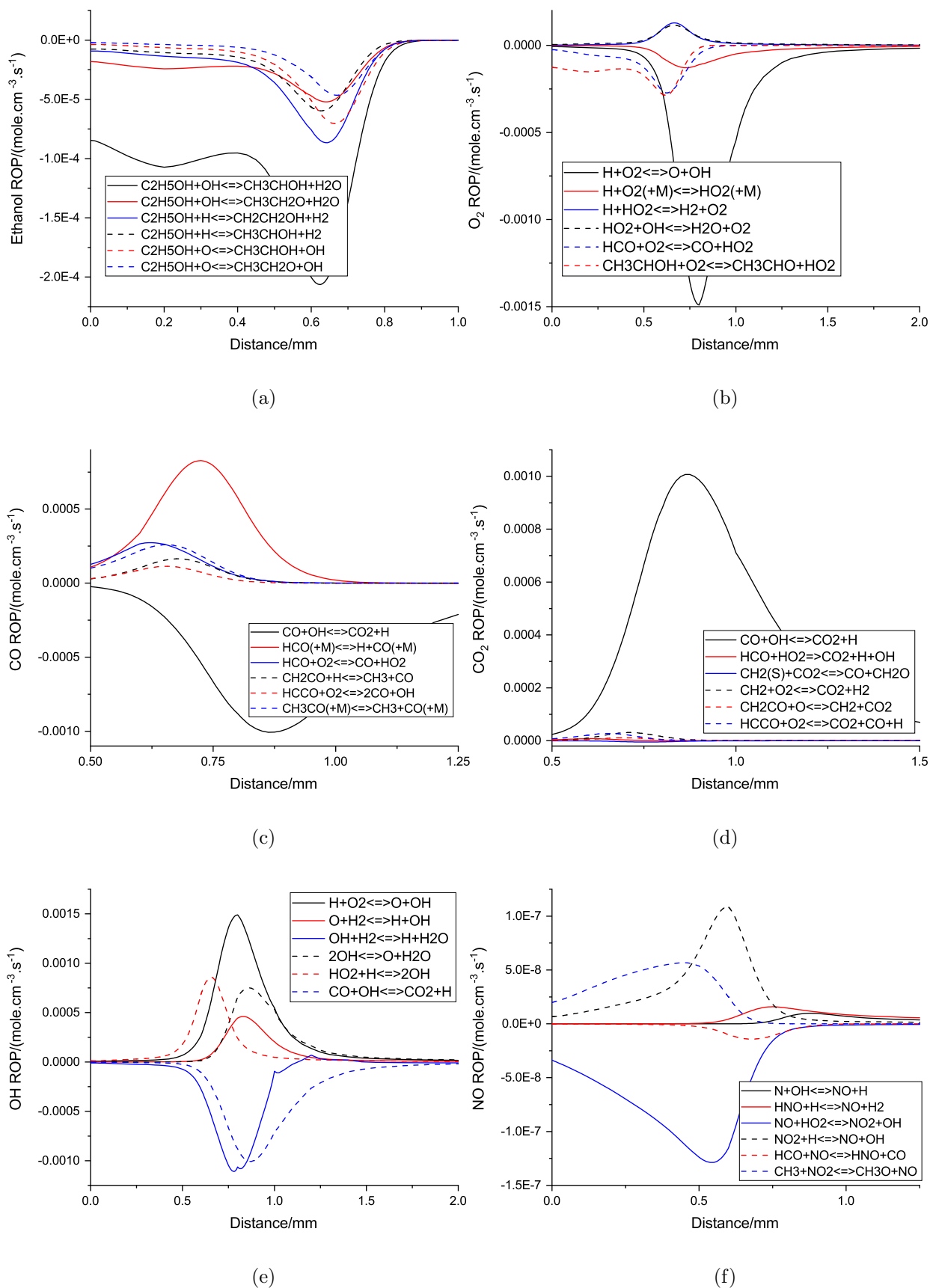
(a)

(b)

(c)

(d)

(e)

(f)

Figure 5.2: Highest production rate of (a) ethanol, (b) O_2, (c) CO, (d) CO_2, (e) OH, and (f) NO in the near stoichiometric ethanol flame from PREMIX using the developed reaction mechanism.
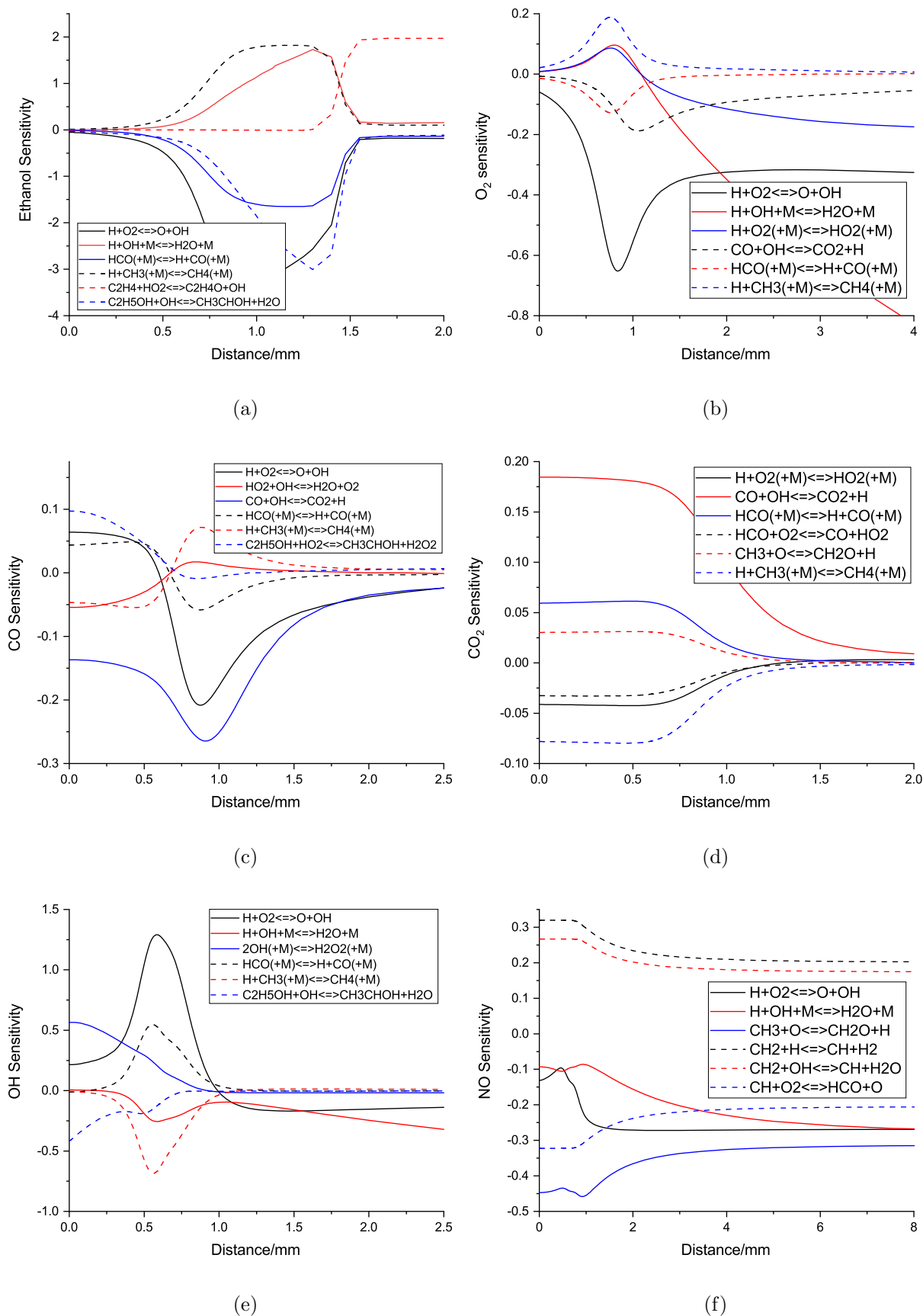
Figure 5.3: Most sensitive reactions with respect to (a) ethanol, (b) O_2, (c) CO, (d) CO_2, (e) OH, and (f) NO in the near stoichiometric ethanol flame from PREMIX using the developed reaction mechanism.

The simulated CO profile has a similar trend to that from the experiment, where the highest CO concentration was found in the rich flame followed by the stoichiometric and lean flames. However, the model over predicts the peak CO concentration in all flames while it under predicts the equilibrium concentration in the stoichiometric and lean flames. In the rich flame, the simulated CO profile is higher than the experimental data in the upper region of the flame. The CO peak was caused by the fast production of CO and slow conversion to CO_2. In the lean flame, the low CO concentration was produced mainly from the reaction of CHO with oxygen and the decomposition of acetyl (CH_3CO) to the methyl radical and CO. Meanwhile, the consumption of CO was mainly by the oxidation reaction to CO_2 through the reaction with OH or HO_2. In the stoichiometric and rich flames, the CO production from formyl radical decomposition and ketene (CH_2CO) reactions with OH or H radical is more active than that in the lean flame at very close to the burner surface.

The model predicted the CO_2 concentration accurately for the stoichiometric ethanol flame while the rich and lean flames have some discrepancies with the experimental data. A clear divergence was shown by the model while the experimental data did not show that. In this case, the accuracy of the CO_2 measurement is questionable because the decrease in the CO_2 concentration after reaching the equilibrium concentration is not supposed to occur. The sum of CO and CO_2 in each flame is approximately similar in the experiment and the model which represents the total carbon in the flames. Mostly, CO_2 was formed from the oxidation of CO, but not necessarily does the higher CO lead to a higher CO_2 concentration as the oxidation requires oxygen. In the lower region of the flame, other production sources of CO are from ketenyl (HCCO), formyl, ethoxy, acetyl, ketene, and methylene (CH_2) radicals reactions with O and H radicals.

The model predicts OH peaks in the stoichiometric and rich flames relatively well while under prediction was found in the lean flame. At all stoichiometry, the model under predicts the OH concentration at 10.0 mm from the burner surface. Despite the OH concentration was quantified using the ethanol flames as a reference, and a discrepancy was found because the difference in the value of $[OH]_{\text{ref}}/I_{ref}$ at different stoichiometry based on the calculation in Table 4.22. Moreover, the reference only considers the OH concentration in the peak and the quenching rate calculation of the OH LIF was simplified. The hydrogen atom in the OH molecules came from the ethanol molecule, and therefore the OH peak is formed during the decomposition of ethanol in the lower region of the flame. The decay of the OH peaks was caused by the formation of water and carbon dioxide, thus the increase of the concentration of these species decreases the OH concentration in the flames.

The simulated NO profile was compared to the experimental data from the LIF measurement of $Q_1(12)$ transition and gas analyser. The solid symbol represents the

LIF data while the hollow symbol represents the gas analyser reading. For ethanol, only the lean flame has a complete NO_x reading from the gas analyser because of the technical problem in the rich and stoichiometric flames. In the lean case, the model agrees with the LIF results while in the other cases the model predicts a lower NO concentration. The gas analyser result for the lean case showed a higher NO concentration than the LIF result. The nitrogen atom in the NO molecule came from the nitrogen in the air since there is no nitrogen molecule in ethanol. In all the flames, the rate of NO production was rapidly increased and peaked at approximately 1.0 mm from the burner surface and dropped to zero at approximately 3.0 mm from the burner surface. In the rich flame, the NO production from the thermal mechanism is more dominant than the non-thermal while in the lean and stoichiometric the non-thermal becomes more dominant.

5.2.2   Jet A-1 Flames

Figure 5.4 presents the prediction of the measured species profiles of the jet A-1 flames from the current mechanism and a comparison with several published jet fuel surrogates and their mechanisms. Also, the sensitivity and rate of production analysis of these species are presented in Figure 5.5 and 5.6 to 5.7, respectively. These models can be identified by using the pattern in the legends while the colours represent the stoichiometry which is analogous to the colour of the symbols. The comparison involves the Aachen [80] and CRECK [148] surrogate model which are modelled with their own mechanism. The Aachen surrogate defines JP-8, jet-A, and jet A-1 as 80 per cent n-decane and 20 per cent 1,2,4-trimethylbenzene by mass while the CRECK surrogate uses n-dodecane/o-xylene/methylcyclohexane with a ratio of 60, 20, and 20 per cent by volume, respectively. Meanwhile, the current mechanism and the AFRM mechanism use n-decane and toluene with 89 and 11 per cent by molar, respectively.

The fuel fraction shows the sum of the total fraction of the surrogate species. There is no significant discrepancy in the stoichiometric flame from all the models. The low fuel fraction in the stoichiometric flame was caused by the high temperature at the burner surface which caused the early formation of water, CO, and CO_2. Meanwhile, in the lean flame, the slow reaction of the fuel was caused by the low temperature at the surface and becomes faster at the region with a temperature above 1000 K. A larger discrepancy was found in the rich flame as well as from the similar surrogate models, such as the AFRM and current mechanisms. This was caused by the different decomposition path of n-decane in each reaction, which the AFRM mechanism has more decomposition pathways than the current mechanism as illustrated in Figure 5.7. In the current mechanism, the major reaction of the n-decane decomposition is the formation of decyl radical through the reaction with H, OH radicals and oxygen.

Meanwhile, the decomposition paths of n-decane to decyl radical in the AFRM mechanism involves methyl radical and also a direct decomposition path to pentyl, butyl, and propyl radicals. For toluene, both models have a similar decomposition route to benzyl ($C_6H_5CH_2$) and benzene (C_6H_6).

In the case of the oxygen concentration profile, all models indicate a similar trend at all stoichiometry. Compared to the experimental data, the models can accurately predict the oxygen profile in the lean and rich cases. Meanwhile, for the stoichiometric flame the oxygen depletion is faster in the model compared to the measurement and also the equilibrium concentration was higher. Ideally, the measurement result shows complete oxygen consumption for the stoichiometric flame. At all stoichiometry, the models predicted the oxygen was rapidly consumed below 1.0 mm from the burner surface while the stoichiometric case has the fastest rate. This was caused by the high temperature in the stoichiometric flame. Mainly, the oxygen was consumed by the large and small hydrocarbon radicals which occurred from the decomposition of the fuel in this region.

The simulated CO profile from all models indicate a similar result while the Aachen surrogate under predicts the peak at all stoichiometry and the current mechanism shows a lower equilibrium concentration in the rich case. Comparison to the experimental data shows that the models predict a much higher CO formation, especially in the rich case. The occurrence of the peak is earlier in the model, especially in the stoichiometric case due to the high flame temperature at this region. The measurement appeared to be insensitive to the early formation of the CO peaks, but this agrees with the models in term of the CO level for all cases. Similar to the ethanol flames, the CO production source came from the formyl radical reactions. In the stoichiometric case, the formyl radical recombination is the most dominant while in the rich and lean cases the reaction of formyl radical with oxygen is the most dominant.

The prediction of the CO_2 concentration for the jet A-1 flames from all models varies by less than one per cent. The models indicate that the stoichiometric case has a slightly higher CO_2 level than the lean case, followed by the rich case. The CO_2 production source was similar to that in the ethanol case, with CO oxidation reactions as the most dominant CO_2 production. The sensitivity analysis of the CO_2 species indicates that the H-abstraction reaction of ethanol with OH is sensitive to the CO concentration. Meanwhile, in the current mechanism, reactions that involve the ethanol species were not sensitive to the CO_2 production. As a consequence of the CO profile, where the Aachen model shows a lower CO peak, it indicates the highest CO_2 concentration at below 1.0 mm from the burner surface.
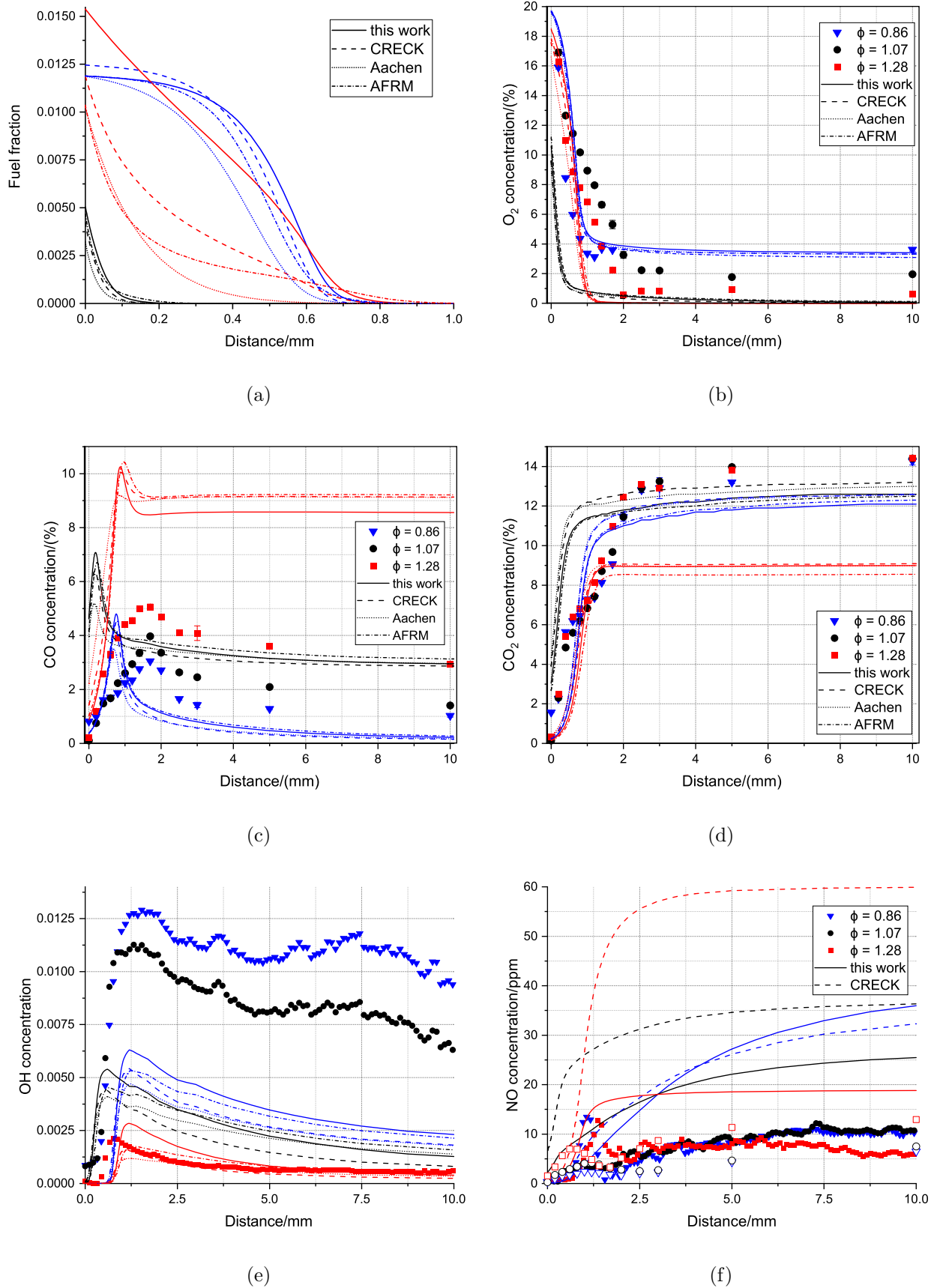
Figure 5.4: Simulated profiles of (a) fuel, (b) O_2, (c) CO, (d) CO_2, (e) OH, and (f) NO of jet A-1 flames from PREMIX.
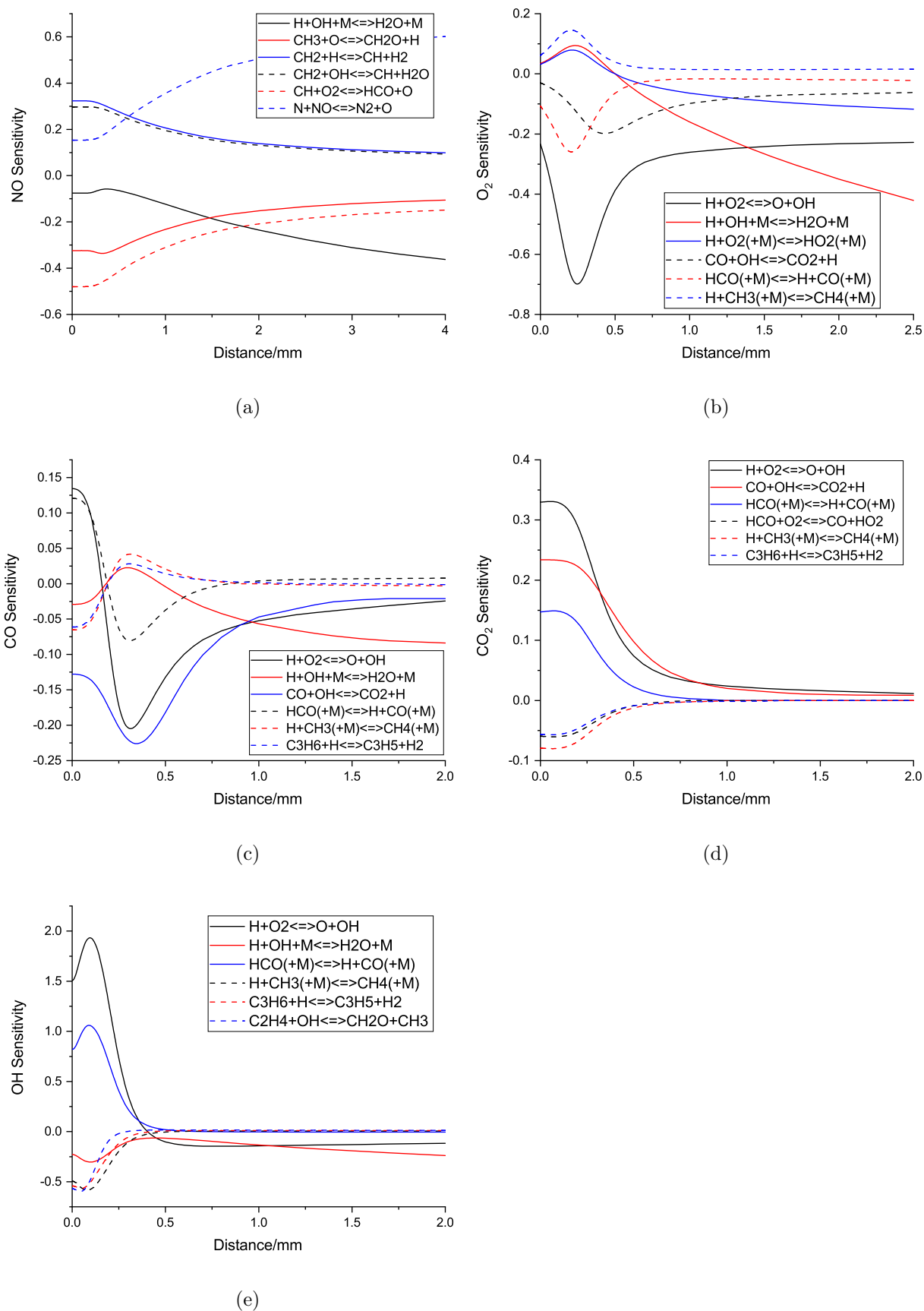
(a)

(b)

(c)

(d)

(e)

Figure 5.5: Most sensitive reactions with respect to (a) NO, (b) O_2, (c) CO, (d) CO_2, and (e) OH, in the near stoichiometric jet A-1 flame from PREMIX using the developed reaction mechanism.
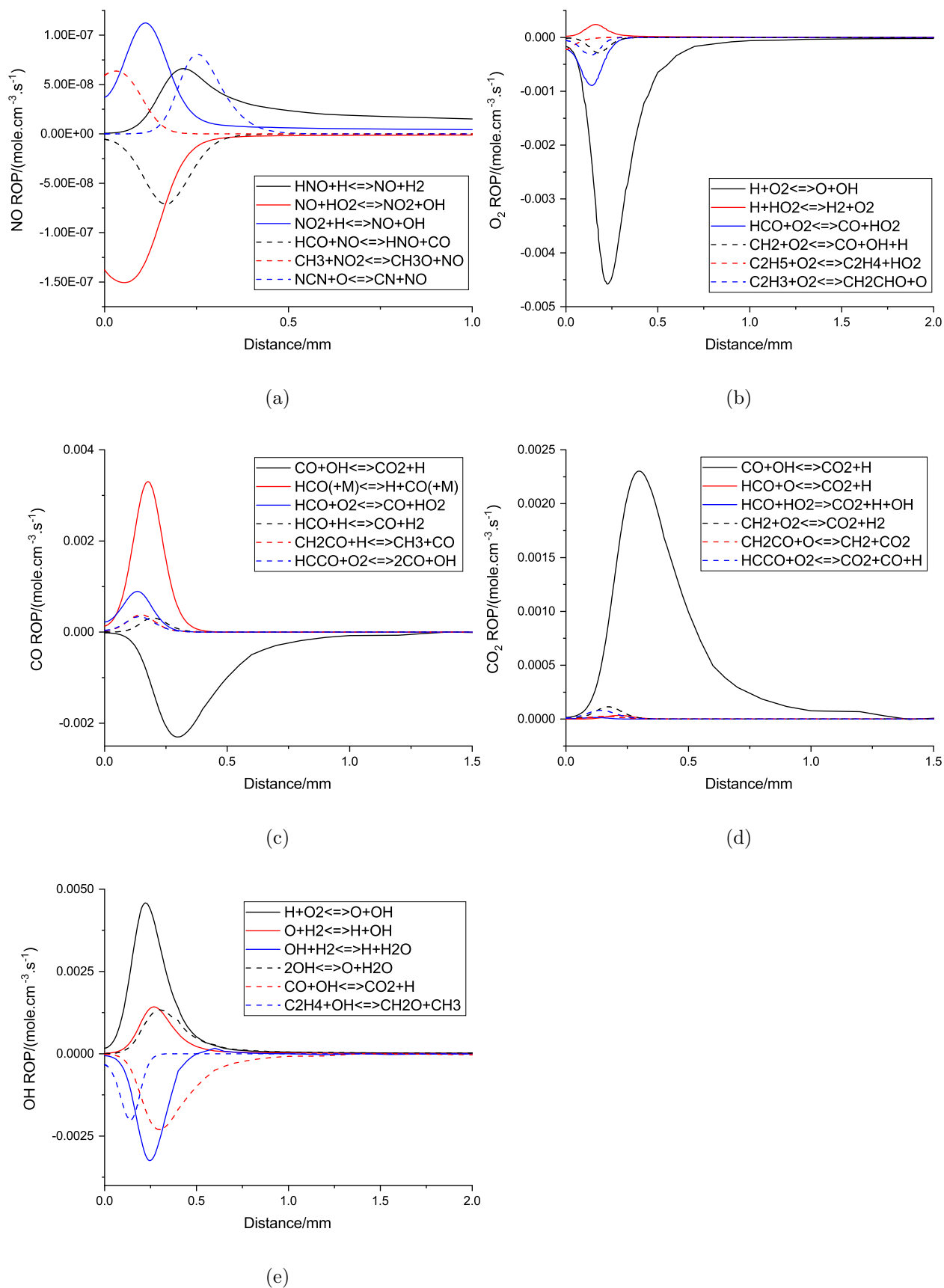
Figure 5.6: Highest rate of production of (a) NO, (b) O_2, (c) CO, (d) CO_2, and (e) OH in the near stoichiometric jet A-1 flame from PREMIX using the developed reaction mechanism.
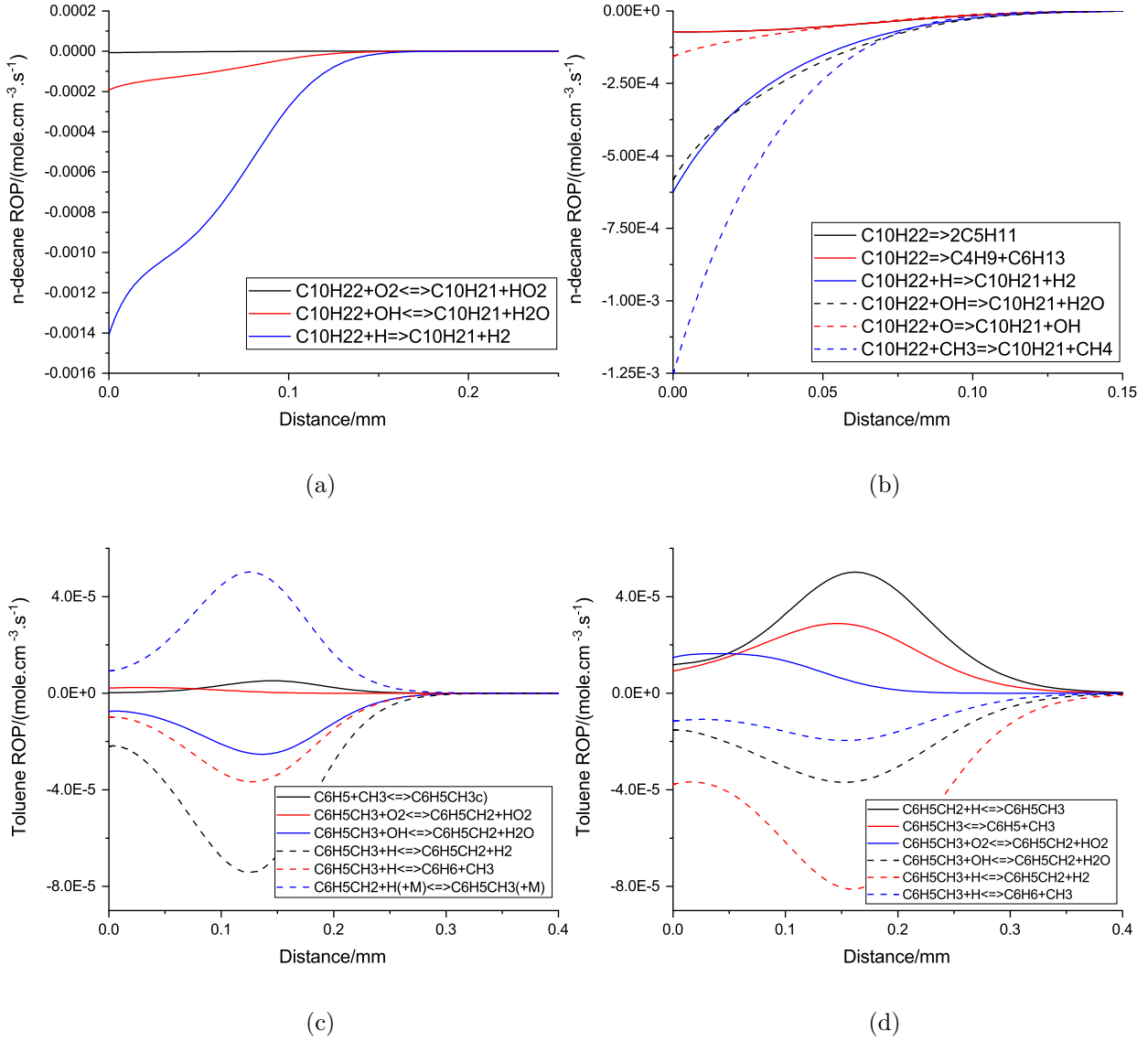
(a)

(b)

(c)

(d)

Figure 5.7: Highest rate of production of (a) n-decane , (b) n-decane (AFRM), (c) toluene, and (d) toluene (AFRM) in the near stoichiometric jet A-1 flame from PRE-MIX using the current and AFRM mechanism.

Compared to the experimental data, the simulated CO_2 concentration was slightly lower for the lean and stoichiometric cases and a large discrepancy was found in the rich case. This was caused by the discrepancy in the CO prediction as well as the possible imperfection in the measurement, which allowed the oxidation of CO to CO_2 inside the probe. The total carbon from the CO and CO_2 concentration indicate approximately similar value for the rich and stoichiometric cases while a slight difference was found in the lean case because of the high CO concentration at 10.0 mm from the burner surface from the measurement.

A similar trend with the experimental data was found in the prediction of the OH radical where the highest OH concentration was found in the lean flame and then was

followed by the stoichiometric and rich flames. Compared to the others, the current model has the highest prediction of OH concentration for all stoichiometry. For the stoichiometric case, all models indicate an earlier OH peak occurrence than the other cases. This was caused by the higher temperature in the stoichiometric case while in the LIF result, there is no clear difference in the location of the OH peak. A larger discrepancy was found in the quantification of the OH concentration compared to the ethanol cases. This might be caused by the occurrence of the more complex hydrocarbon in the jet A-1 flame which affects the quenching rate of the OH molecules. The main production sources of the OH radicals are the reaction of hydrogen or oxygen with radicals. In the lower region of the flame, it was consumed by the hydrocarbon decomposition reaction while in the upper region it was used for the production of water.

Not all of the models in the comparison have the NO_x mechanism, thus only the prediction of the NO concentration from the current model and the CRECK model are presented. The prediction of the NO concentration from both models shows a significant difference, and the CRECK model indicates a higher NO concentration for all stoichiometry than the current model. Both models show continuous production of NO with the increase in the distance from the burner surface, except for the rich case where the NO concentration remained after 3.0 and 5.0 mm from the burner surface for the current and CRECK mechanisms, respectively. In the lean case, the slow rise of the NO concentration was caused by the low temperature of the flame, which delays the reactivity of the thermal NO_x mechanism. At below 1.0 mm from the burner surface, the non-thermal NO_x mechanism dominate the NO production, then at 1.0 mm from the burner surface the thermal NO_x mechanism becomes dominant and the rate slowly decreases until 10.0 mm from the burner surface. For the stoichiometric case, the rapid growth of NO concentration at the lower region was caused by the high NO production from both thermal and non-thermal mechanism, which the non-thermal dominate at the lower region and above 1.0 mm from the burner surface the thermal mechanism dominate the NO production and decrease slowly until 10.0 mm from the burner surface. For the rich case, the NO production from both thermal and non-thermal mechanisms peaked at approximately 1.0 mm from the burner surface and then stopped after above 4.0 mm from the burner surface and causes the constant NO concentration. The comparison to the experimental data indicates over prediction from both models, where the NO measurement from LIF and gas analyser only ranged up to 13 ppm while the current model's prediction was closer than the CRECK mechanism.

5.2.3 Surrogate A Flames

The performance of the Aachen and CRECK mechanisms have been validated against the experimental measurement of a real jet fuel and surrogate fuels from a counterflow flame, ignition delay time, laminar flame speed, and species profile measurement. This work aims to extend the validation of these models to the measurement results of the burner-stabilised premixed laminar flame that was presented in the previous chapter. The discrepancies that was found in the comparison of these models against the experimental data of Jet A-1 flames should be minimised since the composition of the initial fuel and oxidiser species match the experimental condition as well as the temperature profiles and the mass flow rates.

Figure 5.8 shows the results of the PREMIX simulation of the Aachen surrogate model for lean, near stoichiometric, and rich condition as well as its comparison to the experimental data. Figure 5.9 shows the rate of production analysis of the fuel and measured species, respectively. Only the fuel profile that does not have an experimental data validation, because there was no facility to detect the fuel species from the flame. The simulation results show that the temperature profile of the flames affects the initial fuel fraction. Despite that the highest fuel fraction was given for the rich and the lowest was given for the lean, the highest initial fuel fraction was found in the lean flame while the lowest was found in the stoichiometric flame. This corresponds to the water production very close to the burner surface where the stoichiometric flame has most water, followed by the rich and lean flames as illustrated in Figure 5.8(f). The temperature profile also affects the rate of consumption of the fuel fraction and the lowest temperature in the lean flame leads to the lowest consumption rate of the fuel, and adversely the highest temperature in the stoichiometric flame results in the fastest fuel depletion rate.

In the Aachen surrogate model, the fuel fraction consists of n-decane and 1,2,4 trimethylbenzene. In the low region of the flame, the n-decane species reacts with radicals and forms decyl radical as well as water, hydrogen, and other radicals. Furthermore, it decomposes to smaller hydrocarbons, such as the $C_7, C_6, C_4,$ and C_3 species, while in the higher temperature such as in the stoichiometric flame, the branching to C_6 and C_4 is higher. At 1.0 mm from the burner surface, where the flames have achieved the equilibrium temperature, the decomposition of n-decane to pentyl become dominant and then pentyl decomposes to ethylene and propyl. Meanwhile, the trimethylbenzene undergoes an H-abstraction and forms dimethylbenzyl or methyl detachment and forms dimethyl benzene through a reaction with radical species. This methyl abstraction continues until benzene was formed. Furthermore, benzene undergoes a H-abstraction to form a phenyl radical which decompose to C_2 and C_4 species at a higher temperature.
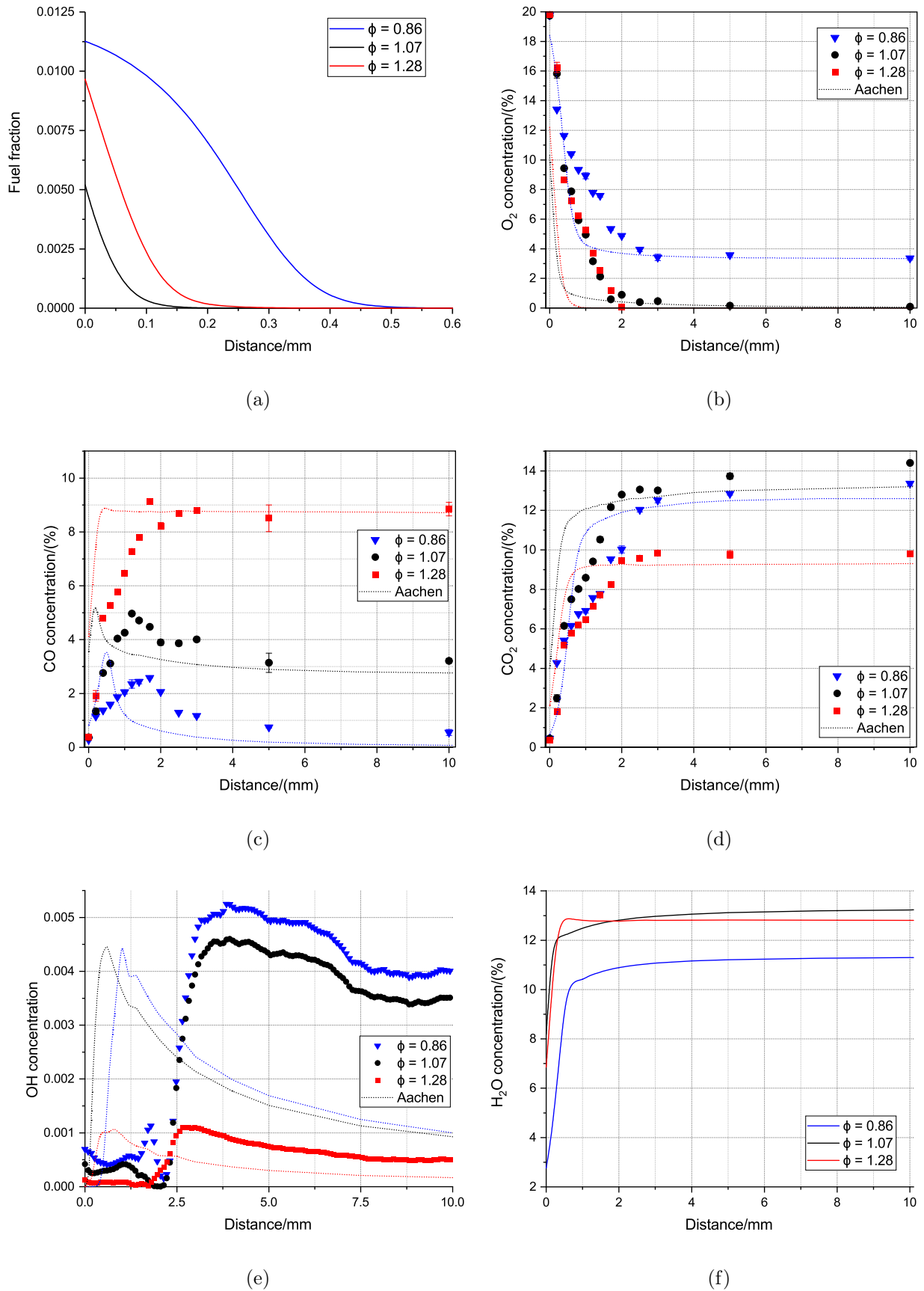
Figure 5.8: Simulated profiles of (a) fuel, (b) O_2, (c) CO, (d) CO_2, (e) OH, and (f) water of surrogate A flames from PREMIX using Aachen model.
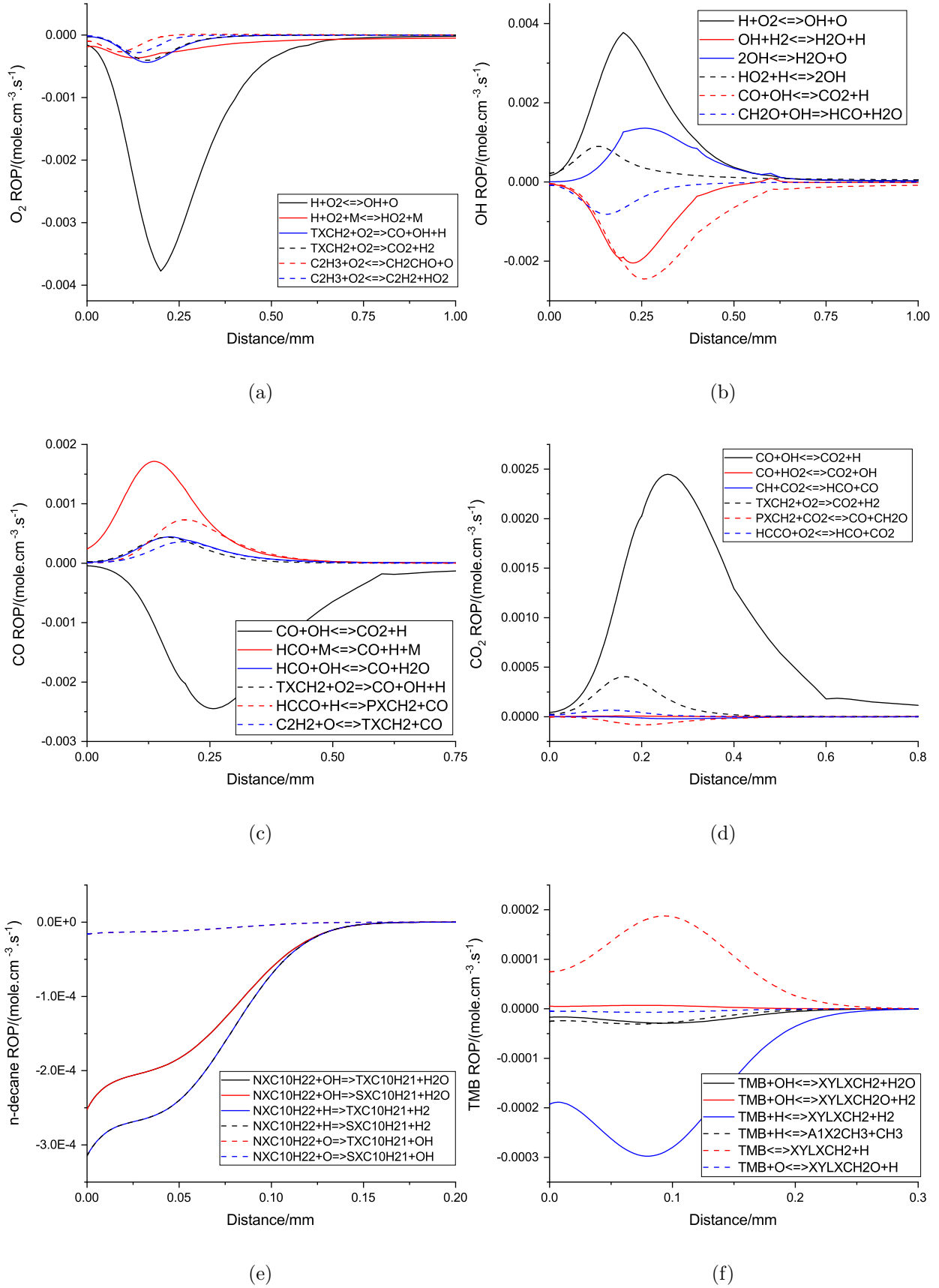
Figure 5.9: Highest rate of production of (a) O_2, (b) OH, (c) CO, (d) CO_2, (e) n-decane, and (f) trimethylbenzene (TMB) in the near stoichiometric surrogate A flame from PREMIX using Aachen model.

The simulated oxygen concentration can predict the equilibrium concentration accurately at all equivalence ratios. This was caused by the elimination of the uncertainty in the concentration of the given reactants, which match the given flow rate in the experimental work. In the validation against the jet A-1 flames, the uncertainty came from the difference between the formula of the real and surrogate fuels which affect the amount of the given fuel and oxidiser. Both the model and the experiment show that the lean flame has the slowest rate of the oxygen depletion while the rich and stoichiometric flames have a faster rate. This was caused by the temperature difference in these flames in which the higher flame temperature leads to faster oxygen consumption. However, the oxygen consumption in the model appears as slower than the experimental data, which might be caused by the probe effect during the measurement. At low temperature, the main consumer of the oxygen molecule was the reaction with decyl radicals while at the higher temperature then the main consumer is the reaction with hydrogen and OH radicals.

The agreement between the model and the experimental data was also found in the CO profile at all stoichiometry. The model can predict the peak and equilibrium concentration of CO, but the formation of the CO peaks appears to be faster than in the experimental data. At all stoichiometry, the major production source of CO came from the decomposition of formyl radical (HCO) and the major consumption of CO was the CO_2 formation through the reaction with OH or hydroperoxyl (HO_2) radicals. At higher temperature, the production of CO_2 becomes more dominant while the production of CO decreases, and this leads to the decay of the CO peaks.

The model also predicts the CO_2 concentration accurately at all stoichiometry with a slight discrepancy in the region below 1.0 mm from the burner surface. In this region, the model prediction of the CO_2 formation is faster than the experimental data. This was caused by the early formation and decay of the CO peak which was also earlier than in the experimental data. The prediction of the equilibrium concentration of CO_2 was slightly lower than the experimental work by less than one per cent. Also, the total carbon in the CO and CO_2 from the model and the experimental data is quite similar.

The prediction of the OH concentration was not much different from the experimental data in terms of the peak concentration and the OH concentration level at each stoichiometry. However, the location of the peak was earlier in the model by approximately 3.0 mm from the burner surface. Unlike the O_2, CO and CO_2 profiles, the OH concentration was not measured by using a probe and thus the probe effect was not responsible for these results. The uncertainty in the PLIF method might cause the delay of the OH peak occurrence in the experimental data. In the region above the peak location, the main consumption routes of the OH peak were the oxidation of the CO to CO_2 and the water formation through the reaction with radicals.
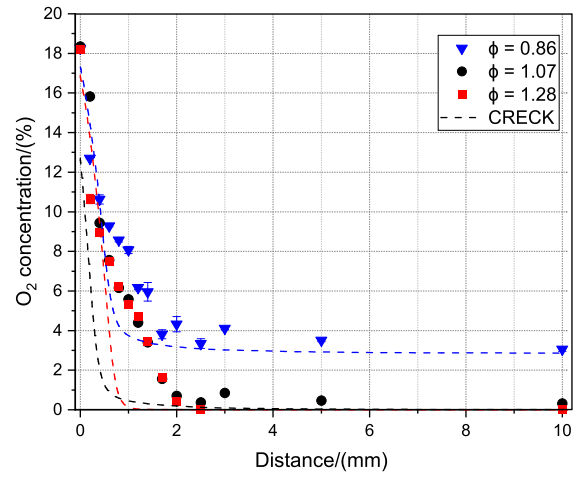
5.2.4 Surrogate B Flames

Figure 5.10 shows the prediction results of the surrogate B flames by the CRECK surrogate model and mechanism while Figure 5.11 and 5.12 indicate the rate of production analysis for the near stoichiometric flame. The fuel fraction consists of 80, 20, and 20 per cent of n-dodecane, o-xylene, and methylcyclohexane by volume. At the burner surface, the temperature of the stoichiometric flame was 150 K higher than in the lean flame while the rich flame was only approximately 50 K higher than the lean flame. Consequently, at this point, the consumption rate of the fuel was fastest in the stoichiometric flame and this was followed by the rich and the lean flames. This is indicated in the fuel fraction profile of the flames in which the stoichiometric flame was fastest in decomposing the fuel while the lean and rich flames were not too much different. The higher fuel fraction in the rich flame was caused by the higher fuel concentration that was given in the input file.

At close to the burner surface, most of the n-dodecane species undergo an H-abstraction reaction and forms the dodecyl radical through the reaction with other radicals species at all stoichiometry. At higher temperature, the thermal decomposition of n-dodecane becomes more reactive which breaks the n-dodecane to C_2, C_3, C_4, C_5, and C_7 species as well as the dodecyl radical. Similarly, the decomposition products of n-dodecane continue to decompose to the smaller hydrocarbons. Also, the H-abstraction reaction dominates the consumption of o-xylene at all stoichiometry while it breaks down to smaller cyclic compounds. Smaller hydrocarbons were also formed during this decomposition process towards the C_2 species. For the consumption of the methylcyclohexane species, the H-abstraction reaction is more dominant at low temperature before the carbon decomposition while at high temperature the direct decomposition to C_3, C_4, and C_7 alkenes becomes more dominant.

The prediction of the oxygen concentration agrees with the experimental data, with slight discrepancy in the lower region for the rich and stoichiometric flames. In this region, the depletion rate of oxygen is much faster than in the experimental data, which might be caused by the characteristics of the quartz probe. The initial concentration of the oxygen at all stoichiometry follows the fuel fraction profile which shows the stoichiometric flame has the highest reactivity than the other. Also, the initial concentration of the oxygen in the stoichiometric was lowest because it has partially reacted to form other species such as water. In lower region, the flame temperature was relatively low and the main consumption source of the oxygen was the reaction with hydrocarbon radicals, such as methyl, formyl, ethyl, and propyl. Meanwhile, at the higher temperature, the main consumption of oxygen was the reaction with a hydrogen atom to form an OH radical.
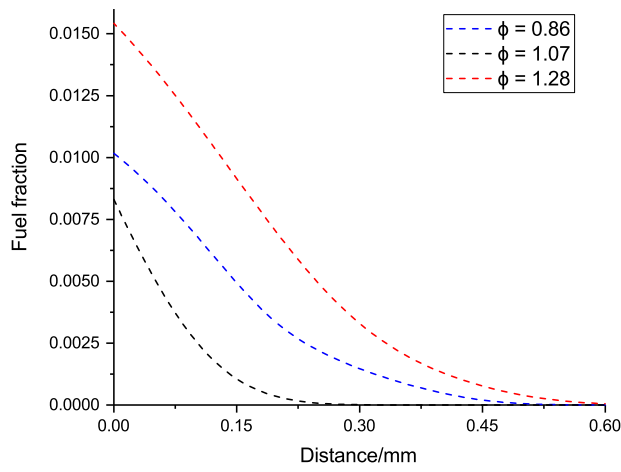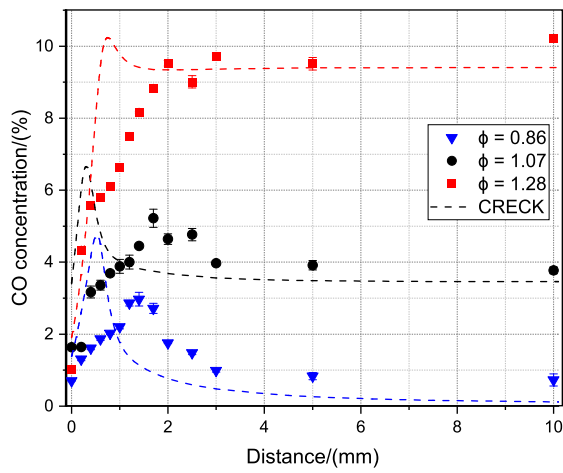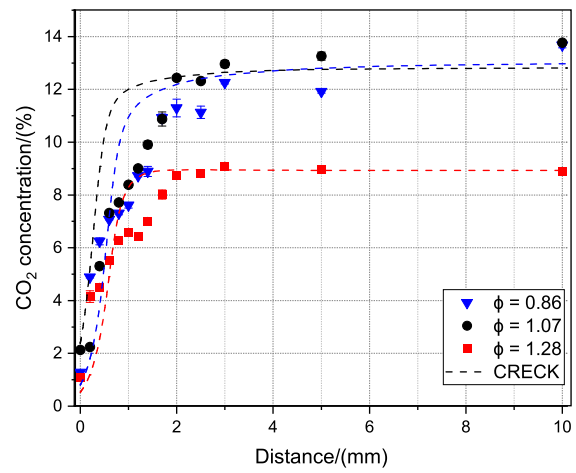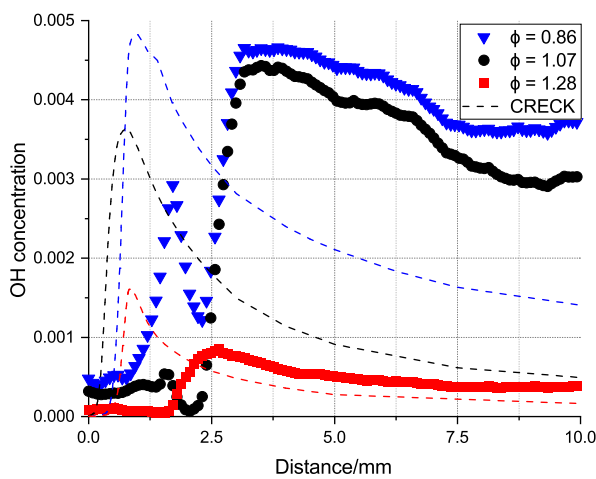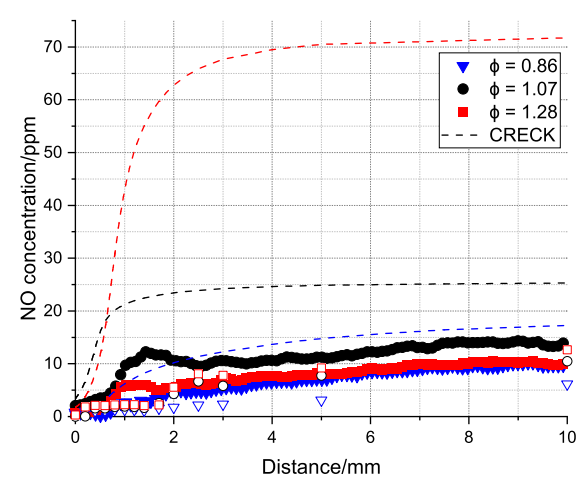
Figure 5.10: Simulated profiles of (a) fuel, (b) O_2, (c) CO, (d) CO_2, (e) OH, and (f) NO of surrogate B flames from PREMIX using CRECK model.
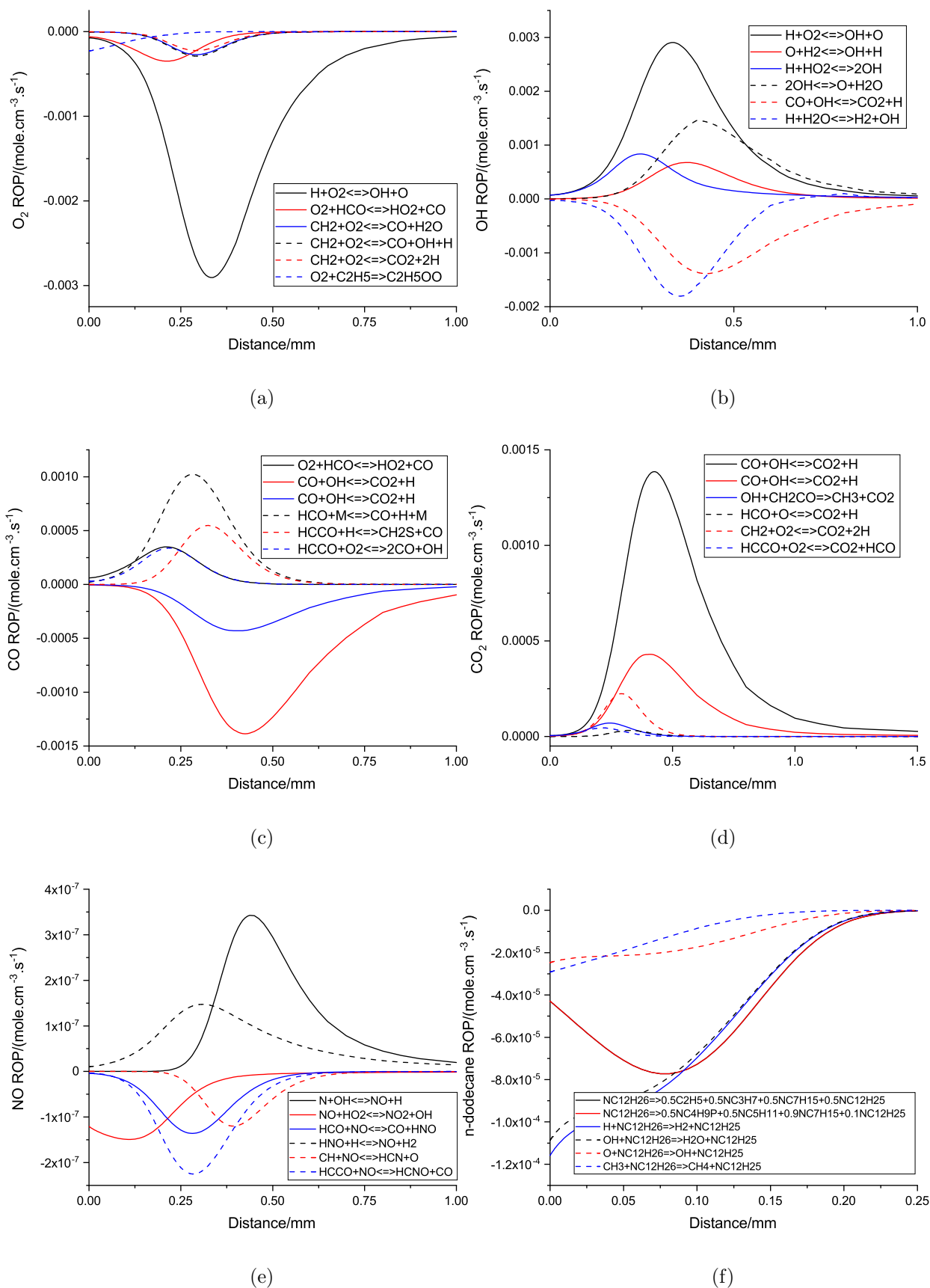
(a)

(b)

(c)

(d)

(e)

(f)

Figure 5.11: Highest rate of production of (a) O_2, (b) OH, (c) CO, (d) CO_2, (e) NO, and (f) n-dodecane in the near stoichiometric surrogate B flame from PREMIX using CRECK model.
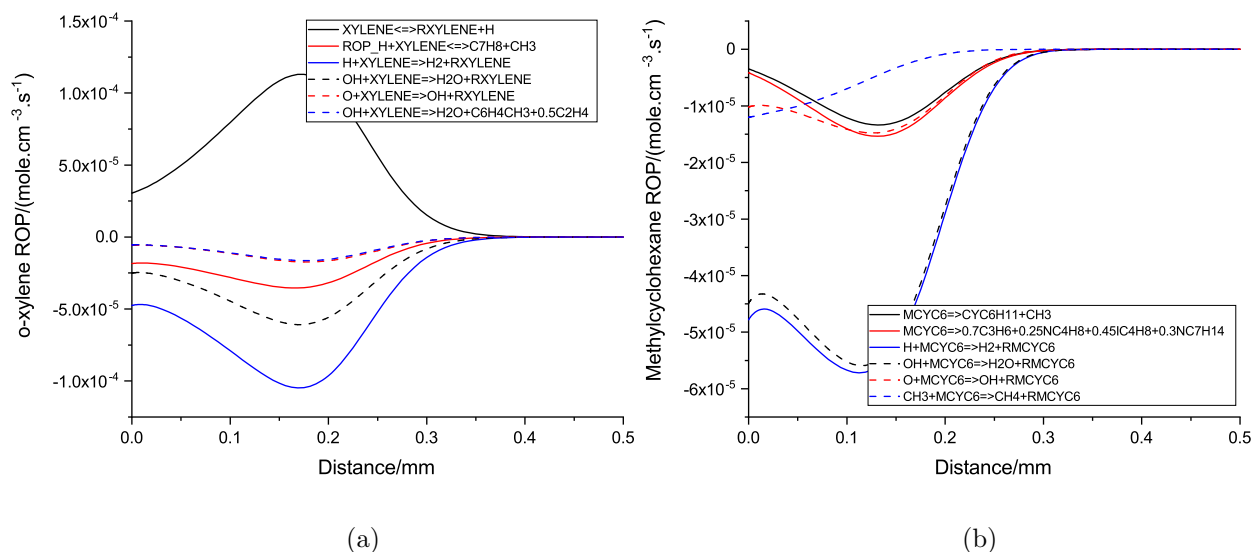
Figure 5.12: Highest rate of production of (a) o-xylene and (b) methylcyclohexane in the near stoichiometric surrogate B flame from PREMIX using CRECK model.

The model can accurately predict the CO profile at all stoichiometry, but slightly over predicts the peak concentration. The similar early peak occurrence was found compared to the experimental data while the equilibrium concentration was close between both results. In the closer region to the burner surface, the hydrocarbon radicals from the decomposition of the fuel species were the main source of the CO production. The main radical that was involved in the CO production was formyl, which reacts with oxygen or decomposes directly to CO. Other sources of CO in this region are the acetyl decomposition, ketenyl reaction with oxygen, and direct production of CO from the decomposition of the cyclic compounds. After the peak occurrence, the decay of the CO peak was caused by the oxidation of CO to CO_2 through the reaction with mainly the OH and O radicals.

The simulated CO_2 from the CRECK model was accurate in most of the region of the flame except at 1.0 mm from the burner surface where the model indicates a higher production rate of CO_2 than the experimental data. The model shows a rapid increase in the CO_2 concentration at below 1.0 mm from the burner surface because in this region, the fuel species breaks and CO was produced mostly. The reaction analyser shows that in this region, CO_2 was not only produced from CO but also as a side product of the hydrocarbon decompositions. In the higher region, the CO_2 production mostly came from the CO oxidation. The total carbon from the CO and CO_2 shows an insignificant discrepancy between the model results and the experimental data.

A similar result to the surrogate A flame was found for the prediction of the OH profile in which the model shows an earlier peak compared to the experimental data. The concentration at the peak was similar between the model and the experimental

data in the lean flame, while over-prediction was found in the rich and under prediction was found in the stoichiometric case. The higher temperature in the stoichiometric flame causes the earlier formation of the OH concentration peak while the other cases have a relatively similar location of the peak. The source of the OH production in the low region was formed by the side product of the hydrocarbon decomposition and the reaction of oxygen with the H radical. Meanwhile, the main consumption of the OH radical after the occurrence of the peak was caused by the formation of water and the involvement in the formation of CO_2.

The results of the prediction of the NO concentration show a large discrepancy between the model results and the experimental data. The targetted experimental data from the LIF and gas analysis indicate that the NO concentration ranged up to 15 ppm while the model over predicts the profile at all stoichiometry. An agreement was found in the relative NO concentration in between the gas analyser and the model prediction, which show that the rich flame has the highest NO concentration, followed by the stoichiometric and the lean flames. In the lean flame, the non-thermal production dominates the NO formation while in the stoichiometric the thermal mechanism was more dominant. In these cases, both thermal and non-thermal production peaked at approximately 1.0 mm from the burner surface and then dropped afterwards. However, in the lean case, the reduction of the NO production rate was slower and this results in the continuous growth of the NO concentration above the burner surface. Meanwhile, in the rich and stoichiometric case, the NO concentration does not gain much above 4.0 mm from the burner surface.

5.2.5 Ethanol/Jet A-1 Blend Flames

For the ethanol and jet fuel blend, only the mechanisms from this work and CRECK were compared because of the unavailability of the ethanol sub-mechanism in the other mechanisms. Figure 5.13 presents the simulation results of the blend flames from both mechanisms as well as the experimental data from the experimental work in the previous chapter. Also, the sensitivity and rate of production analysis of the species are presented in Figure 5.14 to 5.15, and 5.16 to 5.17, respectively. The fuel fraction shows the concentration of all the fuel species in the surrogate model including ethanol. A similar trend of fuel consumption was shown between both models at all stoichiometry. The stoichiometric flame has the fastest fuel consumption rate while the lean flame has the slowest rate. At all stoichiometry, the CRECK model was slightly lower than the model from this work which might be caused by the different surrogate compositions. The given fuel fraction was highest in the rich flame while lowest in the lean flame. The simulation results show that the fuel consumption was slowest in the lean while fastest in the stoichiometric flame due to higher flame temperature in the stoichiometric flame.

In the current model, the fuel species are n-decane, toluene, and ethanol. The n-decane species undergoes H-abstraction reaction with mainly H, OH radicals, and O_2 yielding decyl radical. The H-abstraction via H radical becomes more dominant with increasing temperature such as in the stoichiometric flame and then the decyl radical decomposes to the C_2 and C_3 species. The toluene fraction also undergoes H-abstraction through the reaction with radicals to form benzyl or it directly breaks to form benzene and methyl radical. The H-abstraction reaction also initiates the decomposition of ethanol to form C_2H_5O and then breaks to ethylene or formaldehyde or methyl and carbon monoxide. In the CRECK model, the fuel species for the blend are n-dodecane, o-xylene, methylcyclohexane, and ethanol. The n-dodecane species was mainly converted to the dodecyl radical through the reaction with radicals and also decomposed to the smaller hydrocarbons, such as $C_2, C_3, C_4, C_5,$ and C_7 species. More pathways to the smaller hydrocarbons are available from the dodecyl radical. The o-xylene species also undergoes H-abstraction reaction and breaks to the smaller cyclic compound while producing smaller hydrocarbon during the process. The main route of the methylcyclohexane decomposition was through the H-abstraction reaction which further break to $C_1 - C_5,$ and C_7. A direct route to the $C_3, C_4,$ and C_7 was also available, but it is less dominant than through the H-abstraction. Similar to the current model, the ethanol species was mainly consumed to the H-abstraction with radicals.

The prediction of the oxygen concentration from both models is approximately similar at all stoichiometry. Compared to the experimental data, the lean case is relatively accurate in all the region of the flame while the stoichiometric and rich flames show a faster rate of oxygen consumption in the lower region of the flame. The prediction of the CRECK model was slightly lower than the current model because of the lower oxygen concentration in the given PREMIX input due to the different surrogate components. In the lower region, the current model shows that the oxygen consumption was mainly used for the H-abstraction of the hydrocarbon species and the production of OH radical. The attracted hydrogen atom from the hydrocarbon and the oxygen molecule form hydroperoxyl radical. In the higher region of the flame, the oxygen consumption was mainly used for the production of the OH radical which leads to the formation of water. A similar oxygen consumption route was also found in the CRECK model where the oxygen molecule was used to abstract a hydrogen atom from the hydrocarbon molecule and produce OH radicals. At the higher region, the oxygen species was used for the OH radical production and involved in the reaction of water production.

Both models show an approximately similar trend in the CO concentration at all stoichiometry. The prediction of the CO peaks was higher and its occurrence was earlier than in the experimental data. For the stoichiometric case, the prediction of the

equilibrium concentration from both models in the higher region was close to the experimental data while both models over predict the rich case and underpredict the lean case. The accumulation of the CO production, which causes the occurrence of the peak, was mainly caused by the decomposition of the HCO, CH_3CO, CH_2CO, and HCCO. After the peak, the CO concentration decreases due to the conversion to CO_2 by the reaction with OH radical. Similar reactions was found to be responsible for the CO formation before and after the peak in the CRECK model.

Approximately similar results in the CO_2 prediction were also found from both models at all stoichiometry. The prediction from the CRECK model was relatively closer to the experimental data than the current model in the higher region of the flame. The prediction for the lean and stoichiometric flames was relatively accurate while over-prediction was found in the stoichiometric case at approximately 1.0 mm from the burner surface. A significant discrepancy was found in the rich case where the models show a lower CO_2 concentration than the experimental data in the higher region, while in the lower region the prediction was accurate. In the lower region, the source of CO_2 production came from the oxidation of CO with the OH radical and also the reaction of the hydrocarbons, such as HCCO, HCO, CH_2CO, CH_2, CH_3CH_2O, and CH_3O, with oxygen, hydroperoxyl, and CO. A similar source of CO_2 in the lower region was found in the CRECK model, but in the stoichiometric case, the CO_2 production from the reaction of CH_2CO with OH was more dominant. In the higher region, the CO_2 production from the CO oxidation with OH becomes the most dominant route because of the presence of the hydrocarbon radicals decreasing. Similar results were found in the CRECK model, but higher reactivity in the CO_2 production was found in the reaction involving CH and other radicals.
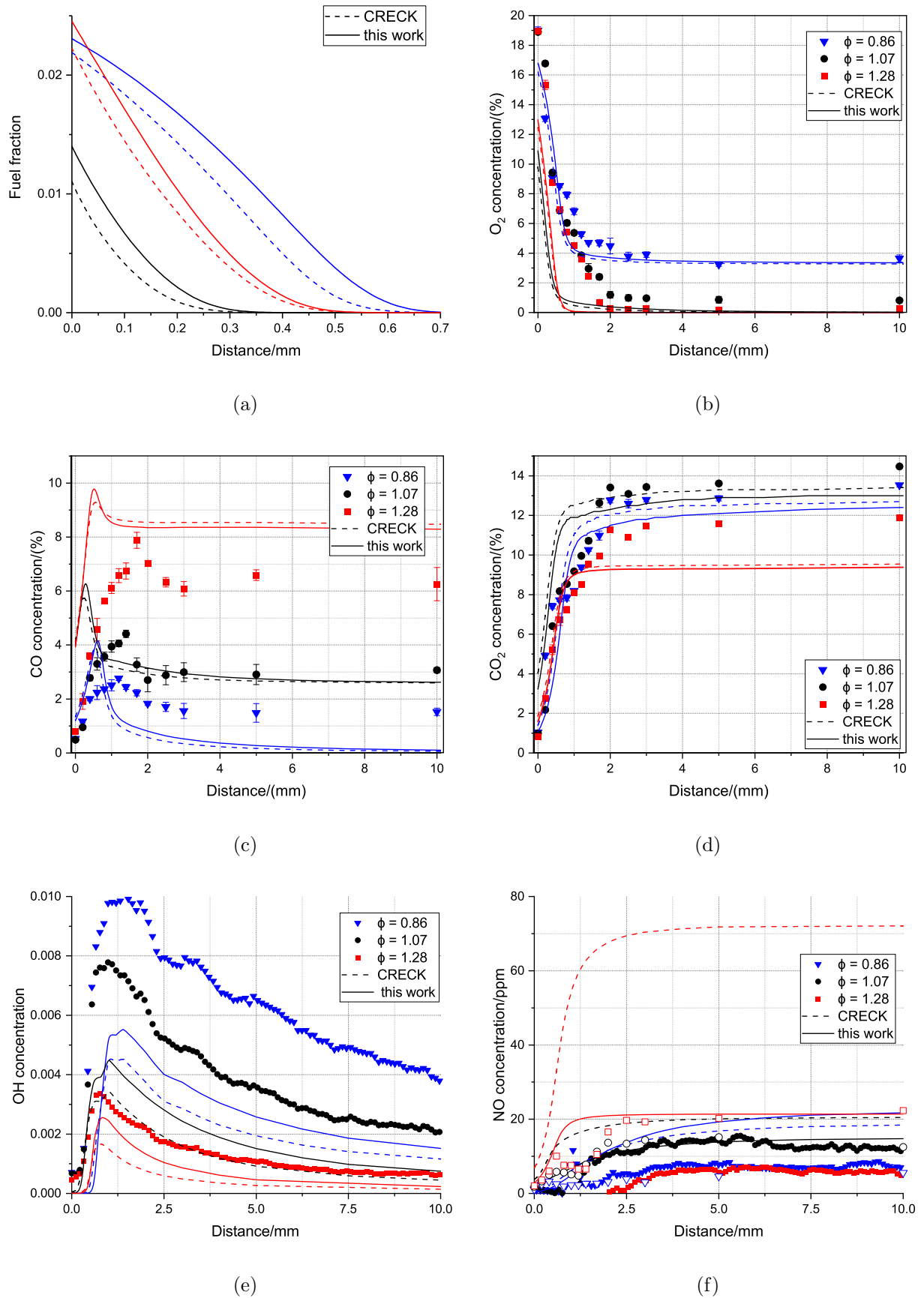
Figure 5.13: Simulated profiles of (a) fuel, (b) O_2, (c) CO, (d) CO_2, (e) OH, and (f) NO of blend flames from PREMIX.
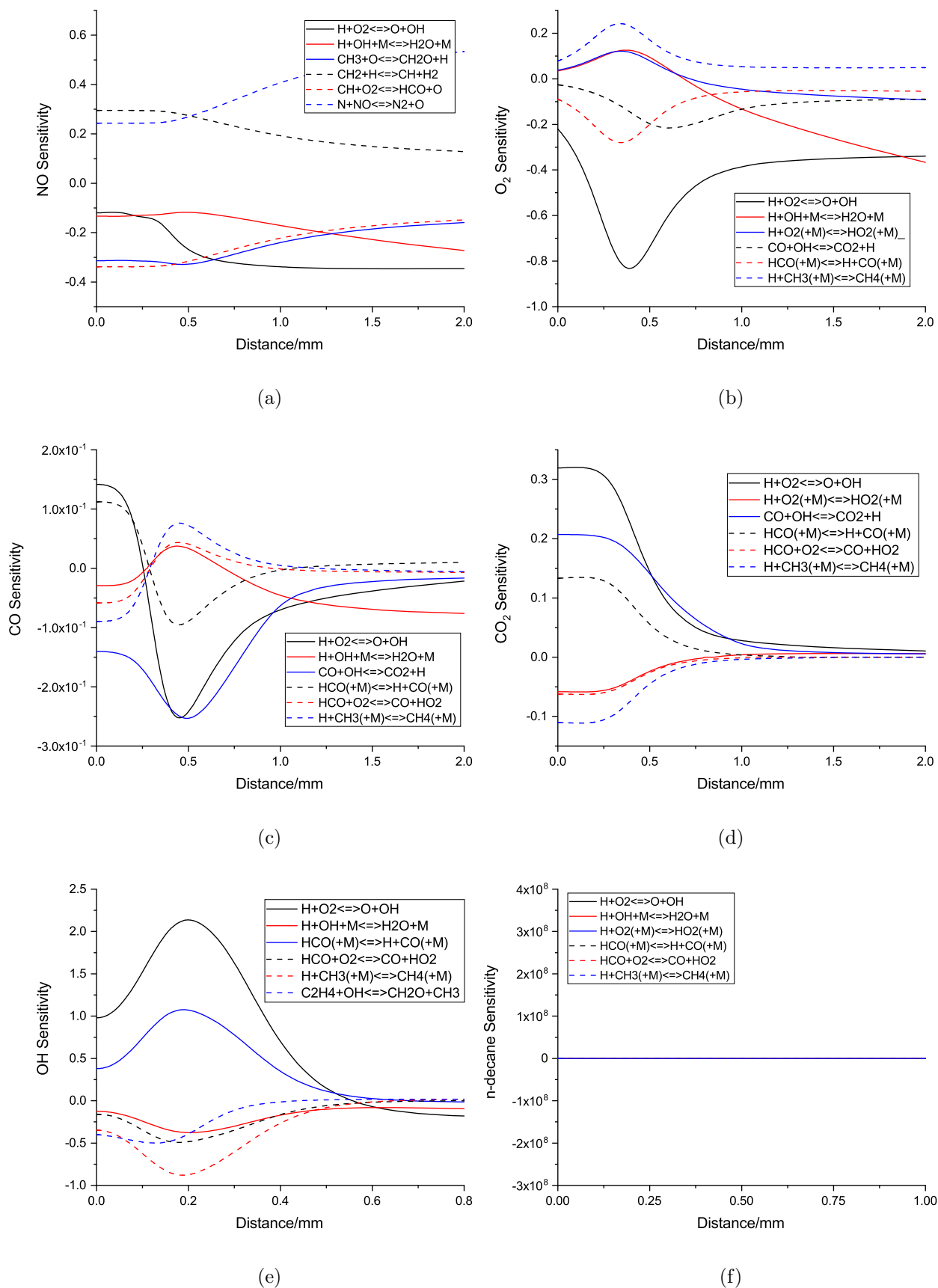
Figure 5.14: Most sensitive reactions with respect to (a) NO, (b) O_2, (c) CO, (d) CO_2, (e) OH, and (f) n-decane in the near stoichiometric blend flame from PREMIX using the developed reaction mechanism.

170

(a)

(b)

Figure 5.15: Most sensitive reactions with respect to (a) toluene and (b) ethanol in the near stoichiometric blend flame from PREMIX using the developed reaction mechanism.

(a)

(b)

Figure 5.16: Highest rate of production analysis with respect to (a) toluene and (b) ethanol in the near stoichiometric blend flame from PREMIX using the developed reaction mechanism.

171

Figure 5.17: Highest rate of production of (a) NO, (b) O_2, (c) CO, (d) CO_2, (e) OH, (f) n-decane in the near stoichiometric blend flame from PREMIX using the developed reaction mechanism.

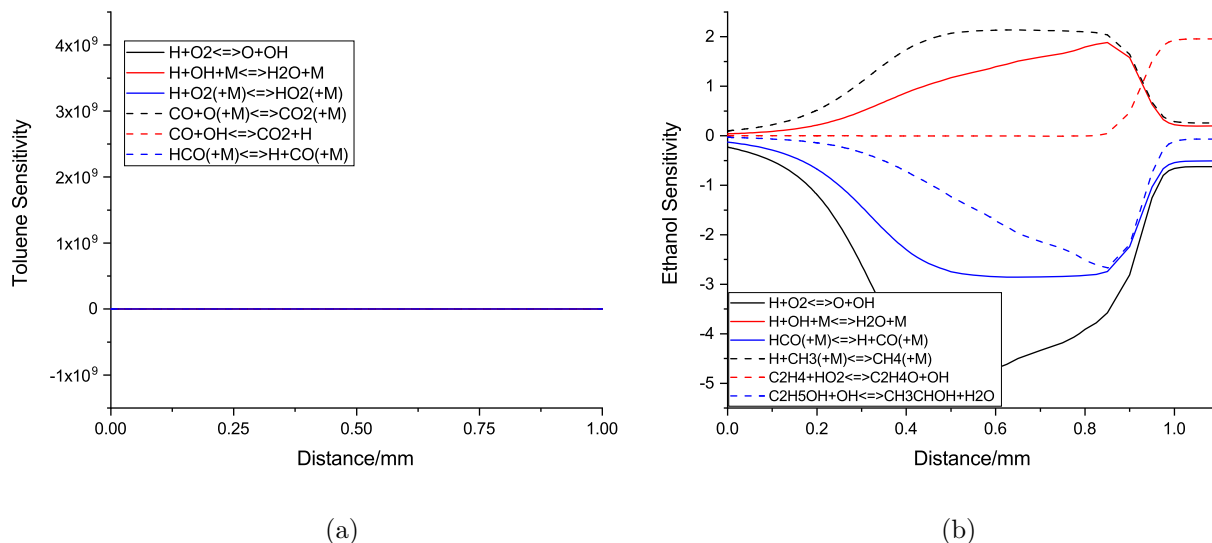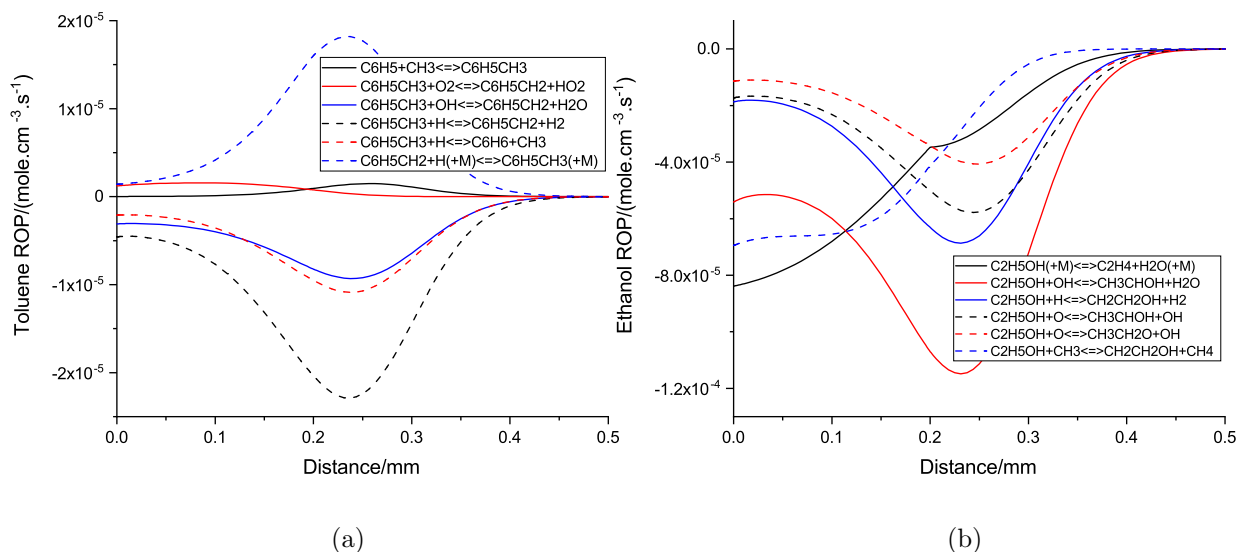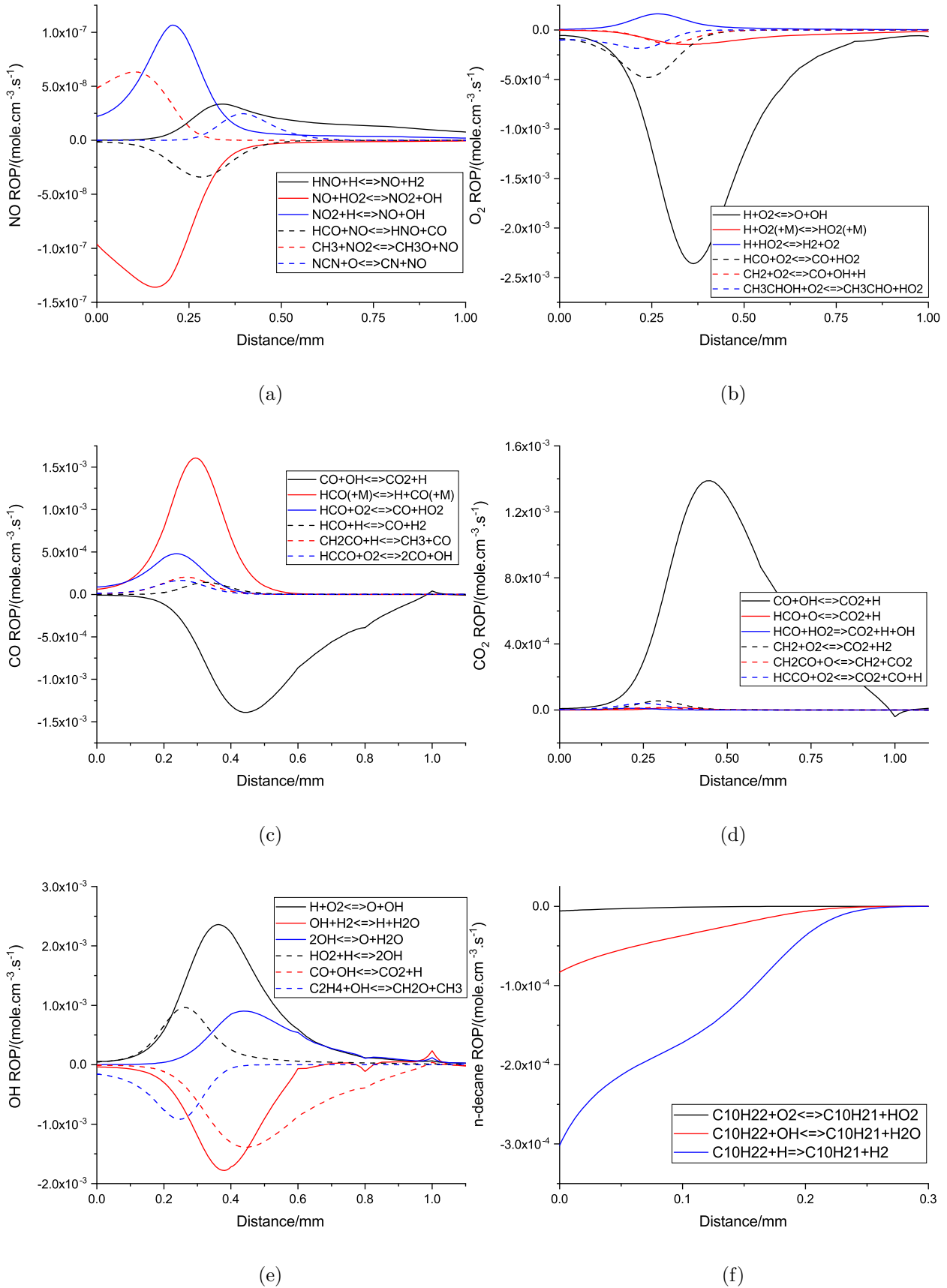Both models agree with the experimental data in terms of the relative concentration of the OH radical and the position of the peak. The results from the CRECK model were relatively lower than the current model at all stoichiometry. Compared to the quantified concentration of OH from the experimental data, both models show relatively lower concentration in all regions. Towards the formation of the OH peak, the OH production mainly came from the reaction of the H atom with oxygen or hydroperoxyl as well as the reaction of an oxygen atom with hydrogen. Also, the water species undergoes a reverse reaction to re-form OH then the resulting radicals reproduce water species. In the lower region, the OH radical is very important in the decomposition of the hydrocarbon species as well as the oxidation of CO and water formation. After the peak, the OH concentration decreases, which was mainly caused by the oxidation of CO to CO_2 and the formation of water.

The NO prediction from both models shows a different trend in the rich and stoichiometric flames while a slight discrepancy was found in the lean flame. The CRECK model prediction was relatively higher than the current model, especially in the rich flame. Compared to the experimental data from the LIF method, both models over predict the NO concentration, except the prediction from the current model for the stoichiometric case which is relatively similar to the experimental data. The prediction from the current model approximately agrees with the measurement from the gas analyser for the rich case. The experimental data from the LIF and gas analysis show similar results and these are lower than the prediction from both models. The production of the NO species in the lean case was initiated by the non-thermal route in both models, then in the higher region, the thermal mechanism generates more NO than the non-thermal mechanism. In the current model, the peak of the NO production rate from the thermal mechanism is much higher than the non-thermal while in the CRECK model, the thermal mechanism was slightly lower than non-thermal mechanism. Both models show a slow reduction of the NO production from the peak and thus the NO concentration increases with distance from the burner surface in the lean case. In the rich case, the current model indicates that the NO production peaked at approximately 1.0 mm from the burner surface then it dropped. This caused the rapid increase in the NO concentration in the lower region and a relatively constant concentration in the higher region. The thermal dominates the non-thermal mechanism in the NO production in the rich flame. In the stoichiometric flame, a discrepancy was found in the current model where the NO production from the thermal mechanism was relatively longer due to the occurrence of two peaks in the NO production rate while the CRECK model indicates that the thermal route of NO was rapidly produced at approximately 1.0 mm from the burner surface. Meanwhile, the non-thermal production rate of NO in the stoichiometric flame was not much different in both models.

Comparison can be made to obtain the benefit of the ethanol addition to the Jet A-1 fuel in terms of the harmful gas emissions. In the post-flame region, the concentration of CO from the model was not much different between the ethanol, jet A-1, and blend flames at the same stoichiometry with the discrepancy being less than one per cent. Meanwhile, the gas analysis shows that for the lean flame, the blend flame has half per cent higher concentration of CO, while for the stoichiometric and rich flames, the jet A-1 flame has approximately 50 per cent lower CO emission than the others. The CO_2 concentration from the model and gas analysis shows that the difference between these fuels was less than 2 per cent. The total CO and CO_2 from the model shows that the discrepancy in all stoichiometry between these fuels was less than one per cent while the measurement shows less than 2 per cent discrepancy. The NO concentration from the model shows that the jet A-1 flame has the highest while the ethanol flame has the least NO concentration in the lean and stoichiometric cases. In the rich case, the NO concentration of the blend flame was slightly higher than the jet-A1 flame. The NO concentration from the LIF and gas analysis method shows a less than 5 ppm difference in each stoichiometry between these flames. Despite that the carbon and NO concentration of the compared fuels were not much different for each stoichiometry, the volumetric flow rate of the unburned gas of the blend flames was lower than that of the jet A-1 flames as presented in Table 3.2. Therefore, for the same stoichiometry, the blend flame might have less carbon and NO emission than the Jet A-1 flames.

5.2.6 Mass Flow Rate Sensitivity

Discrepancies that were found in the burner-flame simulation might be solved by optimising the rate parameters in the reaction mechanisms. However, it was also found that the value of the burner mass flow rate contributes to the uncertainty of the simulation results. In this modelling study, the values of the burner mass flow rate were calculated by dividing the total mass of the given air and fuel flow by the burner area. However, the effective area of the burner might be smaller than the calculation since there are parts of the mesh that have no hole on it as illustrated in Figure 3.2. This yields two scenarios of the mesh area calculation, which are by using the total mesh area and only the area of the holes. Furthermore, they are called as the maximum and minimum effective area of the mesh.

Simulation of both scenarios has been performed for the rich ethanol flame. By applying the minimum effective area of the mesh, the mass flow rate increases to approximately a factor of 10. With the higher flow rate, the rapid consumption of ethanol and oxygen as well as the formation of water and carbon dioxide occur at a higher region of the flame. Also, it increases the magnitude of CO and OH peaks while reducing the prediction of NO concentration. For the further work, the mesh of the

burner could be improved by applying finer drills or a sintered material that results to a closer approximation of the area calculation while producing stable flames.

5.3 Laminar Burning Velocity

Laminar burning velocity, or flame speed, is a measure of the flame front displacement over time in a premixed laminar gas mixture of fuel and oxidiser. Experimentally, the laminar flame speed can be measured by measuring the propagation of the flame front in a spherical bomb, counter-flow combustion rig [60], or using a heat flux method in a flat-flame burner [70]. The laminar flame speed varies with the fuel, equivalence ratio, temperature, and pressure. It is a fundamental validation for a kinetic model since it evaluates the reactivity, diffusivity, and exothermicity of the model [171]. Moreover, in real spark-ignited engines, laminar burning velocity affects engine emission and performance, such as knocking.
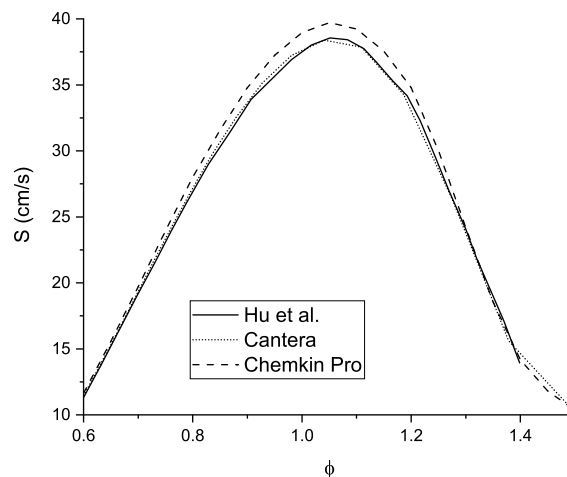
Figure 5.18: Laminar burning velocity prediction of methane/air at 0.1 MPa and 300 K by Hu et al. [8], Chemkin Pro, and Cantera.

Validation with the experimental work was performed to evaluate the current model accuracy in predicting the laminar flame speed data from the experimental work. The flame speed calculation was solved by using a Cantera-python program which was written by Dr Alastair Clements [172]. The Cantera program has an advantage over the PREMIX program in terms of the ability to be executed in the university high-performance computer (HPC). The laminar flame speed calculation requires more computing resources than the flat-flame simulation in Section 5.2 because it solves more equation, such as the energy equation. Therefore, the HPC facility was used to solve the flame speed calculation. In order to validate the model, recent work by Hu et al. [8] was reproduced using the Cantera and PREMIX program. Figure 5.18 shows the com-

parison of the prediction of the laminar flame speed of methane/air mixture at 0.1 MPa and 300 K from the current model and the PREMIX code to the prediction from Hu et al. [8] using the GRI 3.0 mechanism. The result indicates that the current model is accurate in reproducing the work by Hu et al. [8] while the results from the PREMIX code requires optimisations in some input parameters to eliminate the discrepancy.

5.3.1   Jet A-1

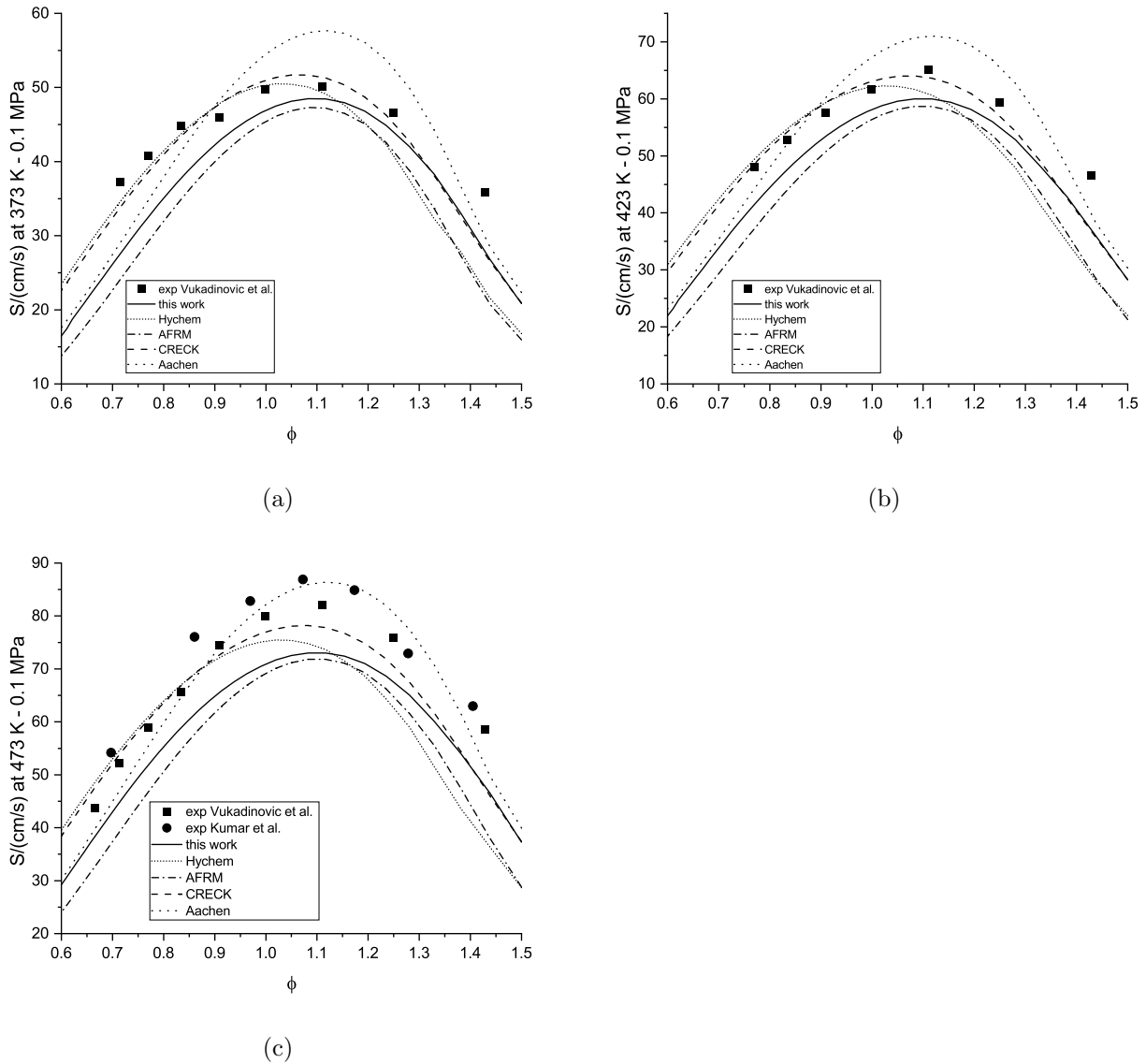(a)

(b)

(c)

Figure 5.19: Laminar burning velocity prediction of Jet A-1 flames at 0.1 MPa and (a) 373 K, (b) 423 K, and (c) 473 K with comparison to experimental work from Vukadinovic et al. [9] and Kumar et al. [10].

Figure 5.19 shows the prediction of the laminar burning velocity of jet A-1 fuel at 0.1 MPa at an elevated temperatures by the current mechanism and several recent jet fuel

mechanisms with the experimental data validation from Vukadinovic et al. [9] and Kumar et al. [10]. The measurement of the laminar flame speed from Vukadinovic et al. [9] employed an explosion vessel while Kumar et al. [10] used a counter-flow flame burner. The jet fuel models and mechanisms that were compared with the current model were the detailed high-temperature Hychem, the AFRM, CRECK kerosene surrogate [173], and Aachen models. The Hychem mechanism [169] assumed the jet fuel to be $C_{11}H_{22}$ while the surrogate definition of the other mechanisms for the jet A-1 was identical to that in Section 5.2.

The prediction of the laminar flame speed of Jet A-1 from all models shows a similar trend with the experimental data. The laminar flame speed profile with the variation of equivalence ratio forms a peak line with the maximum flame speed achieved at equivalence ratio approximately 1.1. The increase of temperature escalates the laminar flame speed which is also shown by the models. The current model was more accurate than the AFRM at all temperatures and equivalence ratios which shows a closer prediction to the experimental data. The prediction from the Aachen model was higher than the experimental data from Vukadinovic et al. [9], while relatively good agreement with the experimental data from Kumar et al. [10] at 473 K. The prediction from the Hychem and CRECK model were relatively similar for the lean region at the same temperature while discrepancy occurred between both models in the rich region where the prediction from the Hychem model was lower than the CRECK model. The CRECK model has the best agreement with the experimental data from Vukadinovic et al. [9] but shows a discrepancy in the rich region, especially at 473 K.

Figure 5.20 shows the prediction of the laminar flame speed from the compared models with the variation of pressure at 473 K and experimental data from Vukadinovic et al. [9]. The prediction from the compared models and the experimental data show a similar trend for the laminar flame speed which decreases with an increase in the pressure. The current mechanism shows a better prediction than the AFRM mechanism at all pressures and equivalence ratios. The Aachen model shows a good agreement with the experimental data at near stoichiometric and rich mixtures while under predicts the laminar flame speed in the lean mixtures. A similar prediction was shown by the Hychem and CRECK model in the lean region while in the near stoichiometric and rich region the Hychem model shows a lower prediction of the laminar flame speed than the CRECK model. The CRECK model was relatively accurate for predicting the laminar flame speed of the jet A-1 flame at the selected pressures but has a lower prediction for the near stoichiometric and rich region than the experimental data.

(a)

(b)

(c)

(d)

Figure 5.20: Laminar burning velocity prediction of Jet A-1 flames at 473 K and (a) 0.2 MPa, (b) 0.4 MPa, (c) 0.6 MPa, and (d) 0.8 MPa with comparison to experimental work from Vukadinovic et al. [9].

5.3.2 Ethanol

The validation of the laminar flame speed prediction of ethanol flames was performed to check the influence of the other sub-mechanisms to the ELTE ethanol mechanism. Thus, only the comparison of the current and ELTE mechanisms are presented as well as the experimental data from various sources. Figure 5.21 shows the prediction of the laminar flame speed of ethanol by the current and ELTE mechanisms at various temperatures. Both models were able to predict the experimental data of the laminar flame speeds of ethanol accurately at the selected temperatures. The results show that there is no significant difference between the current and ELTE mechanisms. However,

at 0.1 MPa the prediction of the current model was slightly lower than the ELTE mechanism in the lean region while slightly higher than that in the rich region.

Figure 5.22 presents the laminar burning velocity prediction of ethanol with a variation of pressure from both models and the experimental data from Bradley et al. [11]. The predictions from the current model at 0.5 and 0.7 MPa were slightly lower than the ELTE mechanism while at 0.2 MPa the prediction from the current model was lower in the lean region while slightly higher in the rich region than the ELTE mechanism. Compared to the experimental data for 0.5 and 0.7 MPa, both models agree with the experimental data at an equivalence ratio less than 1.1 while in the richer region the predictions from both models were lower than the experimental data. Meanwhile, at 0.2 MPa, both models show a good accuracy at equivalence ratios of 0.7 and 1.2.

5.3.3 Ethanol/Jet A-1 Blend

From the above comparison, the ethanol flame has a faster laminar flame speed than the jet A-1 flame at 0.1 MPa and the same temperature at 0.1 MPa. Both the ethanol and jet A-1 laminar flame speeds increase with temperature but decrease with pressure increase. A further simulation was performed to predict the laminar flame speed of 50/50 per cent ethanol/jet A-1 blend by both molar and volume fractions by using the current mechanism which is presented in Figures 5.23 and 5.24, respectively. The results show that the laminar flame speed of the mixture behaves similar to that of the pure ethanol and jet A-1 which increase with temperature and decrease with pressure. From the comparison, the addition of 50 per cent ethanol by molar ratio decreased the laminar flame speed of the mixture to lower than the pure ethanol flame at the same temperature and pressure. Meanwhile, at 0.1 MPa the laminar flame speed of the blend was relatively similar to jet A-1 while slower at higher pressure at 473 K. For the case of 50 per cent ethanol addition by volume, the laminar flame speed of the blend was faster than the pure jet A-1 and slower than the pure ethanol at the same temperature and pressure.
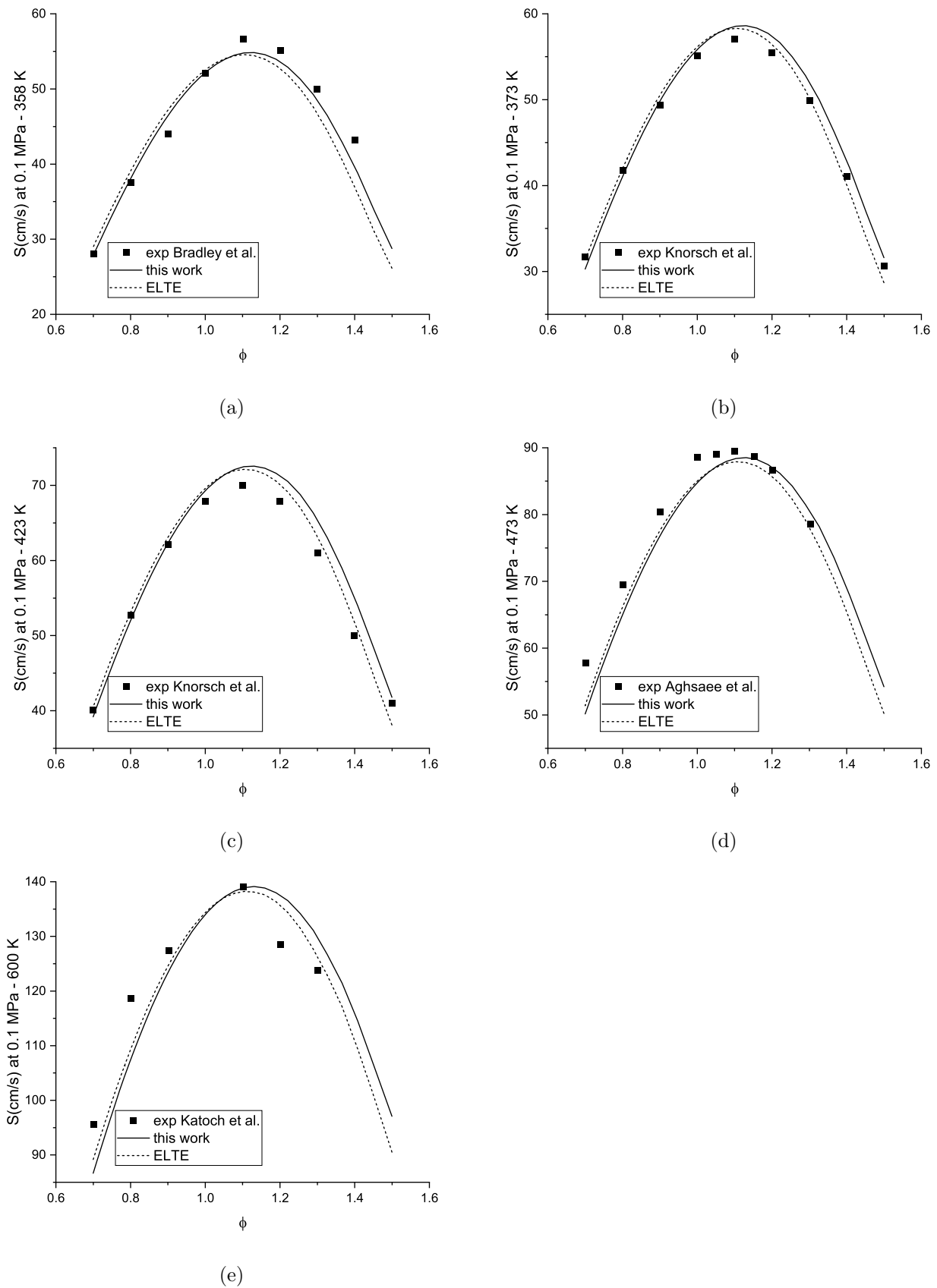
Figure 5.21: Laminar burning velocity prediction of ethanol flames at 0.1 MPa and (a) 358 K, (b) 373 K, (c) 423 K, (d) 473 K and (e) 600 K with comparison to experimental work from Bradley et al. [11], Knorsch et al. [12], Aghsaee et al. [13], and Katoch et al. [14].
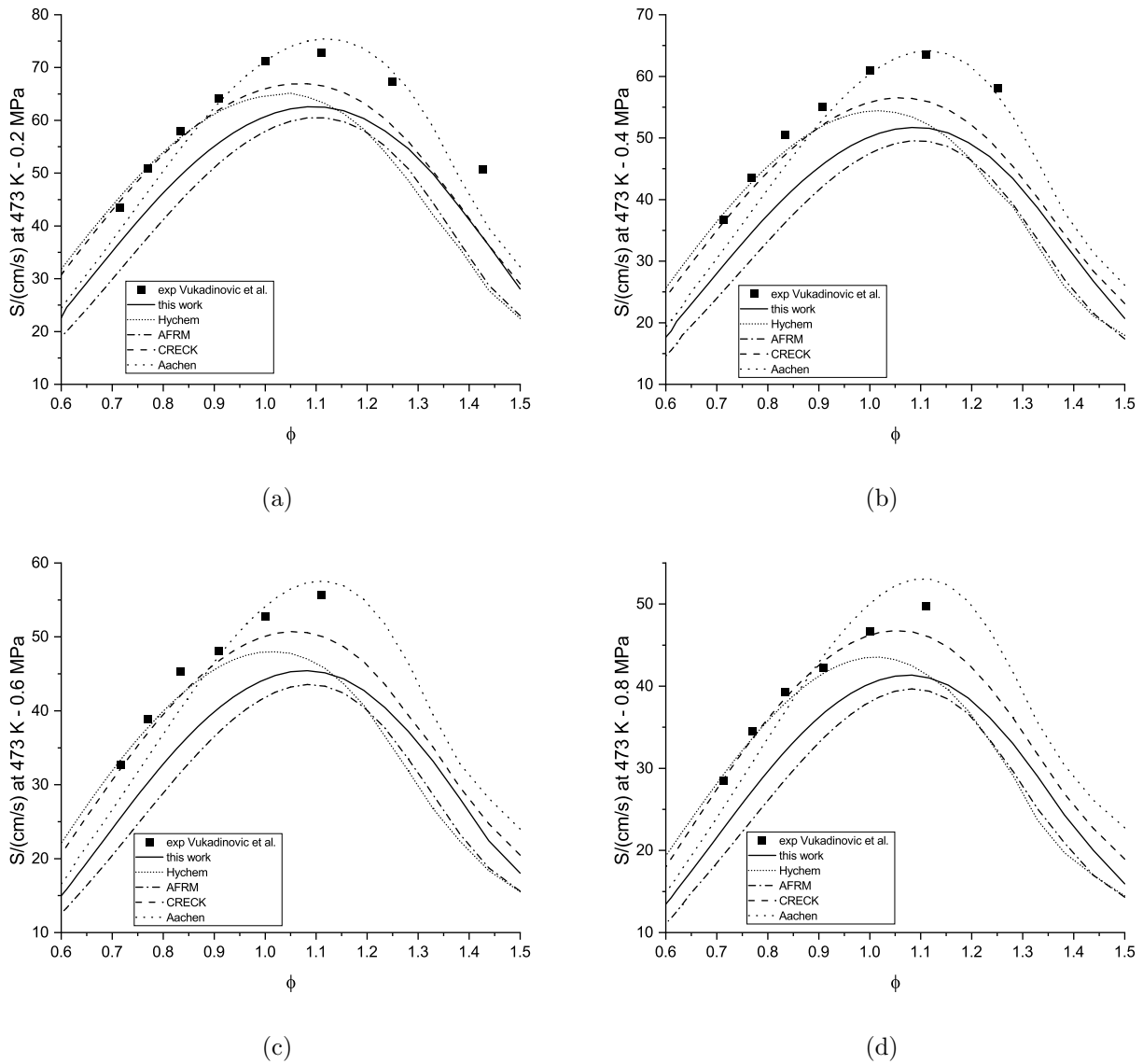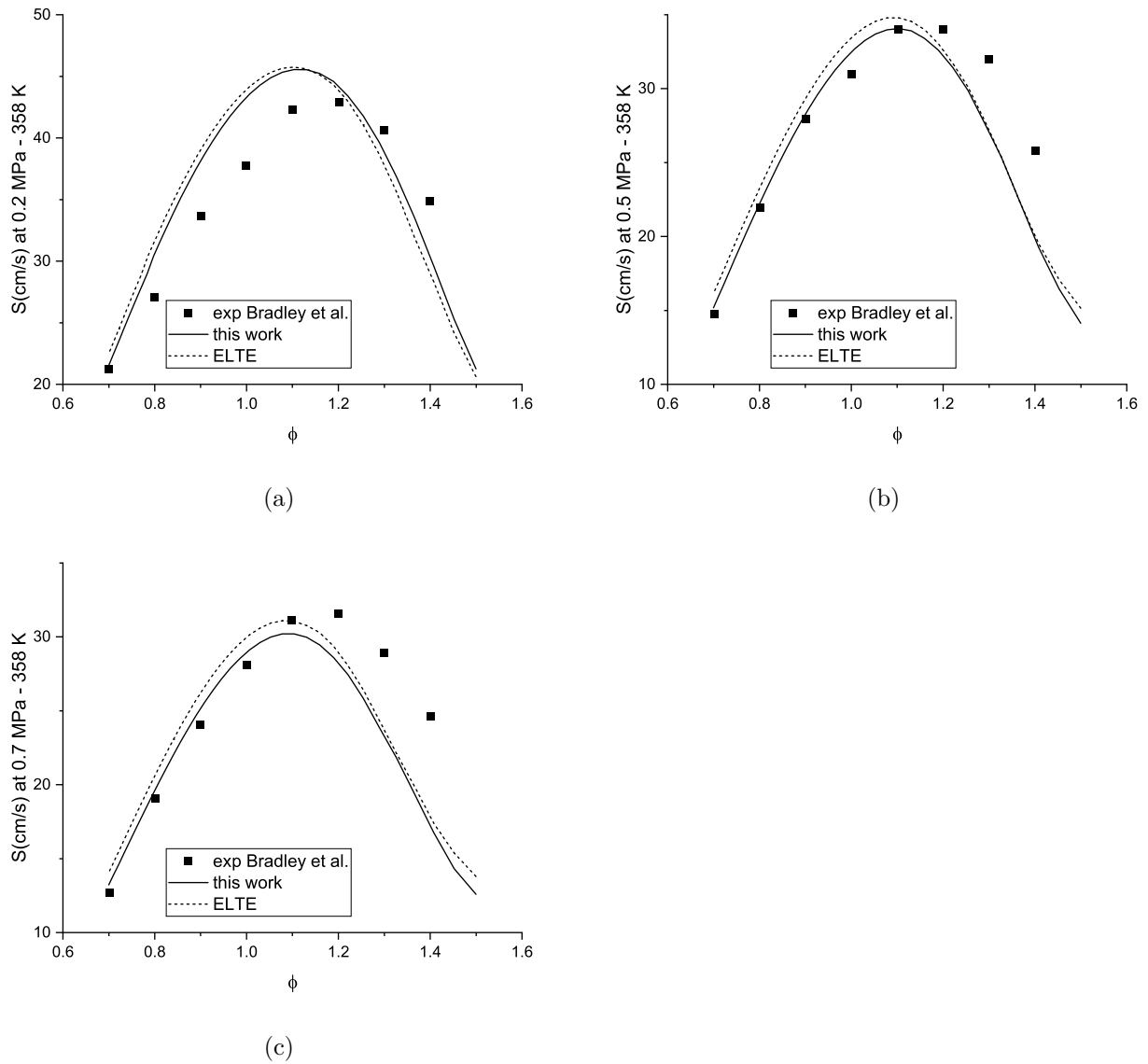
Figure 5.22: Laminar burning velocity prediction of ethanol flames at 358 K and (a) 0.2 MPa, (b) 0.5 MPa, (c) and 0.7 MPa with comparison to experimental work from Bradley et al. [11].

(a)

(b)

(c)
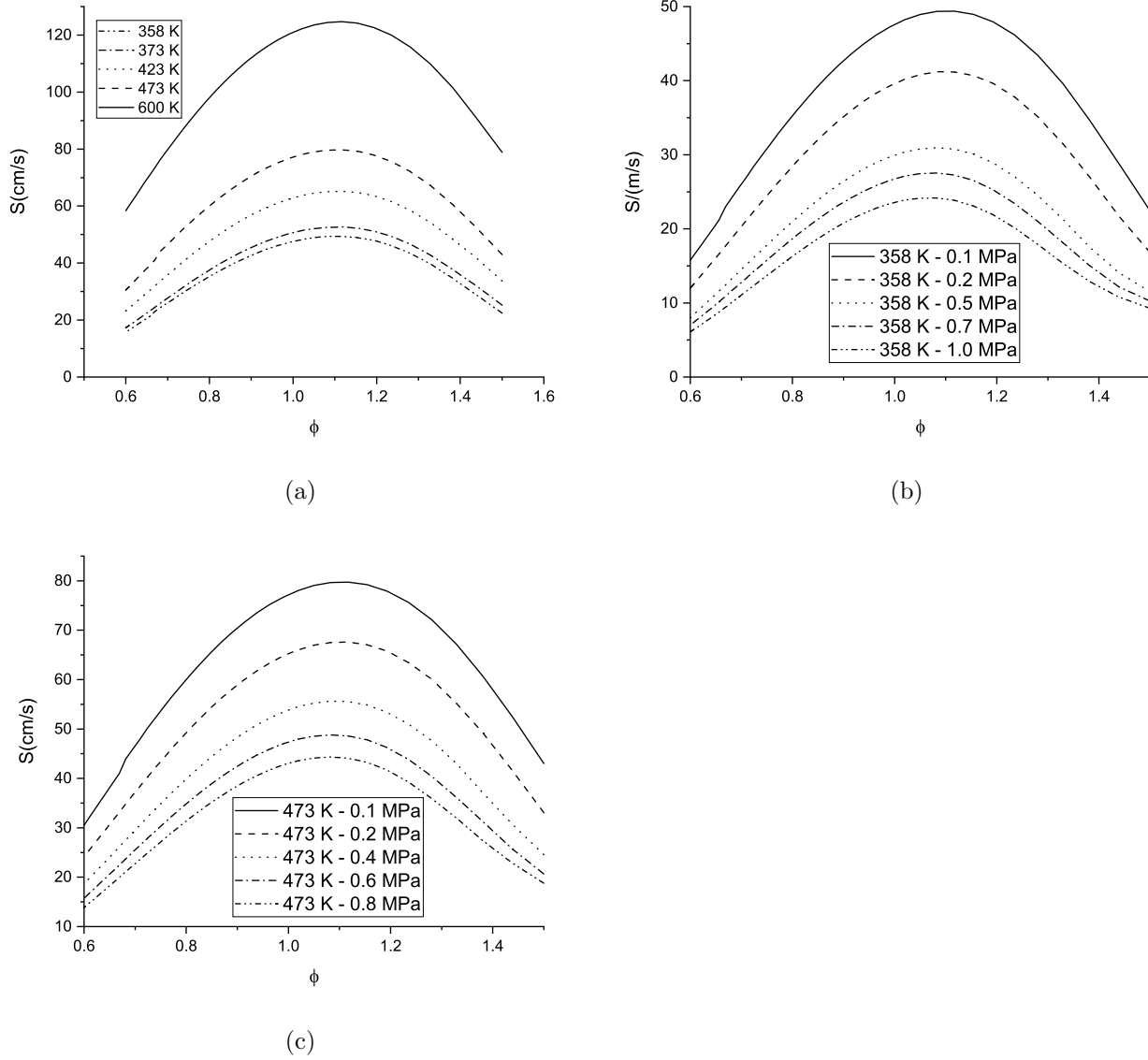
Figure 5.23: Laminar burning velocity prediction of E50 by molar flames at (a) 0.1 MPa, (b) 358 K, (c) and 473 K.
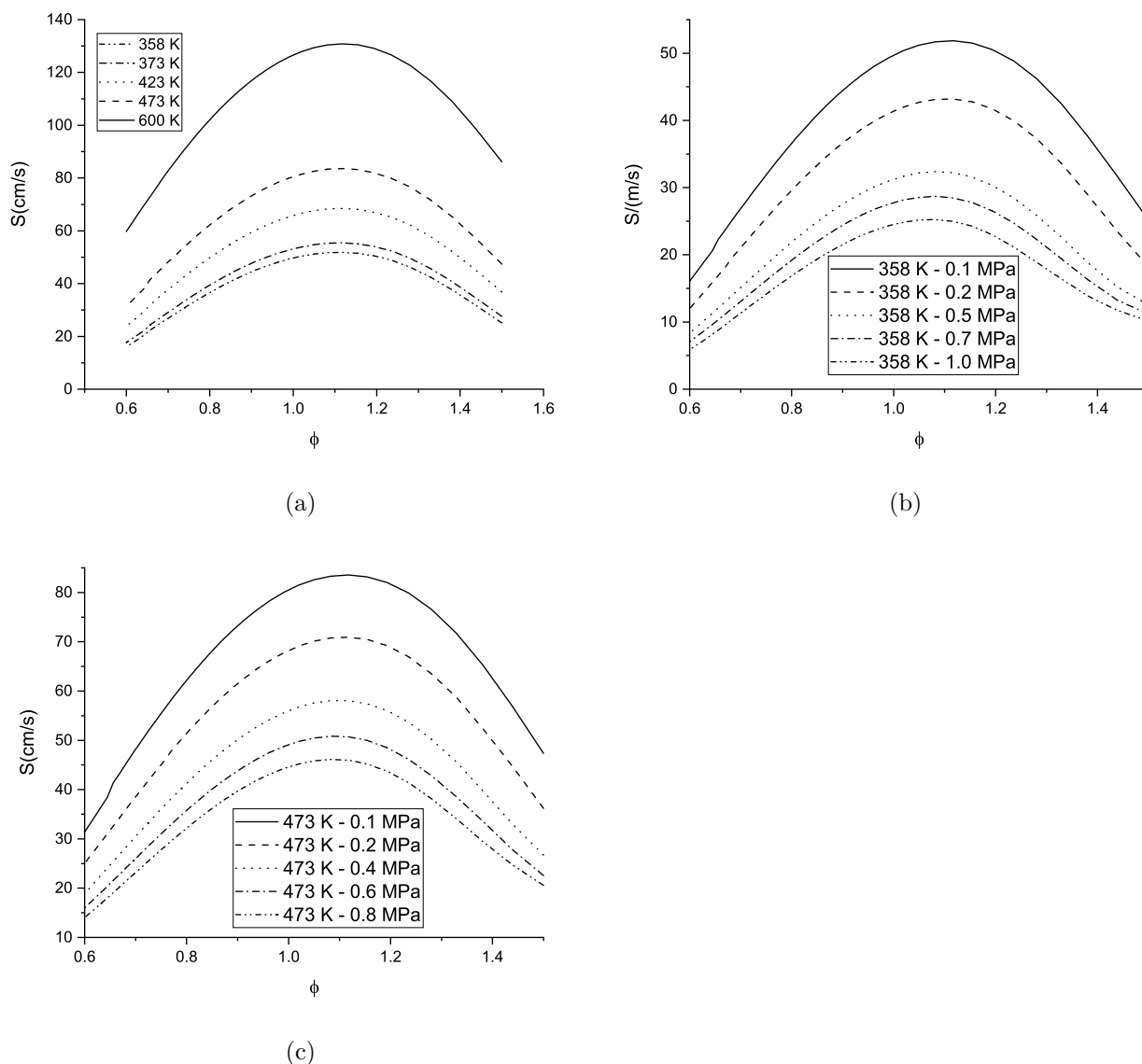
Figure 5.24: Laminar burning velocity prediction of E50 by volume flames at (a) 0.1 MPa, (b) 358 K, (c) and 473 K.

The laminar flame speed with the 50 per cent ethanol/jet A-1 blend by volume was faster than that by molar ratio. This was caused by the greater molar concentration of ethanol in the 50 per cent blend by volume because ethanol molecular weight is much lower than the jet fuel surrogate while the density was not much different. This results in approximately 75 per cent of initial ethanol molar fraction for the 50 per cent volumetric blend. The higher ethanol fraction might cause the laminar flame speed of the blend to be closer to the pure ethanol which was relatively faster than the jet A-1. A sensitivity analysis was performed to identify the most sensitive reactions to the laminar flame speed by using the Cantera code. It was found that in pure ethanol, jet A-1, and the blends, the most sensitive reaction that promotes the laminar burning velocity of the flame was $H + O_2 = O + OH$. Meanwhile, the most sensitive reaction

183

that inhibits the laminar flame speed of the flame was $H + OH + M = H_2O + M$. An exception was found in the ethanol and 50 per cent ethanol blend by volume at 1 MPa and 358 K cases where the reaction $H + O_2 (+M) = HO_2 (+M)$ is the most sensitive reaction that decreases the laminar flame speed. Other than these reactions, the reactions that involve small species, such as CO, HO_2, CH_3, are also important in affecting the laminar flame speed of the fuels as illustrated in Figure 5.25.
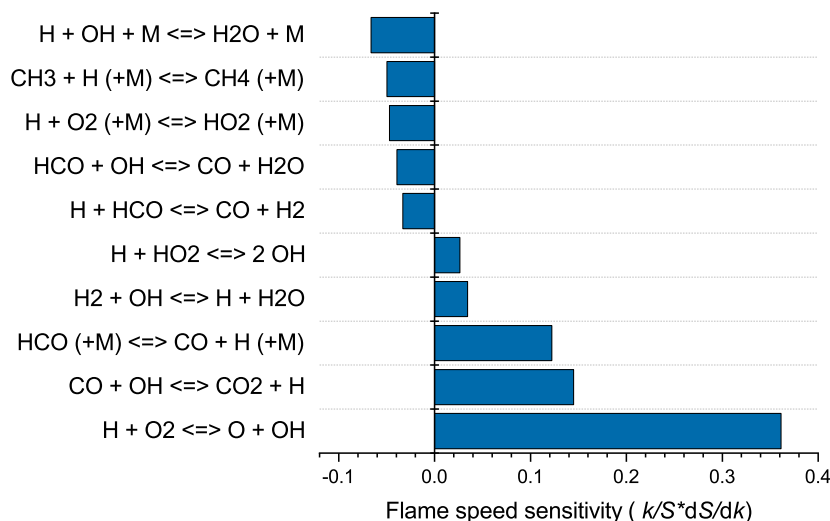
Figure 5.25: Laminar burning velocity sensitivity of stoichiometric 50 per cent ethanol/jet A-1 blend by molar ratio at 0.1 MPa and 373 K.

5.4 Ignition Delay Time

The ignition delay time is an important fuel characteristic, especially for the application in a real engine. It is defined as the required time for the unburned gas mixture to undergo autoignition. Similar to the laminar flame speed, ignition delay time varies with the fuel/oxidiser mixture, equivalence ratio, temperature, and pressure. In a real engine, commonly a higher pressure is used to improve the efficiency of the engine combustion. However, if the fuel mixture cannot sustain the pressure and temperature of the engine compression, the mixture can possibly have early autoignition which causes an engine knocking problem. Experimentally, the ignition delay time can be measured using a rapid compression machine or a shock tube. The definition of the start of the ignition can be the maximum rise of the temperature, pressure, or radical concentration, such as OH.

In this work, the current mechanism was tested for its performance in the prediction of the ignition delay time of the jet A-1, ethanol, and their blend. The calculation was solved by employing the closed homogeneous reactor of CHEMKIN PRO which is

analogous to the SENKIN code that was described in Section 2.2.4. The input for the model was set to be identical to the experimental condition of the data validation with the start of ignition defined by the maximum temperature rise in the reactor. Figure 5.26(a) shows the ability of the model to reproduce the work by Hu et al. [8] for the ignition delay of the stoichiometric methane/air at atmospheric pressure. The comparison shows that the current model generates relatively similar results to the ignition delay prediction by Hu et al. [8] using the same mechanism and reactor condition.

(a)   (b)
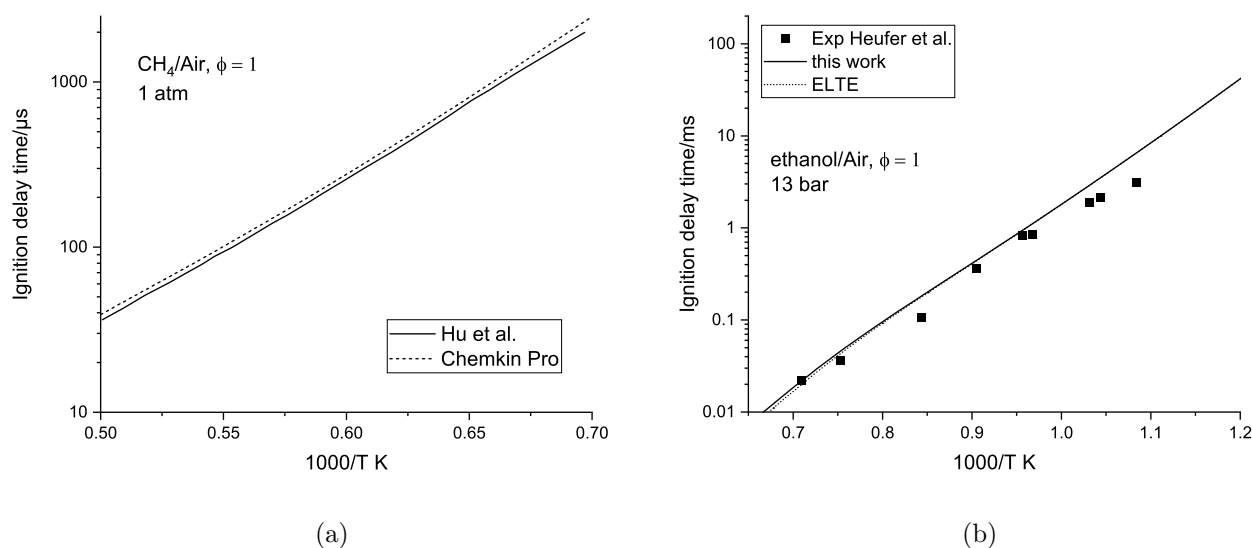
Figure 5.26: Ignition delay time prediction of (a) methane/air flames compared to the simulation by Hu et al. [8] and (b) ignition delay time prediction of ethanol flames compared to the experimental work by Heufer et al. [8].

The original ELTE mechanism was developed by employing many ignition delay data for the validation and thus the current mechanism should be able to predict the ignition delay of ethanol accurately. Figure 5.26(b) shows the prediction of the ignition delay time by the current and ELTE mechanisms for stoichiometric ethanol/air mixture at 13 bar from 830 to 1400 K. The result indicates that the prediction from both models was very similar and the addition of the other sub-mechanism does not affect much to the accuracy of the ignition delay time prediction of the ethanol flame. Compared to the experimental data by Heufer et al. [8], both models are relatively accurate in the temperature range of 900 to 1428 K which shows an ignition delay time reduction with the temperature increase.

Further validation is to determine the accuracy of the current model and mechanism to predict the ignition delay time of jet A-1. Figure 5.27 presents the prediction of the ignition delay time of jet A-1 from this work, AFRM, and Aachen mechanism as well as the experimental data from De Toni et al. [15]. The current mechanism

shows better accuracy than the AFRM mechanism at the compared pressures and stoichiometry. The AFRM mechanism failed to follow the experimental data at low temperature and it is relatively linear with temperature. The Aachen mechanism was closer to the experimental data than the current mechanism in all simulation cases. The inability of the AFRM mechanism was caused by the development of this mechanism which targetted the experimental data from a counter-flow flame and jet-stirred reactor. Meanwhile, the good agreement of the Aachen model was caused by the involvement of the ignition delay time validation in the development of this mechanism and its sub-mechanisms, such as n-decane.

(a)

(b)

(c)

(d)
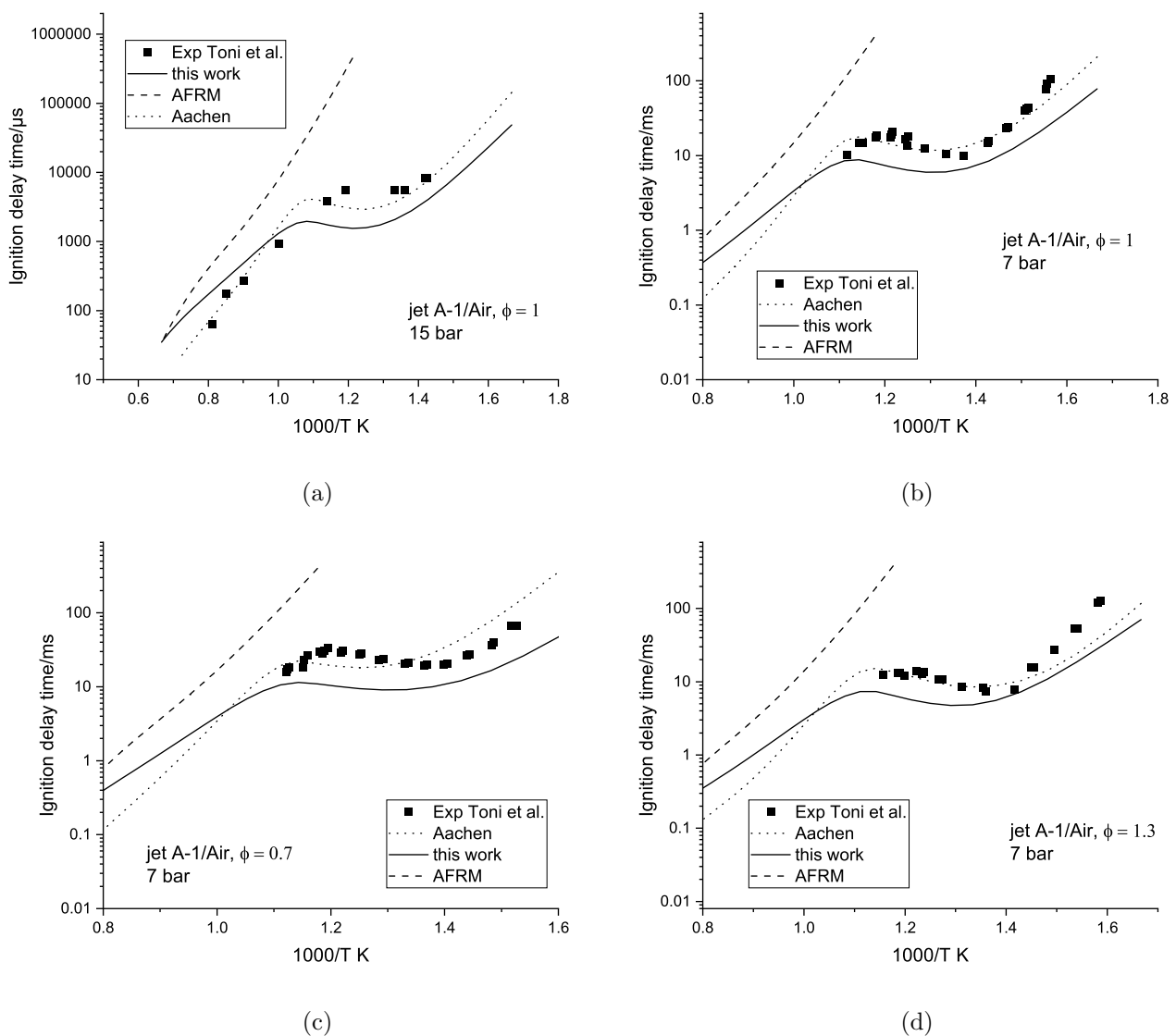
Figure 5.27: Ignition delay time prediction of jet A-1 flames in comparison with the experimental data from De Toni et al. [15].

Figure 5.28(a) and 5.28(b) present the prediction of the ignition delay time of the 50/50 ethanol/jet A-1 blend by molar and volume, respectively. The simulation

covers the effect of the change of the pressure, temperature, equivalence ratio, and ethanol concentration. It can be seen from the results that the ignition delay time of both mixtures becomes faster with temperature increase. At the same pressure and temperature, changing the equivalence ratio to 0.7 increases the ignition delay time to be slower than the stoichiometric condition while increasing the equivalence ratio to 1.3 reduces the ignition delay time to be faster than that. The difference between both mixtures is that the ignition delay time was slower at the 50 per cent volumetric ratio. This was caused by the higher ethanol fraction in the reactants which also affects the reduction of the non-linearity of ignition delay profile with the temperature in low-temperature region.
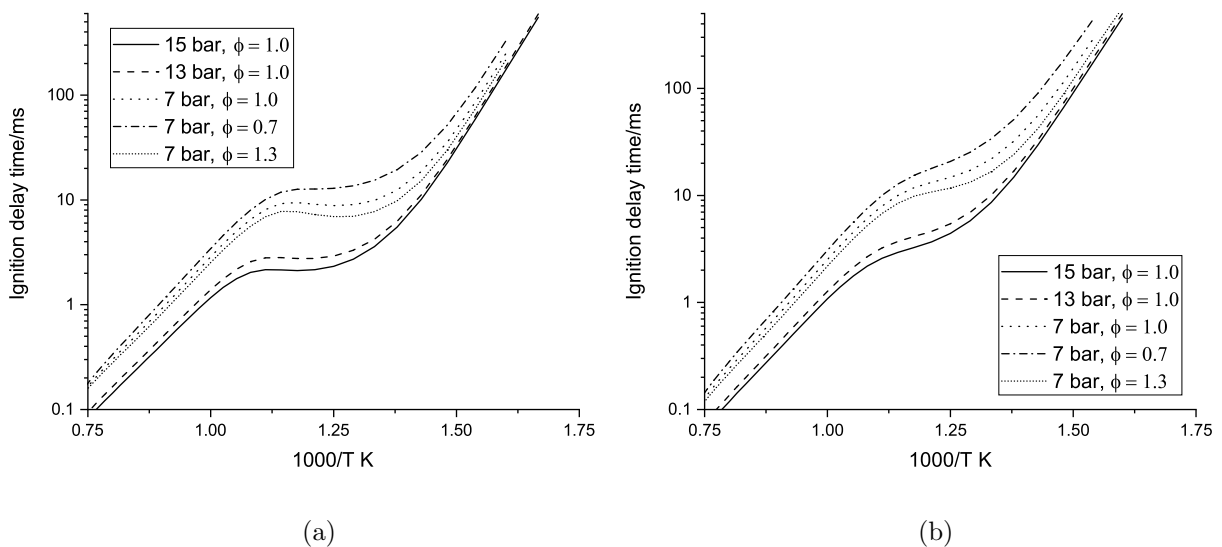
Figure 5.28: Ignition delay time prediction of E50 flames (a) by molar and (b) volume fraction.

5.5 Stirred Reactor

Validation with the experimental data of the species measurement from a stirred reactor was performed to assess the accuracy of the current model as well as other ethanol and jet fuel mechanisms. The calculation of the stirred reactor model was solved using the PSR code that was explained in Section 2.2.2. To validate the input of the PSR model, the modelling work by Burke et al. [16] was reproduced by using the same mechanism and reactor condition as presented in Figure 5.29. Compared to the stirred reactor by Burke et al. [16], the current PSR input shows a relatively similar trend for the species mole fraction with temperature variation. A slight discrepancy was found in the prediction of the oxygen and methanol, in which their profile in the current model was higher than Burke et al. [16] work, while the methanol was sightly lower. This

187

should not be an issue since the given input for this simulation was given as mentioned in the article by Burke et al. [16], which is 2000 ppm methanol and 3000 ppm oxygen.
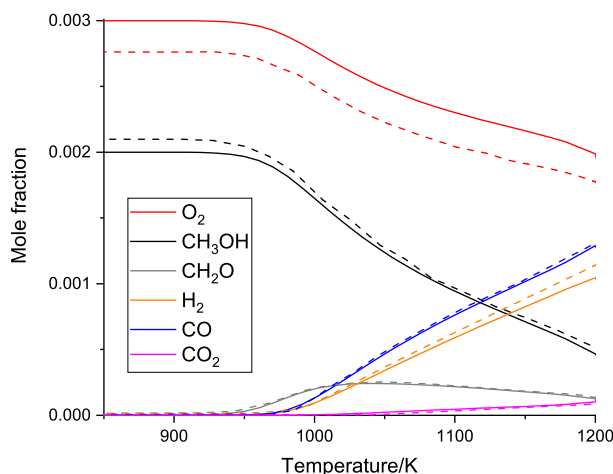
Figure 5.29: Simulated species concentration of 2000 ppm methanol, 3000 ppm O_2, with balance N_2 at 1.0 atm and $\tau = 0.05$ s from PSR and comparison to Burke et al. [16] (dashed lines).

Figure 5.30 shows the simulated mole fraction of the major and minor species of a stoichiometric ethanol/oxygen mixture with a balance nitrogen by the current and ELTE mechanisms at 10 atm and $\tau = 0.7$ s. The prediction from the model was compared to similar experimental data by Dagaut and Togbe [17]. The prediction from both models was relatively similar in predicting the mole fraction of ethanol at a different temperature which is decreasing with the temperature increase. Compared to the experimental data, the prediction of the ethanol profile from both models was lower in the lower temperature region. At low and high temperature, the main consumption of ethanol fraction was the H-abstraction reactions by the radicals.

(a)

(b)
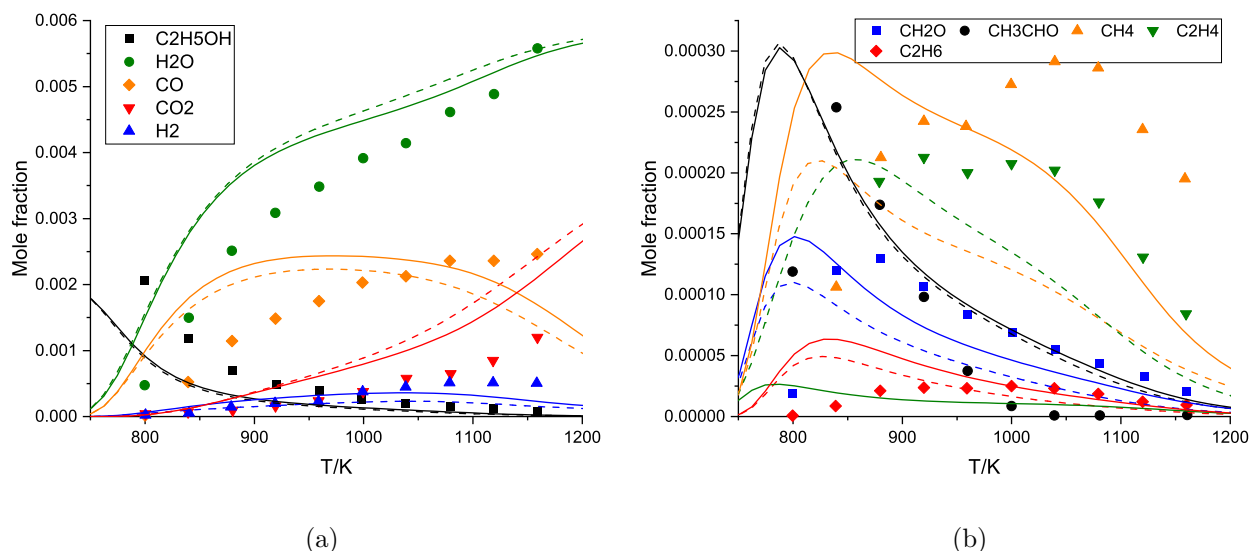
Figure 5.30: Simulated species concentration of stoichiometric ethanol/oxygen mixture balanced with nitrogen at 10 atm and $\tau = 0.7$ s by current model (solid lines), ELTE model (dashed lines), and comparison to the experimental data by Dagaut and Togbe. [17].

Similar prediction for the water concentration was shown by both models which is higher than the experimental data at the intermediate temperature. The production of the water was mainly from the product of the H-abstraction of the hydrocarbon radical, mainly formaldehyde (CH_2O) and hydroxyethyl (C_2H_5O). The prediction of CO from both models over predicts the experimental data at low and intermediate temperatures while underpredicting the CO concentration at the high temperature. Also, the prediction of the CO_2 was higher than the experimental data and a higher discrepancy was found at high temperatures. The prediction from the current mechanism was slightly higher than the ELTE mechanism for CO but lower for CO_2. The concentration of CO and CO_2 were related since the main consumption reaction of CO was the main production of CO_2 which is the oxidation of CO by the OH radical. The concentration of hydrogen was relatively low, which is relatively well predicted by both models. The hydrogen appeared mainly as the product of the H-abstraction of hydrocarbon by the H atom radical and consumed to produce water.

The prediction of the formaldehyde from both models follows the same trend as the experimental data, but the occurrence of the peak was earlier in the model than the experimental data. The current model shows a higher formaldehyde concentration than in the ELTE mechanism at the same temperature because of the promotion of the reactivity of ethylene with the OH radical to form formaldehyde which only happened in the current mechanism. a relatively similar prediction of acetaldehyde (CH_3CHO) concentration was shown by both models and these are relatively similar to the experimental data but over predicts the concentration at high temperatures.

189

The acetaldehyde was mainly formed by the H-abstraction of hydroxyethyl by oxygen resulting in acetaldehyde and hydroperoxyl.

The trend of the methane concentration with temperature by the current and ELTE mechanism was relatively similar but the prediction from the current model was higher than the ELTE mechanism. This was caused by the higher reactivity of the reaction between formaldehyde with methyl which results in methane and formyl radical. The prediction of the ethylene concentration was different between the models while the current mechanism predicts a higher ethylene concentration than the ELTE mechanism. The reaction path analysis shows a different reactivity of consumption and production reactions of ethylene. The predicted mole fraction of ethane between both models was relatively similar while the prediction from the ELTE mechanism was slightly lower than the current mechanism. Compared to the experimental data, the prediction from both models was higher than the experimental data at low temperatures. Also, a similar source of the production and consumption of the ethane was found in both mechanisms. It was mainly formed by the recombination of the methyl radical while it was mostly consumed by the H-abstraction reaction with the OH radical. The higher rate of production in the current mechanism causes a slightly higher concentration of ethane at low and intermediate temperatures.

Further validation in the experimental data of species measurement from jet A-1 in a jet stirred reactor was performed in order to determine the accuracy of the model in predicting the species concentration at various temperatures. The experimental data was taken from Dagaut et al. [18] and the performance of several jet fuel mechanisms was also compared. The results of the simulation are presented in Figures 5.31, 5.32, and 5.33.

The prediction of the oxygen concentration from all models shows a similar trend which lowers the oxygen concentration with a temperature increase. In all the temperature range investigated, the best prediction was demonstrated by the AFRM mechanism while the current mechanism slightly over predicts the oxygen concentration at the high temperatures. The other mechanisms predict a lower oxygen concentration than the experimental data. At low temperatures, the oxygen molecule was consumed by the decomposition of the hydrocarbon species while at the higher temperatures, it was reacting with mostly hydrogen and other radicals. The prediction of the current mechanism was the most accurate in predicting the hydrogen concentration compared to the other species. However, it slightly over predicts the concentration at the low temperatures while under predicts in the high-temperature region. The formation of hydrogen was the result of the H-abstraction reaction by an H atom radical from a hydrocarbon species, mainly n-decane at low temperatures and smaller hydrocarbon at high temperatures.

The current and AFRM mechanisms achieved the best agreement for the prediction of CO_2 compared to the other mechanisms. Also, a good agreement with the CO profile was demonstrated by the current mechanism. The AFRM mechanism could follow the trend of the CO profile but the prediction was lower than the experimental data. The prediction of CO by the other mechanisms was relatively good at low temperatures, but a significant discrepancy was found at the high-temperature simulation. At low temperatures, the conversion of CO to CO_2 by the OH radical was low, but it increases with increasing temperature. This results in the reduction of the CO concentration and the escalation of the CO_2 at high temperature. The prediction of the formaldehyde from the current mechanism was relatively good at following the trend but it was slightly higher than the experimental data. The prediction of the other mechanisms, except the Hychem mechanism, was more accurate especially at lower temperatures, while at high temperatures the prediction by the AFRM mechanism was accurate. Formaldehyde was formed mainly from the ethene and OH radical and consumed by OH to form the formyl radical. The prediction of methane by the current mechanism was the most accurate compared to the other mechanisms at all temperatures. However, it slightly over predicts the methane concentration at low temperatures. Methane formation was mainly from the product of the higher hydrocarbon decomposition and mainly consumed to form methyl radical.

(a)

(b)

(c)

(d)

(e)

(f)
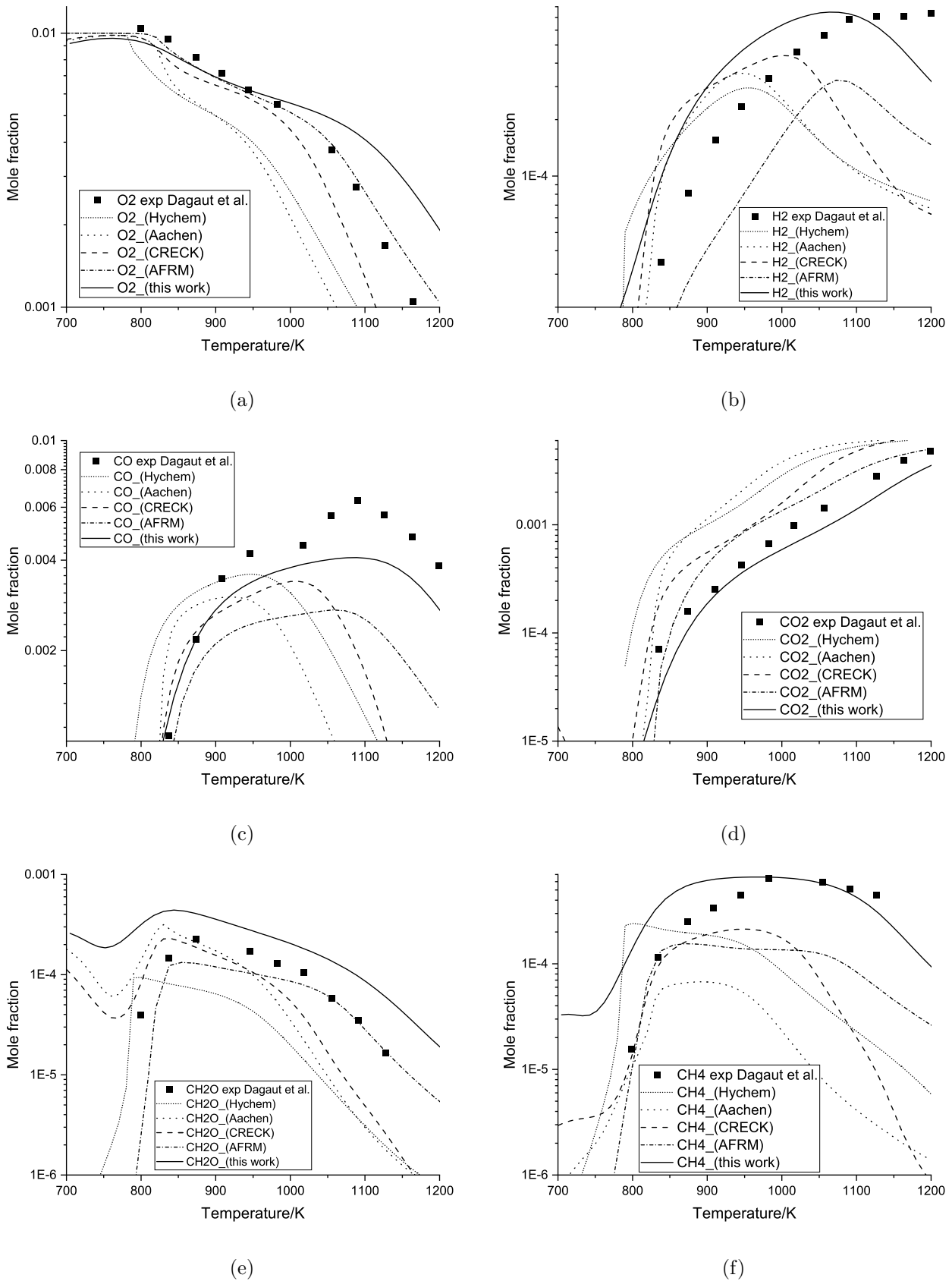
Figure 5.31: Simulated species concentration of stoichiometric jet A-1/oxygen mixture at 10 atm and $\tau = 0.5$ s balanced with nitrogen and comparison to the experimental data by Dagaut et al. [18].

(a)

(b)

(c)

(d)

(e)

(f)
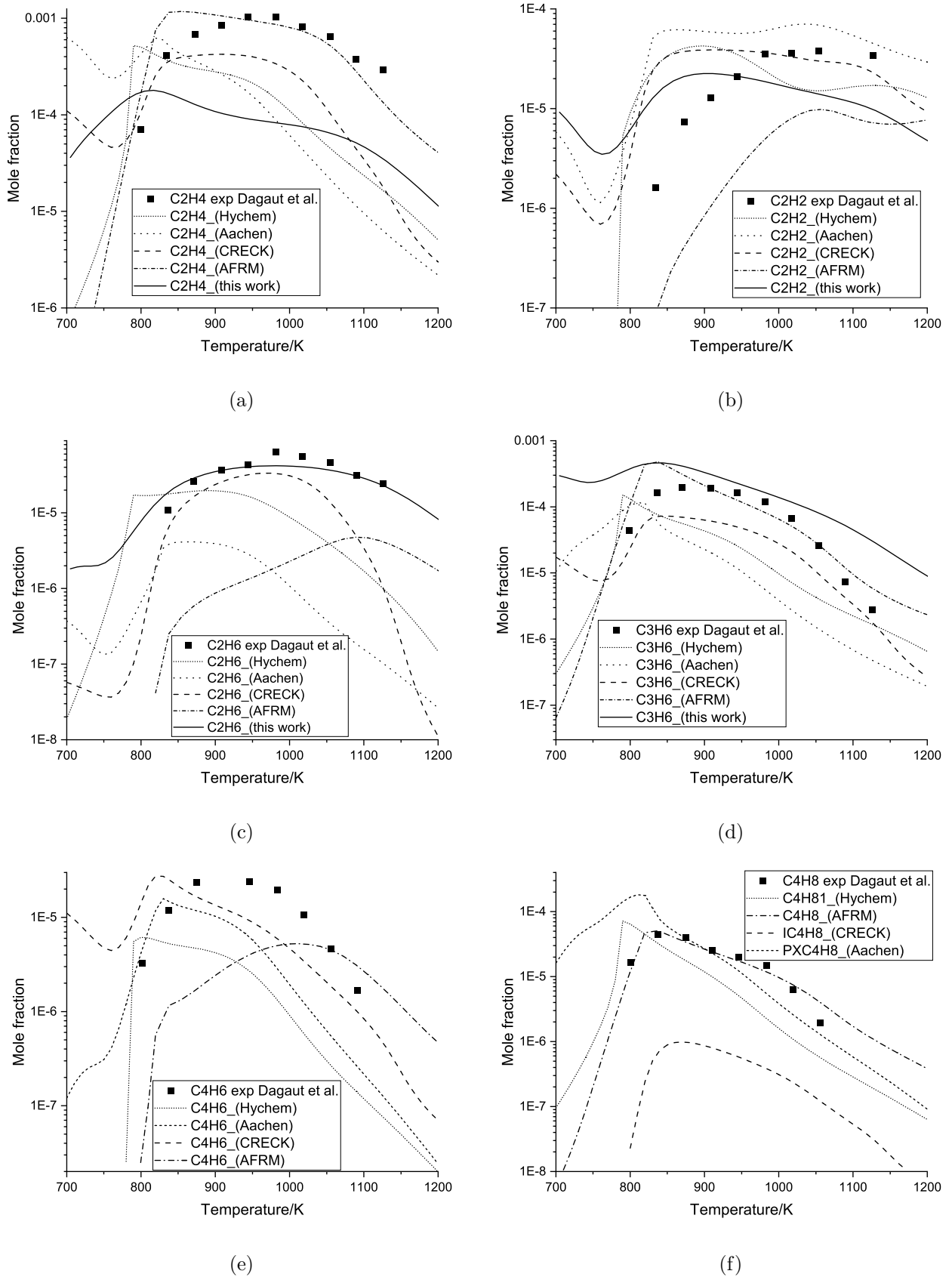
Figure 5.32: Simulated species concentration of stoichiometric jet A-1/oxygen mixture balanced with nitrogen at 10 atm and $\tau = 0.5$ s and comparison to the experimental data by Dagaut et al. [18].

(a)

(b)

(c)
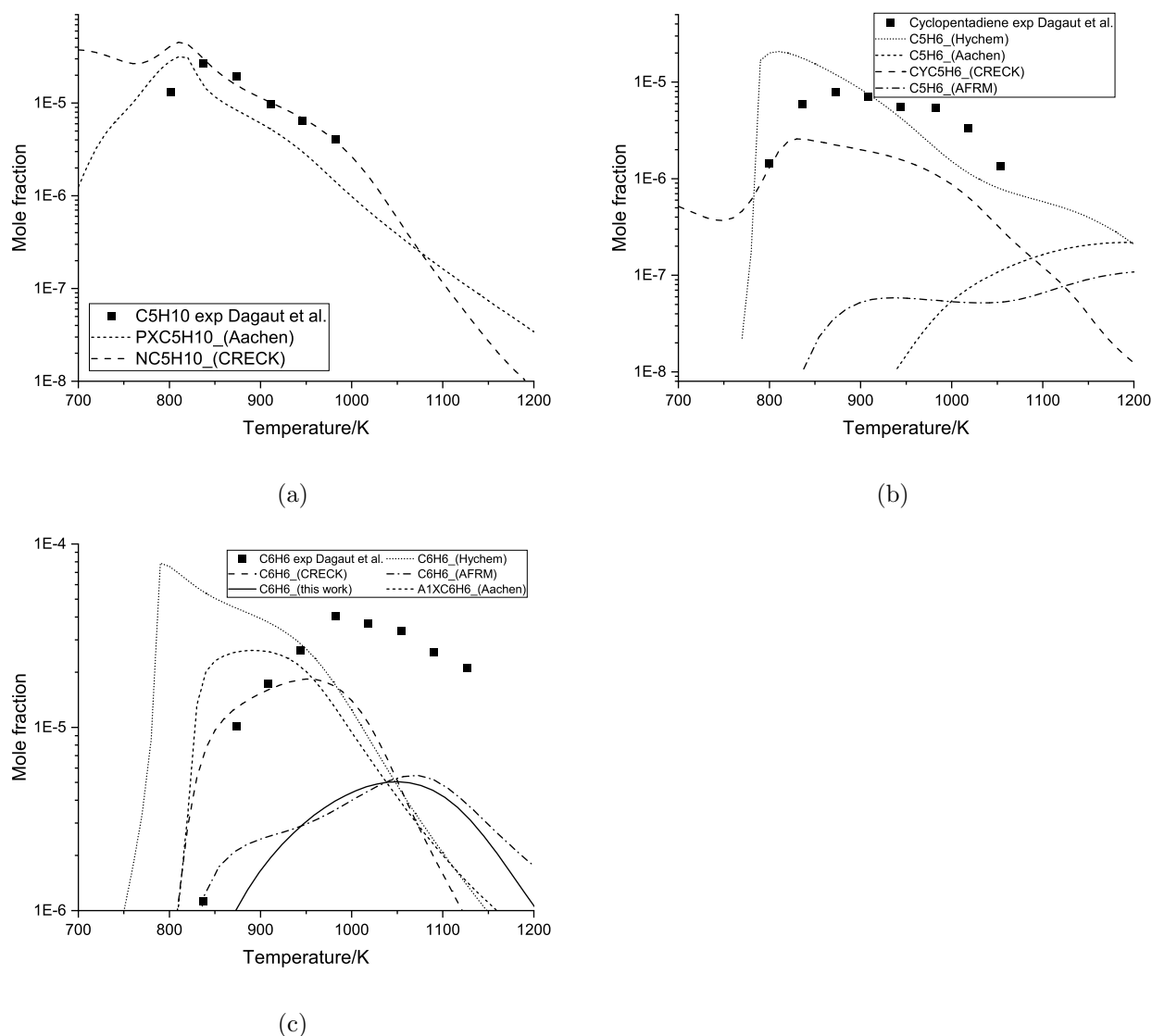
Figure 5.33: Simulated species concentration of stoichiometric jet A-1/oxygen mixture balanced with nitrogen at 10 atm and $\tau = 0.5$ s and comparison to the experimental data by Dagaut et al. [18].

Similar to the ethanol case, a major discrepancy with the experimental data was found for the prediction of ethene while the best agreement was found in the prediction by the AFRM mechanism. The underprediction of the ethene concentration may be caused by the overprediction of the formaldehyde concentration which was formed by the reaction of ethene with the OH radical. Meanwhile, the main production of ethene was the H-abstraction of ethyl or decomposition of decyl radicals. None of the compared models can predict the concentration of acetylene at low temperatures accurately while a good agreement with the CRECK model was found at a higher temperatures. In the current model, the acetylene species was formed from ethylenyl (C_2H_3) at low temperatures and propadiene (C_3H_4) at high temperatures. The best

194

agreement compared to other mechanisms was found in the prediction of the ethane concentration at all simulated temperatures. A relatively similar source of ethane production was found in the low and high temperatures which was mainly from the recombination of the methyl radical. The prediction of the propene concentration from the current mechanism was relatively good, especially at intermediate temperatures. The prediction from the AFRM mechanism was relatively accurate while the prediction from the other mechanisms was lower than the experimental data.

The decomposition path of the jet A-1 surrogate of the current model does not have the C_4 and C_5 species. Thus, it cannot be validated against the concentration of butadiene, butene, pentene, and cyclopentadiene from the experimental data. The CRECK mechanism was the most detailed mechanism compared to the other mechanisms and it has all the species that are targetted for the validation. The prediction of the benzene from the AFRM and current mechanisms was relatively similar at the intermediate temperatures. The production of benzene in both mechanisms was from the decomposition of toluene which is one of the surrogate components apart from n-decane. The prediction from the other mechanisms was closer to the experimental data but was not accurate for predicting the benzene concentration at high temperatures.

5.6 Concluding Remarks

In this chapter, a reaction mechanism of ethanol/jet A-1 blend was developed by employing the recently available sub-mechanisms from the literature. The reaction mechanism was employed to model the experimental work of the premixed laminar burner in the previous chapter and provided more detailed information on the chemical kinetic behaviour of the combustion process, especially by the use of the sensitivity and ROP analysis. The validation of the fundamental kinetic experiment, such as laminar flame speed, ignition delay time, and species concentration measurement from a jet-stirred reaction was relatively good. Some discrepancy was found in some C_1, C_2, and benzene profiles in the jet-stirred reactor validation. Generally, it performs better than the AFRM mechanism, especially for the prediction of the ignition delay time and the current mechanism can be used as an update for the jet fuel mechanism that uses n-decane/toluene as the surrogate. Further, the mechanism was used to predict the laminar burning velocity and ignition delay time for the ethanol/jet fuel blend, but there is no available experimental data for the validation. Considering the amount of the species and reactions in the other jet fuel mechanism, the current mechanism has a fewer amount of species and reactions and this results in the advantage of requiring less computional requirements for the chemical kinetics or reactive flow simulations when using CFD.

Chapter 6

Oxidation Stability

In this chapter, the oxidation stability of the jet A-1/ethanol blends was assessed by employing the PetroOXY method based on ASTM D7545 [174]. The test also involved the assessment of the oxidation stability of the jet fuel surrogates, such as n-decane, n-dodecane, methylcyclohexane, o-xylene, and 1,2,4 trimethyl benzene, the Aachen, and the CRECK surrogates, with the addition of an ethanol blend. Several antioxidants, such as butylated hydroxyanisole (BHA), butylated hydroxytoluene (BHT), 2,6-di-tert-butylphenol (DTBP), tert-butylhydroquinone (TBHQ), propyl gallate (PG), pyrogallol (PY), 2-tert-butyl-4,6-dimethylphenol (TBMP), were evaluated to determine its performance in improving the oxidation stability of ethanol. A modelling of the liquid-phase oxidation phenomena was attempted by employing an automated reaction mechanism generator and a customised python code to calculate the pressure drop as presented by the PetroOXY device.

6.1   Oxidation Stability Assessment Method

The fuel samples were obtained from similar suppliers from the experimental work described in Chapter 3, which was presented in Table 3.1. For each PetroOXY test, a 5 mL sample is required, and this was prepared by using a Costar sterile pipette and a pipette filler with an accuracy of 0.1 mL. For blending and handling the fuel, the sample was introduced in a sample bottle and mixed for approximately one minute to ensure the uniformity of the sample. An accurate scale, similar to the scale that was used for the MFC calibration, which was the TB-125D from Denver Instrument Germany, with an accuracy of 0.1 mg, was used to prepare the antioxidant samples. Approximately 5 mg of the antioxidant samples were introduced to the 5mL ethanol sample, which results in 1 g/L antioxidant concentration.

The PetroOXY was obtained from Anton Paar [175], and it was connected to the Oxy logger software for the data acquisition. A cleaning process was performed prior

to each test to ensure the purity of the testing chamber. When a test was completed, the fuel sample was removed from the testing chamber by using a pipette. Then, a purging procedure was performed to clean any contaminant at the inlet and the outlet of the oxygen supply. In order to clean the surface of the gold dish and the lid, a special soft sheet and acetone were used to ensure that the dish surface was not damaged, and oil was completely removed from the surface. An O-ring was used to seal the testing chamber from leaking, and this ring was replaced after a test run.

During the test, the PetroOXY device was set to the ASTM D7545 standard temperature and pressure, which are 700 kPa and 140 °C, respectively. Once the fuel sample was placed, the testing chamber was pressurised with oxygen to 700 kPa. After it reached the targetted pressure, the pressurised gas in the sampling chamber was purged and then re-pressurised to 700 kPa. This procedure was performed to minimise the nitrogen contamination from the air. The oxygen gas was supplied by BOC with 99.999% purity (N5) and connected using an oxygen-clean tubing. Subsequently, the testing chamber was heated to 140 °C, which caused the increase in the pressure inside the testing chamber. Afterwards, the temperature was maintained, and the data of the reactor pressure, temperature, and heating power was recorded by the PetroOXY device. The pressure inside the testing chamber decreased with time due to the consumption of oxygen by the fuel, which reduced the amount of oxygen gas at the headspace of the testing chamber. After a 10 per cent in the pressure drop was achieved from the maximum pressure, the test was finished, and the data can be downloaded from the data logging software. The time required to achieve the 10 per cent pressure drop is also called the induction period.

The repeatability of the PetroOXY device has an excellent repeatability in the test result. A verification fluid, which was obtained from the manufacturer, was used to check the repeatability of the PetroOXY device. The result showed that the time to achieve a 10 per cent pressure drop, that was indicated by the PetroOXY device, was in the range of the verification fluid certificate. The 10 per cent pressure drop for the fluid was certified by Anton Paar at 93 minutes with 9 minutes deviation for 700 kPa and 140 °C while the test achieved it for 99.55 minutes. Moreover, the repeatability test was performed twice by measuring the pressure drop of 50 per cent ethanol/jet A-1 mixture. The results showed that the time to achieve a 10 per cent pressure drop was shifted by 0.8 minutes from the first test while the maximum pressure shifted by 2 kPa. Therefore, for this study, the samples were only tested once due to the reliability of the PetroOXY test.

6.2 Jet A-1/Ethanol Blend

Figure 6.1 shows the results of the PetroOXY test for the jet A-1/ethanol mixtures at 700 kPa and 140 °C. It is clearly seen that the pure jet A-1 fuel has the highest oxidation stability by achieving 10 per cent pressure drop in approximately 24 hours. Meanwhile, the ethanol has lower oxidation stability than A-1, and required less than six hours to reach 10 per cent pressure drop. Consequently, increasing the ethanol concentration in the jet A-1 blend decreased the stability of the fuel. All samples showed a different pressure rise with the increase in temperature. Jet A-1 showed the lowest maximum pressure, which is approximately 1000 kPa, while ethanol had the highest maximum pressure during the test, which is approximately 1650 kPa. The blends indicate that the peak pressure escalates with the increase of ethanol concentration in the blend. The higher maximum pressure in the ethanol sample might be caused by the higher volatility of ethanol than the jet A-1, where the vapour pressure of ethanol is more than 15 times of that of kerosene at room temperature [176].

(a)   (b)
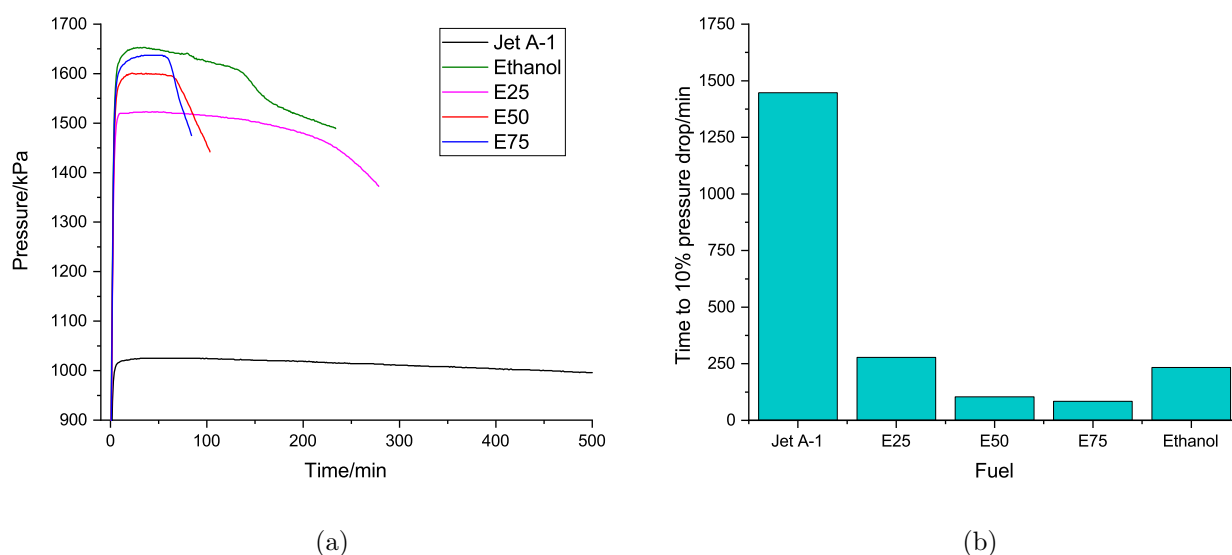
Figure 6.1: (a) Pressure drop time history and (b) required time to 10 per cent pressure drop of the PetroOXY test of the jet A-1/ethanol fuel blends.

The longer induction period in the jet A-1 sample can be caused by several factors, such as the presence of the antioxidant, the chemical characteristic, and the oxygen content in the sample. Unlike the ethanol sample that was obtained from a pure solvent, the jet A-1 sample was taken from commercial jet fuel products. Consequently, antioxidant was added to the jet fuel product up to 24 mg/L as stated in the jet fuel standards and the presence of antioxidant can improve the oxidation stability of the fuel [21]. Also, a natural antioxidant, such as organic sulphur compounds, may exist in the jet A-1 sample, which may have a sulphur content up to 0.3 per cent. It was reported

by Bolshakov [177] that the sulphur compounds inhibit the oxidation of hydrocarbon mixtures.

According to the study by Naegeli [178], the sulphur content in the jet fuel causes the formation of gums and deposits. Also, the fuel sample that requires higher temperature and a longer induction period generates more gums and deposits during the autoxidation process. Figure 6.2 shows the visual appearance of the fuel samples before and after the tests. It is observed that the change of colour was dominant in the jet A-1 sample while by increasing the ethanol concentration, the colour of the sample after the test becomes even more clearer. The increase of oxygen concentration in the liquid may also contribute to the acceleration of the autoxidation process. Referring to Henry's coefficient data in Table 2.1, the coefficient for ethanol is approximately three times greater than that of kerosene, which leads to approximately three times higher oxygen concentration in the fuel at the same partial pressure of oxygen. Moreover, the maximum pressure during the test of the ethanol sample was higher than the jet A-1 sample and this may accelerate the autoxidation process due to the increase in the oxygen concentration.

(a)   (b)   (c)

(d)   (e)
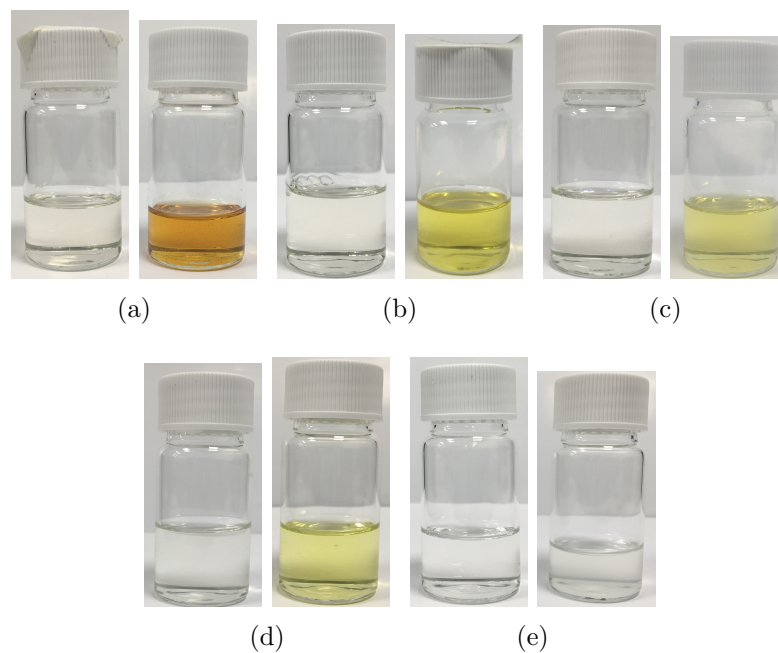
Figure 6.2: The visual appearance of the jet A-1/ethanol blend samples (left) before and (right) after the PetroOXY test for (a) pure jet A-1, (b) E25, (c) E50, (d) E75, and (e) pure ethanol.

6.3 Multi Component Surrogate

Unfortunately, there was no analytical equipment that can be used to detect the contributing species in the autoxidation process. Alternatively, modelling work was attempted to explain the autoxidation process of the samples. Since it was difficult to model the real jet A-1 due to the numerous compounds that exist in the real fuel, two surrogate models were tested to replicate the behaviour of the real jet A-1 fuel. Surrogate A consists of 80:20 n-decane and 1,2,4 trimethyl benzene by mass while Surrogate B comprises of 60:20:20 n-dodecane, o-xylene, and methylcyclohexane by volume. These surrogates were similar to the study of surrogate flames in the previous chapter, which was based on the study from Honnet et al. [80] and Humer et al. [148].

Figures 6.3(b) and 6.4(b) present the results of the PetroOXY test of the surrogate A and B, respectively. The induction time of both surrogates was much less than the real jet A-1. This might be caused by the absence of the additives and natural antioxidant in the sample. The effect of the ethanol addition to the surrogate was also different than the jet A-1. The induction time of both surrogates increased with the increase of ethanol concentration. Meanwhile, pure ethanol has a slightly lower induction time than both surrogates. The behaviour of the pressure history during the test was similar to the jet A-1 samples where the maximum temperature increased with increasing ethanol concentration. Meanwhile, the maximum pressure of the surrogates was similar to that of the jet A-1 sample.

(a)   (b)

Figure 6.3: (a) Pressure drop time history and (b) required time to 10 per cent pressure drop of the PetroOXY test of the surrogate A/ethanol fuel blends.

(a)   (b)

Figure 6.4: (a) Pressure drop time history and (b) required time to 10 per cent pressure drop of the PetroOXY test of the surrogate B/ethanol fuel blends.

6.4 Single Component Surrogate

A modelling work of the multi-component surrogates was attempted using a reaction mechanism generator. However, the multi-component surrogates required more computational resources and time. Alternatively, a single component surrogate was used for the modelling work. Figures 6.5 and 6.6 show the test results of n-decane and n-dodecane sample, respectively. A different effect of ethanol addition to both the n-decane and n-dodecane samples was shown in the 75 per cent ethanol concentration where the induction time decreased from the 50 per cent case. Meanwhile, in both multi-component surrogates, the induction time at 75 per cent ethanol blend was higher than the 50 per cent case.

The maximum pressure during the test was not very different between the real jet A-1, multi, and single component surrogates. The maximum pressure during the test increased to approximately a similar value with a similar increase in the ethanol concentration. This indicates that the maximum pressure during the test was controlled by the volatility of ethanol. By removing the cyclic compound in the single surrogate component, the stability of the 25 and 50 per cent ethanol mixture slightly increased. Meanwhile, the stability of n-decane was slightly higher than the n-dodecane. This might be related to the finding in the study of biodiesel, where the longer molecule chain and a less saturation in the C-H bond caused the reduction of the fuel oxidation stability [55]. In single and multi-component surrogates, the presence of ethanol increases the oxidation stability, while pure ethanol has a slightly higher induction time than the single component surrogates and a lower induction time than the multi-component

201

surrogates.

(a)   (b)

Figure 6.5: (a) Pressure drop time history and (b) required time to 10 per cent pressure drop of the PetroOXY test of the n-decane/ethanol fuel blends.
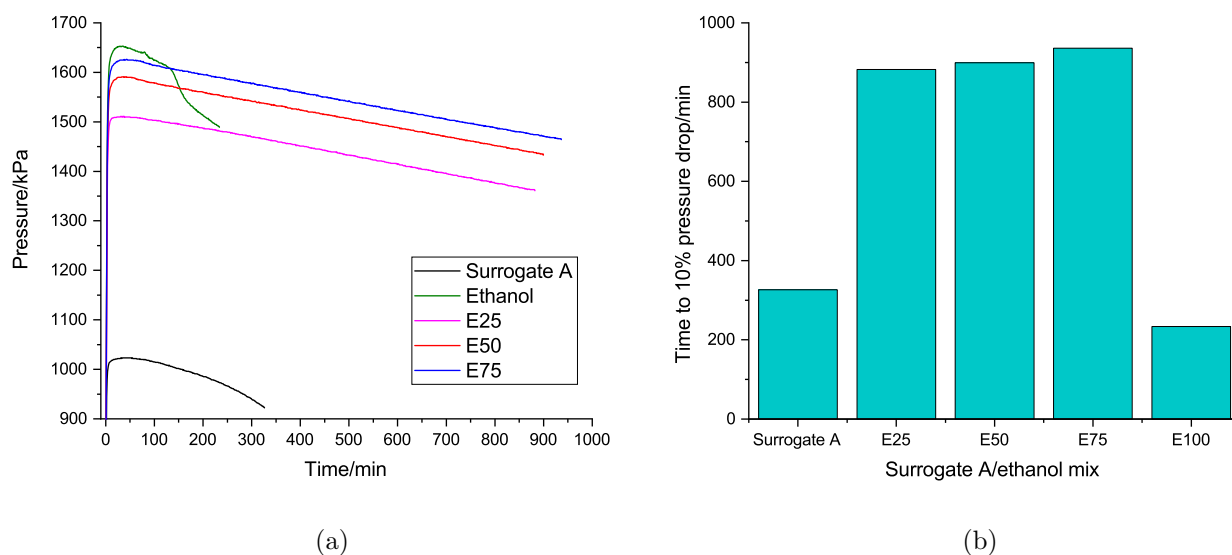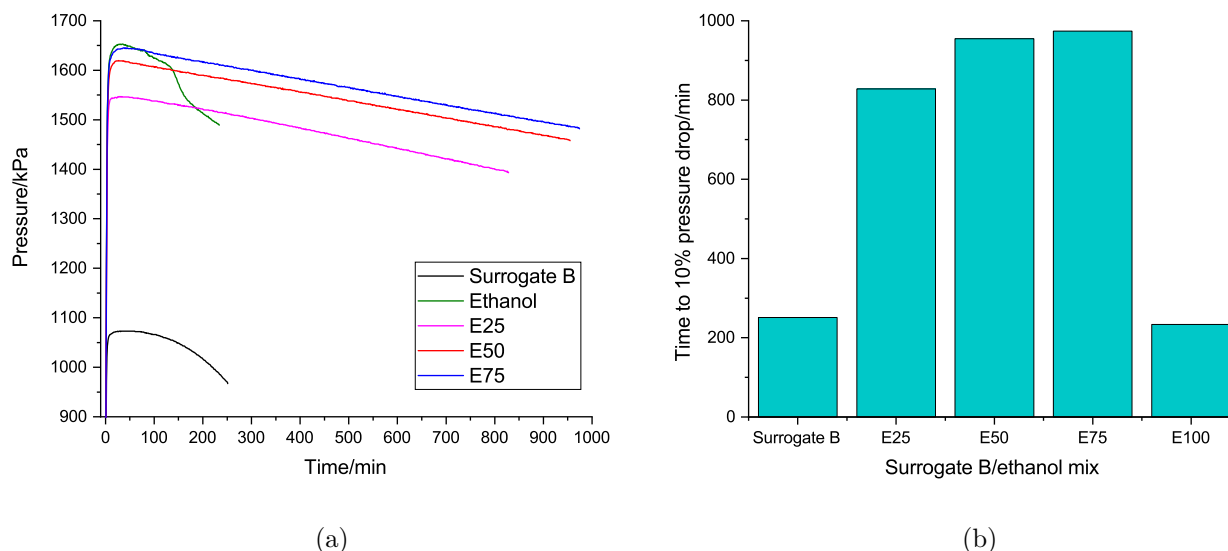

(a)   (b)

Figure 6.6: (a) Pressure drop time history and (b) required time to 10 per cent pressure drop of the PetroOXY test of the n-dodecane/ethanol fuel blends.

6.5 Antioxidant Test

Despite the ethanol addition improving the oxidation stability of the jet fuel surrogates, it behaves contrary to the real jet A-1 fuel. In order to enhance the oxidation stability of ethanol, several antioxidants were tested to determine its effect on the induction time

202

of ethanol during the PetroOXY test. The selected antioxidants were studied in several published studies to improve the fuel oxidation stability. 1 g/L of the antioxidants were added to the ethanol sample while the information about the quality and structure of the antioxidants are presented in Table 6.1 and Figure 6.7, respectively.
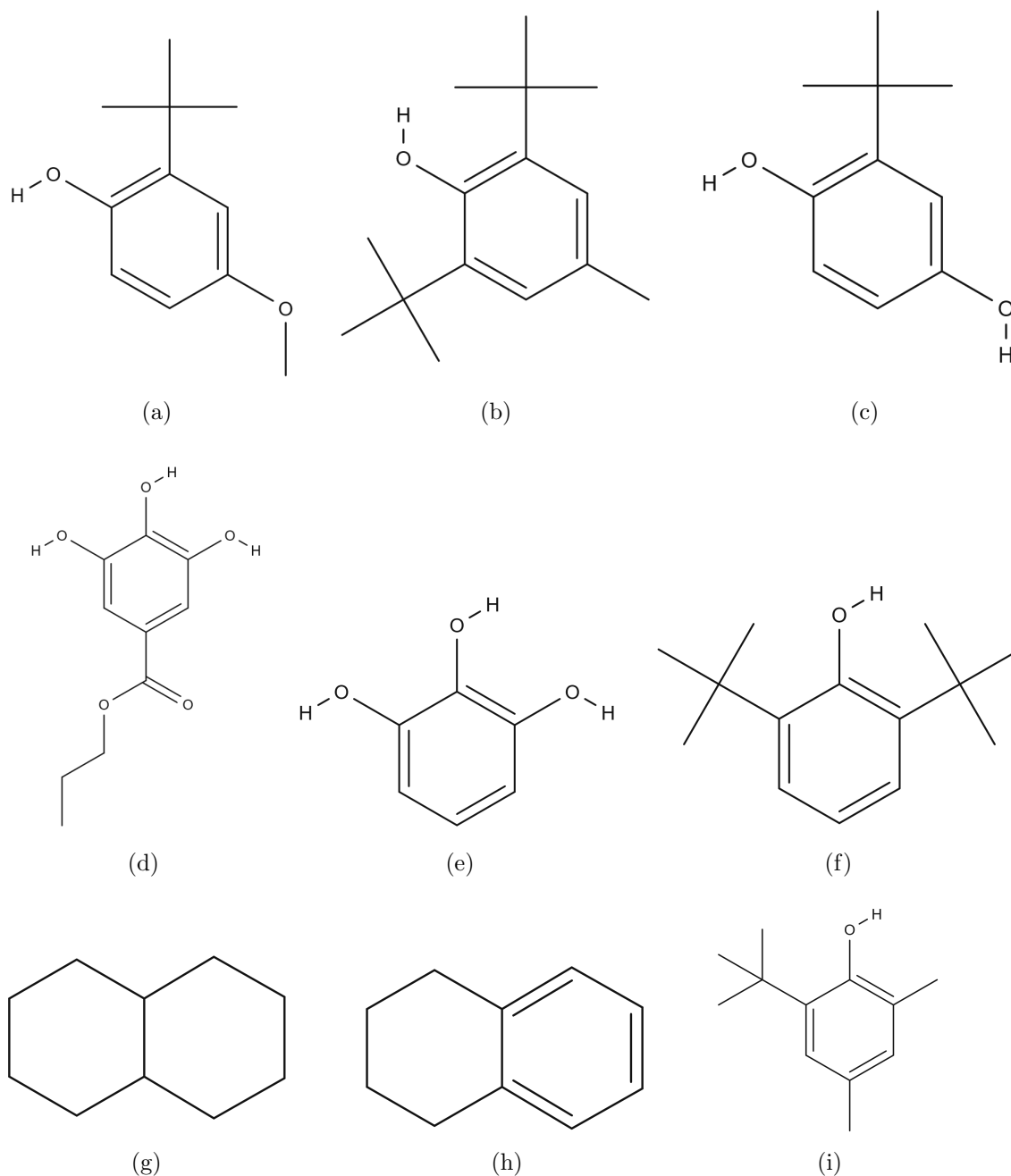
Figure 6.7: Chemical structure of the antioxidants: (a) BHA, (b) BHT, (c) TBHQ, (d) PG, (e) PY, (f) DTBP, (g) decalin, (h) tetralin, and (i) TBMP.

Table 6.1: Supplier and quality of the antioxidants.

Antioxidant	Quality	Supplier
Butylated hydroxyanisole (BHA)	99% (FCC, FG)	Sigma-Aldrich
Butylated hydroxytoluene (BHT)	≥99% (GC)	Sigma-Aldrich
tert-Butylhydroquinone (TBHQ)	97%	Sigma-Aldrich
Propyl gallate (PG)	≥98% (HPLC)	Sigma-Aldrich
Pyrogallol (PY)	≥98% (HPLC)	Sigma-Aldrich
2,6-di-tert-butylphenol (DTBP)	99%	Sigma-Aldrich
Decalin	≥99% anhydrous	Sigma-Aldrich
Tetralin	99% anhydrous	Sigma-Aldrich
2-tert-butyl-4,6-dimethylphenol (TBMP)	98%	ChemCruz

Figure 6.8 presents the time history and the induction time of the ethanol sample with 1 g/L antioxidant addition from the PetroOXY test. From these results, the addition of the antioxidants to the ethanol sample increases the induction time while each antioxidant showed different improvement to the ethanol oxidation stability. A slight extension to the induction time was found in the propyl gallate addition while the other antioxidants enhance the induction time to more than three times. The best improvement of in the ethanol stability was found in the pyrogallol addition. The addition of these antioxidants did not affect the maximum pressure during the test, which reached 1650 kPa and then dropped in a differently manner for each antioxidant.
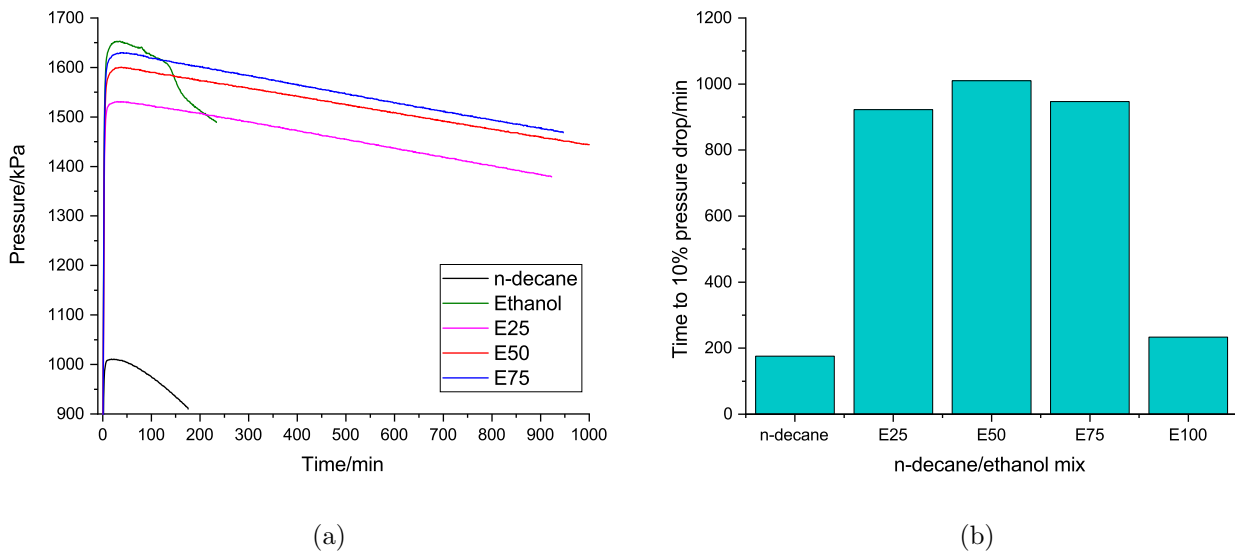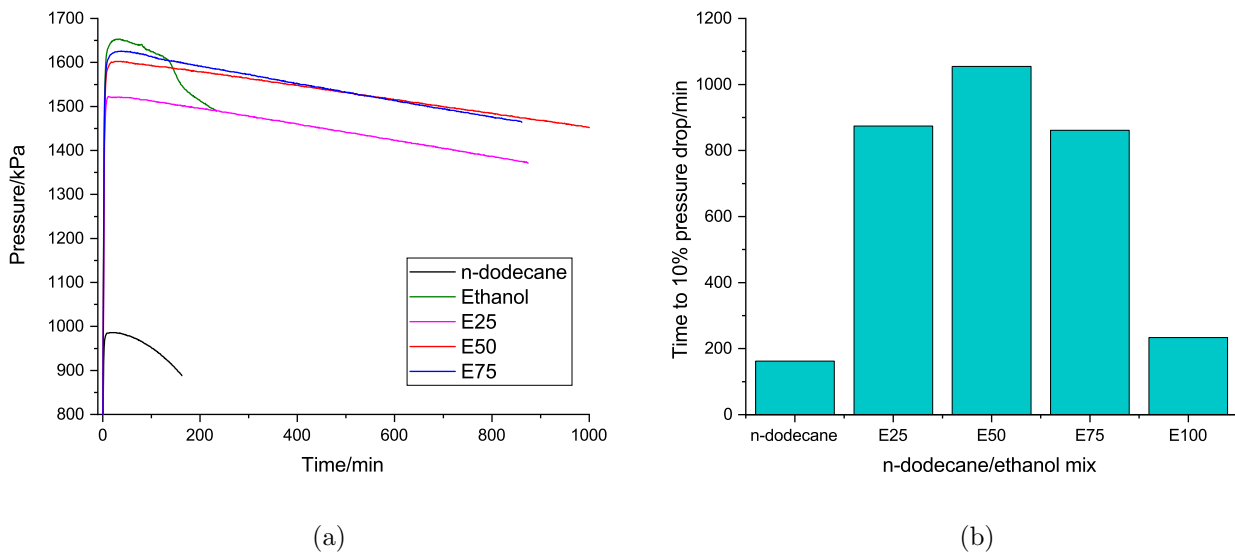

(a)   (b)
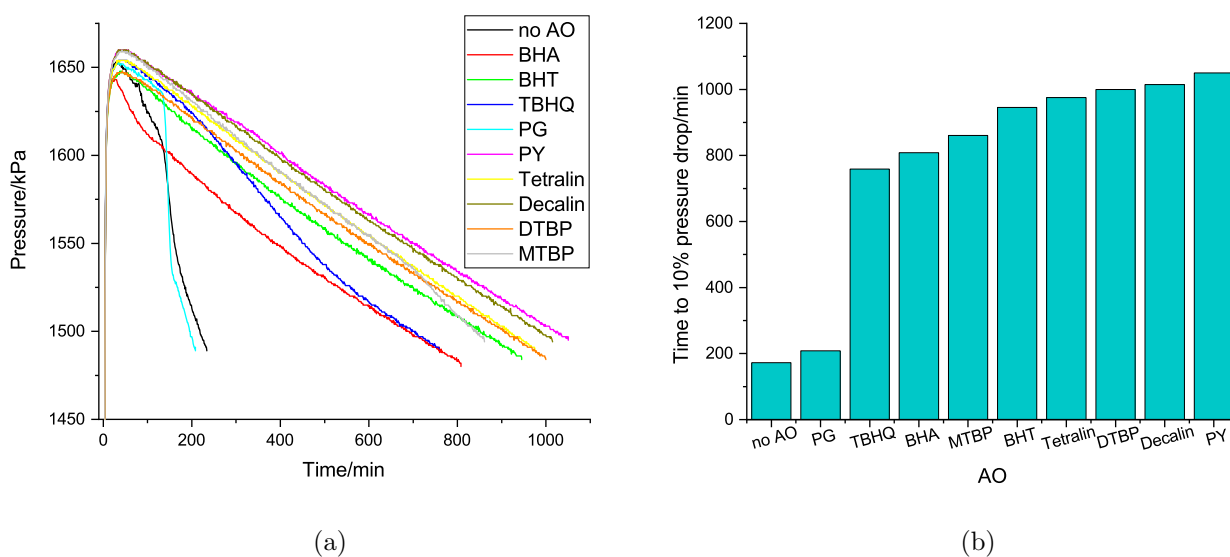
Figure 6.8: (a) Pressure drop time history and (b) required time to 10 per cent pressure drop of the PetroOXY test of the 1 g/L addition of antioxidants to ethanol.

The selected antioxidants, except decalin and tetralin, are monohydroxy or polyhydroxy phenolic antioxidants. Generally, the antioxidants delays the autoxidation process by preventing the formation of the intermediate peroxyl radical [54]. The antioxidants donate the hydrogen atom to the radical and produce less reactive species. The radical antioxidant species is relatively stable due to the delocalisation of radical electron, and furthermore, it can react with other radicals to form a stable species.

The use of PY, PG, TBHQ, BHA and BHT for improving the oxidation stability of biodiesel has been studied by Zhou et al. [54]. The study shows that the stability of the biodiesel sample increased with the increase in the antioxidant concentration while the increase in temperature decreases the induction time. A similar finding with this study was found for the performance of the PY, which was the best in increasing the oxidation stability of the fuel compared to the other antioxidants. Meanwhile, the results of the other four antioxidants were different in this study where the PG showed the least effective antioxidant while in the study of biodiesel, it was slightly less effective than the PY. The performance of decalin and tetralin as an antioxidant for HEFA-SPK has been studied by Amara et al. [112], which shows the inhibition behaviour to the autoxidation process at low concentration. The DTBP and TBMP are commonly used in jet A-1 to inhibit the peroxidation of hydrocarbons which leads to deposit formation by autoxidation [179]. Therefore, while they are effective for increasing the ethanol stability, they are also compatible with jet A-1.

6.6 Modelling The PetroOXY Test

A modelling work was performed to model the autoxidation during the PetroOXY test. There are three samples that were modelled, which are ethanol, n-decane, and n-dodecane. The reaction mechanisms of these samples were generated by employing the Reaction Mechanism Generator (RMG) [127]. The reason for using the RMG is the availability of the liquid phase reactor, which represent the PetroOXY reactor. The version of the RMG and the database was 2.3.0, which was executed in the university high-performance computer facility (ShARC). The RMG requires an input file to specify the initial reactant species, its concentration, reactor temperature, and the duration of the reaction. A similar condition to the real PetroOXY test was given for the temperature and the fuel concentration. Meanwhile, the concentration of the oxygen in the liquid phase was determined by using Henry's law, which was described in Section 2.6, and the maximum pressure during the PetroOXY test. The concentration of oxygen was set to a constant value as recommended by the documentation of the RMG for more optimum reaction mechanism generation.

The output of the RMG run are the reaction mechanism in CHEMKIN and Can-

tera format as well as the simulated mole fraction of the contributing species. For the ethanol case, the generated reaction mechanism has 13 species and 26 reactions. Meanwhile, the n-decane mechanism has 11169 reactions among 193 species, and the n-dodecane mechanism has 262 species and 23083 reactions. The number of species and reactions increase with the larger molecule, and this consumed much of the computational resource to run these mechanisms. Since the RMG liquid reactor was not able to calculate the pressure in the headspace of the PetroOXY testing chamber, a python code was employed to calculate this parameter. The python program was written by Clements [180] and the documentation of this program can be found in Appendix A.
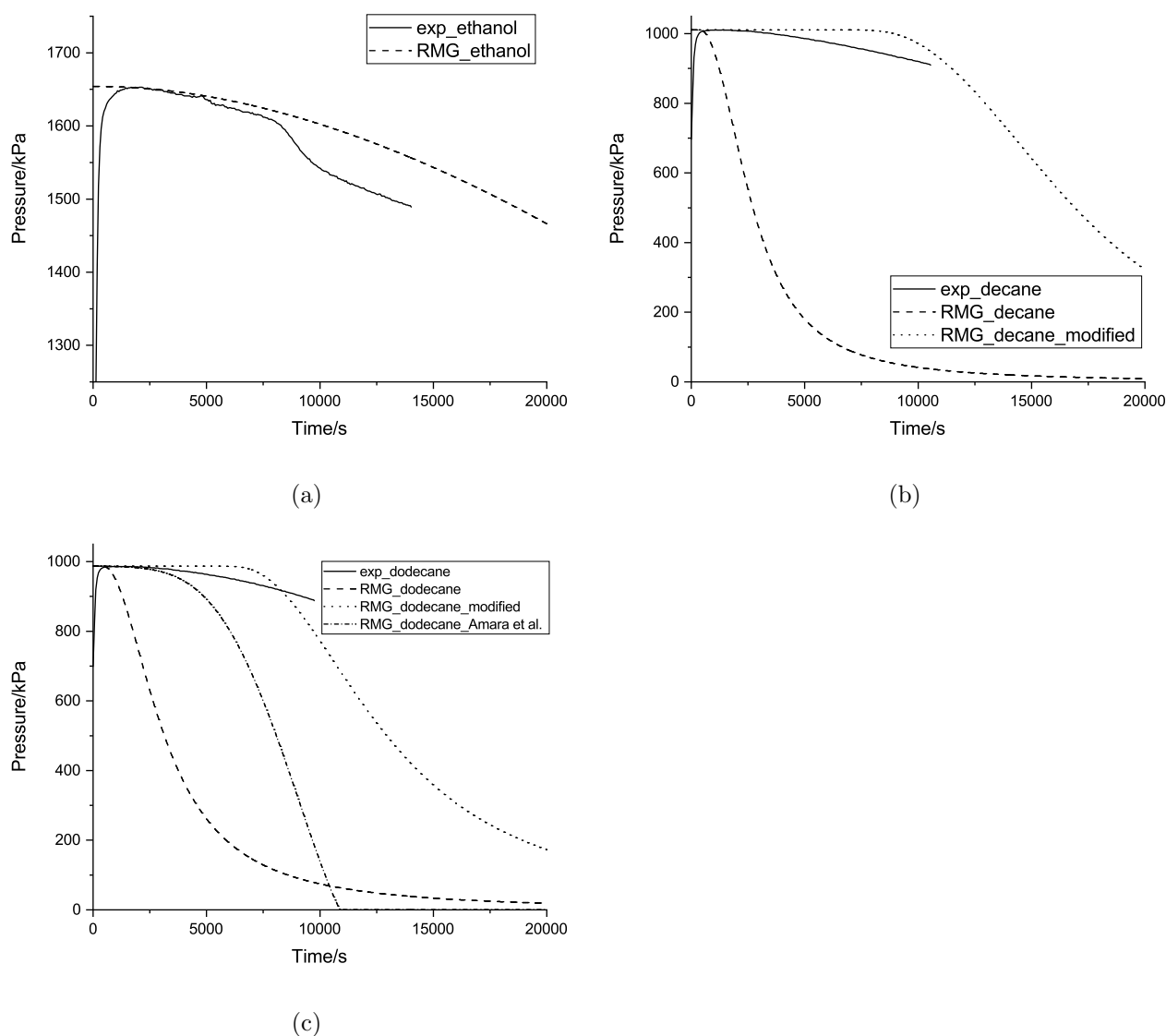

(a)

(b)

(c)

Figure 6.9: Simulation of the PetroOXY tests of the (a) ethanol, (b) n-decane, and (c) n-dodecane samples and the comparison with the experimental data.

Figure 6.9 presents the simulated pressure profile obtained from the model for ethanol, n-decane, and n-dodecane as well as a comparison with the experimental data.

It can be seen that the model ignores the pressure increase due to the temperature rise in the testing chamber. It starts from the maximum pressure and then drops with the oxygen consumption. The prediction of the pressure drop using the RMG mechanism was most accurate for the ethanol case while the prediction for the n-decane and n-dodecane show a faster pressure drop than the experimental data.

The simulated mole fraction of the fuels and oxygen are similar in all cases where it decreases with time. The consumption of the fuels and oxygen is caused by the initiation reactions which produces intermediates. Mostly, n-dodecane, n-decane, and ethanol undergo an H-abstraction reaction with oxygen to form dodecyl, decyl, and ethoxy radicals, respectively. Furthermore, the abstracted hydrogen atom and oxygen molecule produce the hydroperoxyl radical. The profile of the mole fraction of these intermediates radicals is relatively similar, which increases and peaks with the consumption of the fuel and then decreases rapidly with different rates. An exception to this trend was found in the concentration profile of hydroperoxyl in the ethanol case where it increases continuously.

The intermediates that are formed during the initiation process react with more stable species and forms more radicals during the propagation step. Finally, these radicals form stable species which is the termination process of the autoxidation process. In the autoxidation of ethanol, the model indicates that there are three main products of autoxidation which are hydrogen peroxide (H_2O_2), acetaldehyde (C_2H_4O), and hydroperoxy ethanol ($C_2H_6O_3$). For the case of the n-decane and n-dodecane, the RMG reaction path visualiser could not generate the reaction path analysis. This may be caused by the size of the reaction mechanism that is much larger than the ethanol mechanism. Alternatively, the reaction path analyser from the CHEMKIN closed-homogenous reactor was used.

For the n-decane and n-dodecane, relatively similar functional group reactions were found following the formation of the alkyl radical ($R^\bullet$). The alkyl radical reacts with oxygen to form the peroxyl radical (ROO) or with hydroperoxyl (HO_2) to form the hydroperoxide (ROOH). Furthermore, the hydroperoxide can undergo more H-abstraction in the other carbon atom to form more ROOH function through the same mechanism and forms $HOOR_1 - R_2OOH$. The ROOH formation is the termination step of the n-decane and n-dodecane autoxidation, thus the concentration of ROOH increases with the consumption of oxygen. Meanwhile, the concentration of ROO peaks then reduces due to the formation of ROOH. The abundant species in the n-decane and n-dodecane mechanism is caused by the numerous possibility of ROOH isomers of decyl and dodecyl radical.

6.7 Mechanism Optimisation

An attempt to improve the accuracy of the n-decane and n-dodecane mechanisms for predicting the experimental data was performed by tuning the rate parameters of the sensitive reactions to the oxygen consumption. The sensitivity analysis was performed by using the RMG reactor feature as presented in Figure 6.10(a), 6.10(b), and 6.10(c). It was found that the most sensitive reactions to the oxygen consumption were the reactions involving dodecyl or decyl radicals and oxygen in the n-docedane or n-decane cases, respectively. By modifying the reaction rate parameters of these reactions, the prediction of the pressure drop becomes closer to the experimental data as illustrated in Figure 6.9(b) and 6.9(c). Table 6.2 shows the comparison of the modified and original rate parameters that was generated by RMG. However, this adjustment in the rate parameter may not be accurate since the rate parameters of the reactions were changed by up to seven order of magnitude. This might contradict the rate parameter from previous studies.

Many studies have evaluated the rate parameters of $R^{\bullet} + O_2 \longrightarrow ROO$ in the autoxidation reaction mechanism of jet fuels and surrogates. Kuprowicz et al. [181] proposed a reaction mechanism for predicting the autoxidation of jet fuel which was refined by the species detection of the oxidised jet fuel samples. In this study, the proposed value of the A-factor of peroxide species formation of 3×10^{12} $cm^3 \cdot mole^{-1} \cdot s^{-1}$. This value was also used by Liu et al. [182] for modelling the deposition formation in the thermal oxidation of an aviation kerosene.

Amara et al. [183] studied n-dodecane autoxidation in a Rancimat experiment and proposed a reaction mechanism that was validated with the induction period data from the experiment. This study proposed the value of the A-factor as 7.54×10^{12} $cm^3 \cdot mole^{-1} \cdot s^{-1}$, which is similar to the original RMG mechanism in Table 6.2. Also, the reaction mechanism from Amara et al. [183] was employed in the python code for modelling the pressure drop data of n-dodecane from the current work. The results show that by using the model from Amara et al., the pressure drop prediction become closer to the current experimental data as illustrated in Figure 6.9(c), but it still underpredicts the experimental pressure drop data.

Considering these findings, the modified value of the rate parameters of the peroxide formation reaction is much beyond the recommended value from the literature. Thus, a more comprehensive method of optimisation of the RMG mechanism is required to improve the accuracy of the pressure drop prediction.
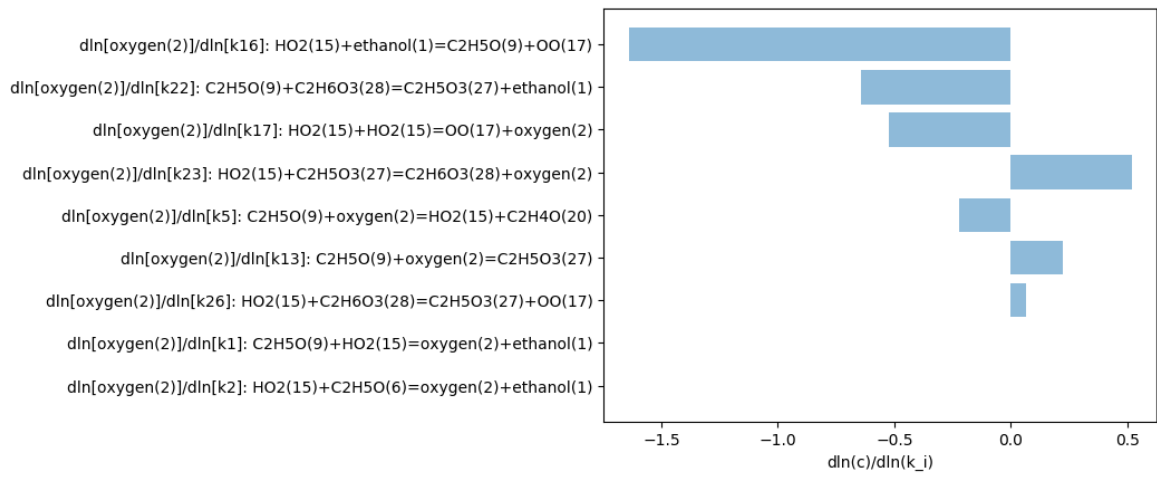
(a)
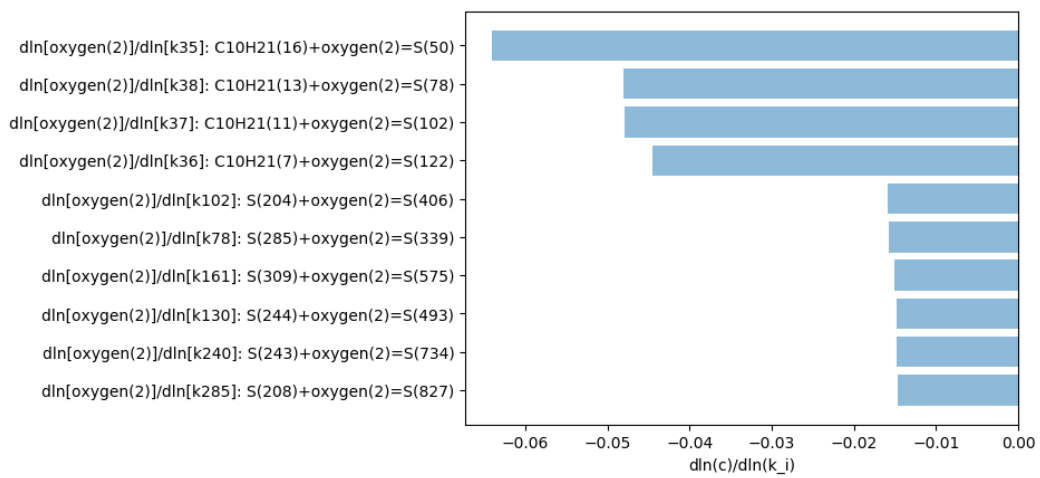
(b)
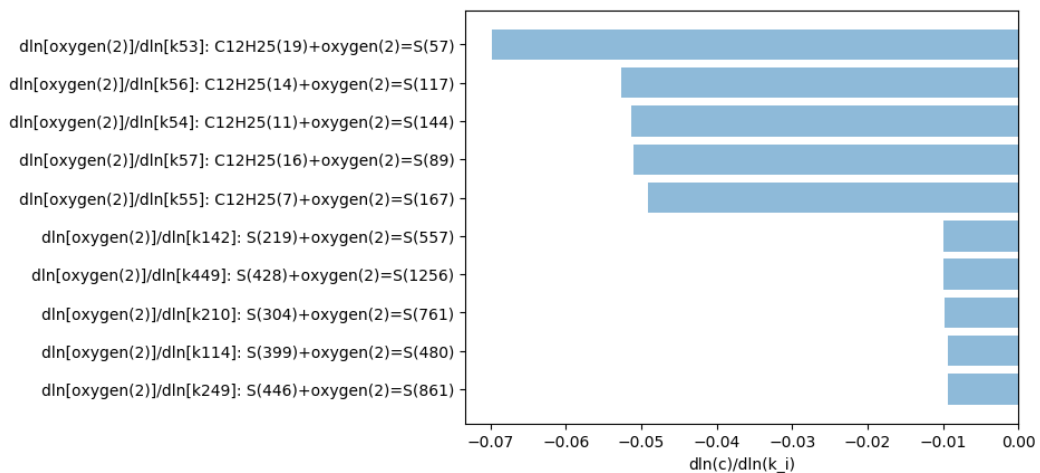
(c)

Figure 6.10: Oxygen sensitivity analysis of the RMG simulations of (a) ethanol, (b) n-decane, and n-dodecane at the PetroOXY test condition.

Table 6.2: The modified recombination reactions ($R^{\bullet} + O_2 = ROO$) in (a) n-decane and (b) n-dodecane mechanisms from RMG.

Modified reactions	$A/(\text{cm}^3.\text{mole}^{-1}.\text{s}^{-1})$	
	original	modified
C10H21(16) + oxygen(2) = S(50)	7.54E+12	7.54E+6
C10H21(11) + oxygen(2) = S(102)	7.54E+12	7.54E+8
C10H21(13) + oxygen(2) = S(78)	7.54E+12	7.54E+6

(a)

Modified reactions	$A/(\text{cm}^3.\text{mole}^{-1}.\text{s}^{-1})$	
	original	modified
C12H25(19) + oxygen(2) = S(57)	7.54E+12	7.54E+7
C12H25(11) + oxygen(2) = S(144)	7.54E+12	7.54E+6
C12H25(14) + oxygen(2) = S(117)	7.54E+12	7.54E+5

(b)

6.8 Concluding Remarks

In this chapter, the oxidation stability of the ethanol/jet A-1 blends was evaluated using the PetroOXY method. Significant degradation of the oxidation stability from the pure jet A-1 was found with the addition of the ethanol concentration to the blend. Moreover, the addition of ethanol increased the maximum pressure of the PetroOXY test due to its volatility. Several antioxidants were evaluated for improving the oxidation stability of ethanol, and the result show that the efficiency of the antioxidants is in the following order: PY > Decalin > DTBP > Tetralin > BHT > MTBP > BHA > TBHQ > PG. A modelling approach was performed by employing the Reaction Mechanism Generator and the PetroOXY model. Relatively good agreement was found for ethanol while further optimisation is required for n-decane and n-dodecane mechanisms. A reaction path analysis was used to explain the autoxidation model from the RMG mechanisms.

Chapter 7

Conclusion and Future Works

7.1   Introduction

In this thesis, bioethanol as an alternative renewable fuel has been studied by using pure ethanol as a drop-in blend for jet A-1. The statistical data shows that the use of air transportation is increasing, thus it demands higher fuel consumption and supply. Despite this, most of the commercial jet fuels are kerosene type, and the characteristics of commercial jet fuel vary in different countries. In this study, jet A-1 is studied since it is the commonly used commercial jet fuel in almost all countries over the world. Similar to other fossil fuels, the use of kerosene in air transportation causes environmental issues, such as global warming and air pollution, due to its combustion emissions from the engine. This has become a concern of global societies and one of the solutions is to promote the use of sustainable alternative fuels, such as biofuels, and low carbon fuel.

Based on the literature study, the properties of aviation fuel have been regulated strictly and the direct use of bioethanol has not been approved yet by the regulations. The benefits and success of bioethanol in replacing gasoline and diesel fuel in engines or burners has motivated many studies on ethanol-blended kerosene or jet A-1 combustion. From these studies, it was found that use of ethanol/kerosene blend for a wick stove does not require any modification to the burner and a different ethanol concentration contributes to a different thermal efficiency. For the application to a gas turbine, many aspects of combustion have been involved. A study in a cylindrical combustor found that the ethanol/kerosene flame blend results in a lower luminosity, soot, CO, CO_2 concentration, and temperature with increase of ethanol concentration due to the lower carbon content in ethanol. A study of spray characteristics shows that a 20 per cent ethanol concentration is ideal for an aviation gas turbine. While a study of droplet combustion showed unique characteristics that were not found in the original entities. More aspects of combustion studies are required to support the promotion of

211

the utilisation of bioethanol as an aviation fuel alternative.

Recently, combustion modelling has been a useful tool to reduce the dependency on the experimental studies as well as providing a more detailed interpretation of the experimental results. This is supported by the availability of an accurate kinetic model of the fuel and the computational capability to execute the model. Based on the findings in the literature, the kinetic models of ethanol have been intensively studied which results in the availability of several ethanol reaction mechanisms. The trend of these mechanisms is becoming more accurate with a wider validation to the experimental data at various reactor conditions and smaller in the number of reactions and species for more efficient computational resources. The negative consequence of the mechanism reduction is that the mechanism loses the details, but this can be solved by keeping the important species and the employment of a certain reduction methods.

For the kinetic studies of jet A-1, the problem becomes more complicated since it has numerous hydrocarbon compounds. Many surrogate models have been proposed to simplify the chemical composition of kerosene for modelling purposes. In this study, a 89% n-decane and 11% toluene mixture was used for modelling jet A-1 because the literature study shows that this surrogate model has been accurate for modelling several experimental studies of kerosene flames in a flat-flame burner. The current research group has been developing the reaction mechanism using similar surrogate models, but it has not been updated for more than fifteen years. Despite this, ethanol and kerosene flames have been extensively studied, they have gaps in the experimental data validation.

Oxidation stability is an important parameter for jet fuels that maintain the quality of the fuel, and by adding ethanol, the stability of the mixture changes from the pure entities. Standard methods for determining the oxidation stability of jet fuels have been formulated and these methods have been employed to assess the stability of biofuels. During this process, chemical species are formed and several studies that identify the species formation in real fuels and surrogates have been highlighted. Also, modelling studies have been conducted for a better understanding of the autoxidation process of liquid fuels.

After identifying the knowledge gap in the literature, this thesis addresses the problem of how to model ethanol/jet A-1 combustion accurately. Therefore, the main aims of this thesis are as follows:

- Propose an updated reaction mechanism that can model the combustion of ethanol /jet A-1 blend accurately at various reactor conditions.

- Design and set up an experimental rig of a laminar flat-flame burner for investigating the temperature and chemical structure of ethanol/jet A-1 flame for the validation of the reaction mechanism.

- Determine the oxidation stability of ethanol/jet A-1 mixture using a standard test method and model, as well as the strategy to improve the stability.

In Chapter 2, the fundamental theory of chemical kinetics has been highlighted as well as the standard reactor models for combustion modelling. Also, the method for developing a reaction mechanism and the standard CHEMKIN format has been discussed. From the literature study, the reaction mechanism of higher hydrocarbon combustion consists of sub-mechanisms that describe its decomposition towards smaller species. The sub-mechanisms of $H_2/O_2, CO, C_1-C_2$, alcohol, alkane, aromatics and NO_x have been reviewed from several combustion textbooks. This information provides the contributing reactions and species in a combustion reaction, but the detailed rate parameters are not given. Therefore, reaction mechanisms from published works are used for developing the reaction mechanism. The general theory of the liquid fuel oxidation mechanism is also reviewed in this chapter.

7.2 Burner Flame Experiment Setup

The design and experimental setup of the burner flame experiment are described in Chapter 3. The experimental rig has been built by employing a refurbished burner from the previous work as well as used and new instrumentation for temperature and species diagnostics. By renewing the burner heater, mesh, and cleaning the spray nozzle, a relatively stable flame can be achieved with occasional fluctuations due to unstable fuel and air supply. The accuracy of the fuel and air ratio has been assured by performing calibration procedures to the air and fuel mass-flow controller. The temperature measurement of the flame has been performed by employing a coated thin type-R thermocouple wire to minimise the disruption to the flame flow as well as a temperature correction due to the heat losses. Moreover, a spring configuration has been applied to the thermocouple wire to solve the tension loss to the thermocouple wire due to the heat from the flame. This method, combined with a calibrated traverse system, provides accurate positioning of the measured points.

An intrusive probing method was employed by using an online gas analyser and a water-cooled quartz probe which provides the concentration of CO, CO_2, O_2, N_2, and NO_x. The setup of the gas analysis is not straight forward due to the failure of the earlier prototype of the quartz probe. This was caused by the limitations in the accuracy in reproducing the probe design in the referred published works to obtain the desired quenching effect. The final prototype of the water-cooled probe was obtained after a series of tests with 12 earlier prototypes. By employing water for cooling the gas sample, the quenching ability of the probe has been increased and provides the desired quenching effect. For both the temperature and gas analysis, 14 data points

were obtained from 0.0 to 10.0 mm above the burner surface with fine increment at below 1.5 mm. Ultimately, the LIF method was employed for detecting OH and NO radicals by using three different wavelengths for each species. These three wavelengths consist of a strong transition and two temperature-sensitive transitions for temperature measurement using LIF thermometry. These methods have been employed for measuring the flame temperature and species concentration from a premixed laminar flat-flame burner.

7.3 Burner Flame Experiment Results

In Chapter 4, the results of the experimental investigation of jet A-1, ethanol, blends, and two jet fuel surrogate flames are presented for lean, near stoichiometric, and rich mixture with equivalence ratio 0.86, 1.07, and 1.28, respectively. The study of the surrogate flames extends the studies of surrogate jet fuel by Honnet et al. [80] and Humer et al. [148] which demonstrates a good accuracy in predicting the combustion of real jet fuel, but they have not been validated against flat-flame burner measurements. The temperature measurement by using thermocouple probing shows that all flames have a similar temperature profile which rapidly increases from the surface and then becomes steady after achieving the maximum temperature at approximately 1.0 to 2.0 mm from the burner surface.

In the ethanol flame, the temperature increase occurred slowly at less than 0.5 mm from the burner surface then rapidly increases due to the higher flame lift-off distance. The near stoichiometric flame has the highest maximum temperature, followed by the rich and lean flames. This agrees with the premixed flame temperature theory that puts the highest flame temperature at the slightly richer than stoichiometry and the higher temperature on the rich side. The jet A-1 flames have the highest flame temperature compared to all other flames while ethanol flames have the lowest. By adding 50% of ethanol to the jet A-1, the flame temperature becomes approximately 100 K lower than jet A-1 and 150 K higher than ethanol.

The temperature difference between ethanol and jet A-1 is caused by the different chemical compositions in the jet A-1 and it has more carbon with a double or triple bond which leads to a higher energy content. The maximum temperature of surrogate B is closer to jet A-1 while both surrogates have a lower temperature than jet A-1. This shows that these surrogates are not completely accurate in representing the chemical composition of the real jet A-1. Unfortunately, the surrogate model that involves toluene could not be measured due to health and safety issues. Apart from the flame temperature assessment, the obtained temperature measurements are employed for the input to the PREMIX models while the species concentration measurements are used

for validating the PREMIX models.

Technical issues were found during the measurement of species concentration using the gas analysis where the O_2 sensor stopped working when measuring the final points of the lean jet A-1 and ethanol flames. Meanwhile, the NO_x calibration failed for several flames and this problem has been solved by performing a correction procedure. The trend of the species measurement showed a similar trend in all measured flames, but the magnitudes are different. The reading of the oxygen concentration is similar in all the flames with the same stoichiometry where the excess air was found to be higher in the lean flames while the stoichiometric and rich flames have no or lower excess air.

The highest CO concentration in all flames was found in the rich flames followed by the stoichiometric and lean flames. Meanwhile, the highest CO_2 concentration was found in the stoichiometric flames, followed by the lean and rich. The high CO concentration in the rich flames was caused by the lack of oxygen, which was unable to oxidise the CO to CO_2. The high CO_2 concentration in the stoichiometric flames was caused by the sufficient oxygen that was able to oxidises CO to CO_2. The concentration of CO and CO_2 in the ethanol, jet A-1 and blend flames are relatively similar at the same stoichiometry. The measurement results in the jet A-1 flames showed close agreement to the results in the CO concentration in all stoichiometry while the CO peaks for rich jet A-1 is lower than the rich cases in ethanol and blend flames.

The NO_x profile increases with distance from the burner surface in all the flames. For the ethanol flames, only the measurement on the lean flame has been completed while the stoichiometric and rich were experiencing technical issues in the NO_x sensor. In all flames, the highest NOx concentration was found in the rich flames, followed by the stoichiometric and lean flames.

Despite the surrogate mixtures being studied to reproduce the chemical composition of the real jet A-1, the gas analysis results of both surrogates show some discrepancies than jet A-1, except for the oxygen concentration. The CO concentration in the surrogate flames is relatively higher than that in jet A-1 flames. Meanwhile, the CO_2 concentration for the rich flames is lower in the surrogate flames. The NO_x concentration in jet A-1 and surrogate flames is relatively similar except in the stoichiometric and rich cases of surrogate A which are higher than jet A-1 at the same stoichiometry.

The detection of OH and NO radicals has been performed by using PLIF method at $Q_1(6)$, $R_2(2)$, and $R_1(12)$ transitions for OH and $Q_1(12)$, $P_2(22)$, and $Q_2(15)$ transition for NO, except the surrogate flames that were not measured at the $Q_1(6)$ transition. The LIF signals from these transitions are corrected for the variation of the laser sheet power, Boltzmann population distribution, and quenching cross-section for OH to obtain the relative concentration. Furthermore, the relative concentration has been quantified by using modelling and measurement of ethanol flames as a reference. The

215

quantification to the relative concentration of OH and NO does not change the profile from the relative concentration. In all fuels, the highest OH concentration was found in the lean flames followed by the stoichiometric and rich flames. The NO detection was more difficult since the lower concentration in the flames and the difference between three stoichiometry is less distinctive compared to the gas analysis results.

The LIF thermometry results show a better result in the OH case than the NO due to the stronger signals and higher concentration. In comparison to the thermocouple method, the LIF thermometry shows a good agreement in several flames and a higher accuracy in the thermocouple method at low temperature in the region close to the burner surface. The 2D-LIF OH signal has been used to assess the influence of the surrounding air. It was found that the unburned fuel in the rich flame reacts with the surrounding air at the flame boundary, but this does not reach the centre part of the flame.

In the literature, a numerous effort has been dedicated to developing a kinetic model that can accurately predict the fuel combustion behaviour and the availability of experimental data to validate the model. For the development of ethanol/jet A-1 blend, there is no available experimental data for this fuel and this work provides a novel data from an experimental flat-flame burner study. The development of Aachen and CRECK surrogates have not involved validation to any flat-flame data before this study. Ethanol and jet A-1 flames have been extensively studied including flat-flame burner experiment. Thus, this study extends the experimental database to a novel stoichiometric ratio which is not available in the literature, especially with premixed real air. The use of a two-line method for OH and NO PLIF thermometry has not been attempted at the selected transition before this work, especially for the measured fuels in this study. Also, the quantification of the OH and NO LIF measurement method using ethanol flame as a reference is evaluated for the first time.

7.4   Kinetic Modelling

In Chapter 5, a reaction mechanism for modelling ethanol/jet A-1 flames has been proposed by using the ethanol mechanism from Olm et al. [56], NO_x mechanism from Saggese et al. [161], n-decane mechanism from Chang et al. [165], and toluene mechanism from Wang et al. [168] and Xu et al. [169] This results in 541 reactions among 85 species while jet A-1 is modelled as 89% n-decane and 11% toluene. The performance of this mechanism has been validated against the experimental data from this work and available literature involving flat-flame experiments, laminar flame speed, ignition delay time, and stirred reactor. Moreover, a reaction path and sensitivity analysis have been used to provide detail information on the model performance.

The performance of this mechanism is also compared to the CRECK, Aachen, and AFRM mechanisms with only the CRECK mechanism has the species for ethanol/jet A-1 mixture. For the burner flame validation, the current model performs well in predicting the ethanol flames. The prediction by these mechanisms for the jet A-1 flames is relatively similar, except for NO where the models show quite different results. All models overpredict the CO concentration while underpredict the CO_2 concentration. The prediction for the OH concentration from these models is lower than the experimental data for lean and stoichiometric flames. The validation of the Aachen and CRECK mechanisms to the measurement of surrogate flames shows good agreement for all measured species at all stoichiometry.

The validation against the laminar flame speed from various reactor conditions has been performed to evaluate the effect of stoichiometry, temperature and pressure variation to the accuracy of the models. All mechanisms follow the experimental laminar flame speed data with different accuracy. The prediction of the jet A-1 laminar burning velocity from the current and AFRM mechanisms is lower than the other mechanisms, especially for lean mixtures. The current mechanism demonstrates a better accuracy than the AFRM mechanism which uses a similar surrogate composition. Validation with the ethanol flame speed data shows that the performance of the current mechanism does not change much from the base ethanol mechanism after the addition of extra sub-mechanisms. The increase in the ethanol concentration in the blend increases the laminar flame speed because of the faster laminar flame speed of ethanol than jet A-1. The prediction of the laminar flame speed of jet A-1, ethanol, and the blends shows a similar trend with a variation of reactor pressure and temperature, which is proportional to the temperature and inversely proportional to the pressure.

The validation against ignition delay time data of ethanol shows that the performance of the current mechanism is relatively similar to the base ethanol mechanism after the addition of sub-mechanisms. The validation against jet A-1 at a different temperature, pressure, and stoichiometry shows that the current mechanism shows a good agreement with the targeted experimental data for the ignition delay time. The current mechanism outperforms the AFRM mechanism in all reactor conditions which is unable to predict the ignition delay accurately. The Aachen mechanism shows better accuracy in predicting the jet A-1 ignition delay time than the other mechanisms while the CRECK model has a computational difficulty in solving the ignition delay time due to the size of the mechanism. With the increase of ethanol concentration, the ignition delay time of the mixture increases, and a rich mixture has a lower ignition delay time than the stoichiometric and lean mixture. The ignition delay time becomes faster by increasing the temperature and pressure of the reactor condition.

The validation against a stirred reactor data of stoichiometric ethanol/oxygen mix-

ture shows that the current mechanism slightly shifted from the original ethanol mechanism in the prediction of major species. Meanwhile, a larger discrepancy between these mechanisms was found in the prediction of the minor species where the current mechanism is closer to the experimental data. The validations against the stirred reactor data of stoichiometric jet A-1/oxygen mixture shows that the current mechanisms are accurate for predicting most of the measured species. However, the prediction of ethylene and benzene is less accurate than the other mechanism while the current mechanism is missing C_4 and C_5 species.

The use of n-decane and toluene as a kerosene surrogate in a model has been found in the literature with a good agreement with experimental data from several reactors. However, the proposed reaction mechanisms have not been updated for more than 15 years. The detailed mechanism from CRECK group might be used for this purpose, but it has numerous reactions and species which causes computational difficulties. This work has updated the reaction mechanism by employing a more recent reaction mechanism as well as the availability of NO_x and ethanol mechanism. Generally, the current mechanism shows better improvement than the AFRM mechanism and is able to model jet A-1 and ethanol flames with a much smaller amount of reaction and species than the CRECK mechanism.

7.5 Oxidation Stability

With regards to the utilisation of ethanol as a drop-in blend for jet A-1, the stability of the fuel needs to be evaluated and there is no published report that studies the autoxidation of these fuel blends. This work reported a novel study on the oxidation stability of the ethanol/jet A-1 blend by employing the PetroOXY method with different ethanol concentrations. The results show that with the increase in the ethanol concentration, the stability of the fuel becomes lower, while the maximum pressure during the test increases with the addition of ethanol concentration. A visual assessment of the sample after the test is presented, where a cleaner sample is obtained with higher ethanol concentration.

This work has extended the autoxidation study of fuels to the multi and single component surrogates to provide an experimental validation to the development of the kinetic model. The effect of ethanol addition to the multi-component surrogates improves the stability of the mixture while the maximum stability was found at 50% for single-component surrogate.

There is an effort of the development of an accurate kinetic modelling of fuel autoxidation and this work evaluated the modelling tools that is available in the literature for modelling the PetroOXY tests. Reaction mechanisms for n-decane, n-dodecane,

and ethanol from RMG have been employed for the modelling PetroOXY by using a custom code. The model shows a good accuracy for the ethanol case while a faster pressure drop, than the experimental data was found for the n-decane and n-dodecane. An optimisation of the reaction rate parameters has been demonstrated to improve the accuracy of the reaction mechanism in predicting the pressure drop validation.

Antioxidant is one of the jet fuel additives that improves the fuel stability, but there is no study on the antioxidant addition to ethanol stability. Nine antioxidants have been tested to improve the stability of ethanol at 1 g/L. The result shows that the effectiveness of the antioxidants is following this order: PY > Decalin > DTBP > Tetralin > BHT > MTBP > BHA > TBHQ > PG. This can be a consideration when selecting an effective antioxidant for bioethanol.

7.6   General Conclusion

Finally, for further development of the utilisation of bioethanol for alternative aviation fuel, this thesis has provided a novel contribution by providing the following outputs:

- An updated reaction mechanism that is able to model ethanol/jet A-1 flames by using n-decane/toluene as a surrogate jet fuel with the NO_x mechanism which relatively while being small in size for more efficient computational resources. The mechanism has been validated against experimental data from various reactor conditions and this has a better accuracy than the previous AFRM mechanism. This can contribute to the development of engine design for ethanol/jet A-1 fuel in a CFD simulation.

- An extension to the availability of experimental data for the jet A-1, ethanol, blend, and two surrogates of jet fuels in a flat-flame burner at equivalence ratios 0.86, 1.07, and 1.28.

- An evaluation to the LIF thermometry method by using OH and NO signal from the selected transition in a premixed laminar flat-flame burner.

- The experimental and simulated data of ethanol flame have been used as a reference to quantify the OH and NO concentration from LIF signal. This can simplify the requirement of methane gas burner that has been commonly used as a reference.

- Assessment of the oxidation stability of ethanol/jet A-1 and the strategy to improve it by assessing the effectiveness of the antioxidants.

7.7 Future Works

There are several aspects that can be improved from this works as well as the continuation of this thesis:

- The flame stability is the main issue in the accuracy of the temperature and species detection by a thermocouple, LIF thermometry, gas analysis, OH and NO LIF. The stability of the burner can be improved by improving the performance of the fuel MFC and the nozzle. Also, the flatness of the flame can be improved by increasing the hole in the burner mesh with a smaller diameter.

- The correction of the thermocouple temperature readings involve the diameter of the bead which might change from the manufacturer specification due to the coating procedure. A more accurate correction could be performed by providing a microscope that is able to measure the bead diameter after the coating procedure without risking the change in the bead surface structure due to the transportation to the microscope facility. The utilisation of a programmable traverse system reduce the required time for the measurement using thermocouples and probes as well as avoiding the thermocouple overheat and over tension at the burner surface.

- The technical issue in the gas analyser has been a large challenge in obtaining accurate measurements of the gas species, especially the oxygen and NO_x sensor. A stable performance of the gas analyser and the availability of more species detection would provide a more sound experimental data set.

- A comparative study of ethanol, jet A-1, and blend fuels in a real engine with a similar burning load can provide a more informative comparison on the emission of these fuel in the real application.

- The LIF images have uncertainty in the determination of the 0.0 mm from the burner surface due to the camera perspective. This could be improved by positioning the centre of the camera lens at the same level as the burner surface. The LIF signal can be improved by narrowing the laser sheet to the region of interest in the flame which is approximately 1.0 mm from the burner surface.

- The correction of the LIF signal for the quenching has been simplified in this study. This can be improved by involving quenching rate variables among the contributing species for a more accurate LIF correction. The NO seeding method can be applied to improve the accuracy of the NO LIF thermometry which lacks of data resolution because of the low NO concentration in flames.

- There is a need for the of improvement in the current reaction mechanism to fit the targeted experimental data. This can be performed by optimising the reaction rate parameters by employing an optimisation method, such as a genetic algorithm approach.

- A more accurate surrogate formulation of the jet A-1 sample could be performed by the availability of a liquid chromatography facility to detect the chemical composition of the sample. Also, the real bioethanol may have water contents and thus the effect of water addition to the blends can be investigated in further studies. This study only investigated 50 per cent ethanol flames and other concentration can be involved in the further study.

- A species detection to the oxidised sample of the PetroOXY test can provide more detailed information which would be beneficial for the model validation.

- In the future, better computational resources and the availability of more reaction databases can be used to develop a reaction mechanism of the fuel blend and the antioxidants for the modelling of the PetroOXY test.

Bibliography

[1] IATA, "IATA Fact Sheet: Industry Statistics," Accessed: 12 December 2018. [Online]. Available: https://www.iata.org/pressroom/facts_figures/fact_sheets/Documents/fact-sheet-industry-facts.pdf viii, 1, 2, 3

[2] R. J. Kee, F. M. Rupley, and J. A. Miller, "Chemkin-II: A Fortran Chemical Kinetics Package for the Analysis of Gas-Phase Chemical Kinetics," Sandia National Labs., Livermore, CA (USA), Tech. Rep., 1989. viii, 25

[3] P. Glarborg, R. J. Kee, J. F. Grcar, and J. A. Miller, "PSR: A FORTRAN Program for Modeling Well-Stirred Reactors," *Sandia Report SAND86-8209*, 1986. viii, 26, 27

[4] RESPECTH, "ReSpecTh," Date accessed: 8 April 2019. [Online]. Available: http://respecth.hu/ viii, 8, 34

[5] E. Catalanotti, "Theoretical and experimental investigation of alternative aviation fuels," Ph.D. dissertation, University of Leeds, 2011. viii, 48, 49, 50, 51, 62, 81, 92, 102, 103, 122, 129

[6] F. Mayinger, *Optical Measurements: Techniques and Applications*. Springer Berlin Heidelberg, 2013. [Online]. Available: https://books.google.co.uk/books?id=BmjrCAAAQBAJ viii, 65, 66

[7] C. Shuang, S. Tie, Z. Yao-Bang, C. Li, L. Ting-Xu, L. Ren-Bing, and Y. Fu-Rong, "Numerical analysis of quantitative measurement of hydroxyl radical concentration using laser-induced fluorescence in flame," *Chinese Physics B*, vol. 25, no. 6, 2016. [Online]. Available: http://cpb.iphy.ac.cn/article/2016/1831/cpb_25_6_060703.html viii, 67

[8] E. Hu, X. Li, X. Meng, Y. Chen, Y. Cheng, Y. Xie, and Z. Huang, "Laminar flame speeds and ignition delay times of methane–air mixtures at elevated temperatures and pressures," *Fuel*, vol. 158, pp. 1–10, 2015. xi, xii, 175, 176, 185

[9] V. Vukadinovic, P. Habisreuther, and N. Zarzalis, "Influence of pressure and temperature on laminar burning velocity and markstein number of kerosene jet a-1: Experimental and numerical study," *Fuel*, vol. 111, pp. 401–410, 2013. xi, xii, 176, 177, 178

[10] K. Kumar, C.-J. Sung, and X. Hui, "Laminar flame speeds and extinction limits of conventional and alternative jet fuels," *Fuel*, vol. 90, no. 3, pp. 1004–1011, 2011. xi, 176, 177

[11] D. Bradley, M. Lawes, and M. Mansour, "Explosion bomb measurements of ethanol–air laminar gaseous flame characteristics at pressures up to 1.4 mpa," *Combustion and Flame*, vol. 156, no. 7, pp. 1462–1470, 2009. xii, 179, 180, 181

[12] T. Knorsch, A. Zackel, D. Mamaikin, L. Zigan, and M. Wensing, "Comparison of different gasoline alternative fuels in terms of laminar burning velocity at increased gas temperatures and exhaust gas recirculation rates," *Energy & Fuels*, vol. 28, no. 2, pp. 1446–1452, 2014. [Online]. Available: https://doi.org/10.1021/ef4021922 xii, 10, 180

[13] M. Aghsaee, D. Nativel, M. Bozkurt, M. Fikri, N. Chaumeix, and C. Schulz, "Experimental study of the kinetics of ethanol pyrolysis and oxidation behind reflected shock waves and in laminar flames," *Proceedings of the Combustion Institute*, vol. 35, no. 1, pp. 393–400, 2015. xii, 180

[14] A. Katoch, A. Millán-Merino, and S. Kumar, "Measurement of laminar burning velocity of ethanol-air mixtures at elevated temperatures," *Fuel*, vol. 231, pp. 37–44, 2018. xii, 180

[15] A. De Toni, M. Werler, R. Hartmann, L. Cancino, R. Schießl, M. Fikri, C. Schulz, A. Oliveira, E. Oliveira, and M. Rocha, "Ignition delay times of jet a-1 fuel: Measurements in a high-pressure shock tube and a rapid compression machine," *Proceedings of the Combustion Institute*, vol. 36, no. 3, pp. 3695–3703, 2017. xii, 185, 186

[16] U. Burke, W. K. Metcalfe, S. M. Burke, K. A. Heufer, P. Dagaut, and H. J. Curran, "A detailed chemical kinetic modeling, ignition delay time and jet-stirred reactor study of methanol oxidation," *Combustion and Flame*, vol. 165, pp. 125–136, 2016. xii, 187, 188

[17] P. Dagaut and C. Togbé, "Experimental and modeling study of the kinetics of oxidation of ethanol- gasoline surrogate mixtures (e85 surrogate) in a jet-stirred reactor," *Energy & Fuels*, vol. 22, no. 5, pp. 3499–3505, 2008. xii, 188, 189

[18] P. Dagaut and M. Cathonnet, "The ignition, oxidation, and combustion of kerosene: A review of experimental and kinetic modeling," *Progress in Energy and Combustion Science*, vol. 32, no. 1, pp. 48 – 92, 2006. [Online]. Available: http://www.sciencedirect.com/science/article/pii/S0360128505000523 xii, xiii, 12, 190, 192, 193, 194

[19] E. T. Denisov and I. B. Afanas'ev, *Oxidation and Antioxidants in Organic Chemistry and Biology.* CRC press, 2005. xiv, 45, 46, 47

[20] United Nations, "Population — United Nations," Accessed: 16 December 2018. [Online]. Available: http://www.un.org/en/sections/issues-depth/population/ 1

[21] Chevron, "Aviation fuels technical review," USA, Tech. Rep., 2007. [Online]. Available: https://www.chevron.com/-/media/chevron/operations/documents/aviation-tech-review.pdf 2, 3, 7, 11, 198

[22] C. Zhang, X. Hui, Y. Lin, and C.-J. Sung, "Recent development in studies of alternative jet fuel combustion: Progress, challenges, and opportunities," *Renewable and Sustainable Energy Reviews*, vol. 54, pp. 120–138, 2016. [Online]. Available: http://www.sciencedirect.com/science/article/pii/S1364032115010266 2

[23] J. Peeters, "Aviation and Air Pollution," *Studies in Environmental Science*, vol. 72, pp. 601–613, jan 1998. [Online]. Available: https://www.sciencedirect.com/science/article/pii/S0166111698800368 2, 3

[24] US EPA, "What is Acid Rain?" Accessed: 14 February 2019. [Online]. Available: https://www.epa.gov/acidrain/what-acid-rain 4

[25] UNFCCC, "The Paris Agreement," Accessed: 01 March 2018. [Online]. Available: http://unfccc.int/paris_agreement/items/9485.php 4

[26] J. Larsson, A. Elofsson, T. Sterner, and J. Åkerman, "International and National Climate Policies for Aviation: a Review," *Climate Policy*, vol. 0, no. 0, pp. 1–13, 2019. [Online]. Available: https://doi.org/10.1080/14693062.2018.1562871 4

[27] IATA, "Fact Sheet Climate Change & CORSIA - A CO_2 Standard for Aircraft," Accessed: 20 February 2019. [Online]. Available: https://www.iata.org/contentassets/c4f9f0450212472b96dac114a06cc4fa/fact-sheet-climate-change.pdf 4

[28] ASTM, "ASTM D1655," Accessed:19 March 2019. [Online]. Available: https://compass.astm.org/EDIT/html_annot.cgi?D1655+19 4, 5, 8

[29] M. Buffi, A. Valera-Medina, R. Marsh, D. Pugh, A. Giles, J. Runyon, and D. Chiaramonti, "Emissions characterization tests for hydrotreated renewable jet fuel from used cooking oil and its blends," *Applied Energy*, vol. 201, pp. 84–93, 2017. 4

[30] D. C. K. Rao, S. Syam, S. Karmakar, and R. Joarder, "Experimental investigations on nucleation, bubble growth, and micro-explosion characteristics during the combustion of ethanol/jet a-1 fuel droplets," *Experimental Thermal and Fluid Science*, vol. 89, pp. 284–294, 2017. [Online]. Available: http://www.sciencedirect.com/science/article/pii/S0894177717302571 4, 15, 47

[31] G. López Juste and J. Salvá Monfort, "Preliminary test on combustion of wood derived fast pyrolysis oils in a gas turbine combustor," *Biomass and Bioenergy*, vol. 19, no. 2, pp. 119–128, aug 2000. [Online]. Available: http://linkinghub.elsevier.com/retrieve/pii/S0961953400000234 4, 5

[32] S. Naik, V. V. Goud, P. K. Rout, and A. K. Dalai, "Production of first and second generation biofuels: A comprehensive review," *Renewable and Sustainable Energy Reviews*, vol. 14, no. 2, pp. 578–597, feb 2010. [Online]. Available: http://linkinghub.elsevier.com/retrieve/pii/S1364032109002342 5

[33] The Engineering Tool Box, "Ethanol Freeze Protected Water Solutions," Accessed:19 March 2019. [Online]. Available: https://www.engineeringtoolbox.com/ethanol-water-d_989.html 5

[34] Z. Habib, R. Parthasarathy, and S. Gollahalli, "Performance and emission characteristics of biofuel in a small-scale gas turbine engine," *Applied Energy*, vol. 87, no. 5, pp. 1701–1709, may 2010. [Online]. Available: http://linkinghub.elsevier.com/retrieve/pii/S0306261909004681 5

[35] V. Lupandin, R. Thamburaj, and A. Nikolayev, "Test results of the OGT2500 Gas Turbine Engine Running on Alternative Fuels: BioOil, Ethanol, BioDiesel and Crude Oil," pp. 421–426, 2005. [Online]. Available: http://dx.doi.org/10.1115/GT2005-68488 5

[36] D. L. Jones, "Potential Air Emission Impacts of Cellulosic Ethanol Production at Seven Demonstration Refineries in the United States," *Journal of the Air & Waste Management Association*, vol. 60, no. 9, pp. 1118–1143, 2010. [Online]. Available: https://doi.org/10.3155/1047-3289.60.9.1118 4

[37] H. Timonen, P. Karjalainen, E. Saukko, S. Saarikoski, P. Aakko-Saksa, P. Simonen, T. Murtonen, M. Dal Maso, H. Kuuluvainen,

M. Bloss, E. Ahlberg, B. Svenningsson, J. Pagels, W. H. Brune, J. Keskinen, D. R. Worsnop, R. Hillamo, and T. Rönkkö, "Influence of fuel ethanol content on primary emissions and secondary aerosol formation potential for a modern flex-fuel gasoline vehicle," *Atmospheric Chemistry and Physics*, vol. 17, no. 8, pp. 5311–5329, 2017. [Online]. Available: https://www.atmos-chem-phys.net/17/5311/2017/ 4

[38] S. C. Bhatia, "26 - Issues relating to biofuels," in *Advanced Renewable Energy Systems*, S. C. Bhatia, Ed. Woodhead Publishing India, 2014, pp. 688–718. [Online]. Available: http://www.sciencedirect.com/science/article/pii/B9781782422693500267 4

[39] H. Zabed, J. N. Sahu, A. Suely, A. N. Boyce, and G. Faruq, "Bioethanol production from renewable sources: Current perspectives and technological progress," *Renewable and Sustainable Energy Reviews*, vol. 71, pp. 475–501, 2017. [Online]. Available: http://www.sciencedirect.com/science/article/pii/S1364032116311339 5

[40] S. Kim and B. E. Dale, "Global potential bioethanol production from wasted crops and crop residues," *Biomass and Bioenergy*, vol. 26, no. 4, pp. 361–375, 2004. [Online]. Available: http://www.sciencedirect.com/science/article/pii/S0961953403001375 5

[41] P. Chansauria and R. K. Mandloi, "Effects of Ethanol Blends on Performance of Spark Ignition Engine-A Review," *Materials Today: Proceedings*, vol. 5, no. 2, Part 1, pp. 4066–4077, 2018. [Online]. Available: http://www.sciencedirect.com/science/article/pii/S2214785317329413 5

[42] S. A. Shahir, H. H. Masjuki, M. A. Kalam, A. Imran, and A. M. Ashraful, "Performance and emission assessment of diesel–biodiesel–ethanol/bioethanol blend as a fuel in diesel engines: A review," *Renewable and Sustainable Energy Reviews*, vol. 48, pp. 62–78, 2015. [Online]. Available: http://www.sciencedirect.com/science/article/pii/S1364032115002026 5, 6

[43] K. L. Tay, W. Yang, B. Mohan, H. An, D. Zhou, and W. Yu, "Development of a robust and compact kerosene–diesel reaction mechanism for diesel engines," *Energy conversion and management*, vol. 108, pp. 446–458, 2016. 6

[44] H. J. Curran, "Developing detailed chemical kinetic mechanisms for fuel combustion," *Proceedings of the Combustion Institute*, vol. 37, no. 1, pp. 57–81, 2019. [Online]. Available: http://www.sciencedirect.com/science/article/pii/S1540748918302372 6

[45] C. K. Westbrook and F. L. Dryer, "Chemical kinetics and modeling of combustion processes," *Symposium (International) on Combustion*, vol. 18, no. 1, pp. 749–767, 1981. [Online]. Available: http://www.sciencedirect.com/science/article/pii/S0082078481800793 6

[46] G. P. Smith, D. M. Golden, M. Frenklach, N. W. Moriarty, B. Eiteneer, M. Goldenberg, C. T. Bowman, R. K. Hanson, S. Song, W. C. Gardiner, Jr., V. V. Lissianski, , and Z. Qin, "GRI-Mech 3.0," Date accessed: 5 April 2019. [Online]. Available: http://combustion.berkeley.edu/gri-mech/version30/text30.html{#}cite 6, 23, 25, 28, 144

[47] LLNL, "Primary Reference Fuels (PRF): iso-Octane / n-Heptane Mixtures," Date accessed: 6 April 2019. [Online]. Available: https://combustion.llnl.gov/archived-mechanisms/surrogates/prf-isooctane-n-heptane-mixture 6, 9

[48] CRECK, "CRECK Modeling - Kinetics," Date accessed: 6 April 2019. [Online]. Available: http://creckmodeling.chem.polimi.it/menu-kinetics 6, 9, 15, 45, 47

[49] H. Wang, E. Dames, B. Sirjean, D. A. Sheen, R. Tango, A. Violi, J. Y. W. Lai, F. N. Egolfopoulos, D. F. Davidson, R. K. Hanson, C. K. L. C. T. Bowman and, W. Tsang, N. P. Cernansky, D. L. Miller, and R. P. Lindstedt, "JetSurF 2.0," Date accessed: 7 April 2019. [Online]. Available: https://web.stanford.edu/group/haiwanglab/JetSurF/JetSurF2.0/howtocite.html 6

[50] B. D. Batts and A. Z. Fathoni, "A literature review on fuel stability studies with particular emphasis on diesel oil," *Energy & Fuels*, vol. 5, no. 1, pp. 2–21, 1991. [Online]. Available: https://doi.org/10.1021/ef00025a001 7

[51] L. M. Balster, W. J. Balster, and E. G. Jones, "Thermal stability of jet-fuel/paraffin blends," *Energy & Fuels*, vol. 10, no. 6, pp. 1176–1180, 1996. [Online]. Available: https://doi.org/10.1021/ef960061b 7

[52] J. Zhou, Y. Xiong, and X. Liu, "Evaluation of the oxidation stability of biodiesel stabilized with antioxidants using the rancimat and pdsc methods," *Fuel*, vol. 188, pp. 61 – 68, 2017. [Online]. Available: http://www.sciencedirect.com/science/article/pii/S0016236116309747 8

[53] G. Karavalakis, S. Stournas, and D. Karonis, "Evaluation of the oxidation stability of diesel/biodiesel blends," *Fuel*, vol. 89, no. 9, pp. 2483 – 2489, 2010. [Online]. Available: http://www.sciencedirect.com/science/article/pii/S001623611000147X 8

[54] J. Zhou, Y. Xiong, and S. Xu, "Evaluation of the oxidation stability of biodiesel stabilized with antioxidants using the petrooxy method," *Fuel*, vol. 184, pp. 808 – 814, 2016. [Online]. Available: http://www.sciencedirect.com/science/article/pii/S0016236116306846 8, 205

[55] R. K. Saluja, V. Kumar, and R. Sham, "Stability of biodiesel – a review," *Renewable and Sustainable Energy Reviews*, vol. 62, pp. 866 – 881, 2016. [Online]. Available: http://www.sciencedirect.com/science/article/pii/S1364032116301113 8, 201

[56] C. Olm, T. Varga, v. Valkó, S. Hartl, C. Hasse, and T. Turányi, "Development of an ethanol combustion mechanism based on a hierarchical optimization approach," *International Journal of Chemical Kinetics*, vol. 48, no. 8, pp. 423–441, 2016. [Online]. Available: https://onlinelibrary.wiley.com/doi/abs/10.1002/kin.20998 8, 9, 103, 119, 143, 216

[57] A. Millán-Merino, E. Fernández-Tarrazo, M. Sánchez-Sanz, and F. A. Williams, "A multipurpose reduced mechanism for ethanol combustion," *Combustion and Flame*, vol. 193, pp. 112 – 122, 2018. [Online]. Available: http://www.sciencedirect.com/science/article/pii/S0010218018301056 9

[58] UCSD, "Chemical-Kinetic Mechanisms for Combustion Applications," Date accessed: 24 April 2019. [Online]. Available: web.eng.ucsd.edu/mae/groups/combustion/mechanism.html 9

[59] Aramco, "AramcoMech 2.0," Date accessed: 24 April 2019. [Online]. Available: http://c3.nuigalway.ie/combustionchemistrycentre/mechanismdownloads/aramcomech20/ 9

[60] S. M. Sarathy, P. Oßwald, N. Hansen, and K. Kohse-Höinghaus, "Alcohol combustion chemistry," *Progress in Energy and Combustion Science*, vol. 44, pp. 40 – 102, 2014. [Online]. Available: http://www.sciencedirect.com/science/article/pii/S0360128514000240 9, 49, 175

[61] F. Egolfopoulos, D. Du, and C. Law, "A study on ethanol oxidation kinetics in laminar premixed flames, flow reactors, and shock tubes," *Symposium (International) on Combustion*, vol. 24, no. 1, pp. 833 – 841, 1992, twenty-Fourth Symposium on Combustion. [Online]. Available: http://www.sciencedirect.com/science/article/pii/S0082078406801013 9

[62] N. M. Marinov, "A detailed chemical kinetic model for high temperature ethanol oxidation," *International Journal of Chemical Kinetics*, vol. 31, no. 3, pp. 183–220, 1999. 9

[63] P. Saxena and F. A. Williams, "Numerical and experimental studies of ethanol flames," *Proceedings of the Combustion Institute*, vol. 31, no. 1, pp. 1149 – 1156, 2007. [Online]. Available: http://www.sciencedirect.com/science/article/pii/S1540748906003609 9, 143

[64] C. Lee, S. Vranckx, K. A. Heufer, S. V. Khomik, Y. Uygun, H. Olivier, and R. X. Fernandez, "On the chemical kinetics of ethanol oxidation: Shock tube, rapid compression machine and detailed modeling study," *International journal of research in physical chemistry and chemical physics*, vol. 226, no. 1, pp. 1–28, 2011. 9

[65] N. Leplat, P. Dagaut, C. Togbé, and J. Vandooren, "Numerical and experimental study of ethanol combustion and oxidation in laminar premixed flames and in jet-stirred reactor," *Combustion and Flame*, vol. 158, no. 4, pp. 705 – 725, 2011, special Issue on Kinetics. [Online]. Available: http://www.sciencedirect.com/science/article/pii/S0010218010003627 10

[66] A. Ergut, S. Granata, J. Jordan, J. Carlson, J. B. Howard, H. Richter, and Y. A. Levendis, "Pah formation in one-dimensional premixed fuel-rich atmospheric pressure ethylbenzene and ethyl alcohol flames," *Combustion and Flame*, vol. 144, no. 4, pp. 757 – 772, 2006. [Online]. Available: http://www.sciencedirect.com/science/article/pii/S0010218005002695 10

[67] T. Kasper, P. Oßwald, M. Kamphus, and K. Kohse-Höinghaus, "Ethanol flame structure investigated by molecular beam mass spectrometry," *Combustion and Flame*, vol. 150, no. 3, pp. 220 – 231, 2007. [Online]. Available: http://www.sciencedirect.com/science/article/pii/S0010218007000314 10

[68] N. Leplat, A. Seydi, and J. Vandooren, "An experimental study of the structure of a stoichiometric ethanol/oxygen/argon flame," *Combustion Science and Technology*, vol. 180, no. 3, pp. 519–532, 2008. [Online]. Available: https://doi.org/10.1080/00102200701741467 10

[69] L.-S. Tran, P.-A. Glaude, R. Fournet, and F. Battin-Leclerc, "Experimental and modeling study of premixed laminar flames of ethanol and methane," *Energy & Fuels*, vol. 27, no. 4, pp. 2226–2245, 2013. [Online]. Available: https://doi.org/10.1021/ef301628x 10

[70] A. Konnov, R. Meuwissen, and L. de Goey, "The temperature dependence of the laminar burning velocity of ethanol flames," *Proceedings of the Combustion Institute*, vol. 33, no. 1, pp. 1011 – 1019, 2011. [Online]. Available: http://www.sciencedirect.com/science/article/pii/S1540748910002865 10, 175

[71] J. van Lipzig, E. Nilsson, L. de Goey, and A. Konnov, "Laminar burning velocities of n-heptane, iso-octane, ethanol and their binary and tertiary mixtures," *Fuel*, vol. 90, no. 8, pp. 2773 – 2781, 2011. [Online]. Available: http://www.sciencedirect.com/science/article/pii/S0016236111002365 10

[72] F. R. Gillespie, "An experimental and modelling study of the combustion of oxygenated hydrocarbons," *NUI Galway Theses (PhD Theses)*, mar 2014. 11

[73] G. Mittal, S. M. Burke, V. A. Davies, B. Parajuli, W. K. Metcalfe, and H. J. Curran, "Autoignition of ethanol in a rapid compression machine," *Combustion and Flame*, vol. 161, no. 5, pp. 1164 – 1171, 2014. [Online]. Available: http://www.sciencedirect.com/science/article/pii/S0010218013004185 11

[74] W. K. Metcalfe, S. M. Burke, S. S. Ahmed, and H. J. Curran, "A hierarchical and comparative kinetic modeling study of c1 c2 hydrocarbon and oxygenated fuels," *international Journal of Chemical Kinetics*, vol. 45, no. 10, pp. 638–675, 2013. [Online]. Available: https://onlinelibrary.wiley.com/doi/abs/10.1002/kin.20802 11

[75] H. Xu, C. Yao, T. Yuan, K. Zhang, and H. Guo, "Measurements and modeling study of intermediates in ethanol and dimethy ether low-pressure premixed flames using synchrotron photoionization," *Combustion and Flame*, vol. 158, no. 9, pp. 1673 – 1681, 2011. [Online]. Available: http://www.sciencedirect.com/science/article/pii/S0010218011000198 11

[76] J. Liang, G. Li, Z. Zhang, Z. Xiong, F. Dong, and R. Yang, "Experimental and numerical studies on laminar premixed flames of ethanol–water–air mixtures," *Energy & Fuels*, vol. 28, no. 7, pp. 4754–4761, 2014. [Online]. Available: https://doi.org/10.1021/ef4024178 11

[77] J. Li, "Experimental and numerical studies of ethanol chemical kinetics," Ph.D. dissertation, Princeton University, 2004. 11

[78] S. Blakey, L. Rye, and C. W. Wilson, "Aviation gas turbine alternative fuels: A review," *Proceedings of the Combustion Institute*, vol. 33, no. 2, pp. 2863 – 2885, 2011. [Online]. Available: http://www.sciencedirect.com/science/article/pii/S1540748910003950 11

[79] V. Alekseev, J. Soloviova-Sokolova, S. Matveev, I. Chechet, S. Matveev, and A. Konnov, "Laminar burning velocities of n-decane and binary kerosene surrogate mixture," *Fuel*, vol. 187, pp. 429 – 434, 2017. [Online]. Available: http://www.sciencedirect.com/science/article/pii/S0016236116309486 11, 12

[80] S. Honnet, K. Seshadri, U. Niemann, and N. Peters, "A surrogate fuel for kerosene," *Proceedings of the Combustion Institute*, vol. 32, no. 1, pp. 485 – 492, 2009. [Online]. Available: http://www.sciencedirect.com/science/article/pii/S1540748908002381 11, 12, 44, 48, 52, 151, 200, 214

[81] J.-L. Delfau, M. Bouhria, M. Reuillon, O. Sanogo, R. Akrich, and C. Vovelle, "Experimental and computational investigation of the structure of a sooting decane-o2-ar flame," *Symposium (International) on Combustion*, vol. 23, no. 1, pp. 1567 – 1572, 1991, twenty-Third Symposium (International) on Combustion. [Online]. Available: http://www.sciencedirect.com/science/article/pii/S0082078406804273 12

[82] C. Vovelle, J.-L. Delfau, and M. Reuillon, *Formation of Aromatic Hydrocarbons in Decane and Kerosene Flames at Reduced Pressure*. Berlin, Heidelberg: Springer Berlin Heidelberg, 1994, pp. 50–65. [Online]. Available: https://doi.org/10.1007/978-3-642-85167-4_4 12

[83] C. Vovelle, J. Delfau, M. Reuillon, R. Ackrich, M. Bouhria, and O. Sanogo, "Comparison of aromatics formation in decane and kerosene flames," *Proceedings of the ACS national meeting,*, vol. 36, no. 4, pp. 1456 – 1463, 1991. 12, 13

[84] C. Douté, J.-L. Delfau, R. Akrich, and C. Vovelle, "Chemical structure of atmospheric pressure premixed n-decane and kerosene flames," *Combustion Science and Technology*, vol. 106, no. 4-6, pp. 327–344, 1995. [Online]. Available: https://doi.org/10.1080/00102209508907785 12, 13, 144

[85] C. Douté, J.-L. Delfau, and C. Vovelle, "Modeling of the structure of a premixed n-decane flame," *Combustion Science and Technology*, vol. 130, no. 1-6, pp. 269–313, 1997. [Online]. Available: https://doi.org/10.1080/00102209708935746 12

[86] R. P. Lindstedt and L. Q. Maurice, "Detailed chemical-kinetic model for aviation fuels," *Journal of Propulsion and Power*, vol. 16, no. 2, pp. 187–195, 2000. [Online]. Available: https://doi.org/10.2514/2.5582 12, 144

[87] E. Riesmeier, S. Honnet, and N. Peters, "Flamelet modeling of pollutant formation in a gas turbine combustion chamber using detailed chemistry for a kerosene model fuel," in *ASME 2002 Internal Combustion Engine Division Fall Technical Conference*. American Society of Mechanical Engineers, 2002, pp. 149–157. 13

[88] G. Bikas and N. Peters, "Kinetic modelling of n-decane combustion and autoignition: Modeling combustion of n-decanem," *Combustion and Flame*, vol. 126, no. 1-2, pp. 1456–1475, 2001. 13, 44

[89] G. Bikas, "Kinetic mechanism for hydrocarbon ignition," Ph.D. dissertation, Bibliothek der RWTH Aachen, 2001. 13

[90] A. Violi, S. Yan, E. G. Eddings, A. F. Sarofim, S. Granata, T. Faravelli, and E. Ranzi, "Experimental formulation and kinetic model for jp-8 surrogate mixtures," *Combustion Science and Technology*, vol. 174, no. 11-12, pp. 399–417, 2002. [Online]. Available: https://doi.org/10.1080/00102200215080 13

[91] P. Patterson, A. Kyne, M. Pourkashanian, A. Williams, and C. Wilson, "Combustion of kerosene in counterflow diffusion flames," *Journal of Propulsion and Power*, vol. 17, no. 2, pp. 453–460, 2001. 13, 44, 144

[92] M. Cathonnet, D. Voisin, A. Etsouli, C. Sferdean, M. Reuillon, J. Boettner, and P. Dagaut, "Kerosene combustion modelling using detailed and reduced chemical kinetic mechanisms," in *RTO Meeting proceedings*, 1999. 13

[93] A. Kyne, P. Patterson, M. Pourkashanian, C. Wilson, and A. Williams, "Prediction of premixed laminar flame structure and burning velocity of aviation fuel-air mixtures," in *ASME Turbo Expo 2001: Power for Land, Sea, and Air*. American Society of Mechanical Engineers, 2001, pp. V002T02A022–V002T02A022. 13

[94] L. Elliott, D. Ingham, A. Kyne, N. Mera, M. Pourkashanian, and C. Wilson, "Genetic algorithms for optimisation of chemical kinetics reaction mechanisms," *Progress in Energy and Combustion Science*, vol. 30, no. 3, pp. 297–328, 2004. 13

[95] ——, "A novel approach to the reduction of an aviation fuel/air reaction mechanism using a genetic algorithm," in *Proceedings of the ASME turbo expo GT-2004-53053*. American Society of Mechanical Engineers, 2004. 13

[96] P. Dagaut, M. Reuillon, J.-C. Boettner, and M. Cathonnet, "Kerosene combustion at pressures up to 40 atm: Experimental study and detailed chemical kinetic modeling," in *Symposium (International) on Combustion*, vol. 25, no. 1. Elsevier, 1994, pp. 919–926. 13

[97] E. Catalanotti, K. Hughes, M. Pourkashanian, I. Uryga-Bugajska, and A. Williams, "Development of a high temperature oxidation mechanism for bio-aviation fuels," in *ASME 2008 International Mechanical Engineering Congress and Exposition*. American Society of Mechanical Engineers, 2008, pp. 321–330. 13

[98] E. Catalanotti, K. Hughes, M. Pourkashanian, and C. Wilson, "Development of a chemical reaction mechanism for alternative aviation fuels," *Energy & Fuels*, vol. 25, no. 4, pp. 1465–1473, 2011. 14, 44, 144

[99] I. Shafagh, K. J. Hughes, E. Catalanotti, Z. Liu, M. Pourkashanian, and C. W. Wilson, "Experimental and modeling studies of the oxidation of surrogate bio-aviation fuels," *Journal of Engineering for Gas Turbines and Power*, vol. 134, no. 4, p. 041501, 2012. 14

[100] E. Catalanotti, K. Hughes, M. Pourkashanian, and C. Wilson, "Experimental and modelling studies of the combustion of alternative aviation fuels," *13th International Conference on Stability, Handling and Use of Liquid Fuels 2013*, pp. 176–189, 2013, cited By 0. [Online]. Available: https://www.scopus.com/inward/record.uri?eid=2-s2.0-84905827342&partnerID=40&md5=cf97532b6b2569cfc8f8b7a67d9199c8 14

[101] H. Xu, C. Yao, G. Xu, Z. Wang, and H. Jin, "Experimental and modelling studies of the effects of methanol and ethanol addition on the laminar premixed low-pressure n-heptane/toluene flames," *Combustion and Flame*, vol. 160, no. 8, pp. 1333–1344, 2013. [Online]. Available: http://www.sciencedirect.com/science/article/pii/S0010218013000680 14

[102] M. Y. Khan, F. A. Khan, and M. S. Beg, "Ethanol-kerosene blends: Fuel option for kerosene wick stove," *Fuel*, vol. 2, p. 5, 2013. 14, 47

[103] J. Patra, P. Ghose, A. Datta, M. Das, R. Ganguly, S. Sen, and S. Chatterjee, "Studies of combustion characteristics of kerosene ethanol blends in an axi-symmetric combustor," *Fuel*, vol. 144, no. Supplement C, pp. 205–213, 2015. [Online]. Available: http://www.sciencedirect.com/science/article/pii/S0016236114012459 14, 47

[104] L. Song, T. Liu, W. Fu, and Q. Lin, "Experimental study on spray characteristics of ethanol-aviation kerosene blended fuel with a high-pressure common rail injection system," *Journal of the Energy Institute*, 2016. [Online]. Available: http://www.sciencedirect.com/science/article/pii/S1743967116305530 15, 47

[105] D. Ju, X. Sun, X. Jia, Z. Huang, X. Qiao, D. Han, and Z. Huang, "Experimental investigation of the atomization behavior of ethanol and kerosene in acoustic fields," *Fuel*, vol. 202, no. Supplement C, pp. 613–619, 2017. [Online]. Available: http://www.sciencedirect.com/science/article/pii/S0016236117304635 15, 47

[106] M. Sicard, J. Boulicault, K. Coulon, C. Thomasset, J. Ancelle, B. Raepsaet, and F. Ser, "Oxidation stability of jet fuel model molecules evaluated by rapid

small scale oxidation tests." in *The 13th International Conference on Stability, Handling and Use of Liquid Fuels 2013 IASH 2013*, 2013. 15

[107] R. L. Webster, D. J. Evans, P. M. Rawson, B. S. Mitrevski, and P. J. Marriott, "Oxidation of neat synthetic paraffinic kerosene fuel and fuel surrogates: Quantitation of dihydrofuranones," *Energy & Fuels*, vol. 27, no. 2, pp. 889–897, 2013. [Online]. Available: https://doi.org/10.1021/ef301638a 16

[108] D. C. Mielczarek, "Autoxidation behaviour of hydrocarbons in the context of conventional and alternative aviation fuels," *University of Leeds Theses (PhD Theses)*, November 2015. 16, 45

[109] P. M. Rawson, C.-A. Stansfield, R. L. Webster, D. Evans, and U. Yildirim, "The oxidative stability of synthetic fuels and fuel blends with monoaromatic blending components," *Fuel*, vol. 161, pp. 97 – 104, 2015. [Online]. Available: http://www.sciencedirect.com/science/article/pii/S0016236115008479 16

[110] P. M. Rawson, C.-A. Stansfield, R. L. Webster, and D. Evans, "Re-addition of antioxidant to aged merox and hydroprocessed jet fuels," *Fuel*, vol. 139, pp. 652 – 658, 2015. [Online]. Available: http://www.sciencedirect.com/science/article/ pii/S001623611400917X 16

[111] R. L. Webster, D. J. Evans, and P. J. Marriott, "Detailed chemical analysis using multidimensional gas chromatography–mass spectrometry and bulk properties of low-temperature oxidized jet fuels," *Energy & Fuels*, vol. 29, no. 4, pp. 2059–2066, 2015. 17

[112] A. B. Amara, S. Kaoubi, and L. Starck, "Toward an optimal formulation of alternative jet fuels: Enhanced oxidation and thermal stability by the addition of cyclic molecules," *Fuel*, vol. 173, pp. 98 – 105, 2016. [Online]. Available: http://www.sciencedirect.com/science/article/pii/S0016236116000491 17, 205

[113] D. C. Mielczarek, M. Matrat, A. B. Amara, Y. Bouyou, P. Wund, and L. Starck, "Toward the accurate prediction of liquid phase oxidation of aromatics: A detailed kinetic mechanism for toluene autoxidation," *Energy & Fuels*, vol. 31, no. 11, pp. 12 893–12 913, 2017. [Online]. Available: https://doi.org/10.1021/acs.energyfuels.7b00416 17, 45

[114] K. Baczewski and P. Szczawiński, "Investigation of the impact of a jet a 1 aviation turbine fuel admixture on selected biodiesel properties and on its ageing process," *Archiwum Motoryzacji*, vol. 78, no. 4, 2017. 17

[115] R. L. Webster, P. M. Rawson, C. Kulsing, D. J. Evans, and P. J. Marriott, "Investigation of the thermal oxidation of conventional and alternate aviation fuels with comprehensive two-dimensional gas chromatography accurate mass quadrupole time-of-flight mass spectrometry," *Energy & Fuels*, vol. 31, no. 5, pp. 4886–4894, 2017. 17

[116] K. Chatelain, A. Nicolle, A. Ben Amara, L. Starck, and L. Catoire, "Structure–reactivity relationships in fuel stability: Experimental and kinetic modeling study of isoparaffin autoxidation," *Energy & fuels*, vol. 32, no. 9, pp. 9415–9426, 2018. 18

[117] K. Kuo, *Principles of combustion*. John Wiley, 2005. [Online]. Available: https://books.google.co.uk/books?id=jAYoAQAAMAAJ 21, 22, 35, 37, 38, 39, 41, 44

[118] A. Burcat, W. Gardiner, G. Dixon-Lewis, M. Frenklach, R. Hanson, S. Salimian, J. Troe, J. Warnatz, and R. Zellner, *Combustion Chemistry*. Springer New York, 2012. [Online]. Available: https://books.google.co.uk/books?id=VF4FCAAAQBAJ 21

[119] T. Turányi and A. Tomlin, *Analysis of Kinetic Reaction Mechanisms*. Springer Berlin Heidelberg, 2014. [Online]. Available: https://books.google.co.uk/books?id=11sEBgAAQBAJ 21, 23, 31, 34

[120] S. Arrhenius, "Über die reaktionsgeschwindigkeit bei der inversion von rohrzucker durch säuren," *Zeitschrift für physikalische Chemie*, vol. 4, no. 1, pp. 226–248, 1889. 22

[121] F. A. Lindemann, S. Arrhenius, I. Langmuir, N. Dhar, J. Perrin, and W. M. Lewis, "Discussion on "the radiation theory of chemical action"," *Transactions of the Faraday Society*, vol. 17, pp. 598–606, 1922. 23

[122] P. Atkins and J. de Paula, *Atkins' Physical Chemistry*. OUP Oxford, 2010. [Online]. Available: https://books.google.co.uk/books?id=BV6cAQAAQBAJ 24

[123] R. J. Kee, J. F. Grcar, M. D. Smooke, J. A. Miller, and E. Meeks, "Premix: a fortran program for modeling steady laminar one-dimensional premixed flames," *Sandia National Laboratories Report*, no. SAND85-8249, 1985. 28

[124] R. J. Kee, G. Dixon-Lewis, J. Warnatz, M. E. Coltrin, and J. A. Miller, "A fortran computer code package for the evaluation of gas-phase multicomponent transport properties," *Sandia National Laboratories Report SAND86-8246*, vol. 13, pp. 80 401–1887, 1986. 29

[125] A. E. Lutz, R. J. Kee, and J. A. Miller, "SENKIN: A FORTRAN program for predicting homogeneous gas phase chemical kinetics with sensitivity analysis," Sandia National Labs., Livermore, CA (USA), Tech. Rep., 1988. 30

[126] D. G. Goodwin, R. L. Speth, H. K. Moffat, and B. W. Weber, "Cantera: An object-oriented software toolkit for chemical kinetics, thermodynamics, and transport processes," https://www.cantera.org, 2018, version 2.4.0. 31

[127] C. W. Gao, J. W. Allen, W. H. Green, and R. H. West, "Reaction mechanism generator: Automatic construction of chemical kinetic mechanisms," *Computer Physics Communications*, vol. 203, pp. 212–225, 2016. 31, 205

[128] C. K. Law, *Combustion physics*. Cambridge university press, 2010. 33, 37, 38, 39, 40, 41, 42, 43, 81

[129] W. H. Green. (Accessed: 23 July 2019) Combustion, fuels, and chemistry kinetics. [Online]. Available: https://cefrc.princeton.edu/combustion-summer-school/archived-programs/2017-session/lecture-notes 33

[130] J. A. Manion, R. E. Huie, R. D. Levin, D. R. B. Jr., V. L. Orkin, W. Tsang, W. S. McGivern, J. W. Hudgens, V. D. Knyazev, D. B. Atkinson, E. Chai, A. M. Tereza, C.-Y. Lin, T. C. Allison, W. G. Mallard, F. Westley, J. T. Herron, R. F. Hampson, and D. H. Frizzell. (Accessed: 25 July 2019) Nist chemical kinetics database, nist standard reference database 17, version 7.0. [Online]. Available: https://kinetics.nist.gov/kinetics/index.jsp 34

[131] Z. Reyno-Chiasson, N. Nettyam, G. Goteng, M. Speight, B. Lee, S. Baskaran, J. Oreluk, A. Farooq, H. Im, M. Frenklach *et al.*, "Cloudflame and prime: accelerating combustion research in the cloud," in *9th International Conference on Chemical Kinetics, Ghent, Belgium*, 2015. 34

[132] B. W. Weber and K. E. Niemeyer, "Chemked: A human-and machine-readable data standard for chemical kinetics experiments," *International Journal of Chemical Kinetics*, vol. 50, no. 3, pp. 135–148, 2018. 34

[133] E. Blurock. (Accessed: 25 July 2019) Chemconnect. [Online]. Available: www.chemicalkinetics.info 34

[134] A. Kéromnès, W. K. Metcalfe, K. A. Heufer, N. Donohoe, A. K. Das, C.-J. Sung, J. Herzler, C. Naumann, P. Griebel, O. Mathieu *et al.*, "An experimental and detailed chemical kinetic modeling study of hydrogen and syngas mixture oxidation at elevated pressures," *Combustion and Flame*, vol. 160, no. 6, pp. 995–1011, 2013. 35, 36

[135] T. Varga, T. Nagy, C. Olm, I. G. Zsély, R. Pálvölgyi, É. Valkó, G. Vincze, M. Cserháti, H. J. Curran, and T. Turányi, "Optimization of a hydrogen combustion mechanism using both direct and indirect measurements," *Proceedings of the Combustion Institute*, vol. 35, no. 1, pp. 589–596, 2015. 35, 36

[136] M. Ó Conaire, H. J. Curran, J. M. Simmie, W. J. Pitz, and C. K. Westbrook, "A comprehensive modeling study of hydrogen oxidation," *International journal of chemical kinetics*, vol. 36, no. 11, pp. 603–622, 2004. 35

[137] T. J. Kim, R. A. Yetter, and F. L. Dryer, "New results on moist co oxidation: high pressure, high temperature experiments and comprehensive kinetic modeling," in *Symposium (international) on combustion*, vol. 25, no. 1. Elsevier, 1994, pp. 759–766. 35

[138] M. Mueller, T. Kim, R. A. Yetter, and F. Dryer, "Flow reactor studies and kinetic modeling of the h2/o2 reaction," *International Journal of Chemical Kinetics*, vol. 31, no. 2, pp. 113–125, 1999. 35, 37

[139] S. Turns, *An introduction to combustion: concepts and applications*, ser. McGraw-Hill series in mechanical engineering. McGraw-Hill, 1996. [Online]. Available: https://books.google.co.uk/books?id=k-ZSAAAAMAAJ 36

[140] I. Glassman, R. A. Yetter, and N. G. Glumac, *Combustion*. Academic press, 2014. 36, 80, 81

[141] S. G. Davis, A. V. Joshi, H. Wang, and F. Egolfopoulos, "An optimized kinetic model of h2/co combustion," *Proceedings of the Combustion Institute*, vol. 30, no. 1, pp. 1283–1292, 2005. 37

[142] P. Saxena and F. A. Williams, "Testing a small detailed chemical-kinetic mechanism for the combustion of hydrogen and carbon monoxide," *Combustion and Flame*, vol. 145, no. 1-2, pp. 316–323, 2006. 37

[143] H. Sun, S. Yang, G. Jomaas, and C. K. Law, "High-pressure laminar flame speeds and kinetic modeling of carbon monoxide/hydrogen combustion," *Proceedings of the Combustion Institute*, vol. 31, no. 1, pp. 439–446, 2007. 37

[144] J. Li, Z. Zhao, A. Kazakov, M. Chaos, F. L. Dryer, and J. J. Scire Jr, "A comprehensive kinetic mechanism for co, ch2o, and ch3oh combustion," *International Journal of Chemical Kinetics*, vol. 39, no. 3, pp. 109–136, 2007. 37, 144, 145

[145] K. Hughes, T. Turányi, A. Clague, and M. Pilling, "Development and testing of a comprehensive chemical mechanism for the oxidation of methane," *International Journal of Chemical Kinetics*, vol. 33, no. 9, pp. 513–538, 2001. 40, 144

[146] D. Baulch, C. Cobos, R. Cox, P. Frank, G. Hayman, T. Just, J. Kerr, T. Murrells, M. Pilling, J. Troe *et al.*, "Summary table of evaluated kinetic data for combustion modeling: Supplement 1," *Combustion and flame*, vol. 98, no. 1-2, pp. 59–79, 1994. 41

[147] J. A. Miller and C. T. Bowman, "Mechanism and modeling of nitrogen chemistry in combustion," *Progress in energy and combustion science*, vol. 15, no. 4, pp. 287–338, 1989. 43

[148] S. Humer, A. Frassoldati, S. Granata, T. Faravelli, E. Ranzi, R. Seiser, and K. Seshadri, "Experimental and kinetic modeling study of combustion of jp-8, its surrogates and reference components in laminar nonpremixed flows," *Proceedings of the Combustion Institute*, vol. 31, no. 1, pp. 393–400, 2007. 45, 48, 53, 151, 200, 214

[149] K. Bacha, A. B. Amara, M. A. Fortunato, P. Wund, B. Veyrat, P. Hayrault, A. Vannier, M. Nardin, and L. Starck, "Original experimental approach for assessing transport fuel stability," *JoVE (Journal of Visualized Experiments)*, no. 116, p. e54361, 2016. 46

[150] K. J. Hughes, M. Pourkashanian, and C. W. Wilson, "Oh concentration measurements in a jet engine exhaust," *International Journal of Energy for a Clean Environment*, vol. 8, no. 4, pp. 305–320, 2007. 49, 102, 103

[151] D. Bradley and K. Matthews, "Measurement of high gas temperatures with fine wire thermocouples," *Journal of Mechanical Engineering Science*, vol. 10, no. 4, pp. 299–305, 1968. 55

[152] W. Kaskan, "The dependence of flame temperature on mass burning velocity," in *Symposium (International) on Combustion*, vol. 6, no. 1. Elsevier, 1957, pp. 134–143. 55, 57

[153] L. Chiappetta and M. Colket, "Design considerations for aerodynamically quenching gas sampling probes," *Journal of heat transfer*, vol. 106, no. 2, pp. 460–466, 1984. 60

[154] K. Maeda, M. L. Wall, and L. D. Carr, "Hyperfine structure of the hydroxyl free radical (oh) in electric and magnetic fields," *New Journal of Physics*, vol. 17, no. 4, p. 045014, 2015. 66

[155] J. Luque and D. Crosley, "Lifbase: Database and spectral simulation (version 2.0. 60, 2008)," *SRI International Rept. MP*, pp. 99–009, 1999. 67

[156] R. Schießl, U. Maas, A. Hoffmann, J. Wolfrum, and C. Schulz, "Method for absolute oh-concentration measurements in premixed flames by lif and numerical simulations," *Applied Physics B*, vol. 79, no. 6, pp. 759–766, 2004. 101, 102

[157] C. M. Arndt, R. Schießl, and W. Meier, "Oh planar laser-induced fluorescence measurements with high spatio-temporal resolution for the study of auto-ignition," *Applied optics*, vol. 58, no. 10, pp. C14–C22, 2019. 101, 102

[158] M. Tamura, P. A. Berg, J. E. Harrington, J. Luque, J. B. Jeffries, G. P. Smith, and D. R. Crosley, "Collisional quenching of ch (a), oh (a), and no (a) in low pressure hydrocarbon flames," *Combustion and Flame*, vol. 114, no. 3-4, pp. 502–514, 1998. 102, 106

[159] J. W. Daily, "Laser induced fluorescence spectroscopy in flames," *Progress in energy and combustion science*, vol. 23, no. 2, pp. 133–199, 1997. 103

[160] R. J. Cattolica, "Oh radical nonequilibrium in methane-air flat flames," *Combustion and Flame*, vol. 44, no. 1-3, pp. 43–59, 1982. 106, 107

[161] C. Saggese, K. Wan, R. Xu, Y. Tao, C. T. Bowman, J.-W. Park, T. Lu, and H. Wang, "A physics-based approach to modeling real-fuel combustion chemistry–v. nox formation from a typical jet a," *Combustion and Flame*, vol. 212, pp. 270–278, 2020. 119, 144, 216

[162] T. Varga, C. Olm, T. Nagy, I. G. Zsély, É. Valkó, R. Pálvölgyi, H. J. Curran, and T. Turányi, "Development of a joint hydrogen and syngas combustion mechanism based on an optimization approach," *International journal of chemical kinetics*, vol. 48, no. 8, pp. 407–422, 2016. 143

[163] K. Hughes, A. Tomlin, E. Hampartsoumian, W. Nimmo, I. G. Zsély, M. Ujvári, T. Turányi, A. Clague, and M. Pilling, "An investigation of important gas-phase reactions of nitrogenous species from the simulation of experimental measurements in combustion systems," *Combustion and Flame*, vol. 124, no. 4, pp. 573–589, 2001. 144

[164] P. Glarborg, J. A. Miller, B. Ruscic, and S. J. Klippenstein, "Modeling nitrogen chemistry in combustion," *Progress in Energy and Combustion Science*, vol. 67, pp. 31–68, 2018. 144

[165] Y. Chang, M. Jia, Y. Liu, Y. Li, and M. Xie, "Development of a new skeletal mechanism for n-decane oxidation under engine-relevant conditions based on a decoupling methodology," *Combustion and Flame*, vol. 160, no. 8, pp. 1315–1332, 2013. 144, 216

[166] C. K. Westbrook, W. J. Pitz, O. Herbinet, H. J. Curran, and E. J. Silke, "A comprehensive detailed chemical kinetic reaction mechanism for combustion of n-alkane hydrocarbons from n-octane to n-hexadecane," *Combustion and flame*, vol. 156, no. 1, pp. 181–199, 2009. 144

[167] S. J. Klippenstein, L. B. Harding, M. J. Davis, A. S. Tomlin, and R. T. Skodje, "Uncertainty driven theoretical kinetics studies for ch3oh ignition: Ho2+ ch3oh and o2+ ch3oh," *Proceedings of the Combustion Institute*, vol. 33, no. 1, pp. 351–357, 2011. 144

[168] H. Wang, R. Xu, K. Wang, C. T. Bowman, R. K. Hanson, D. F. Davidson, K. Brezinsky, and F. N. Egolfopoulos, "A physics-based approach to modeling real-fuel combustion chemistry-i. evidence from experiments, and thermodynamic, chemical kinetic and statistical considerations," *Combustion and Flame*, vol. 193, pp. 502–519, 2018. 145, 216

[169] R. Xu, K. Wang, S. Banerjee, J. Shao, T. Parise, Y. Zhu, S. Wang, A. Movaghar, D. J. Lee, R. Zhao *et al.*, "A physics-based approach to modeling real-fuel combustion chemistry–ii. reaction kinetic models of jet and rocket fuels," *Combustion and Flame*, vol. 193, pp. 520–537, 2018. 145, 177, 216

[170] D. Pugh, P. Bowen, A. Crayford, R. Marsh, J. Runyon, S. Morris, and A. Giles, "Catalytic influence of water vapor on lean blow-off and nox reduction for pressurized swirling syngas flames," *Journal of Engineering for Gas Turbines and Power*, vol. 140, no. 6, 2018. 145

[171] KAUST Clean Combustion Research Center, "Flame Speeds of Real Fuels," Accessed: 18 January 2020. [Online]. Available: https://ccrc.kaust.edu.sa/aramco/Pages/flame-speed.aspx 175

[172] A. G. Clements, personal communication, 21 December 2016. 175

[173] E. Ranzi, A. Frassoldati, A. Stagni, M. Pelucchi, A. Cuoci, and T. Faravelli, "Reduced kinetic schemes of complex reaction systems: fossil and biomass-derived transportation fuels," *International Journal of Chemical Kinetics*, vol. 46, no. 9, pp. 512–542, 2014. 177

[174] ASTM, "ASTM D7545," Accessed:24 January 2020. [Online]. Available: https://compass.astm.org/EDIT/html_annot.cgi?D7545+14(2019)e1 196

[175] Anton Paar, "PetroOxy Oxidation Stability Tester," Accessed: 4 February 2020. [Online]. Available: https://www.anton-paar.com/?eID=documentsDownload&document=54739&L=0 196

[176] The Engineering Tool Box, "Vapor and saturation pressure for some common liquids," Accessed:30 January 2020. [Online]. Available: https://www.engineeringtoolbox.com/vapor-pressure-d_312.html 198

[177] G. Bolshakov, "The effect of organic sulfur compounds on oxidation processes of hydrocarbon fuels," *Sulfur Reports*, vol. 7, no. 5, pp. 379–392, 1987. 199

[178] D. W. Naegeli, "The role of sulfur in the thermal stability of jet fuel," in *ASME 1999 International Gas Turbine and Aeroengine Congress and Exhibition.* American Society of Mechanical Engineers Digital Collection, 1999. 199

[179] M. Bernabei, G. Bocchinfuso, P. Carrozzo, and C. De Angelis, "Determination of phenolic antioxidants in aviation jet fuel," *Journal of Chromatography A*, vol. 871, no. 1-2, pp. 235–241, 2000. 205

[180] A. G. Clements, personal communication, 28 May 2019. 206, 243

[181] N. J. Kuprowicz, S. Zabarnick, Z. J. West, and J. S. Ervin, "Use of measured species class concentrations with chemical kinetic modeling for the prediction of autoxidation and deposition of jet fuels," *Energy & fuels*, vol. 21, no. 2, pp. 530–544, 2007. 208

[182] Z. Liu, S. Tang, Z. Li, Z. Qin, S. Yuan, L. Wang, L. Wang, X. Zhang, and G. Liu, "An improved kinetic model for deposition by thermal oxidation of aviation hydrocarbon fuels," *Fuel*, vol. 258, p. 116139, 2019. 208

[183] A. Ben Amara, A. Nicolle, M. Alves-Fortunato, and N. Jeuland, "Toward predictive modeling of petroleum and biobased fuel stability: Kinetics of methyl oleate/n-dodecane autoxidation," *Energy & fuels*, vol. 27, no. 10, pp. 6125–6133, 2013. 208

Appendix A: PetroOXY Model Documentation [180]

1 Introduction

The PetroOxy experiments are set up so that a liquid fuel sample is heated and pressurised in pure O_2. As the O_2 reacts with the liquid sample, the pressure decreases. The rate of reaction with O_2 is then characterised by the length of time it takes for the pressure to drop by a specified percentage, allowing the comparison of thermal stability between different fuels.

2 Model development

In order to model this experimental approach, it is necessary to calculate how much O_2 dissolves into the liquid phase, and is therefore available to react. As the dissolved O_2 reacts, it is replaced by O_2 from the gas phase, which reduces the pressure. Everything is modelled assuming no spatial variations in concentration, and reaction progress is monitored across time.

Typical perfectly stirred reactor (PSR) calculations solve the following ordinary differential equations (ODEs) for species

$$\frac{\mathrm{d}Y_k}{\mathrm{d}t} = \frac{\dot{\omega}_k MW_k}{\rho} \tag{1}$$

where Y_k is the mass fraction for species k, $\dot{\omega}_k$ is the net molar production rate for species k from reactions, MW_k is the molecular weight of species k and ρ is the total density, usually calculated from the equation of state (EoS) model, which will often be the ideal gas model. For the liquid phase kinetics in this work, the density is assumed to be constant, and the ODE solver is instead used to integrate the simpler equation for molar concentration

$$\frac{\mathrm{d}[X_k]}{\mathrm{d}t} = \dot{\omega}_k \tag{2}$$

The concentration of O_2 in the liquid phase is assumed to obey Henry's law at all times, such that

$$[O_2] = \frac{P}{k_H} \tag{3}$$

where P is the gas pressure and k_H is the Henry's constant. Using the ideal gas law, this can be represented in terms of the number of moles of O_2 in the headspace as

$$[O_2] = \frac{n_{O_2} RT}{k_H V_h} \tag{4}$$

where n_{O_2} is the number of moles of O_2 in the headspace, R is the universal gas constant, T is the gas temperature (kept constant throughout) and V_h is the volume of the headspace.

It is assumed that any consumption of O_2 in the liquid phase is instantaneously replenished by Henry's law, so any chemical consumption of O_2 is directly taken from the

gas-phase, so the consumption of n_{O_2} can be described by

$$\frac{\mathrm{d}n_{O_2}}{\mathrm{d}t} = \dot{\omega}_{O_2}V_s - \frac{\mathrm{d}[O_2]}{\mathrm{d}t}V_s \tag{5}$$

where V_s is the volume of the liquid sample. The first term on the right hand side of Equation (5) represents any chemical consumption of O_2 and the second term represents any O_2 absorbed (or released) from the liquid phase. By differentiating Equation (4) and substituting it into Equation (5) produces

$$\frac{\mathrm{d}n_{O_2}}{\mathrm{d}t} = \dot{\omega}_{O_2}V_s - \frac{\mathrm{d}n_{O_2}}{\mathrm{d}t}\frac{RTV_s}{k_H V_h} \tag{6}$$

Rearranging Equation (6) gives

$$\frac{\mathrm{d}n_{O_2}}{\mathrm{d}t} = \frac{\dot{\omega}_{O_2}V_s}{1 + \frac{V_s RT}{V_h k_H}} \tag{7}$$

The set of ODEs to solve are now Equation (2) for each specie, and Equation (7) for the number of moles of O_2 in the headspace (and thus the pressure of the system).

Finally, the total volume, V_t, of the PetroOxy is kept constant at 27.7 ml. Nominally, the fuel sample is measured to be 5 ml. The thermal expansion of the fuel sample is taken into account based on the density of the fuel at standard conditions and at elevated temperature, usually at 413 K, and the volume of the headspace is calculated as $V_h = V_t - V_s$.

3 Implementation

The implementation is based on the custom ODE example from the Cantera installation. Cantera is used for the basic thermodynamic and kinetic calculations, and the underlying system of equations are solved using the SciPy integrator. The solution is provided in the form of two python scripts, one containing the base reactor class, and the other containing the case information for each run.

The base `PetroOxyReactor` class contains all the code to call up the SciPy integrator and to initialise and write out results. The `PetroOxyODE` class is used to return the $\frac{\mathrm{d}Y}{\mathrm{d}t}$ required for the ODE solver, Equations (2) and (7). The file to run the reactor contains all the information to run a single case. Ideally, all runs should be made with the same `PetroOxyReactor` class, but with different settings to maintain consistency in the calculations.